Columnar-to-Equiaxed Grain Transition in Gas Tungsten Arc Welds in Aluminum-Copper Alloys

by

Jo Ann Clarke

A thesis
presented to the University of Waterloo
in fulfilment of the
thesis requirement for the degree of
Doctor of Philosophy
in
Mechanical Engineering

Waterloo, Ontario, Canada, 1998

0-612-30596-1

The University of Waterloo requires the signatures of all persons using or photocopying this thesis. Please sign below, and give address and date.

ABSTRACT

A columnar-to-equiaxed grain transition (CET) in gas tungsten arc (GTA) welds may reduce susceptibility to solidification cracking and brittle fracture and improve weld properties, such as toughness, ductility, and strength. A CET may be promoted in the weld pool by providing both (i) a supply of embryos from which equiaxed grains may develop and (ii) thermal conditions which favour the nucleation and growth of these embryos into equiaxed grains. However, the relationship between solidification and thermal conditions in the weld pool and process parameters which are controllable during welding is not well understood.

Since it is experimentally difficult to control and characterize the thermal conditions in a moving weld pool, numerical simulations of the macroscopic heat and fluid flow behaviour in the GTA weld pool were made using a detailed thermofluids model. This finite element model was formulated for three-dimensional, steady-state, moving GTA welds. The model incorporated temperature-dependent material properties, latent heat of fusion, Gaussian-distributed arc heat and current inputs, and heat losses due to convection and radiation. Turbulent fluid flow driven by buoyancy, electromagnetic forces, and surface tension temperature gradient forces was also modelled. The numerical thermofluids model was used to simulate moving GTA welds on thin sheets of aluminum-copper alloy using an experimentally realistic range of welding currents and steady-state welding speeds. Results from the simulations were post-processed to obtain estimates of weld pool thermal and solidification parameters, such as thermal gradient, interface growth rate, and growth undercooling, and thus predict the influence of welding process parameters on weld pool thermal conditions in Al-Cu alloys.

An analytical model was then evoked to predict the CET based on the thermal conditions in the weld pool as predicted by the numerical thermofluids model. The analytical CET model was based on Hunt's expression for the CET [1], modified for welding by incorporating the marginal stability dendrite growth model developed by Kurz *et al.* [2, 3]. The coupled thermofluids model and analytical model predicted that, given an adequate supply of nucleants, the welding conditions which favour a CET are (i) for a

given current, decreasing welding speed, or (ii) a high current and welding speed combination. It was also predicted that, although a large population density of heterogeneous nucleants having low nucleation undercooling will promote a CET for any of the welding conditions, particularly at higher solute contents, the welding conditions become increasingly important when the population density of heterogeneous nucleants is small or their efficacy decreases.

A complementary experimental program was performed to examine the model's predictions. Experiments were executed using autogenous, alternating-current GTA welding for a range of welding currents and steady-state welding speeds. Full-penetration welds were produced on thin plates to ensure two-dimensional heat flow and thus facilitate subsequent microstructural interpretation. Binary aluminum-copper alloys were selected as a model solidification system since this alloy system is well-characterized with respect to material properties and is also particularly susceptible to solidification cracking.

For the purpose of model validation, a series of experiments was performed in which thermocouples were embedded in Al-Cu plates prior to welding. Comparisons in GTA welds in Al-Cu alloys of experimental measurements of peak temperatures, temperature distributions, and weld widths, with predictions from the thermofluids model demonstrated excellent accord.

To study the CET, experiments were performed on thin plates of aluminum alloys containing 2 and 4% copper. These alloys were inoculated with varying amounts of TiB_2 particles which acted as nucleants for equiaxed grains. Measurements were made of % equiaxed grains in the weld bead and compared to the CET predictions made using the coupled thermofluids and analytical CET models. In comparison with experiment, the CET model was able to correctly predict whether or not a CET would occur and the general trends, as follows: (i) a fully columnar grain structure is produced at low current-welding speed combinations when TiB_2 levels are low, (ii) the % equiaxed grains in the weld bead increases with increasing TiB_2 content, (iii) the % equiaxed in the weld bead is greater for the alloy containing 4% Cu compared to that containing 2% Cu; *i.e.*, the % equiaxed increases with increasing Cu content, (iv) the % equiaxed is greater for welds performed with higher current-welding speed combinations, and (v) for a given current, the % equiaxed is greater with lower welding speed. The numerical comparison of the predicted values of % equiaxed with the experimental measurements accorded moderately. The discrepancies between the observed and predicted % equiaxed were suggested to be due to two factors: (i) the assumption of a constant value for ΔT_N, (ii) the assumption that the latent heat of fusion evolved by the growing equiaxed grains was conducted away and did not influence the thermal conditions in the weld pool.

The study revealed that the technique of coupling the predictions of a macroscopic thermofluids model with a microstructural model for the CET is an effective technique for the predictions of qualitative trends with respect to the CET as a function of GTA weld process parameters, alloy composition, and heterogeneous nucleant population density. Good correlation between experimental measurements of weld widths, peak temperatures, and temperature profiles and the numerical predictions was only possible when the effects of turbulent fluid flow were incorporated in the numerical model. The study demonstrated that a CET is favoured in GTA welds in Al-Cu alloys by (i) for a given current, decreasing welding speed, (ii) a high current and welding speed combination, (iii) increasing copper content, and (iv) increasing the wt% of the nucleating agent for equiaxed grains. Although a CET will be produced at all welding conditions in the presence of a large population density of heterogeneous nucleants, if the nucleants are inefficient or their numbers are low the welding conditions become increasingly important for CET promotion. Better agreement between the measured and predicted % equiaxed values would require (i) a more sophisticated CET model which is capable of accounting for a distributed nucleation undercooling, and (ii) an iterative coupling between the macroscopic thermofluids model and the CET model to account for the synergistic relationship between the latent heat of fusion released by the equiaxed grains ahead of the columnar grain interface and the growth of these equiaxed grains as well as the thermal gradients in the weld pool.

ACKNOWLEDGEMENTS

I wish to extend my warm and sincere appreciation to my supervisors, Hugh Kerr and Dave Weckman for their support and direction throughout my studies.

I express my sincere gratitude to Alcan International Limited for their technical support and their donation of the aluminum alloy and the welding power supply used in the study. In particular, my fond thanks go to Bill Christy for teaching me how to weld aluminum, and to Bernie Altshuller for his unceasing technical and moral support during the past four years.

Special thanks are due to Steve Hitchman for his technical assistance concerning all things computer-related; to Marius Vanreenen for technical support with the welding apparatus and data acquisition system; and especially to my dear friend and colleague, Tam Nguyen for the many insightful discussions and fruitful brain-storming sessions.

I heartily thank the Waterloo Centre for Groundwater Research, in particular Joel VanderKwaak, for the Iterative Sparse Matrix Solver.

Finally, I gratefully acknowledge the financial support of the Natural Sciences and Engineering Research Council of Canada throughout the research project.

Φύσις κρύπτεσθαι φιλεῖ

Ἡράκλειτος

NOMENCLATURE

a_o	interface diffusion length (m)
A	proportionality constant in Hunt's CET model [1] (μms^{-1}wt%$^{-1}$K^2)
A_{ij}	elements of the global coefficient matrix
A_t	characteristic area in vorticity-based turbulence model (m^2)
b_i	elements of the global load vector
$\vec{B}$	magnetic flux intensity (Wb/m^2)
B_θ	component of magnetic flux intensity in the θ direction
C	constant in vorticity-based turbulence model
C_E	eutectic composition (wt%)
C_L	composition of the liquid (wt%)
C_o	bulk alloy composition (wt%)
C_p	specific heat (J/kg·K)
C_S	composition of the solid (wt%)
D	diffusion coefficient (m^2/s)
D_i	interface diffusion coefficient (m^2/s)
D_o	pre-exponential term in the diffusion equation (m^2/s)
f_E	fraction of untransformed metal at the eutectic temperature
$\vec{F}_b$	buoyancy force (N/m^3)
$\vec{F}_{em}$	Lorentz force (N/m^3)
F_{I+},F_{I-}	calibration factors for rectified and filtered current signals
F_{V+},F_{V-}	calibration factors for rectified and filtered voltage signals
$\vec{F}_m$	Marangoni force (N)
F_x,F_y,F_z	body forces in the x, y, and z directions, respectively (N/m^3)
$\vec{g}$	gravitational constant (9.8 m/s^2)
G_L	thermal gradient in the liquid (K/m)
h	plate thickness (m)
h_c	convection coefficient (W/m^2·K)
ΔH_f	latent heat of fusion (J/kg)

$\vec{i},\vec{j},\vec{k}$	unit vectors in the x, y, and z directions, respectively
I	welding current (A)
I_+,I_-	positive and negative components of current (A)
$\vec{j}$	current density (A/m^2)
j_r	component of current density in the r direction (A/m^2)
j_z	component of current density in the z direction (A/m^2)
J_0,J_1	Bessel functions of the zeroth and first order, respectively
k	thermal conductivity (W/m·K)
k_{eff}	effective thermal conductivity (W/m·K)
k_o	equilibrium distribution coefficient, $k_o = C_S/C_L$
k_t	turbulent thermal conductivity (W/m·K)
k_v	velocity-dependent distribution coefficient
K	kinetic energy (m^2/s^2)
l	location on the T_L or T_E isotherm (m)
l_m	mixing length (m)
$l_{m,K}$	mixing length for transport of kinetic energy (m)
L	characteristic length in Rayleigh and Reynolds numbers (m)
m_L	equilibrium liquidus slope (K/wt%)
m_S	equilibrium solidus slope (K/wt%)
Ma	Marangoni number, $Ma = Re \times Pr = \dfrac{\partial\gamma}{\partial T}\left(\dfrac{\rho C_p L T_o}{\mu k}\right)$
n	number of nodes
$\vec{n}$	outward normal unit vector
N	elemental shape function
N_o	heterogeneous nucleant population density (nucleants/m^3)
P	Pressure (Pa)
P_i	interface Peclet number, $P_i = \dfrac{a_o R}{D_i}$
Pr	Prandtl number, $Pr = \dfrac{C_p\mu}{k}$
Pr_t	turbulent Prandtl number, $Pr_t = l_m/l_{m,K}$
q_a	heat flux from arc (W/m^2)

q_c	convective heat loss (W/m^2)
q_f	heat flux due to latent heat of fusion evolved at T_E (W/m^2)
q_r	radiative heat loss (W/m^2)
q_{uc}	heat flux due to latent heat of fusion evolved by equiaxed grains (W/m^2)
Q	activation energy for diffusion (J/mol)
Q	volumetric heat source due to ohmic heating (W/m^3)
r	radius of equiaxed grains (m)
r_a	radial distance from the arc centreline (m)
r_{tip}	dendrite tip radius (m)
R	growth rate of columnar front (m/s)
R_e	growth rate of equiaxed grains (m/s)
R_g	gas constant (8.31 J/mol)
Ra	Rayleigh number, $Ra = \frac{\rho^2 C_p \beta \vec{g}(T_2 - T_1) L^3}{k\mu}$
Re	Reynolds number, $Re = \frac{\rho U L}{\mu}$
Re_t	turbulent Reynolds number, $Re_t = \mu_t/\mu$
$REC(i)$	recorded data aquisition signal (V)
RES	residual for a system of equations
RMS	root mean square of all residuals in a system of equations
t	time (s)
T	temperature (K)
T_e	equilibrium eutectic temperature (K)
T_L	equilibrium liquidus temperature (K)
$T_L(C_o)$	equilibrium liquidus temperature at composition C_o (K)
T_m	melting temperature of a pure metal (K)
T_o	initial plate temperature (K)
T_r	reference temperature (K)
T_S	equilibrium solidus temperature (K)
T_∞	ambient temperature (K)
ΔT	growth undercooling (K)

ΔT_C	growth undercooling of columnar front (K)
ΔT_N	heterogeneous nucleation undercooling (K)
ΔT_o	equilibrium freezing range (K)
u,v,w	velocity components in the x,y, and z directions, respectively (m/s)
U	constant velocity in the x direction (m/s)
v_{ws}	welding speed (m/s)
V	welding voltage (V)
V_d	volume of the solution domain (m^3)
w_p	weld pool width (m)
x,y,z	Cartesian coordinates of the solution domain (m)
x_{uc}	length of undercooled zone (m)
α	fraction of solid formed per Kelvin (K^{-1})
β	thermal expansion coefficient (K^{-1})
γ	surface tension (N/m)
Γ	Gibbs-Thompson parameter (K·m)
ϵ	emissivity
ϵ	dissipation rate in $K - \epsilon$ model (m^2/s^3)
η	process efficiency
θ	angle between welding direction and local crystal growth direction (rad)
λ	wavelength
λ_i	wavelength of instability of a perturbed interface
μ	liquid viscosity (Pa · s)
μ_{eff}	effective liquid viscosity (Pa·s)
μ_m	magnetic permeability (Henry/m)
μ_t	turbulent viscosity (Pa·s)
ρ	density (kg/m^3)
σ	Stefan-Boltzmann constant (5.6696×10^{-8} $W/K^4 \cdot m^2$)
σ_j	distribution coefficient for current flux (m)
σ_h	distribution coefficient for arc heat flux (m)

τ_{ij}	components of the shear stress tensor (N/m^2)
ϕ_i	elements of the field variable solution vector
ϕ	volume fraction
ϕ_e	extended volume fraction
$\vec{\omega}$	vorticity (s^{-1})

Contents

List of Tables

List of Figures

Chapter 1

INTRODUCTION

Welding is the most ubiquitous joining technique for metals. Welded construction encompasses such diverse applications as space vessels, automobiles, and microelectronics. As a joining technique for metals, welding is unmatched in joint quality, versatility, cost, and growth potential compared to other mechanical fastening techniques [4].

Of the non-solid-state joining techniques, fusion welding is the most important [5]. Fusion welding is the coalescence of two metallic parts due to a heat source applied at the joint. This incident heat flux causes melting followed by solidification of the metal in the proximity of the joint. While there are numerous fusion welding processes which employ a filler metal to add reinforcement to the weld bead, gas tungsten arc (GTA) welding is a fusion welding process that employs a tungsten electrode which is not consumed during welding. GTA welding may be non-autogenous, *i.e.*, filler metal may be introduced into the melt; however, autogenous GTA welding is the process chosen for the present study due to its inherent simplicity compared to other fusion welding techniques.

A schematic of the GTA welding process is shown in Figure 1.1. The torch holds a tungsten electrode a predetermined distance above a metallic workpiece. An electric arc is struck between the electrode and the workpiece. An inert gas, such as argon, is directed in a laminar stream through the nozzle and becomes ionized by the arc, producing a plasma. This plasma imparts thermal energy to the workpiece which causes melting of the base metal. The inert gas stream also shields the molten metal from reactive

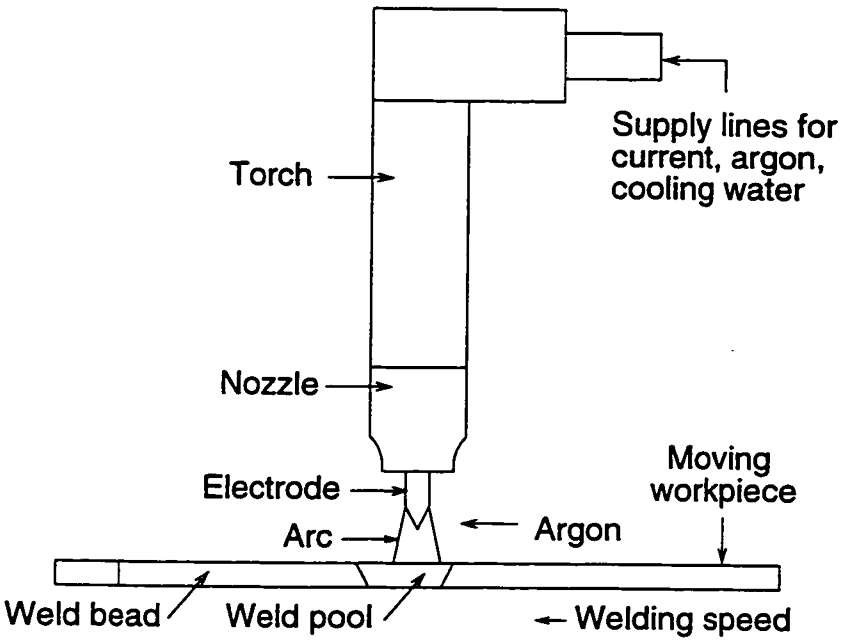

Figure 1.1: Schematic of the GTA welding process.

elements, such as oxygen, in the air. As the workpiece travels forward at a steady-state welding speed, the arc produces a molten weld pool which solidifies after the arc has passed to produce the weld bead.

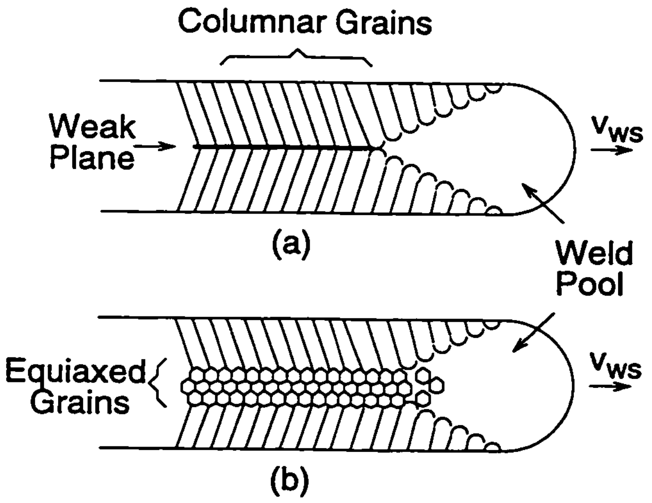

Figure 1.2: Solidification of a weld pool with (a) columnar grains and (b) a CET.

Under normal welding conditions, solidification of a GTA weld often results in a columnar grain structure, as depicted in Figure 1.2(a). The alignment of grain boundaries along the centreline produces a continuous, often relatively weak plane which may be susceptible to brittle fracture or solidification cracking [6]. The presence of equiaxed grains in the fused zone, as shown in Figure 1.2(b), may reduce the susceptibility to cracking and improve mechanical properties, such as toughness, ductility, and strength, compared to welds in which only columnar grains are present [7]. A columnar-to-equiaxed grain transition, or CET, may be promoted in a weld pool by providing both (i) a supply of embryos or nucleants from which equiaxed grains may develop, and (ii) thermal conditions which favour the nucleation and growth of these embryos into equiaxed grains such that the continued growth of the columnar grains is blocked [8].

Figure 1.3(a) is a photomicrograph of a GTA welded specimen of Al-2%Cu exhibiting a columnar grain structure with a centreline solidification crack. Figure 1.3(b) is a micrograph of a GTA welded specimen of Al-2%Cu which was inoculated with 0.015% TiB_2 and exhibits a CET with 50% equiaxed grains.

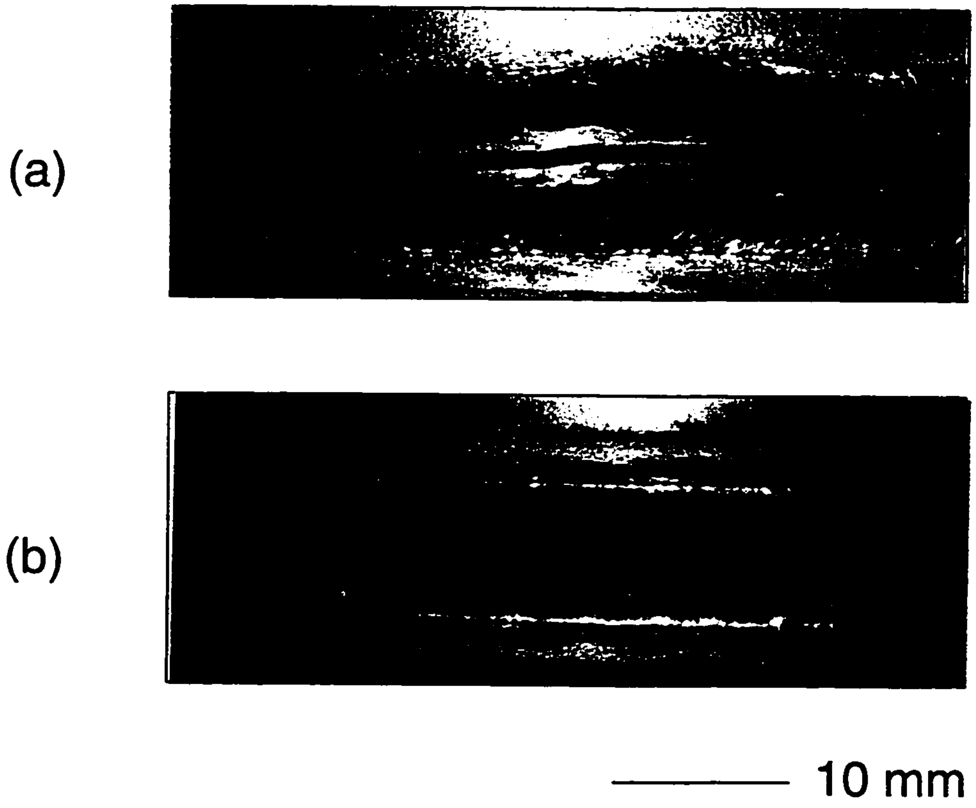

Figure 1.3: GTA welded specimens of Al-2%Cu exhibiting (a) columnar structure with a centreline solidification crack (b) a weld with 50% equiaxed grains.

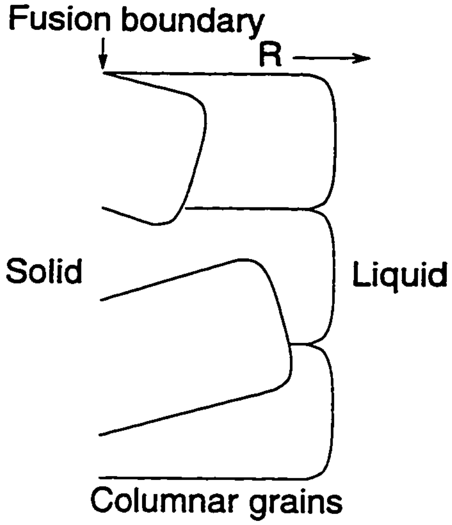

Figure 1.4: Solidification of columnar grains at the interface.

The initial stage of the weld pool solidification process is depicted schematically in Figure 1.4. Solidification of the weld initiates by epitaxial growth from base metal grains at the fusion boundary. Columnar grain growth proceeds in the direction of steepest thermal gradient in the liquid, G_L, at a local growth rate R. Those grains with their preferred growth direction (<100> for cubic crystals) oriented parallel to the steepest thermal gradient in the liquid will soon outgrow the grains with other crystal orientations.

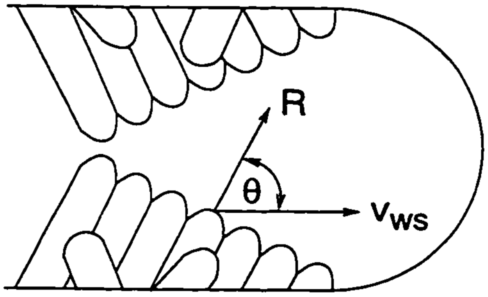

Figure 1.5: Schematic of weld pool indicating θ.

For a weld, R varies around the weld pool tail but is related to the welding speed, v_{ws}, and the shape of the weld pool according to [5]

$$R = v_{ws} \cos\theta \tag{1.1}$$

where θ is the angle between the welding direction and the local crystal growth direction, as depicted in Figure 1.5. Thus, values of R will range from approximately 0 at the fusion boundary to v_{ws} at the weld pool tail.

As the columnar grains solidify, solute is rejected into the liquid directly ahead of the solid/liquid interface. This solute will accumulate and eventually produce a steady-state, solute-enriched diffusion boundary layer ahead of the solid/liquid interface, as shown in Figure 1.6(a). As indicated in the phase diagram in Figure 1.6(b), this local change in the composition of the liquid will lower the local equilibrium liquidus temperature, T_L, compared to that of the bulk liquid, $T_L(C_o)$, since the local equilibrium liquidus temperature is a function of composition [9]:

$$T_L = T_L(C_o) - m_L(C_o - C_L) \tag{1.2}$$

where C_o is the bulk composition and m_L is the liquidus slope. The resultant new equilibrium liquidus temperature profile is shown in Figure 1.6(c).

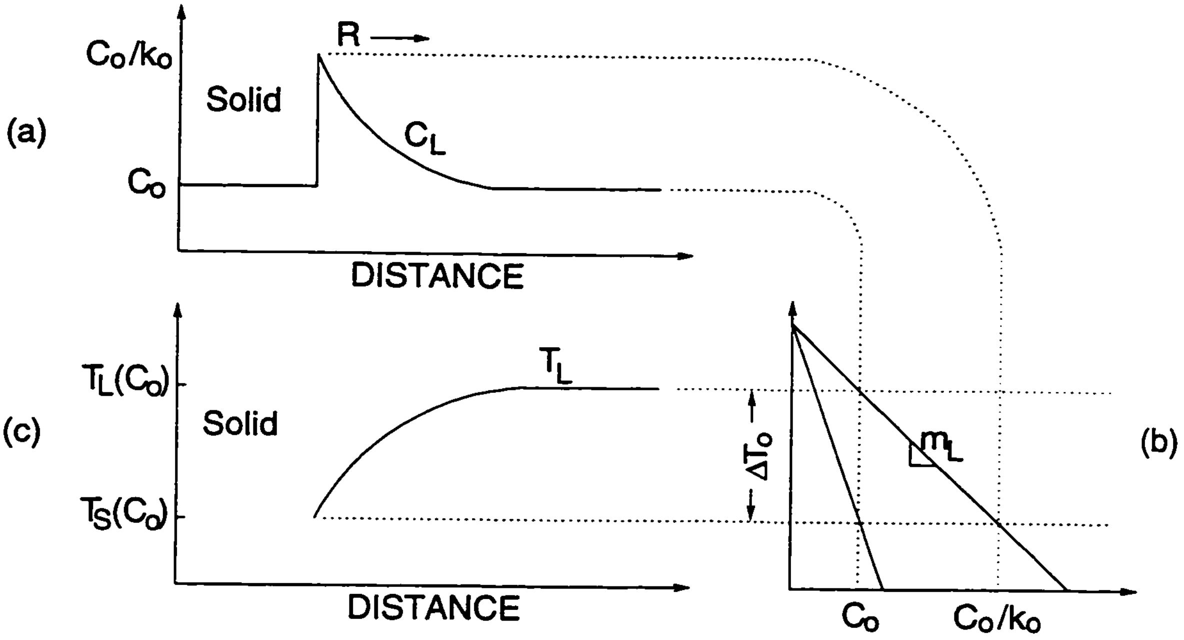

Figure 1.6: (a) Solute accumulation ahead of the solid/liquid interface. (b) Equilibrium phase diagram. (c) Variation in equilibrium liquidus temperature. (After [9].)

As indicated in Figure 1.7(a), if the actual temperature gradient in the liquid is higher than the new liquidus temperature profile, then a planar interface is stable. This is because any naturally occurring perturbation due to a random disturbance of the interface will be growing into a liquid having a temperature above T_L; thus, the perturbation will melt back. However, depending on the magnitudes of the interface growth rate, R, and the local thermal gradient in the liquid, G_L, compared to T_L, there may exist a region ahead of the solid/liquid interface in which the actual temperature is below that of T_L for that local composition, as shown in Figure 1.7(b). This region, shown cross-hatched in Figure 1.7(b), is termed 'constitutionally undercooled'. Any interface perturbation growing in this constitutionally undercooled zone will be stable since it remains below T_L, and the interface will develop a cellular morphology as shown in Figure 1.7(b). With increased constitutional undercooling, the interface morphology changes from cellular to dendritic, as shown in Figure 1.7(c).

Mathematically, for an interface solidifying under steady-state conditions, a zone of constitutional undercooling exists if [9]

$$G_L/R < \frac{\Delta T_o}{D}$$

$$< \frac{m_L C_o(k_o - 1)}{k_o D} \tag{1.3}$$

where ΔT_o is the equilibrium freezing range at C_o, D is the diffusion coefficient of the solute in the liquid.

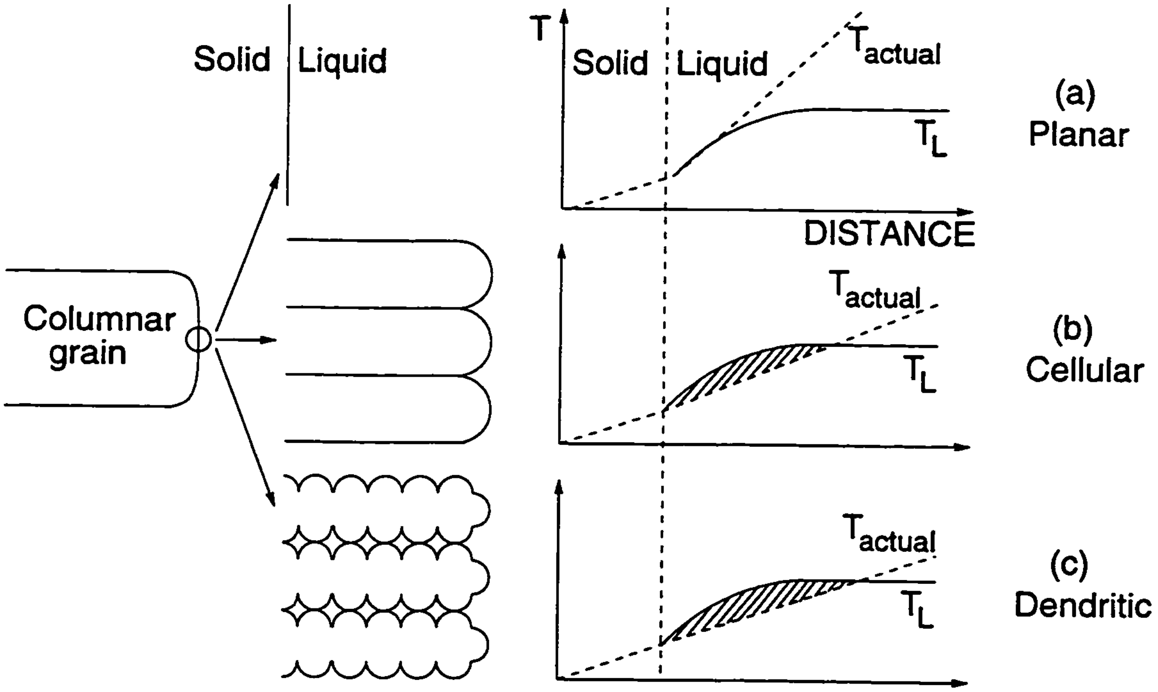

Figure 1.7: Possible interface morphologies of the solidifying columnar grain with increasing constitutional undercooling.

The foregoing discussion applies for alloys which have an equilibrium distribution coefficient, k_o, less than unity. Here, $k_o = C_S/C_L$, where C_S and C_L are the compositions of the solid and liquid phases in equilibrium at a given temperature, respectively. Often k_o is reasonably constant over a large temperature range, as was assumed in the present work.

After the solid/liquid interface has broken down and the cellular or dendritic morphology has developed, solute can diffuse laterally and the constitutionally undercooled zone is largely eliminated [9]. Thus the temperature profiles in Figure 1.7(b) and (c) are hypothetical. However, the solidification still requires a growth undercooling, ΔT_C. This undercooling is comprised primarily of 'solutal undercooling' due to the compositional difference between the solid and liquid at the cell or dendrite tip and 'Gibbs-Thomson undercooling' due to the cell or dendrite tip curvature [9].

In the present study, the solid/liquid interface has a fully developed dendritic morphology. Predictions of the growth undercooling, ΔT_C, for these well-developed dendrites generally take the form [2, 9]

$$\Delta T_C \propto (C_o R)^{\frac{1}{2}} \tag{1.4}$$

Several researchers, for example [1, 3, 10, 11], have developed empirical and analytical relations to predict growth undercooling for dendrites.

For example, Hunt's model [1] (presented later) employs an empirical expression for the growth undercooling, ΔT_C, of the aligned dendrites comprising the columnar front:

$$\Delta T_C = \left(\frac{C_o R}{A}\right)^{\frac{1}{2}} \tag{1.5}$$

The proportionality constant, $A = 300\ \mu\text{ms}^{-1}\text{wt\%}^{-1}\text{K}^2$, was experimentally determined during casting experiments using Al-3%Cu [12]. Since this empirical relation was correlated to casting experiments in which the interface growth rates were much smaller than those experienced in welding, this relation cannot be expected to apply in the present study.

An approximate analysis by Burden and Hunt [11] is

$$\Delta T_C = 2\left[\frac{-2m_L(1-k_o)\Gamma C_o R}{D}\right]^{\frac{1}{2}} \tag{1.6}$$

This expression was developed with the assumption of that the dendrites are growing at the 'extremum', *i.e.*, at their maximum growth rate. This is equivalent to assuming that the dendrites grow at the minimum undercooling. However, comparisons with experiment have shown that the actual dendrite undercooling is larger than predicted by a maximum growth rate criterion, and that instead the undercooling is closer to that predicted by a maximum dendrite tip radius criterion, termed 'marginal stability' [2, 3]. As a dendrite grows, its tip radius depends on some balance between a small radius which can reject solute efficiently and thus grow rapidly (maximum growth rate criterion), and a larger radius requiring less surface energy. The marginal stability criterion is based on the assumption that the dendrite will grow with the largest stable radius [9, 13].

An analytical 'marginal stability' expression for ΔT_C was developed by Kurz *et al.* [2, 3]:

$$\Delta T_C = m_L C_o \left(1 - \frac{1}{1 - (1 - k_o)\pi \sqrt{\dfrac{R\Gamma}{D \Delta T_o k_o}}} \right) \tag{1.7}$$

Equation 1.7 is applicable for interface growth rates in which

$$R > \frac{G_L D}{\Delta T_o k_o} \tag{1.8}$$

As shown later, typical growth rates and thermal gradients obtained during the welding simulations in the present study satisfy Equation 1.8.

The weld pool solidification process is depicted schematically in Figure 1.8. The aligned dendrites comprising the columnar grains grow at the local growth rate, R, in the direction of the steepest thermal gradient in the liquid G_L, with a growth undercooling, ΔT_C. Thus, the liquid directly ahead of the solid/liquid interface is undercooled below the equilibrium liquidus temperature of the alloy. Now, any nucleant in this region should begin to grow into an equiaxed grain if this local growth undercooling exceeds the nucleation undercooling ΔT_N. Hence, if $\Delta T_C > \Delta T_N$ and if there is an adequate population density of nucleants, N_o, equiaxed grains will grow and block the growth of the columnar grains, thereby producing a CET [5, 8, 14].

With respect to the CET, a larger columnar growth undercooling, ΔT_C, is desirable since this will enlarge the region within which equiaxed grains may nucleate and grow (*cf.* Figure 1.8) and thus increase the probability of a CET. Now, the G_L/R ratio given in Equation 1.3 is a good indicator of the conditions necessary for the destabilization of an

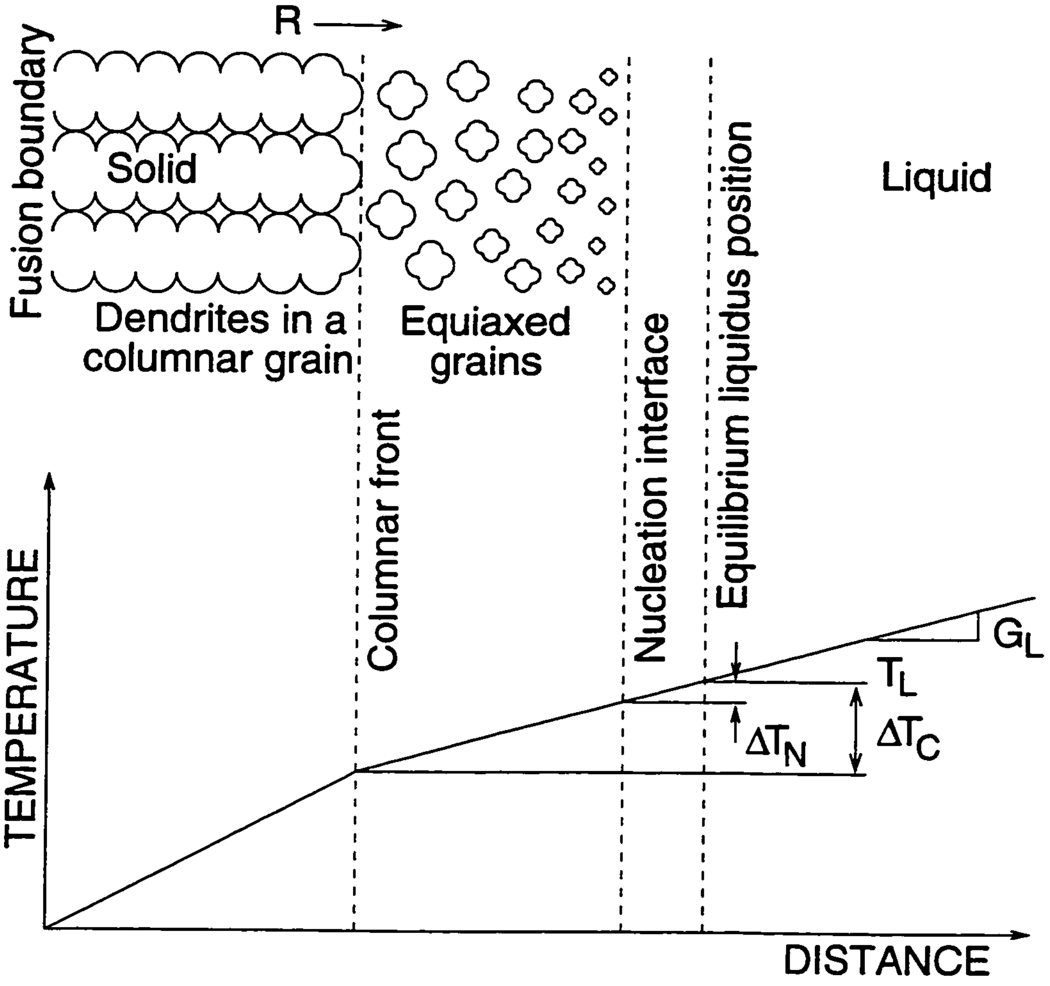

Figure 1.8: Solidification of columnar and equiaxed grains at the weld pool interface.

initially planar interface and the morphological change from a planar to cellular to dendritic interface. It should be noted, however, that since the constitutional undercooling is largely eliminated once the solid/liquid interface has destabilized, its contribution to the growth undercooling of the columnar front, ΔT_C, is very small. Instead, the effect of G_L (as shown schematically in Figure 1.8) on the relative positions of possible columnar and equiaxed interfaces must be considered, as discussed in the next section. Thus the G_L/R ratio as given in Equation 1.3 cannot be used to predict the CET.

The relationship between the solidification parameters relevant to the CET, namely thermal gradient in the liquid, G_L, solid/liquid interface velocity, R, and growth undercooling of the columnar grain front, ΔT_C, and the controllable welding process parameters, such as current, I, and steady-state welding speed, v_{ws}, is not well understood. The integrity and performance of a weldment depends ultimately on the microstructure of the weld bead after it solidifies; therefore, characterization of this relationship between the controllable welding process parameters and the solidification process is paramount to producing a desirable microstructure. Arc welding processes, such as GTA welding, may appear simple, but in fact involve many complex scientific principles, as discussed later. Moreover, it is experimentally difficult to control and characterize the solidification process, particularly in a moving weld pool. Analytical and numerical models of the welding process may provide some insight into the relationship between the welding parameters and the solidification process, but only if they incorporate the important relevant physical phenomena. In the present study, therefore, the relationship between the controllable welding process parameters and the solidification process was investigated by means of a numerical thermofluids model of the GTA welding process. The modelling predictions were compared with the results from a detailed experimental program.

Subsequent sections in this chapter comprise a review of the literature relevant to the present work, encompassing (i) modelling and experimental studies of the CET and (ii) modelling studies of GTA weld pool behaviour.

1.1 The Columnar-to-Equiaxed Grain Transition

1.1.1 Models for the CET

Many models have been developed to predict the occurrence of the CET in castings [15]-[29]. Some recent modelling research [30, 31] has also focussed on predictions of microstructure in welds, although not specifically the CET. The CET models may be loosely grouped, as follows:

- numerical models
- cellular automata models
- coupled macro/micro models
- analytical models (Hunt's model)

These models will be briefly described in the remainder of this section.

Numerical Models

Flood and Hunt [15, 16, 17] and Spittle and co-workers [18, 19] developed finite difference models to simulate the simultaneous growth of columnar and equiaxed grains in a casting. In these models, a cross-section of the casting was discretized into an array of control volumes over which conservation of enthalpy was imposed. A series of equiaxed grain embryos were placed ahead of the solid/liquid interface. During each time step of the simulation, the growth rate of the columnar grains was calculated based on their growth undercooling and the columnar front was allowed to advance at that rate.

As the critical nucleation undercooling for each equiaxed grain was exceeded, it also was allowed to grow. Once the volume fraction of equiaxed grains exceeded 50%, the columnar grain growth was assumed to be effectively blocked and thus only equiaxed grains continued to grow until the solution domain was completely solid.

In the work by Spittle and co-workers [18, 19], the equiaxed and columnar grains were assumed to grow at a fixed undercooling at equal growth rates. The latent heat of fusion evolved by the columnar and equiaxed grains was accounted for; however, fluid flow in the bulk of the casting was not modelled. In the work by Flood and Hunt [15, 16, 17], fluid flow in the bulk of the melt was not actually modelled; however, the effect of convection was emulated by decreasing the diffusion boundary layer ahead of the columnar grain front. The growth undercooling of the columnar front was assumed to depend on interface growth rate, R, and composition, C_o. This assumption was validated experimentally by Burden and Hunt [11, 12]. The release of latent heat of fusion by the columnar grains was modelled using the Scheil equation; however, the latent heat of fusion evolved by the equiaxed grains was assumed to be immediately conducted away due to the high thermal diffusivity of the metal.

These numerical CET models were used to study the effect of alloy composition, cooling rate, convection, and superheat on the cast microstructure. Although these models are very useful in providing insight into the effects of casting variables on the CET, they were designed specifically for castings which generally have much slower growth rates than in welding, and, as such, are not applicable to studying the CET in GTA welds. However, some of the features included in these models, such as fluid flow and the dependence of interface growth undercooling on composition and growth rate, are important considerations in a welding situation such as in the present work. In addition, due to the large numbers of heterogeneous nucleants that are present in the weld pool, the evolution of latent heat of fusion by equaxed grains may be expected to be significant.

Cellular Automaton Models

Spittle and co-workers [20, 21, 22] developed a probabilistic cellular automata model for predicting the effect of process and alloy parameters on grain structure in castings. The cellular automaton technique employs an array of microscopic scale lattice points or cells which initially correspond to liquid sites. During the simulation, the liquid sites transformed to solid sites depending on the imposed nucleation and growth conditions. The simulation resulted in predicted microstructures which clearly showed relative amounts and sizes of columnar and equiaxed grains.

More recently, Rappaz and co-workers [23, 24, 25] developed both two- and three-dimensional probabilistic models for predicting microstructure formation and the CET in castings which also used a cellular automaton technique. These models are very sophisticated in that they accounted for the influence of nucleation parameters, growth kinetics, alloy composition, cooling rate, and the preferential <100> growth direction of the dendrite trunks and arms.

Although cellular automaton CET models are sophisticated and account for many of the physical phenomena relevant to the solidification event as well as provide excellent correlation with casting experiments, the development of such models represents many years of research which prohibited their implementation in the current study. However, the implementation of such a sophisticated microstructural model would certainly represent an appropriate future direction of the present work.

Coupled Macro/Micro Models

Several researchers have coupled macroscopic heat transfer models with microstructural CET models. Beckermann and Wang [26] and Li and Anyalebechi [27] used a finite element heat transfer model to predict temperature fields and then invoked analytical expressions to predict the grain structure in castings. Gandin and Rappaz [28] coupled their cellular automaton model with a finite element model which was used to predict the temperatures at the cell locations. Recently, Rappaz and co-workers [29] applied this coupled model to predict the CET in a variety of solidification processes including laser remelting/welding of a steel plate. Although coupling of microstructural models with macroscopic heat transfer models is an effective means of studying microstructural evolution, until recently, this work has been restricted to castings.

Recent work by DebRoy and co-workers [30, 31] focussed on welding. Their model employed a finite difference algorithm to solve for heat and fluid flow in the weld pool. The predicted heating and cooling rates were then used in conjunction with a phase transformation model to predict the weld microstructure in low alloy steels; however, this model was not designed to predict the CET. This technique of coupling macroscopic heat and fluid flow predictions with an analytical microstructure model is an effective tool for microstructural predictions and would be easily implementable in the present study of GTA welding. However, for this to be possible, an analytical CET model, such as that developed by Hunt [1], would be required.

Hunt's model

Hunt [1] analysed the conditions necessary for the growth of equiaxed grains ahead of a columnar grain interface during directional solidification of a casting. This analysis permits the qualitative examination of the effects of solidification parameters, namely thermal gradient in the liquid, G_L, solid/liquid interface growth rate, R, alloy composition, C_o, and grain refiner efficacy, N_o and ΔT_N, on the CET.

Hunt's analysis assumed that equiaxed grains in an undercooled zone will grow at a rate

$$R_e = \frac{A(\Delta T_C)^2}{C_o} \tag{1.9}$$

Here, the proportionality constant, $A = 300\ \mu\text{ms}^{-1}\text{wt\%}^{-1}\text{K}^2$, was experimentally determined for Al-3%Cu castings [12]; however, in general, A is a function of liquidus slope, distribution coefficient, and solid/liquid surface energy. After a time t, a spherical equiaxed grain growing in the undercooled zone will reach a radius

$$r = \int_0^t R_e dt \tag{1.10}$$

Substituting Equation 1.9 for R_e in Equation 1.10 and changing the limits of integration gives

$$\begin{aligned} r &= \int_{\Delta T_N}^{\Delta T_C} \frac{A(\Delta T)^2}{R G_L C_o} d(\Delta T) \\ &= \frac{A[(\Delta T_C)^3 - (\Delta T_N)^3]}{3 R G_L C_o} \end{aligned} \tag{1.11}$$

Here, it is implicitly assumed that the growth undercooling of the equiaxed grains is equivalent to that of the columnar grains, ΔT_C.

Hunt [1] assumed that a volume fraction of $\phi = 0.49$ of equiaxed grains was sufficient to block columnar grain growth. To correct for the impingement of equiaxed grains upon each other, Hunt [1] used the extended volume fraction concept, *i.e.*, in a small time interval

$$d\phi = (1 - \phi)d\phi_e \tag{1.12}$$

$$\phi = 1 - \exp(-\phi_e) \tag{1.13}$$

thus $\phi_e = 0.66$, and so

$$\phi_e = \frac{4\pi r^3 N_o}{3} > 0.66 \tag{1.14}$$

where N_o is the number of nucleants per unit volume. Rearranging Equation 1.14 gives

$$r > 0.54 \left(\frac{1}{N_o}\right)^{\frac{1}{3}} \tag{1.15}$$

Substituting Equation 1.15 into Equation 1.11 results in a simple expression for predicting the CET; *i.e.*, a fully equiaxed grain structure is predicted when

$$G_L < 0.617 N_o^{\frac{1}{3}} \left[1 - \frac{(\Delta T_N)^3}{(\Delta T_C)^3}\right] \Delta T_C \tag{1.16}$$

The growth undercooling, ΔT_C, of the columnar grain front (also assumed to apply for equiaxed growth) is given by:

$$\Delta T_C = \left(\frac{C_o R}{A}\right)^{\frac{1}{2}} \tag{1.17}$$

Equation 1.16 is often plotted as $\log(R)$ versus $\log(G_L)$, as shown schematically in Figure 1.9(a). The equation predicts that, for a given C_o, N_o and ΔT_N, a CET is expected at low thermal gradients above a critical growth rate, *i.e.*, at low G_L and high R. Hunt's model also predicts that an increase in the population density of heterogeneous nucleants, N_o, a decrease in their nucleation undercooling, ΔT_N, or an increase in composition, C_o, is favourable to CET promotion, as shown in Figures 1.9(b), (c), and (d).

The effect of C_o on the CET may be more complex than represented in Figure 1.9(d). As mentioned earlier, the constant A in Equations 1.9 and 1.17 depends on other quan-

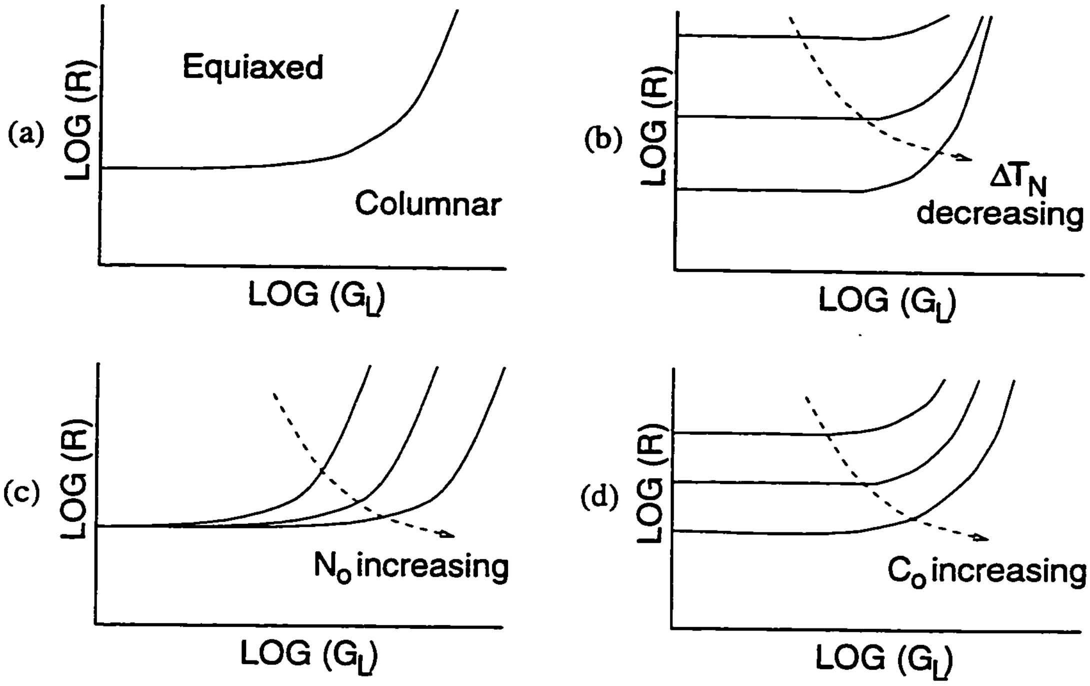

Figure 1.9: Schematic of Hunt's model [1] showing (a) predicted grain structure as a function of R and G_L (b) effect of ΔT_N (c) effect of N_o and (d) effect of C_o.

tities. For example, consider the approximate analysis by Burden and Hunt [11] (Equation 1.6). From this relation, it is seen that $\Delta T_C \propto [-m_L(1-k_o)C_o]^{1/2}$. Thus, ΔT_C does not necessarily increase (and a larger equiaxed zone will not necessarily occur) with increasing C_o, but also depends on the phase change behaviour of the material, *i.e.* whether m_L and k_o are positive or negative quantities.

Although Hunt's analytical model [1] was developed for castings, it captures the essence of the CET, irrespective of its application to either casting or welding. Furthermore, Hunt's model is easily adapted to the process parameters that are of interest in this study of GTA welding. As discussed previously, coupling macroscopic heat and fluid flow predictions with an analytical microstructure model represents an effective technique for studying the CET in welds.

1.1.2 Experimental Studies of the CET in Welds

As discussed previously, promoting the CET requires both a sufficient supply of nucleants as well as solidification conditions, namely a low thermal gradient and a high solid/liquid interface velocity, which will favour their nucleation and growth. Experimentally, attempts have been made to promote the CET in welds by influencing the weld pool thermal gradients and increasing the nucleant supply, as discussed subsequently.

Weld Pool Thermal Conditions

Early researchers, for example Sharir *et al.* [32] and Bardokin *et al.* [33], attempted to influence GTA weld pool thermal conditions and promote a CET by oscillating the arc and pulsing the arc current. Refined equiaxed grain structures were achieved in both cases. Sharir *et al.* [32] attributed the nucleation of equiaxed grains to local undercooling brought about by the displacement of the heat source and cycling of the current; however, exactly how this was accomplished was not clear. Alternatively, Bardokin *et al.* [33] proposed that the fine equiaxed grain structure was a consequence of fluctuations in the temperature gradient in the weld pool which produced a zone of constitutional undercooling ahead of the columnar front. As discussed in a previous section, constitutional undercooling is largely eliminated once the interface has destabilized, thus this explanation may be an oversimplification of the situation.

Many researchers [34]-[39] have studied the effect of varying heat input and welding speed on the CET in moving GTA welds. These investigations demonstrated that increasing both welding speed and heat input favours the production of equiaxed grains. It was proposed that these welding conditions favoured the CET by lowering the thermal gradients in the weld pool. These researchers estimated G_L along the weld centreline at the tail of the pool using an analytical model for heat conduction in moving welds derived by Rosenthal [40, 41]. However, this analytical model neglects such physical phenomena as latent heat of fusion evolution, fluid flow, temperature dependence of material properties, and the spatial distribution of the arc. In the most recent study by Villefuerte *et* *al.* [39], G_L was also estimated in ferritic stainless steel using a numerical heat transfer model and was found to be much lower than those values estimated using the analytical model. They attributed this discrepancy to the incorporation of latent heat of fusion in the numerical model. The use of analytical and numerical models to study weld pool thermal conditions will be discussed in detail in a later section.

Ganaha *et al.* [37] and Kou and Le [38] indicated that higher welding speeds and greater heat inputs favoured a CET in GTA welds on aluminum alloys, but that the presence of titanium as a heterogeneous nucleant was also important. Consistent with Hunt's model [1], Kou and Le [38] showed experimentally that although higher welding speeds increased both G_L and R, and larger heat inputs decreased G_L, the net effect was to decrease G_L and increase R, thus enhancing heterogeneous nucleation and promoting a CET. Kou and Le [38] proposed that the ratio G_L/R was an appropriate parameter to predict the CET and suggested that a low G_L/R value implies a larger constitutionally undercooled zone ahead of the columnar grain front, which they believed increases the possibility for nucleation of equiaxed grains.

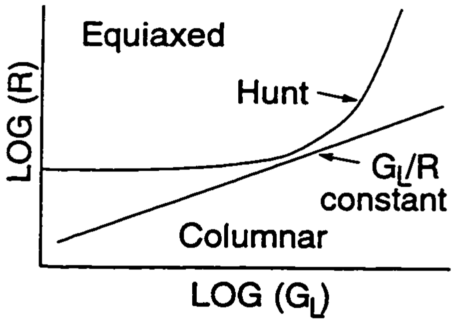

Figure 1.10: Schematic of Hunt's model with constant G_L/R.

The limitations to the approach of Kou and Le [38], as pointed out by Villefuerte *et al.* [39], are (i) they employed centreline values of growth rate and thermal gradient when, in fact, the CET may occur at some distance from the centreline, particularly when the pool becomes teardrop-shaped at high welding speeds, and (ii) using a minimum G_L/R criterion implies that the CET occurs as a straight line on a log(R) versus log(G_L) plot, as indicated in Figure 1.10. Hunt's model [1] (Equation 1.16 with $\Delta T_N = 0$) is also plotted in Figure 1.10. According to Hunt's model, the CET occurs when sufficient growth undercooling and sufficient nucleants are available to block columnar grain growth. Although N_o is generally fixed for a given alloy, sufficient undercooling is only possible above a critical value of R. In addition, the equiaxed grains require sufficient time to grow to a critical size, and this time is a function of G_L. Thus employing G_L/R to predict the CET represents an oversimplification. Furthermore, the G_L/R ratio may indicate the extent of the 'constitutionally' undercooled zone, but as this undercooling contributes little to the growth undercooling, G_L/R is not a good indicator for the CET.

The most serious shortcoming of the preceding research is that the changes brought about on the solidification parameters relevant to the CET, namely R, ΔT_C, and G_L, by changes in welding speed and heat input are unclear due to limitations in understanding of the relationships between the welding process parameters and these solidification parameters. Previous investigations were based on experimental examinations of the effects of the welding process parameters on the occurrence of a CET. However, they were not able to examine directly the effects of the welding process parameters on the solidification parameters, in particular G_L at the solid/liquid interface. Instead, estimates of G_L were made through the use of a simple analytical expression which neglects important physical phenomena such as latent heat of fusion, fluid flow, temperature dependence of material properties, and the spatial distribution of the arc, all of which are known to significantly influence G_L. Although it was often recognized that the welding conditions influence the local solidification conditions, until recently only analytical solutions of the temperature distributions were available.

Nucleant Supply

In welds, the nuclei for equiaxed grains have two general sources:

- nuclei composed of the base material, created by dendrite fragmentation, grain detachment, or surface nucleation; these grain fragments have $\Delta T_N \approx 0$ and will nucleate equiaxed grains if they survive in the melt and the correct thermal conditions are present, and
- heterogeneous nuclei composed of second-phase particles present in the melt which will nucleate equiaxed grains if the correct thermal conditions are available [8].

Experimentally, attempts have been made to increase the population density of nucleants in the weld pool in many ways. However, the specific mechanism for the nucleation event and the promotion of a CET in welds has been the subject of many studies.

Surface Nucleation occurs when undercooling at the weld pool surface causes solid nuclei to form which then sink into the weld pool due to their higher density [14, 42]. Surface nucleation to promote a CET was caused by Garland [42] in GTA welds in aluminum by directing a stream of argon gas at the molten weld pool ahead of the arc. He postulated that this cooled the surface sufficiently to allow the formation of solid nuclei ahead of the advancing solid/liquid interface. Ganaha and Kerr [36] also attributed the formation of some equiaxed grains in plain carbon steels to heterogeneous surface nucleation, since the high melt temperature of steel augments heat loss by radiation from the weld pool surface. Indeed, welds with larger surface areas contained more equiaxed grains. Surface nucleation was also observed by Villefuerte *et al.* [39, 43] in GTA welds in ferritic stainless steel. Again, this was attributed to increased undercooling due radiative heat loss from the pool surface which is increased by the presence of high emissivity surface oxides. However, as pointed out by Villefuerte and Kerr [43], the surface undercooling was not sufficient alone: the presence of TiN to form heterogeneous nucleants was also required. Furthermore, it was suggested that the surface oxides might also facilitate nucleation of the titanium-rich particles.

Grain Detachment is a mechanism by which small grains in the partially molten region of the heat affected zone detach and become entrained in the weld pool [8, 14, 44]. In GTA welds in aluminum, Pearce and Kerr [44] showed evidence that a CET was produced by grain detachment using electromagnetic stirring (EMS) of the weld pool.

Dendrite Fragmentation occurs by weld pool convection in the presence of branched dendrites. Sufficient convection dislocates dendrite fragments from the mushy zone and sweeps them into the pool where they grow into equiaxed grains when the thermal gradients permit [14]. Hallum and Baeslack [45] suggested that EMS produced grain refinement in GTA welds in titanium by causing dendrite fragmentation. Matsuda *et al.* [46] similarly found that EMS promoted the CET in aluminum GTA welds and attributed this to dendrite fragmentation. Garland [42] mechanically vibrated the torch to promote a CET, which he attributed to backwashing of the molten metal over the solidification interface, resulting in fragmentation of dendrites at the tail of the weld pool. Garland [42] also obtained significant grain refinement in stainless steel GTA weldments by pulsing the arc current. These current pulses were presumed to have caused growth rate fluctuations which, in turn, yielded solid nuclei by dendrite arm remelting and detachment. Kerr *et al.* [36, 47] suggested that EMS facilitates promotion of the CET by locally decreasing the thermal gradients in the pool and increasing the interface growth rate as well as providing nucleants for equiaxed grains by grain detachment and dendrite fragmentation. More recently, however, Villefuerte *et al.* [48], found no evidence of equiaxed grain formation by dendrite fragmentation despite the presence of highly branched dendrites in ferritic stainless steel GTA welds. This was thought to mean that dendrite fragments which may have been present remelted when they got close to the arc, or that the flow velocities were too low to cause fragmentation. When the CET did occur, there was evidence that it was caused by heterogeneous nucleation on TiN particles.

Heterogeneous Nucleation occurs by the nucleation of one phase on second-phase particles or at a surface (*e.g.*, grain boundary). This process is energetically more favourable than homogeneous nucleation since fewer atoms are required to form an embryo of critical radius required for survival [14]. Consistent with Hunt's model [1], it was found that the presence of heterogeneous nucleants ahead of the solidification front is not in itself sufficient for a CET, but that high heat input and high welding speeds are also required to produce the necessary low thermal gradients and high interface growth rates [37, 38, 44]. Heterogeneous nucleants can be provided in the weld pool by introducing filler wire containing inoculants into the weld pool, or by adding grain refiner during the casting of the base metal. In aluminum alloys, many researchers [34, 35, 37, 38, 44, 46, 49, 50] have found that equiaxed dendrites were formed around titanium- or zirconium-rich nuclei, while the nucleants of equiaxed dendrites in stainless steels were found to be rich in aluminum or titanium [39, 43, 47, 48, 51]. Heintze and McPherson [52] inoculated submerged arc welds (SAW) of C-Mn steel and found that equiaxed grains were nucleated on TiN particles. Hallum and Baeslack [45] inoculated titanium alloy GTA welds with

Ti-6Al-4V powder. They speculated that the powder additions reduced the melt temperature and lowered the thermal gradients near the tail of the weld pool, thus favouring equiaxed grain growth by heterogeneous nucleation on partially melted powder particles, though how exactly G_L was lowered was not clearly explained. Garland [42] inoculated mild steel SAWs with powdered Fe-Ti. He proposed that grain refinement was achieved through heterogeneous nucleation on TiC particles plus solutal undercooling due to Ti in solution. Similarly, Petersen [53] obtained an equiaxed structure in a series of arc welds in Cr-Ni stainless steels by inoculating with a filler metal containing Al-Ni, but it is not clear if these particles provided nucleants or increased the solutal undercooling.

Thus, introducing inoculation agents into the weld pool may affect the growth undercooling of the solid/liquid interface and the thermal gradients in the weld pool, as well as provide heterogeneous nucleants for equiaxed grains. However, these different possibilities generally have not been clearly differentiated in previous experimental work.

The issue of alloy composition is not separate from that of nucleation since alloying agents introduced into the melt may provide nucleants for equiaxed grains [39] as well as potentially increase the growth undercooling. Previous research with aluminum alloys by Matsuda *et al.* [34, 35] showed that increasing the alloy composition, C_o, favours a CET. This result is consistent with Hunt's model since, for many alloys having $k_o < 1$, an increase in C_o will enlarge the growth undercooling, ΔT_C, (Equation 1.4) which will increase the probability of a CET. These researchers performed moving GTA welds on sheets of pure aluminum and commercial aluminum alloys with varying compositions. They found that a CET did not occur in the pure aluminum sheets for any of the welding conditions. However, welds in commercial alloy sheets produced increasingly large equiaxed zones with increasing solute content. Furthermore, alloys having high solute content produced at CET at lower welding speeds and heat inputs than did the alloys with less solute, consistent with Hunt's model [1]. Thus, depending of the phase diagram behaviour of the alloy in question, increasing C_o will promote a CET.

Although the CET has been successfully promoted in welds, the precise mechanism is often not fully understood. While techniques such as EMS may be specifically designed to affect N_o, they also inherently modify the thermofluids conditions in the weld pool, such that it is not clear which effect, if any, is predominantly responsible for the CET in the weld for any given situation. Attempts have be made to characterize the effects on G_L and R of these different techniques for promoting an increase in nucleant population densities. However, even for steady-state conditions, further research is needed to study the relationship between welding parameters, *i.e.*, current (heat input) and welding speed, and the parameters important in weld solidification and nucleation of equiaxed grains, *i.e.* G_L, R, ΔT_C, C_o, N_o, and ΔT_N.

1.2 Modelling of GTA Weld Pool Behaviour

It is difficult to obtain accurate experimental measurements of the thermal conditions in a moving weld due to the relatively small size of the weld pool, the rapid thermal fluctuations, and the hostile environment which the high temperatures of the molten metal and arc plasma present to instrumentation. Therefore, only a few researchers [37, 38, 39] have directly studied the effects of welding process parameters on the weld pool thermal behaviour, in particular G_L. Analytical and numerical models, however, may be employed to study the effects of the controllable welding process parameters on weld pool thermal behaviour. However, most previous models of welding have focussed more on predictions of weld pool geometry or fluid flow behaviour, rather than local solidification conditions, as would be required for a study of the CET in welds.

1.2.1 Analytical Models

Rosenthal [40] developed the first analytical solutions for steady-state thermal fields in GTA welds. One analytical solution was developed by assuming a line source and two-dimensional heat flow conditions and would be applicable to welds in thin plates. From this solution, an analytical expression for thermal gradient along the weld centreline at the weld pool tail may be obtained:

$$G_L = 2\pi k \rho C_p \left(\frac{h}{\eta V I} \right)^2 v_{ws} (T_L - T_o)^3 \tag{1.18}$$

The growth rate along the weld centreline is assumed to be equal to the welding speed, *i.e.*, $R = v_{ws}$. As discussed previously, these expressions have been used by researchers studying the CET in welds [34, 37, 38] to estimate centreline G_L and R. Equation 1.18 predicts that G_L may be reduced and, therefore, a CET may be promoted by increasing the welding current (or power input, ηVI) which is consistent with previous experimental findings [34]-[39].

However, the analytical model from which Equation 1.18 was derived does not incorporate several physical phenomena in GTA welds, including latent heat of fusion, spatial distribution of the arc heat input, temperature dependence of material properties, and sensitivity to fluid flow [8, 39]. Indeed, large discrepancies were noted by Kou and Le [38] between centreline values of thermal gradient measured using thermocouples and those calculated using Equation 1.18. Moreover, the CET may occur at some distance from the centreline, particularly at high welding speeds when the pool becomes teardrop-shaped. Thus, using centreline estimates of G_L to predict the CET is inevitably erroneous [39].

1.2.2 Numerical Models

A three-dimensional finite element conduction model which accurately models the solid-liquid interface and incorporates latent heat of fusion was developed by Pardo and Weckman [54, 55]. In this model, a block of liquid elements was mapped into a volume defined by the interfacial surface as determined by the melting temperature isotherm. Thus, the geometry of the interface was accurately modelled. The release and absorption of latent heat of fusion was simulated as a flux acting over the surface of interfacial elements. The effects of convection in the weld pool were emulated by artificially enhancing the thermal conductivity of the liquid. This model was later adapted and employed by Villefuerte *et al.* [39] to study the effect of welding conditions on local values of R and G_L along the weld pool edge. This study demonstrated that the CET is favoured with increasing welding speed and current and that, for fixed welding conditions, the CET is most favoured in a region of low thermal gradient and high interface growth rate which occurs close to the centreline at the tail of the pool. Although this model approximates the effects of convective heat transfer on the thermal conditions in the weld pool, it does not actually model fluid flow phenomena. Hence, accurate predictions of G_L cannot be expected.

Several researchers [56]-[61] have shown using numerical models that fluid flow in the weld pool strongly affects the weld pool geometry. Fluid flow in the weld pool has several driving forces:

- an upward acting buoyancy force due to temperature-induced changes in density of the liquid,

- an electromagnetic (Lorentz) force due to the interaction of the arc current with its magnetic field which forces fluid in a downwards motion,
- surface tension temperature gradient (Marangoni) force due to changes in surface tension, γ, with temperature across the free surface(s) of the weld pool. For many metals, $\partial\gamma/\partial T$ is negative and the Marangoni force drives fluid outwards; however, the presence of surface active elements (such as sulphur in stainless steel) may produce a positive $\partial\gamma/\partial T$ which causes a flow inversion towards the centre of the pool [14].

Other researchers [62]-[65] have found that arc pressure and viscous drag force of the arc plasma on the surface of the weld pool are significant fluid flow driving forces, but only at high welding currents (200-300 A), which might be used in the welding of steels, but not aluminum alloys as in the present study. Kou *et al.* [57, 58] and Zacharia *et al.* [59, 60] obtained good agreement between predicted and experimentally observed fusion boundaries by incorporating fluid flow in numerical models of moving GTA welds. In particular, incorporation of Marangoni surface flow permitted accurate simulations of the observed effect of surface active elements on the weld pool profile and depth of penetration.

Zacharia *et al.* [66] found that the choice of material properties has a significant influence on the weld pool thermofluids behaviour and geometry. In particular, incorporating both the temperature dependence of material properties and the evaporation of low vapour pressure elements from the surface of the molten weld pool improved comparisons to experiments.

Modelling the deformation of the weld pool free surface was demonstrated by Tsai and Kou [67]-[69] and Zacharia *et al.* [70]-[72] to be necessary for accurate predictions of weld pool fluid flow, as well as surface phenomena such as surface ripple, and depression and elevation of regions of the pool surface due to Marangoni and Lorentz forces. Kim and Na [62] and Wu and Dorn [73] incorporated free surface geometry and found that viscous drag due to the arc also caused significant surface deformation, but only at high welding currents ($>$ 300 A). However, Hong [74] found in stationary GTA welds in Al and

304 stainless steel that although the weld pool surface did experience some deformation at welding currents < 300 A, this had little effect on the overall flow fields and thermal gradients in the weld pool, particularly near the solid/liquid interface where the CET occurs.

The behaviour of the arc is another concern for accurately modelling the weld pool shape and thermal conditions. The distribution of the arc heat and current flux were shown [75]-[78] to have a significant effect on the convective and thermal fields in the weld pool as well as the surface geometry. The spatial distribution of the arc heat and current flux was determined experimentally [76, 77, 79] and numerically [80, 81] to be well represented by Gaussian distributions. Dutta *et al.* [82] modelled the arc heat input with a Gaussian distribution, but numerically solved for three-dimensional, non-axisymmetric current flow. The electrode angle and arc length were also suggested [80, 81, 83] as having a significant influence on the shape and distribution of the arc and therefore should be incorporated in an accurate model. The electrode tip angle has a large effect on the shape of the arc: the larger the enclosed angle of the electrode tip, the more focussed the arc and the more intense the incident heat and current flux on the weld pool surface. The electrode-to-workpiece distance, or arc length, also has an influence on the arc shape and weld quality. A long arc length will allow the arc to spread out before contacting the workpiece surface which decreases the intensity of the heat input, producing a shallow and wide weld pool [84]. A long arc length will also decrease the efficiency of the arc by increasing heat loss to the surrounding environment, as well as compromise weld quality by increasing the possibility of entraining reactive elements from the air which may then cause porosity and impurities in the weld bead. A short arc length will produce a more focussed intense arc, resulting in a deeper and narrower weld pool.

Finally, Choo and Szekely [85] and Hong *et al.* [86, 87] postulated that the weld pool fluid flow is, in fact, turbulent. They demonstrated that incorporating turbulence in their numerical models improved correlation with experimental observations of weld pool dimensions in stationary GTA welds in 304 stainless steel, while in high-conductivity alloys such as aluminum, the level of turbulence may be higher but the effect on temperatures and weld dimensions was less pronounced [86, 87].

Although these numerical models provided reasonable estimates of thermal and fluid flow behaviour in the bulk weld pool, they have not been employed specifically to study the CET, for which accurate prediction of R and G_L at the interface are required. This information would be difficult to obtain from most previous models since they generally employ fixed grids in which the interface geometry is modelled as a series of rectangular steps. Numerical models which incorporate fluid flow phenomena and also employ dynamic grid remapping for accurate modelling of the interface geometry have been developed [86, 87, 88, 89]; however, until now they have been restricted to stationary GTA welding and have not been applied to CET predictions.

It is clear that the success of a model to correctly simulate weld pool behaviour for the purpose of studying the CET directly depends on its ability to both account for the effects of most important thermal and fluid flow phenomena in the weld pool, and accurately model the geometry of the solid-liquid interface. Given a detailed model, however, much insight may be gained into both overall weld pool behaviour and details of the solidification process. This, in turn, should permit better investigation and understanding of the effects of welding process parameters on the CET in moving GTA welds.

1.3 Objectives of the Present Work

The overall objective of the present work is to examine the relationships between controllable welding process parameters and weld pool thermal conditions, in order to better understand and predict the CET in full-penetration moving GTA welds. To this end, the research has three major components:

- modelling the macroscopic thermofluids behaviour in the bulk weld pool,
- modelling the main aspects of growth at the weld pool solid/liquid interface, and
- comparing the predictions of the macroscopic and microscopic models with experimental observations.

Numerical simulations of the macroscopic heat and fluid flow behaviour in the GTA weld pool were made using a detailed thermofluids model. This finite element model was formulated for three-dimensional, steady-state, moving GTA welds. The model incorporated temperature-dependent material properties, latent heat of fusion, Gaussian-distributed arc heat and current inputs, heat losses due to convection and radiation. Turbulent fluid flow driven by buoyancy, electromagnetic forces, and surface tension temperature gradient forces was also modelled. The model was then used to simulate moving GTA welds on thin sheets of aluminum-copper alloy using an experimentally realistic range of welding currents and steady-state welding speeds. Results from the simulations were post-processed to obtain estimates of weld pool thermal and solidification parameters, such as thermal gradient, interface growth rate, and growth undercooling.

An analytical model was employed to predict the CET based on the thermal conditions in the weld pool determined by the numerical macroscopic model. The analytical model incorporates Hunt's expression for the CET [1] in a modified form.

Experiments were performed using autogenous, alternating-current GTA welding for a range of welding currents and steady-state welding speeds. Full-penetration welds were produced on thin specimen plates to ensure two-dimensional heat flow and thus facilitate subsequent microstructural interpretation. Binary aluminum-copper alloys were selected as a model solidification system since this alloy system is well-characterized with respect to material properties and is also particularly susceptible to solidification cracking. These alloys were inoculated with varying amounts of TiB_2 particles which acted as nucleants for equiaxed grains.

The remainder of this thesis is structured as follows: Chapter 2 describes the macroscopic thermofluids model. Chapter 3 outlines the experimental program and materials. The results of the models and of the experiments are presented and discussed in Chapter 4. Finally, conclusions, contributions of the present work, and possibilities for future work are summarized in Chapter 5.

Chapter 2

THE THERMOFLUIDS MODEL

The objective of the present work was to establish the relationships between controllable welding process parameters and weld pool thermal conditions in order to better understand the CET in full-penetration moving GTA welds. Since it is experimentally difficult to control and characterize the thermal conditions in a moving weld pool, a large portion of the work was devoted to development of a numerical thermofluids model. The model was then used to perform simulations of the macroscopic heat and fluid flow behaviour in the GTA weld pool. This model is described in the present chapter.

2.1 The Mathematical Model

The mathematical model definition for the GTA welding process is shown in Figure 2.1. In this study, the workpiece was a thin plate with a full-penetration weld. The three-dimensional xyz Cartesian coordinate system was used in conjunction with an Eulerian coordinate framework in which the origin was fixed relative to the arc and the base plate travelled in the negative y direction at a constant welding speed, v_{ws}, relative to the arc. Steady-state welding conditions were assumed. Due to symmetry, the solution domain was reduced to half of the workpiece, as indicated in Figure 2.1.

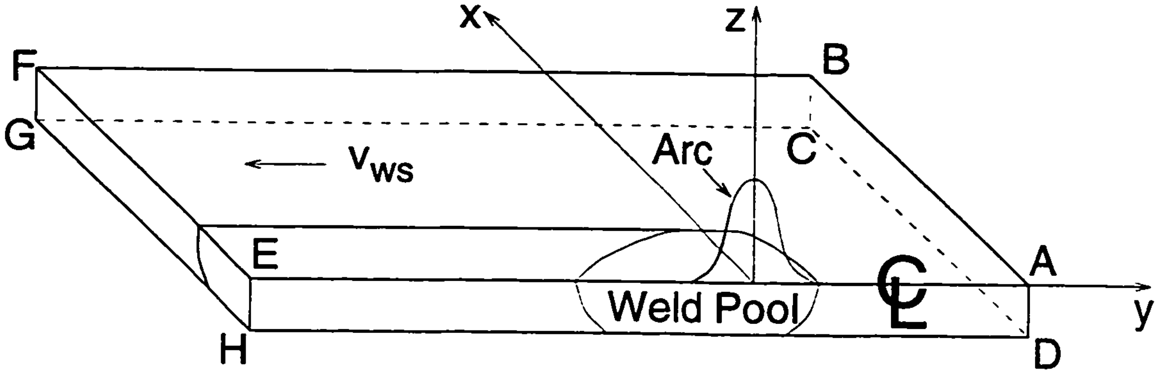

Figure 2.1: Model definition for full-penetration, steady-state GTA welding.

At the inlet boundary of the solution domain (ABCD), the workpiece was at an initial temperature, which for this study was equal to room temperature, but may also be a specified preheat temperature. As the workpiece moved into the vicinity of the arc, distributed arc heat and current fluxes were input to the workpiece from the arc. The arc heat input caused localized melting of the workpiece, thereby forming the weld pool. The arc heat and current fluxes were modelled as Gaussian distributions based on experimental measurements [77] using the same electrode geometry and arc length as used in the experiments in the present study. The flow of liquid metal in the weld pool was assumed to be driven by buoyancy, electromagnetic (Lorentz) forces, and surface tension temperature gradient (Marangoni) forces. Since the values of current used in this study were relatively low, viscous drag due to the arc plasma was not considered as a fluid flow driving force. The fluid flow was assumed to be turbulent. Since a binary Al-

4.5%Cu alloy was modelled, there existed a partially molten or mushy zone surrounding the molten weld pool. The locations of the interfaces between the liquid and the mushy zone and between the mushy zone and solid phase were not known *a priori*.

The top and bottom free surfaces of the molten weld pool were modelled as flat, non-deforming interfaces, since the values of current used in the present work were not sufficiently high to significantly deform the surface. This assumption was verified through experimental observations. Heat was lost through convection and radiation from the top and bottom surfaces of the workpiece. Heat loss through vaporization was assumed to be negligible since aluminum-copper alloys are not subject to the selective evaporation of low vapour pressure elements. Heat transfer was modelled over the entire solution domain; however, fluid flow was modelled only in the liquid weld pool.

2.1.1 The Governing Equations

To model the thermofluids phenomena within the domain of the liquid weld pool, the governing equations in the liquid weld pool are the coupled, non-linear (i) conservation of mass, (ii) conservation of momentum, and (iii) conservation of energy equations. The equation for conservation of mass for steady-state, three-dimensional incompressible flow is [90]

$$\frac{\partial}{\partial x}(\rho u) + \frac{\partial}{\partial y}(\rho v) + \frac{\partial}{\partial z}(\rho w) = 0 \tag{2.1}$$

The equations for conservation of momentum for steady-state, three-dimensional incompressible flow are [90]

$$\begin{aligned}
\rho\left(u\frac{\partial u}{\partial x} + v\frac{\partial u}{\partial y} + w\frac{\partial u}{\partial z}\right) &= F_x - \frac{\partial P}{\partial x} + \frac{\partial \tau_{xx}}{\partial x} + \frac{\partial \tau_{yx}}{\partial y} + \frac{\partial \tau_{zx}}{\partial z} \\
\rho\left(u\frac{\partial v}{\partial x} + v\frac{\partial v}{\partial y} + w\frac{\partial v}{\partial z}\right) &= F_y - \frac{\partial P}{\partial y} + \frac{\partial \tau_{xy}}{\partial x} + \frac{\partial \tau_{yy}}{\partial y} + \frac{\partial \tau_{zy}}{\partial z} \\
\rho\left(u\frac{\partial w}{\partial x} + v\frac{\partial w}{\partial y} + w\frac{\partial w}{\partial z}\right) &= F_z - \frac{\partial P}{\partial z} + \frac{\partial \tau_{xz}}{\partial x} + \frac{\partial \tau_{yz}}{\partial y} + \frac{\partial \tau_{zz}}{\partial z}
\end{aligned} \tag{2.2}$$

Here, P represents the hydrodynamic component of pressure.

Equations 2.1 and 2.2 apply for instantaneous values of u, v, w, and P; however, the field variables can be separated into mean and fluctuating components:

$$\phi = \bar{\phi} + \phi' \tag{2.3}$$

where ϕ represents a field variable and the mean value, $\bar{\phi}$, is averaged over a time scale which is large compared to the turbulent fluctuation time scale:

$$\bar{\phi} = \frac{1}{\Delta t}\int_{t}^{t+\Delta t} \phi dt \tag{2.4}$$

Equations 2.1 and 2.2 can now be expressed as

$$\frac{\partial}{\partial x}(\rho\bar{u}) + \frac{\partial}{\partial y}(\rho\bar{v}) + \frac{\partial}{\partial z}(\rho\bar{w}) = 0 \tag{2.5}$$

and

$$\begin{aligned}
\rho\left(\bar{u}\frac{\partial\bar{u}}{\partial x} + \bar{v}\frac{\partial\bar{u}}{\partial y} + \bar{w}\frac{\partial\bar{u}}{\partial z}\right) &= \bar{F}_x - \frac{\partial\bar{P}}{\partial x} + \frac{\partial}{\partial x}(\bar{\tau}_{xx} - \rho\overline{u'u'}) \\
&+ \frac{\partial}{\partial y}(\bar{\tau}_{xy} - \rho\overline{u'v'}) + \frac{\partial}{\partial z}(\bar{\tau}_{xz} - \rho\overline{u'w'}) \\
\\
\rho\left(\bar{u}\frac{\partial\bar{v}}{\partial x} + \bar{v}\frac{\partial\bar{v}}{\partial y} + \bar{w}\frac{\partial\bar{v}}{\partial z}\right) &= \bar{F}_y - \frac{\partial\bar{P}}{\partial y} + \frac{\partial}{\partial x}(\bar{\tau}_{yx} - \rho\overline{v'u'}) \\
&+ \frac{\partial}{\partial y}(\bar{\tau}_{yy} - \rho\overline{v'v'}) + \frac{\partial}{\partial z}(\bar{\tau}_{yz} - \rho\overline{v'w'}) \\
\\
\rho\left(\bar{u}\frac{\partial\bar{w}}{\partial x} + \bar{v}\frac{\partial\bar{w}}{\partial y} + \bar{w}\frac{\partial\bar{w}}{\partial z}\right) &= \bar{F}_z - \frac{\partial\bar{P}}{\partial z} + \frac{\partial}{\partial x}(\bar{\tau}_{zx} - \rho\overline{w'u'}) \\
&+ \frac{\partial}{\partial y}(\bar{\tau}_{zy} - \rho\overline{w'v'}) + \frac{\partial}{\partial z}(\bar{\tau}_{zz} - \rho\overline{w'w'})
\end{aligned} \tag{2.6}$$

In this study, the turbulent Reynolds stresses in Equation 2.6 were modelled using the Boussinesq gradient diffusion hypothesis [91]:

$$\begin{aligned}
\rho\overline{u'u'} &= -2\mu_t\frac{\partial\bar{u}}{\partial x}+\frac{2}{3}K & \rho\overline{u'v'} = \rho\overline{v'u'} &= -\mu_t\left(\frac{\partial\bar{u}}{\partial y}+\frac{\partial\bar{v}}{\partial x}\right) \\
\rho\overline{v'v'} &= -2\mu_t\frac{\partial\bar{v}}{\partial y}+\frac{2}{3}K & \rho\overline{u'w'} = \rho\overline{w'u'} &= -\mu_t\left(\frac{\partial\bar{u}}{\partial z}+\frac{\partial\bar{w}}{\partial x}\right) \\
\rho\overline{w'w'} &= -2\mu_t\frac{\partial\bar{w}}{\partial z}+\frac{2}{3}K & \rho\overline{v'w'} = \rho\overline{w'v'} &= -\mu_t\left(\frac{\partial\bar{v}}{\partial z}+\frac{\partial\bar{w}}{\partial y}\right)
\end{aligned} \tag{2.7}$$

where K is the kinetic energy, defined as

$$K = \frac{1}{2}(\overline{u'u'}+\overline{v'v'}+\overline{w'w'}) \tag{2.8}$$

and μ_t is the turbulent viscosity, the evaluation of which will be discussed in a later section.

The molten weld pool was assumed to behave as a Newtonian fluid [92] and the Stokes' viscosity relation for shear stress was employed [93], *i.e.*, in time averaged form:

$$\begin{aligned}
\bar{\tau}_{xx} &= 2\mu\frac{\partial\bar{u}}{\partial x} & \bar{\tau}_{xy} = \bar{\tau}_{yx} &= \mu\left(\frac{\partial\bar{u}}{\partial y}+\frac{\partial\bar{v}}{\partial x}\right) \\
\bar{\tau}_{yy} &= 2\mu\frac{\partial\bar{v}}{\partial y} & \bar{\tau}_{xz} = \bar{\tau}_{zx} &= \mu\left(\frac{\partial\bar{u}}{\partial z}+\frac{\partial\bar{w}}{\partial x}\right) \\
\bar{\tau}_{zz} &= 2\mu\frac{\partial\bar{w}}{\partial z} & \bar{\tau}_{yz} = \bar{\tau}_{zy} &= \mu\left(\frac{\partial\bar{v}}{\partial z}+\frac{\partial\bar{w}}{\partial y}\right)
\end{aligned} \tag{2.9}$$

Substitution of Equations 2.7 and 2.9 into Equation 2.6 gives the mass and momentum equations in the following form:

$$\frac{\partial}{\partial x}(\rho u)+\frac{\partial}{\partial y}(\rho v)+\frac{\partial}{\partial z}(\rho w) = 0 \tag{2.10}$$

and

$$
\begin{aligned}
\rho\left(u\frac{\partial u}{\partial x}+v\frac{\partial u}{\partial y} + w\frac{\partial u}{\partial z}\right) &= F_x-\frac{\partial P}{\partial x}\\
&+ \frac{\partial}{\partial x}\left(\mu_{eff}\frac{\partial u}{\partial x}\right)+\frac{\partial}{\partial y}\left(\mu_{eff}\frac{\partial u}{\partial y}\right)+\frac{\partial}{\partial z}\left(\mu_{eff}\frac{\partial u}{\partial z}\right)\\
&+ \frac{\partial}{\partial x}\left(\mu_{eff}\frac{\partial u}{\partial x}\right)+\frac{\partial}{\partial y}\left(\mu_{eff}\frac{\partial v}{\partial x}\right)+\frac{\partial}{\partial z}\left(\mu_{eff}\frac{\partial w}{\partial x}\right)\\
\\
\rho\left(u\frac{\partial v}{\partial x}+v\frac{\partial v}{\partial y} + w\frac{\partial v}{\partial z}\right) &= F_y-\frac{\partial P}{\partial y}\\
&+ \frac{\partial}{\partial x}\left(\mu_{eff}\frac{\partial v}{\partial x}\right)+\frac{\partial}{\partial y}\left(\mu_{eff}\frac{\partial v}{\partial y}\right)+\frac{\partial}{\partial z}\left(\mu_{eff}\frac{\partial v}{\partial z}\right) \qquad (2.11)\\
&+ \frac{\partial}{\partial x}\left(\mu_{eff}\frac{\partial u}{\partial y}\right)+\frac{\partial}{\partial y}\left(\mu_{eff}\frac{\partial v}{\partial y}\right)+\frac{\partial}{\partial z}\left(\mu_{eff}\frac{\partial w}{\partial y}\right)\\
\\
\rho\left(u\frac{\partial w}{\partial x}+v\frac{\partial w}{\partial y} + w\frac{\partial w}{\partial z}\right) &= F_z-\frac{\partial P}{\partial z}\\
&+ \frac{\partial}{\partial x}\left(\mu_{eff}\frac{\partial w}{\partial x}\right)+\frac{\partial}{\partial y}\left(\mu_{eff}\frac{\partial w}{\partial y}\right)+\frac{\partial}{\partial z}\left(\mu_{eff}\frac{\partial w}{\partial z}\right)\\
&+ \frac{\partial}{\partial x}\left(\mu_{eff}\frac{\partial u}{\partial z}\right)+\frac{\partial}{\partial y}\left(\mu_{eff}\frac{\partial v}{\partial z}\right)+\frac{\partial}{\partial z}\left(\mu_{eff}\frac{\partial w}{\partial z}\right)
\end{aligned}
$$

where the modified pressure $P = \bar{P} + \frac{2}{3}\rho K$, and the effective viscosity $\mu_{eff} = \mu + \mu_t$. Note that the use of the overbar has been discontinued at this time, and from this point onwards all variables are assumed to be the time averaged values.

Fluid flow in the weld pool was assumed to be driven by buoyancy, surface tension gradient (Marangoni), and electromagnetic (Lorentz) forces. The buoyancy force, $\vec{F_b}$, and the electromagnetic force, $\vec{F_{em}}$, were incorporated as body forces in the momentum equations:

$$\vec{F}_b = -\rho\beta(T - T_r)\vec{g} \tag{2.12}$$

$$\vec{F}_{em} = \vec{j} \times \vec{B} \tag{2.13}$$

The current density, $\vec{j}$, and the magnetic flux intensity, $\vec{B}$, were assumed to be axisymmetric about the z axis [74]. The cross product $\vec{j} \times \vec{B}$ may be expressed as

$$\vec{j} \times \vec{B} = B_\theta(j_r\vec{z} - j_z\vec{r}) \tag{2.14}$$

in which [74]:

$$j_z = \frac{I}{2\pi}\int_0^\infty \lambda J_0(\lambda r)\exp\left(-\frac{\lambda^2\sigma_j^2}{2}\right)\frac{\sinh[\lambda(l-z)]}{\sinh(\lambda l)}d\lambda$$

$$j_r = \frac{I}{2\pi}\int_0^\infty \lambda J_1(\lambda r)\exp\left(-\frac{\lambda^2\sigma_j^2}{2}\right)\frac{\cosh[\lambda(l-z)]}{\sinh(\lambda l)}d\lambda \tag{2.15}$$

$$B_\theta = \frac{\mu_m I}{2\pi}\int_0^\infty J_1(\lambda r)\exp\left(-\frac{\lambda^2\sigma_j^2}{2}\right)\frac{\sinh[\lambda(l-z)]}{\sinh(\lambda l)}d\lambda$$

Here, σ_j is the effective radius of the Gaussian distributed current flux incident on the weld pool surface, defined as

$$j_z(r,0) = \frac{I}{2\pi\sigma_j^2}\exp\left(-\frac{r^2}{2\sigma_j^2}\right) \tag{2.16}$$

The governing equation which is applicable over the entire solution domain (*i.e.*, over the entire workpiece including the molten weld pool) is the three-dimensional, steady-state, convection-diffusion equation for conservation of energy:

$$\frac{\partial}{\partial x}\left(k_{eff}\frac{\partial T}{\partial x}\right) + \frac{\partial}{\partial y}\left(k_{eff}\frac{\partial T}{\partial y}\right) + \frac{\partial}{\partial z}\left(k_{eff}\frac{\partial T}{\partial z}\right) + Q$$

$$= u\frac{\partial(\rho C_p T)}{\partial x} + v\frac{\partial(\rho C_p T)}{\partial y} + w\frac{\partial(\rho C_p T)}{\partial z} \tag{2.17}$$

Similarly to the mass and momentum equations, the temperature was time averaged. The effective thermal conductivity is defined as $k_{eff} = k + k_t$, where k is the molecular thermal conductivity and k_t is the turbulent thermal conductivity, the evaluation of which will be discussed in a later section. In the liquid weld pool, u, v, and w are the flow velocities; in the solid, $v = v_{ws}$ and $u = w = 0$. The internal volumetric heat source term, Q, due to ohmic heating was assumed in this case to be negligible compared to the relatively large arc heat input [74]. Finally, latent heat of fusion, ΔH_f, was assumed to be evolved or absorbed according to the Scheil equation in the partially molten (mushy) zone. The algorithms used to model latent heat of fusion are described in a later section.

2.1.2 Material Properties

The thermophysical properties of Al-4.5%Cu were incorporated into the governing equations. The temperature-independent properties for this alloy were taken from references [94]-[97] and are given in Table 2.1. The thermophysical material properties, k, C_p, and ρ were assumed to be temperature dependent. These temperature-dependent properties were taken from references [94, 95, 98, 99] and are given in Table 2.2.

Table 2.1: Temperature-independent properties for Al-4.5%Cu alloy.

(Taken from references [94]-[97].)

T_E (K)	T_L (K)	ϵ	ΔH_f (J/kg)	$\partial\gamma/\partial T$ (N/m·K)	μ (Pa·s)	β (K^{-1})
821	921	0.09	397 500	-0.00035	0.0020	70×10^{-6}

Table 2.2: Temperature-dependent properties for Al-4.5%Cu alloy. (Taken from references [94, 95, 98, 99]; T in K.)

C_p	1059	$921 <$	T	
$(J/kg \cdot K)$	$1286.75\text{-}0.25T$	$844 \leq$	T	< 921
	$748.74+0.44T$		T	< 844
	$52.56+0.033T$	$921 <$	T	
k	$818.67\text{-}0.808T$	$844 \leq$	T	< 921
$(W/m \cdot K)$	192.5	$573 \leq$	T	< 844
	$144.37+0.084T$	$523 \leq$	T	< 573
	188.3		T	< 523
ρ (kg/m^3)	$1000/(0.397\text{-}4.53\times10^{-3}C_o+ 4.09\times10^{-5}T+1.11\times10^{-6}C_oT+ 2.75\times10^{-5}C_o^2)$	$844 \leq$	T	
	$2966.7\text{-}0.22T$		T	< 844

2.1.3 Turbulence Model

To account for the effects of turbulence in the weld pool fluid flow, an algebraic vorticity-based turbulence model [74, 100] was employed. This model was formulated based on the consideration that the mixing of the weld pool by the fluid flow driving forces, buoyancy, Lorentz forces, and Marangoni forces, is similar to the mixing of a fluid induced by a rotating paddle in a chemical processing unit. It can be speculated, then, that the turbulent viscosity, μ_t, of the fluid is directly proportional to the fluid vorticity, $\vec{\omega}$. Thus, the turbulent viscosity, μ_t, is defined by the relationship

$$\mu_t = \rho C A_t |\vec{\omega}| \tag{2.18}$$

Here, the "swept area" $A_t = w_p/2 \times h$ for full-penetration welds and $\vec{\omega}$ is the vorticity, defined in three dimensions as

$$\vec{\omega} = \left(\frac{\partial w}{\partial y} - \frac{\partial v}{\partial z}\right)\vec{\imath} + \left(\frac{\partial u}{\partial z} - \frac{\partial w}{\partial x}\right)\vec{\jmath} + \left(\frac{\partial v}{\partial x} - \frac{\partial u}{\partial y}\right)\vec{k} \tag{2.19}$$

The constant $C = 0.5$ and is based on correlation between weld pool temperatures predicted with the thermofluids model employing the vorticity-based turbulence model and those measured experimentally with thermocouples. These thermocouple measurements were performed for the purpose of model validation and will be described in detail in a later section.

The turbulent viscosity was incorporated into the momentum equations by defining an effective viscosity:

$$\mu_{eff} = \mu + \mu_t \tag{2.20}$$

where μ is the molecular liquid viscosity. In the energy equation (Equation 2.17):

$$k_{eff} = k + k_t \tag{2.21}$$

where k is the molecular thermal conductivity. In the solid, $k_t = 0$; in the liquid

$$k_t = C_p\mu_t/Pr_t \tag{2.22}$$

in which the turbulent Prandtl number, $Pr_t = l_m/l_{m,K} = 0.9$ for metals [101], where l_m is the mixing length and $l_{m,K}$ is mixing length for transport of kinetic energy.

Predictions using this vorticity-based turbulence model were shown by Hong [74] to compare well with the so-called $K - \epsilon$ (where K is kinetic energy and ϵ is dissipation rate) turbulence model predictions for stationary GTA welds in both aluminum alloys and stainless steel. However, unlike the $K - \epsilon$ model which requires the solution of two more coupled, non-linear partial differential equations, this algebraic vorticity-based turbulence model has the advantage of minimal computational intensity, particularly given a three-dimensional formulation such as in the present study.

2.1.4 Boundary Conditions

The boundary for fluid flow is the physical boundary of the molten weld pool in which the following boundary conditions apply:

- no-slip at the liquidus interface

$$v = v_{ws} \tag{2.23}$$

$$u = w = 0 \tag{2.24}$$

- slip at the plane of symmetry (AEHD)

$$u = \frac{\partial v}{\partial x} = \frac{\partial w}{\partial x} = 0 \tag{2.25}$$

- a tangential Marangoni force acting on both the top and bottom pool surfaces

$$\vec{F_m} = -\frac{\partial \gamma}{\partial T}\,(\vec{\nabla} T)\Big|_{along\ surface} \tag{2.26}$$

The domain boundary for the energy equation is the physical boundary of the base plate for which the following boundary conditions apply:

- constant initial temperature at the inlet plane (ABCD)

$$T = T_o \tag{2.27}$$

- no heat conduction out of the plate edge (BFGC)

$$k\frac{\partial T}{\partial x} = 0 \tag{2.28}$$

- no heat conduction out of the outlet plane (EFGH)

$$k\frac{\partial T}{\partial y} = 0 \tag{2.29}$$

- an adiabatic condition on the plane of symmetry (AEHD)

$$k\frac{\partial T}{\partial x} = 0 \tag{2.30}$$

- a Gaussian-distributed arc heat flux input [77] and heat loss through radiation and convection on the top surface of the plate (ABFE)

$$k\frac{\partial T}{\partial z} = q_a - q_r - q_c \tag{2.31}$$

in which

$$q_a = \frac{\eta V I}{2\pi\sigma_h^2}\, exp\left(\frac{-r_a^2}{2\sigma_h^2}\right) \tag{2.32}$$

$$q_r = \sigma\epsilon(T^4 - T_\infty^4) \tag{2.33}$$

$$q_c = h_c(T - T_\infty) \tag{2.34}$$

- heat loss through radiation and convection on the bottom surface of the plate

$$k\frac{\partial T}{\partial z} = -q_r - q_c \tag{2.35}$$

Heat loss through evaporation of low vapour pressure elements was considered to be negligible for this alloy. The convection heat transfer coefficient was assumed to be $h_c = 24$ W/m^2·K [97]. The value used for emissivity, ϵ, is given in Table 2.1.

2.1.5 Welding Process Parameters

The welding process parameters used for the simulations are given in Table 2.3. These parameters were selected to closely match those obtainable during actual GTA welding of Al-Cu alloys with alternating current. These parameters were shown experimentally to provide two-dimensional heat flow conditions with parallel fusion boundaries through the thickness of the welded specimen. As discussed later, this facilitated subsequent microstructural interpretation. The process efficiencies, η, listed in Table 2.3 incorporate both arc efficiency and alternating-current duty cycle. The values of current, I, and voltage, V, listed in the table are peak values.

Table 2.3: Welding process parameters used in the simulations. (Values for σ_j and σ_h are based on reference [77].)

h (mm)	η	Peak I (A)	Peak V (V)	σ_j (mm)	σ_h (mm)	v_{ws} (mm/s)
2.0	0.50	100	13	1.40	1.60	3 to 6
2.0	0.46	120	13	1.57	1.78	4 to 7
2.0	0.45	140	13	1.72	1.94	6 to 9
2.0	0.45	160	13	1.84	2.08	7 to 10
2.2	0.50	100	13	1.40	1.60	2
2.2	0.46	120	13	1.57	1.78	3
2.2	0.45	140	13	1.72	1.94	4.5

2.2 The Numerical Formulation

2.2.1 The Finite Element Formulation

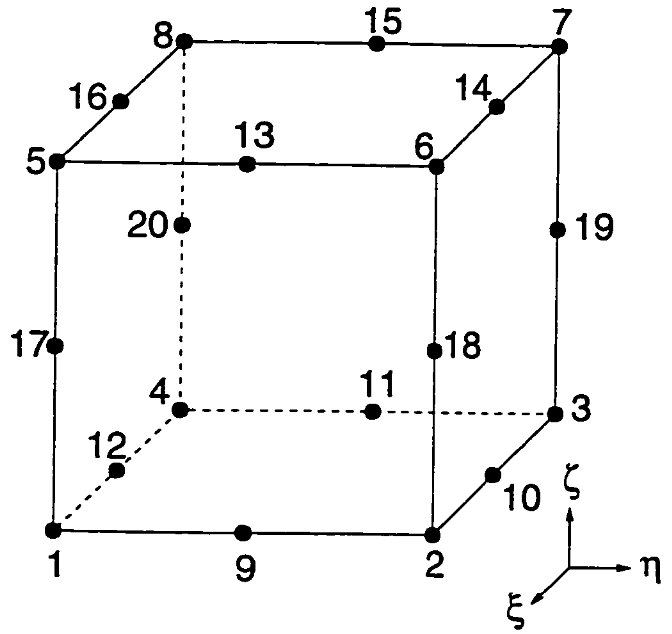

Figure 2.2: Schematic of a 20-node element.

The finite element method was selected for this GTA welding model due to its inherent ability to model irregular geometries. The solution domain was discretized into a finite element mesh using 3-dimensional, 20-node isoparametric elements, as shown in Figure 2.2. These higher-order elements are suitable for modelling both the curved geometry of the weld pool and the large thermal and velocity gradients which occur there. Any field variable, ϕ, may be defined at any location in such an element by the relationship

$$\phi = \sum N_i \phi_i \tag{2.36}$$

where ϕ_i is the value of the field variable at node i and N_i is the interpolation or shape function. Quadratic shape functions were used to interpolate the temperature and fluid velocity; since the pressure must be interpolated one order lower than the velocity [102], linear shape functions were used to interpolate pressure. These shape functions appear in many standard texts, such as [102], and will not be repeated here. The governing partial differential equations were expressed for each element using the Galerkin weighted residual method and assembled for solution into a global matrix using standard finite element method techniques. These procedures are well described in standard texts, for example [102], and will not be repeated here.

2.2.2 Dynamic Mesh Remapping and ΔH_f Evolution

To accurately model the solidification interface geometry and thermal gradients in the weld pool as well as facilitate the treatment of latent heat of fusion in the mushy zone, dynamic remapping of the finite element mesh was employed.

To facilitate the initial generation and the subsequent dynamic remapping of the finite element mesh, the solution domain was divided into three sectors, as indicated in Figure 2.3. The finite element mesh (also called 'grid') was then created by designating the number of elements contained in each sector as well as the number of elements through the thickness of the plate. As indicated in the figure, Sector 1 was predesignated as belonging to the weld pool, Sector 2 to the mushy zone, and Sector 3 to the solid plate.

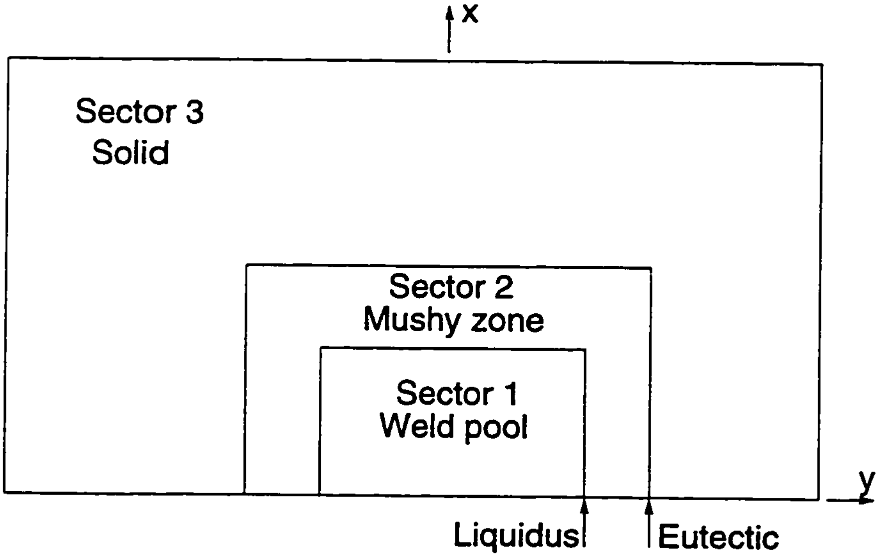

Figure 2.3: Schematic of the solution domain divided into sectors for mesh generation.

Figure 2.4 shows an example of an initial rectangular mesh. This is a graded mesh in which the elements were concentrated primarily in the weld pool and mushy zone sectors, since this is where the more severe temperature and velocity gradients are expected. The element distribution appears to be very uneven and some of the elements have large aspect ratios. However, this rectangular mesh is an initial mesh only and was dynamically remapped, as described subsequently.

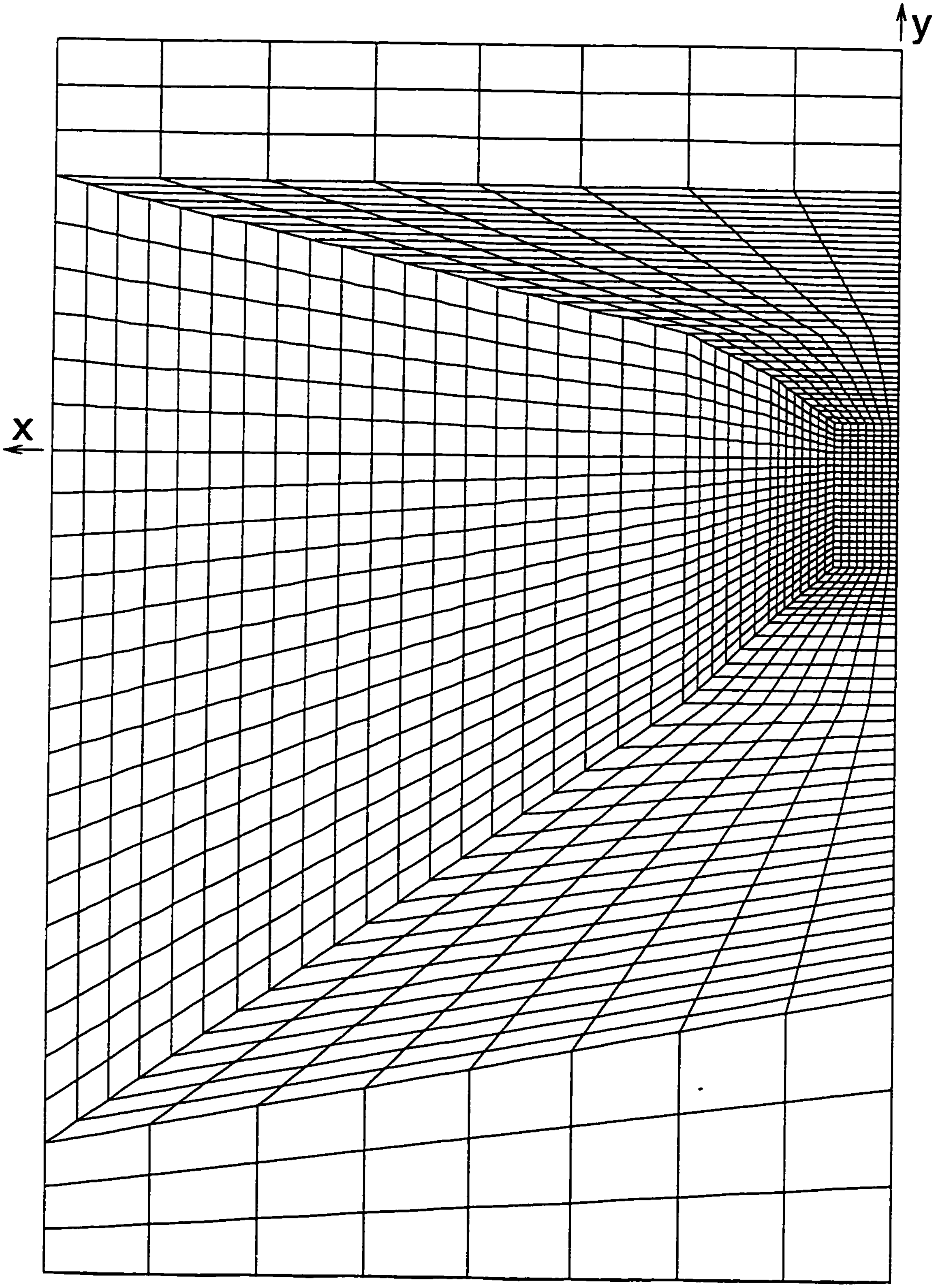

Figure 2.4: Top view of an initial rectangular mesh.

The initial step in the dynamic mesh remapping routine is represented schematically in Figure 2.5. In the interest of clarity, the elements in the solid sector are not shown in the figure. The temperature field for this initial rectangular mesh was solved and new estimates of the equilibrium liquidus, T_L, and eutectic, T_E, isotherm locations were determined, as indicated by dashed lines in the figure.

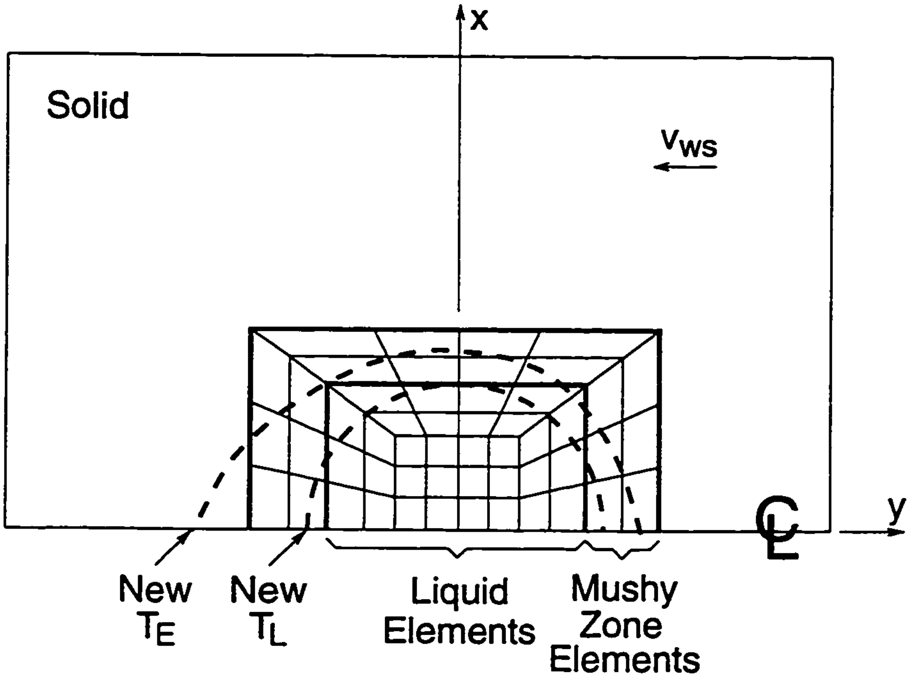

Figure 2.5: Schematic of the initial rectangular mesh. Only weld pool and mushy zone elements are shown.

The mesh was then dynamically remapped so that the edges of the predesignated weld pool and mushy zone interface elements coincided with the newly determined T_L and T_E isotherms. Based on the location of the liquidus and eutectic isotherms at $x = 0$ and $y = 0$, a temporary rectangle was constructed, as illustrated in Figure 2.6(a). For simplicity, the figure shows the liquidus only. The sides of this rectangle were divided according to the designated number of elements in the sector. A series of construction lines joined the origin to each of the points. The intersection of each of these construction lines with the liquidus isotherm was determined, and the coordinates of the nodes along the interface of the weld pool were altered such that they were located at these intersections of the

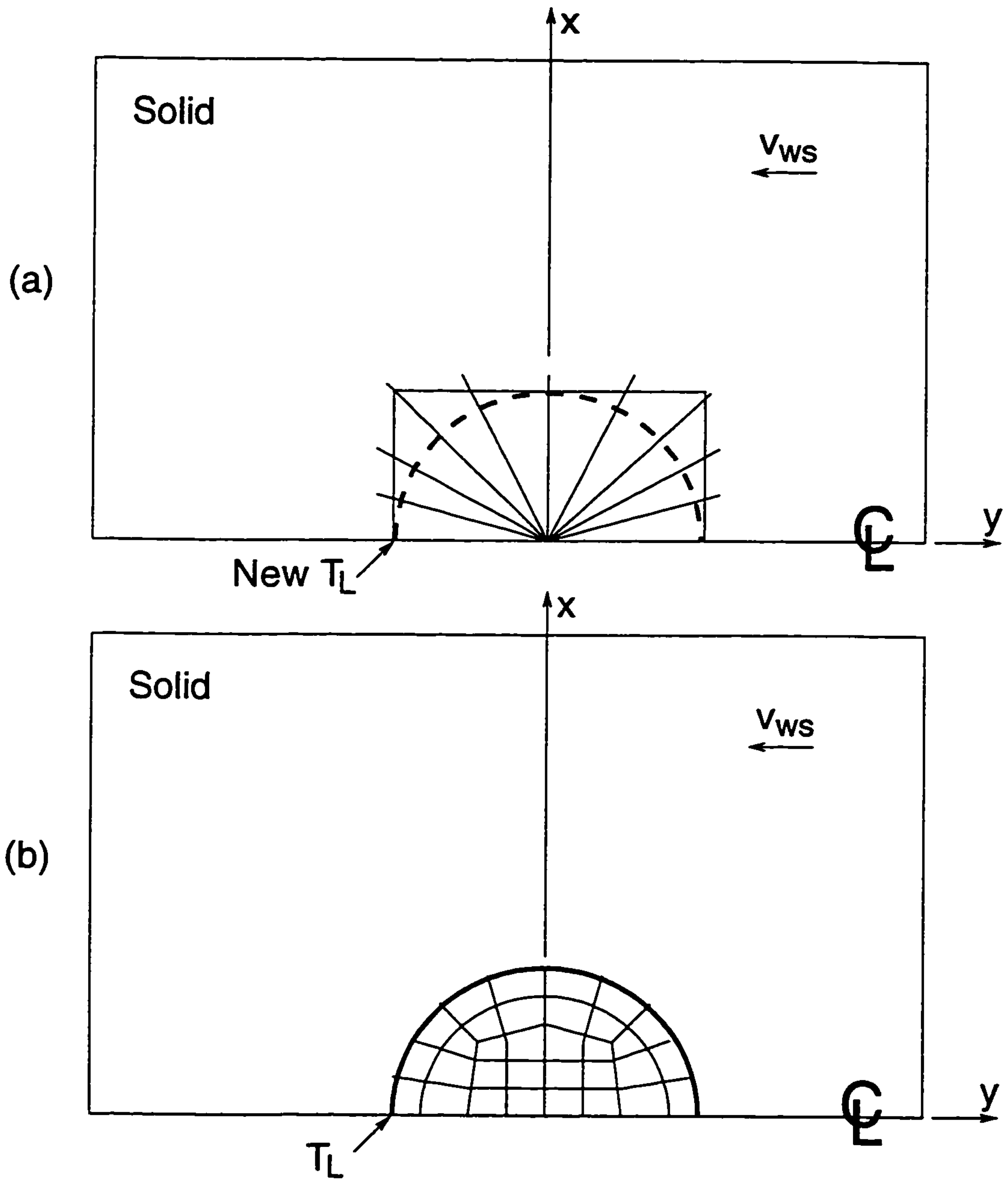

Figure 2.6: Schematic of (a) dynamic remapping routine and (b) the dynamically remapped mesh. Only liquid elements are shown.

construction lines and the predicted liquidus isotherm location. The new locations of the remaining elements and nodes within the sector were determined in a similar fashion. Thus all the elements within the liquid sector and along its interface were mapped into the predicted liquid weld pool domain and along the liquidus isotherm surface, respectively, as indicated in Figure 2.6(b). This procedure was repeated for each layer of nodes present in the z direction (*i.e.*, through the thickness of the plate). Similarly, the nodal coordinates along the mushy zone interface were determined and the elements in the mushy zone sector were mapped into that domain. Finally, the nodal coordinates of the the remaining solid sector were adjusted appropriately and the solid elements mapped into the domain.

Once a new mesh is formed, the governing equations are solved for the new configuration and the mesh is once again remapped. This process continues until convergence is achieved for all field variables as well as the liquidus and eutectic isotherm locations. This solution strategy will be described in detail in a later section. Figure 2.7 shows the top view of a dynamically remapped mesh, obtained from a simulation using a welding current of 100 A at a welding speed of 4 mm/s.

The evolution or absorption of latent heat of fusion, ΔH_f, in the mushy zone was modelled as a volumetric heat source through modification of the specific heat;

$$C_p = C_p + \alpha \Delta H_f \tag{2.37}$$

where α is the fraction of solid formed per unit temperature drop according to the Scheil equation [103];

$$\alpha = \frac{1}{k_o C_o} \frac{1}{m_S} \frac{1}{(k_o - 1)} \left(\frac{C_S}{k_o C_o} \right)^{(2-k_o)/(k_o-1)} \tag{2.38}$$

Here, the composition of the solid, C_S, varies with temperature according to the equilibrium phase diagram, as

$$C_S = \frac{1}{m_S}(T - T_m) \tag{2.39}$$

where m_S is the equilibrium solidus slope and T_m is the melting point of the pure metal, in this case pure aluminum, $T_m = 933$ K. At the eutectic temperature, $T_E = 821$ K, the

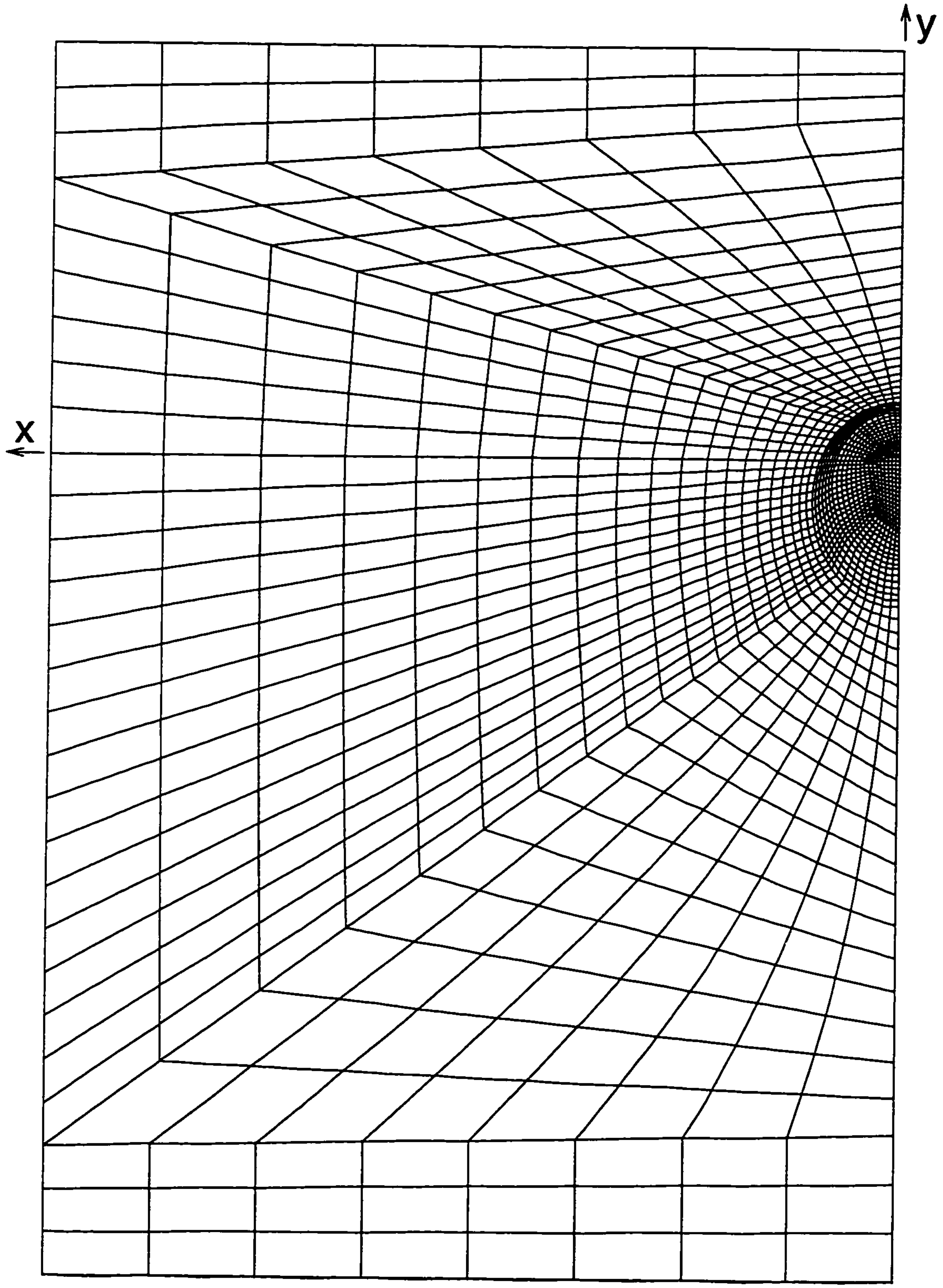

Figure 2.7: Top view of dynamically remapped mesh. Welding conditions: 100 A at 4 mm/s.

remaining fraction of untransformed metal is

$$f_E = \left(\frac{C_E}{C_o}\right)^{1/(k_o-1)} \tag{2.40}$$

The latent heat of fusion released or absorbed at the eutectic temperature due to the transformation of this remaining material was treated as a surface heat flux acting on the surface of the elements at the eutectic interface. The magnitude of this flux is given by

$$q_f = -\rho(\vec{n} \cdot \vec{v}_{ws}) f_E \Delta H_f \tag{2.41}$$

where $\vec{n}$ is the unit vector normal to the interface.

This dynamic mesh remapping technique not only facilitates the treatment of latent heat of fusion evolution in the mushy zone, but allows accurate geometric representation of the weld pool geometry. This, in turn, will provide more accurate estimates of the thermal gradients in the weld pool at the solid/liquid interface which are so important for CET promotion. Such accurate predictions would not be possible with earlier, fixed-grid models, since they necessarily model the solid/liquid interface with a series of rectangular steps.

The fact that the mesh was dynamically remapped to the equilibrium liquidus and eutectic isotherm positions neglects the influence of the growth undercoolings associated with the primary solid and eutectic phases. Since these undercoolings are small (shown later to be less than 8 K for the liquidus), their influence on the macroscopic positions of the isotherms was assumed to be negligible.

2.2.3 Solution Strategies

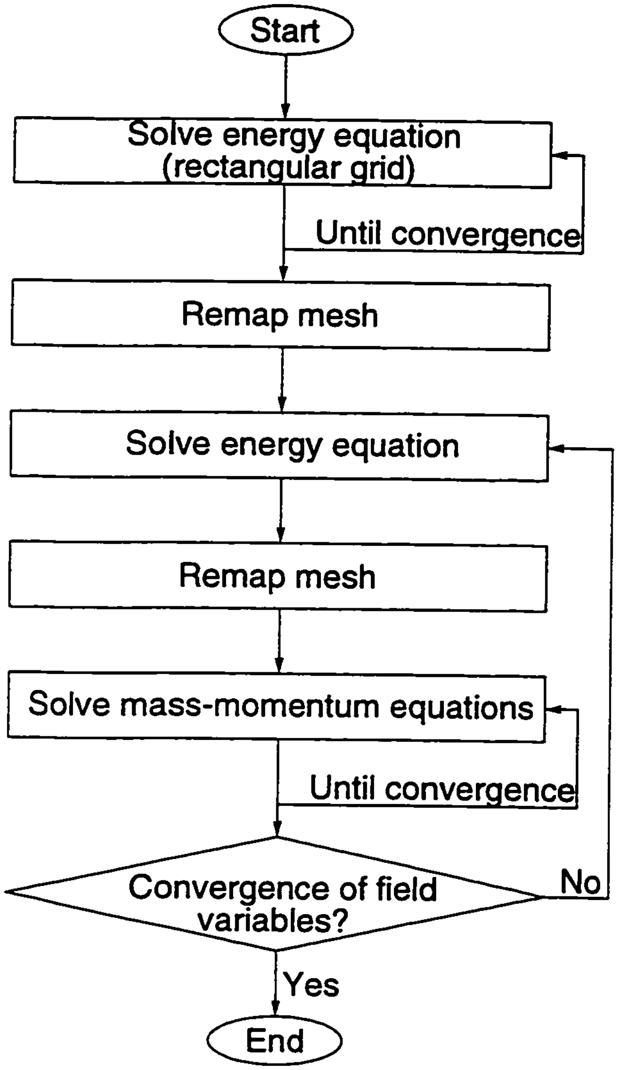

Figure 2.8: Flow chart of solution scheme.

The mass-momentum and energy equations were decoupled, linearized, and then solved using a nested iterative scheme until convergence was achieved for all field variables, *i.e.*, temperature, pressure, and velocity fields as well as the T_L and T_E isotherm locations. The iteration scheme is shown in Figure 2.8. For all equations, the most recently updated temperature and flow fields were used to evaluate temperature-dependent material properties and flow-field-dependent quantities. To eliminate the numerical oscillations inherent in a convection dominated flow field such as this, a streamline upwinding scheme [74, 104, 105] was applied in the local flow direction.

Due to the high order of complexity of this 3-dimensional finite element formulation, an iterative solver [106] was used to solve the matrix equation sets. This iterative solver employs conjugate gradient stabilized (CGSTAB) acceleration, right preconditioning by variable level incomplete lower/upper factorization, an ia-ja compressed data structure, and includes ordering of unknowns [106]. Simulations using a direct solver were also performed to validate the efficacy of the iterative solver.

The criterion used to establish convergence of the isotherm locations of both T_L and T_E was

$$|l_i - l_i^{old}| < 5 \times 10^{-4} \text{ mm} \tag{2.42}$$

where l_i represents various key locations, as indicated in Figure 2.9, along the T_L and T_E isotherms on both the top and bottom of the plate.

The criterion used to establish convergence of the flow velocity and pressure was

$$\frac{\sum_i |\phi_i - \phi_i^{old}|}{\sum_i |\phi_i|} < 10^{-3} \tag{2.43}$$

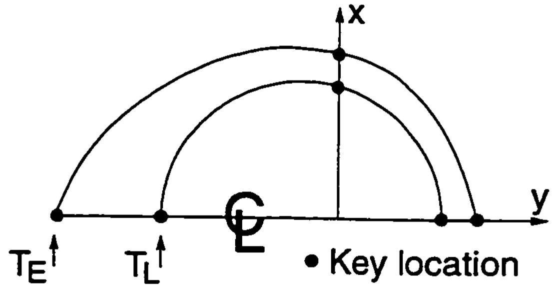

Figure 2.9: Schematic of T_L and T_E.

The decoupling of the energy and mass-momentum equations required that an under-relaxation factor be applied to the solution vectors before each iteration. Since under-relaxing may damp a solution to a false convergence according to Equation 2.43 and since the thermal solution tended to converge unstably, the maximum residual and the root-mean-square residual were used to track convergence for the thermal solution during the calculations. For any given system of equations

$$[A_{ij}]\phi_j = b_i \tag{2.44}$$

the residual, RES_i, for a given node i is

$$RES_i = b_i^{old} - \sum_{j=1}^{n} A_{ij}\phi_j^{old} \tag{2.45}$$

where b_i^{old} and ϕ_j^{old} are the load vector and solution vector, respectively, for the previous iteration and A_{ij} are the elements in the newly formed coefficient matrix. The root mean square of all n residuals is defined as

$$RMS = \sqrt{\frac{\sum_{i=1}^{n} RES_i^2}{n}} \tag{2.46}$$

As the thermal solution approached convergence, both the maximum RES_i value and the RMS value decreased to a minimum value which was specific to each simulation.

2.2.4 Substructuring

The thermal solution, and therefore values of thermal gradient, G_L, at the solid/liquid interface, were found to be mesh-independent with far fewer elements than was required for mesh independence of the fluid flow solution. However, refining the mesh sufficiently to capture finer details of the fluid flow solution, for example small eddies near interfaces, would be prohibitively expensive. As well, for the primary purpose of the present study, it was not necessary to predict the flow field with absolute precision, but only to incorporate its influence on the thermal field with sufficient accuracy for mesh-independent values of G_L. In cases where improved predictions of the weld pool flow fields were desired, a weld pool substructuring routine was developed. The strategy is depicted in Figure 2.2.4. First, the solution was driven to convergence for the original mesh. The weld pool was then extracted from the original mesh and refined. Finally, the fluid flow solution was driven to convergence for this refined pool-only mesh using the converged thermal field from the original mesh.

2.2.5 Post-Processing

Since the simulations predict temperatures and flow velocities, post-processing of these results was required to obtain values relevant to the solidification process, *i.e.*, thermal gradient, G_L, growth rate, R, and growth undercooling, ΔT_C. For these calculations, it was assumed that the local growth direction, *i.e.*, the direction of steepest thermal gradient, was perpendicular to the fusion interface. Values of G_L in the growth direction were determined along the liquidus from the tail of the weld pool to the extreme width of the weld pool based on the predicted thermal field. Values of R and ΔT_C were calculated along the liquidus from the tail of the weld pool to the extreme width of the weld pool using expressions discussed in a later chapter.

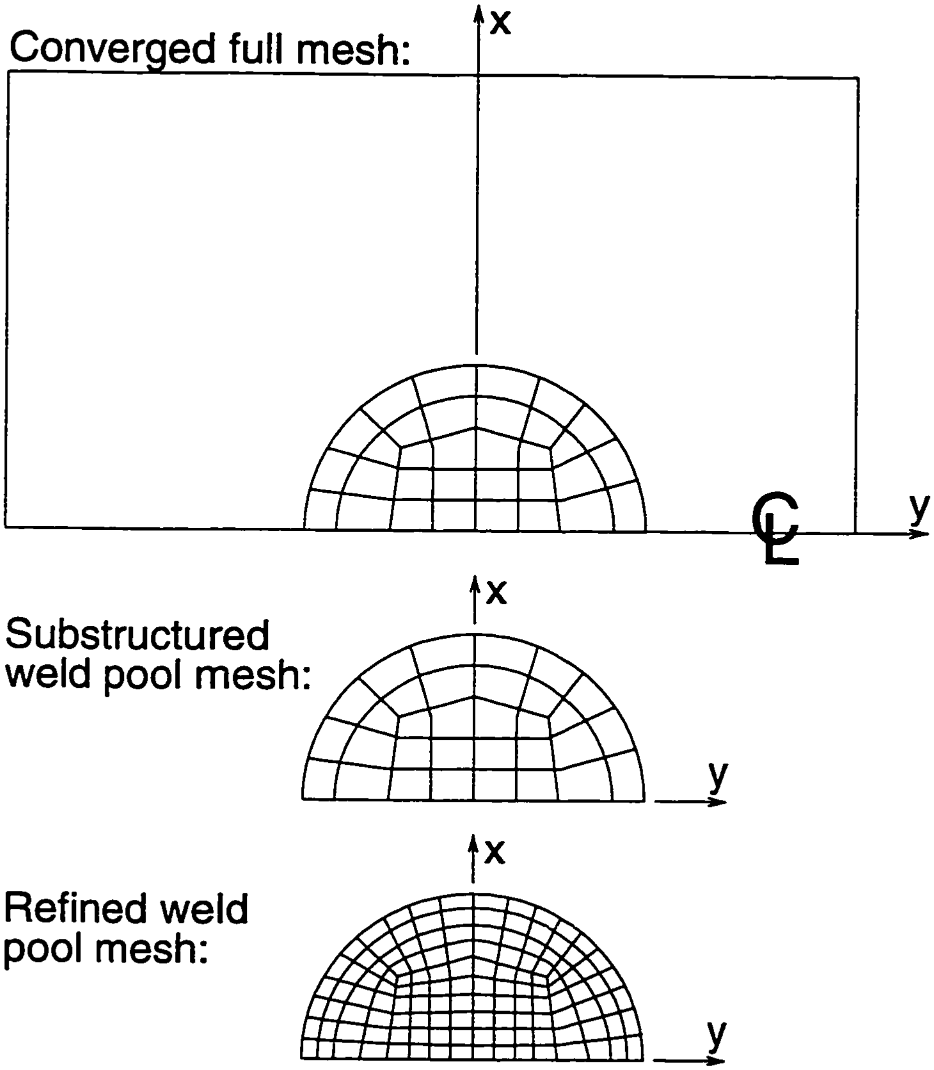

Figure 2.10: Schematic of weld pool substructuring routine for improved weld pool fluid flow predictions.

2.3 Model Verification

In order to ensure correct operation of the thermal and fluid flow modules contained in the GTA welding code, a series of simple geometry test cases was performed. The performance of the code was evaluated using the following test cases:

- steady-state heat transfer with advection
- steady-state isothermal laminar flow
- steady-state non-isothermal laminar flow

The results of each test case were compared to available analytical and benchmark solutions.

2.3.1 Steady-State Heat Flow

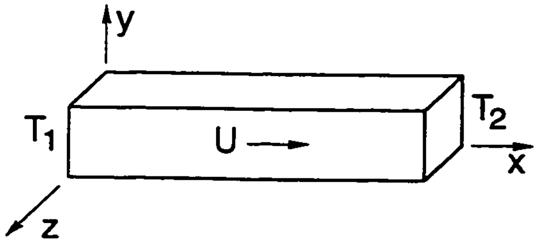

Figure 2.11: One-dimensional advection-diffusion problem configuration and boundary conditions.

The finite element thermal model was evaluated with a one-dimensional advection-diffusion heat flow test case. The governing equation for this scenario is

$$\frac{\partial^2 T}{\partial x^2} - \rho C_p u \frac{\partial T}{\partial x} = 0 \qquad (2.47)$$

The boundary conditions are shown in Figure 2.11: Dirichlet boundary conditions were imposed on each end, *i.e.*, $T = T_1$ and $T = T_2$, and a steady-state x-direction velocity, $u = U$, was assigned to all nodes. The test case was performed for a range of x-direction velocities using a uniform mesh consisting of 10 three-dimensional isoparametric elements arranged in the x direction.

The advection-diffusion test case gives a temperature distribution that depends on the Dirichlet temperatures, T_1 and T_2, density, ρ, thermal conductivity, k, specific heat, C_p, and steady-state velocity, $u = U$. Assuming all thermophysical properties are constant and equal to unity, an analytical solution for this problem may be derived:

$$T = \frac{1 - e^{Ux}}{1 - e^{U}} \tag{2.48}$$

The test case was performed with $T_1 = 1$, $T_2 = 0$, and U = -10, -1, 1, and 10. Figure 2.12 shows that there is excellent agreement between the predicted numerical and analytical temperature distributions for the range of steady-state velocities examined.

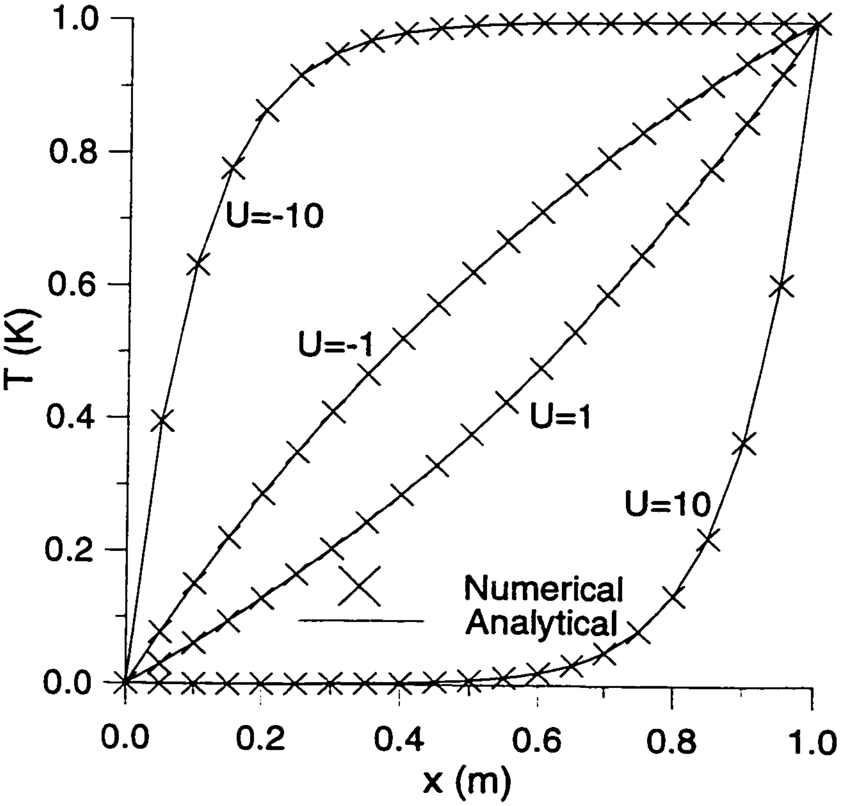

Figure 2.12: Comparison of the predicted numerical and analytical solutions for the one-dimensional advection-diffusion test case.

2.3.2 Steady-State Isothermal Laminar Flow

The fluid dynamics module was evaluated with two isothermal laminar fluid flow test cases: Poiseuille (pressure-driven) steady duct flow and lid-driven cavity flow.

Poiseuille Steady Duct Flow

Poiseuille flow under an imposed pressure gradient in a rectangular duct is a three-dimensional steady-state fluid flow test case for which an analytical solution exists [107]. The solution domain and boundary conditions are shown in Figure 2.13. A no-slip boundary condition is imposed on the duct walls, as shown, and a pressure gradient, $\partial P/\partial x = C$, is imposed across the domain in the x direction. The flow is assumed to be fully developed. The test case was performed for a range of pressure gradients in a solution domain with 5×10×10 uniform elements, in the x, y, and z directions, respectively.

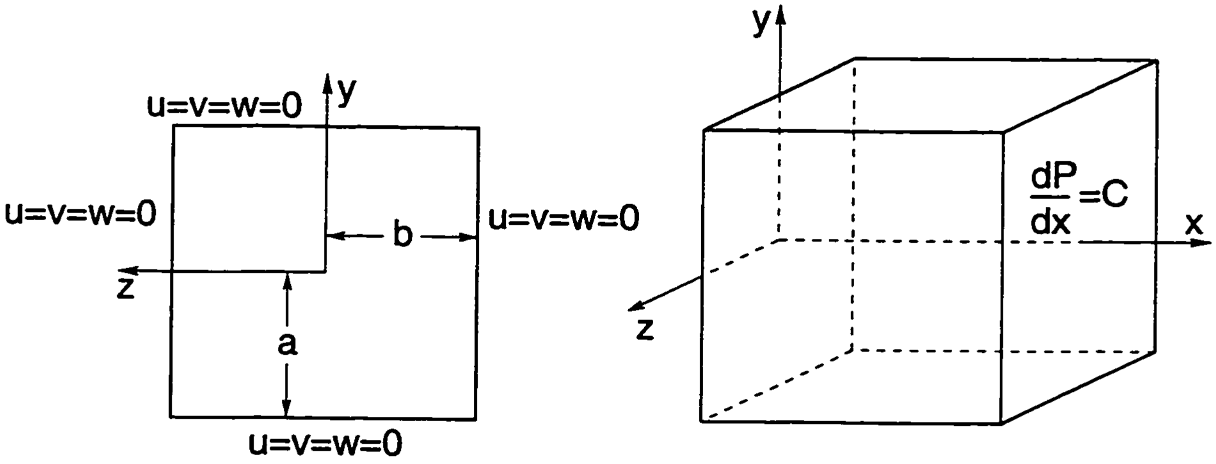

Figure 2.13: Poiseuille flow problem configuration and boundary conditions.

An analytical solution is available for this flow [107] with an imposed pressure gradient of $\partial P/\partial x$ and a constant viscosity μ; *i.e.*, the velocity in the x direction for any value of y and z is given by

$$u = \frac{16a^2}{\mu\pi^3}\left(-\frac{\partial P}{\partial x}\right)\sum_{i=1,3,5,\ldots}^{\infty}(-1)^{\frac{(i-1)}{2}}\left[1-\frac{cosh(i\pi z/2a)}{cosh(i\pi b/2a)}\right]\times\frac{cos(i\pi y/2a)}{i^3} \qquad (2.49)$$

The test case was performed using $a = b = 1$, $\mu = 1$, and $\partial P/\partial x = -10$ and 10. Figure 2.14 is a plot of predicted numerical and analytical x-direction velocity versus y at $z = 0$. As seen in the figure, the numerical predictions are in good agreement with the analytical solution.

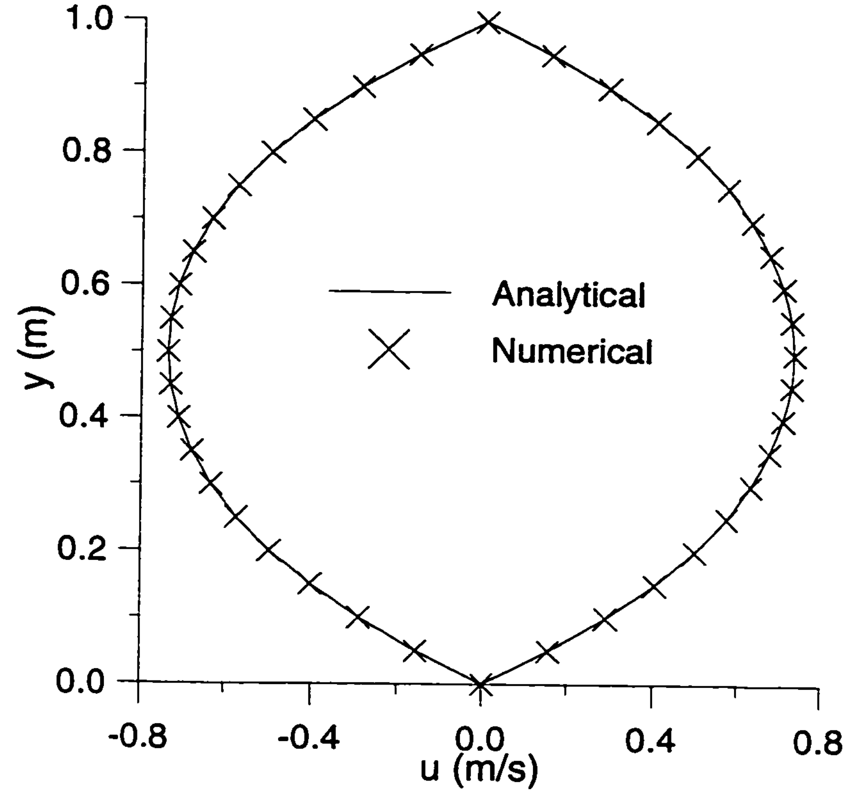

Figure 2.14: Comparison of the numerical and analytical solutions for the Poiseuille flow test case.

Lid-Driven Cavity Flow

The solution domain and boundary conditions for the two-dimensional lid-driven cavity flow test-case are given in Figure 2.15. This test case produces a recirculating, two-dimensional flow in the $x - y$ plane in which the cross-stream velocities reach the same order of magnitude as the streamwise velocities, similar to weld pool fluid flow.

There is no analytical solution for this test case; however, several researchers, for example, [108, 109, 110], have performed this test case with similar results. Following Bercovier and Engelman [109], the test case was performed for four different Reynolds numbers: ≈0, 100, 400, and 1000. The Reynolds number, as defined by

$$Re = \frac{\rho U L}{\mu} \tag{2.50}$$

was adjusted by setting all parameters equal to 1 and varying only the viscosity, μ. A

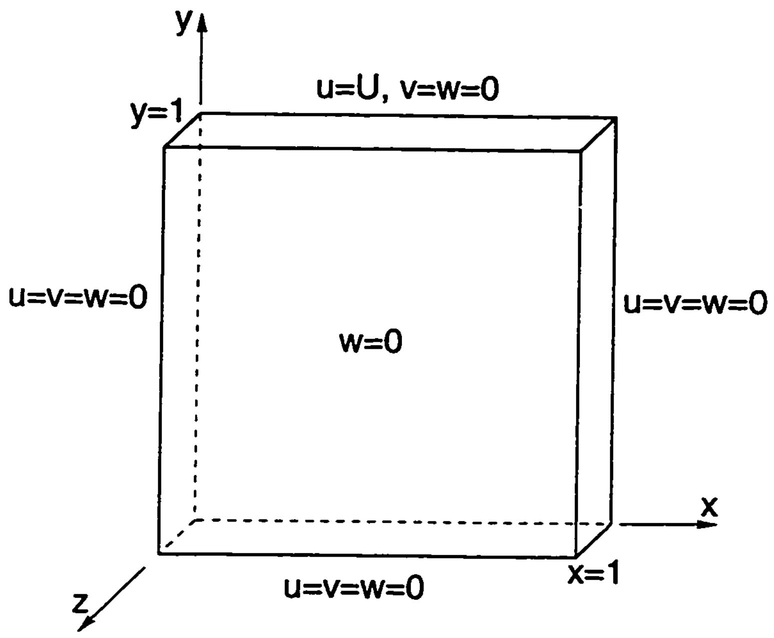

Figure 2.15: Lid-driven cavity flow problem configuration and boundary conditions.

grid refinement study ensured mesh independence for the test case was obtained with a uniform mesh having 20×20×1 elements.

Figure 2.16 shows predicted values of x-direction velocity (u) at $z = 1/2$ versus y at $z = 1/2$ for the four Reynolds numbers. These predicted x velocity profiles compare well with Bercovier and Engelman [109]. In the figure, the presence of a thin boundary layer is apparent at $Re = 1000$, a thicker boundary layer is seen at $Re = 400$, but no boundary layer is present at the two lowest Reynolds numbers.

The test case for the four different Reynolds numbers also produced flow patterns which agreed well with Bercovier and Engelman [109]. As an example, Figure 2.17 is the flow pattern for the $Re = 1000$ case. The flow patterns for this test case at the four different Reynolds numbers show the circulation of a main eddy around a centre point of zero velocity. The location of this $\vec{v} = 0$ centre point for the main eddy is a function of Reynolds number: the centre point migrates towards the right and also downwards with increasing Reynolds number. Visible in the flow pattern are very small eddies in the lower corners which become more pronounced as the Reynolds number increases. Details

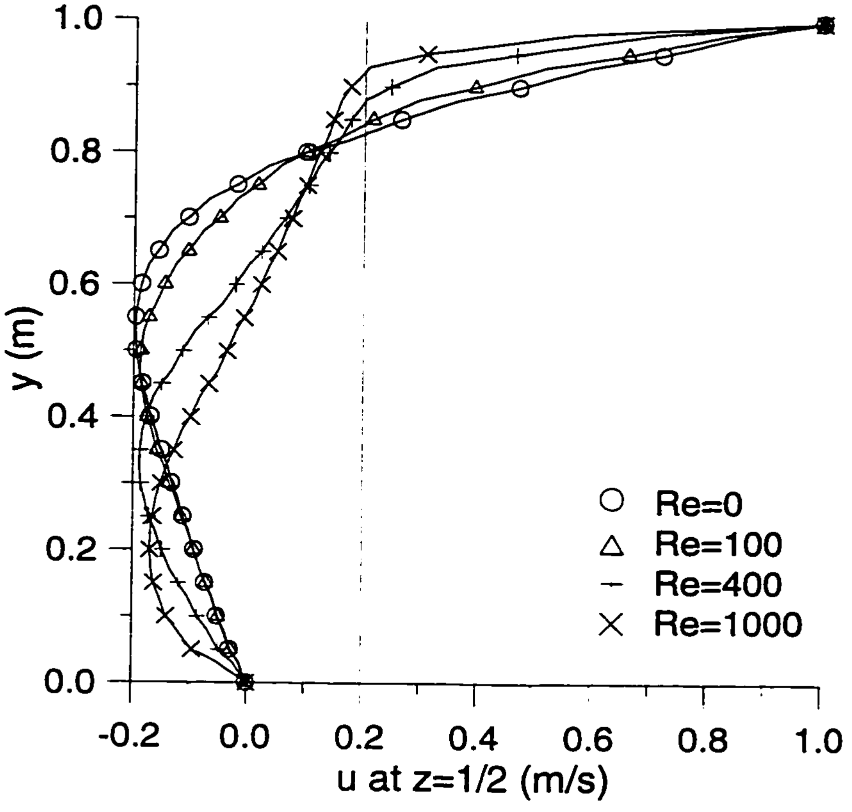

Figure 2.16: Predicted y versus u at $z = 1/2$.

of these eddies would be more apparent with increased mesh refinement.

Centrepoints ($\vec{v} = 0$) of the main eddy for the four Reynolds numbers are compared with those predicted by Bercovier and Engelman [109] in Table 2.4 which indicates good agreement.

Table 2.4: Comparison of predicted centrepoints ($\vec{v} = 0$) of the main eddy.

Re	Present work	Bercovier & Engelman [109]	% Difference
≈0	(0.50,0.76)	(0.50,0.74)	(0,2.7)
100	(0.63,0.73)	(0.62,0.73)	(1.6,0)
400	(0.58,0.62)	(0.57,0.61)	(1.7,1.6)
1000	(0.57,0.57)	(0.54,0.56)	(5.6,1.8)

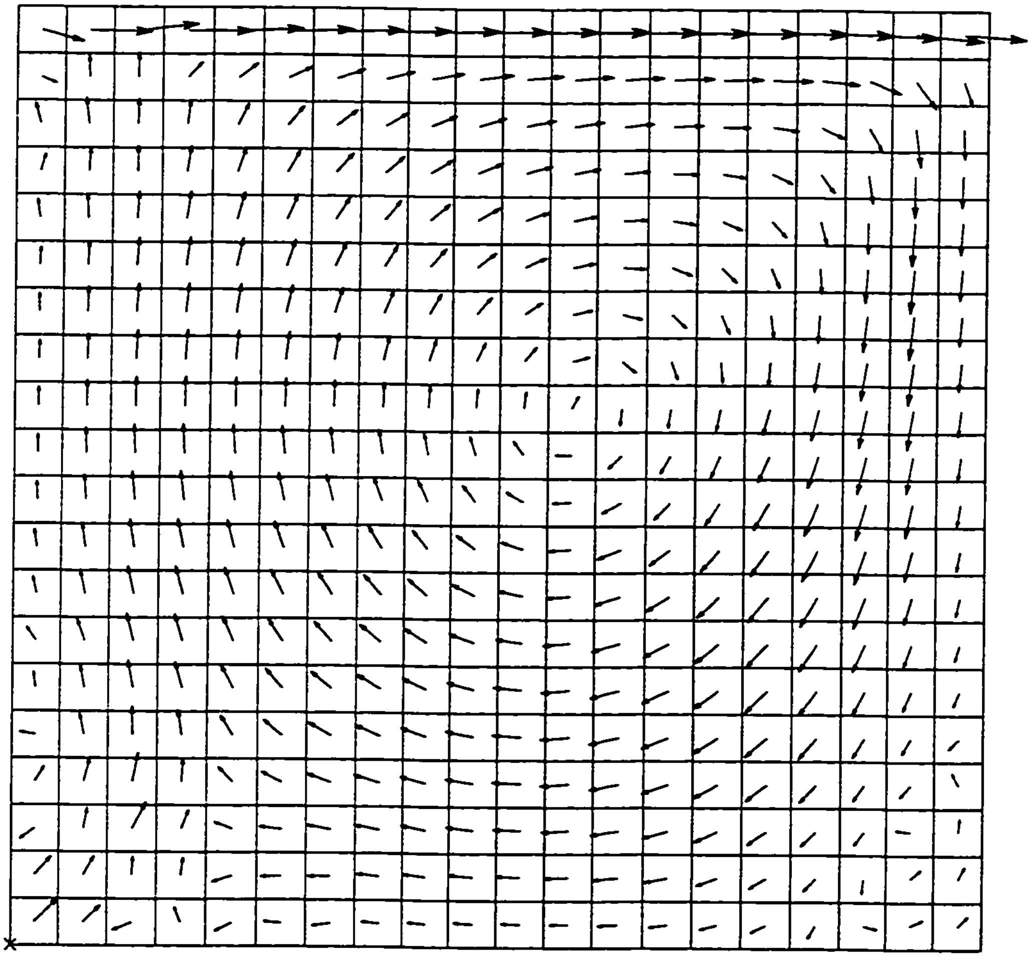

Figure 2.17: Flow pattern for square wall-driven cavity flow with $Re = 1000$.

2.3.3 Non-Isothermal Laminar Flow

The combination of the thermal and fluid dynamics models were evaluated with two non-isothermal laminar fluid flow test cases: buoyancy-driven flow (natural convection) and Marangoni flow (surface tension gradient-driven flow) in square cavities.

Buoyancy-Driven Flow

The buoyancy-driven flow test case is a two-dimensional problem which consists of a square cavity with differentially heated vertical sides. The boundary conditions are shown in Figure 2.18. The test case was performed using a mesh composed of 40×40×1 elements. A benchmark solution for this test case has been compiled by De Vahl Davis and Jones [111]. Following the benchmark, the test case was performed for Rayleigh numbers, $Ra = 10^3$, 10^4, and 10^5, where Ra is defined by

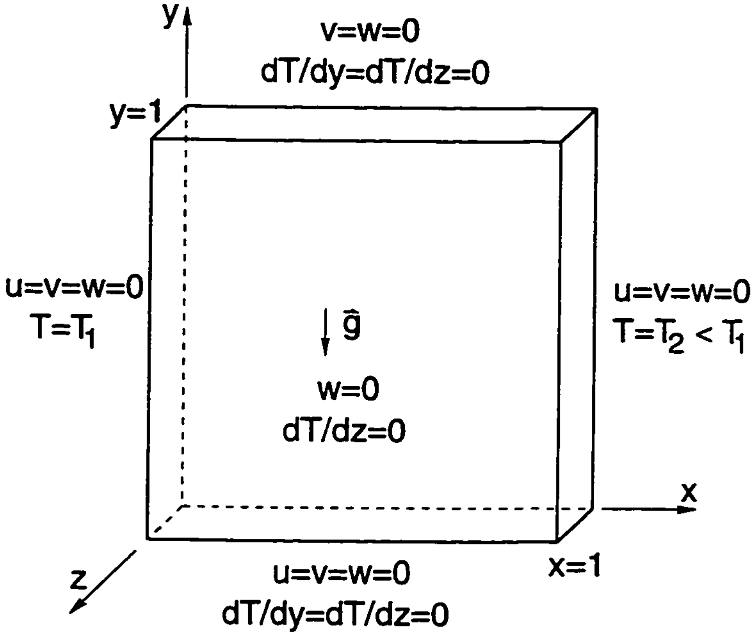

Figure 2.18: Buoyancy-driven flow problem configuration and boundary conditions.

$$Ra = \frac{\rho^2 C_p \beta \vec{g}(T_2 - T_1)L^3}{k\mu} \tag{2.51}$$

An additional constraint is the Prandtl number $Pr = 0.71$, where

$$Pr = \frac{C_p \mu}{k} \tag{2.52}$$

Figures 2.19 and 2.20 are plots of the predicted flow fields for $Ra = 10^3$ and $Ra = 10^5$. As seen in Figure 2.19, there is a large-scale recirculation loop at the lowest Rayleigh number which develops into two smaller eddies at the highest Rayleigh number (Figure 2.20). These flow patterns agree well with those reported by De Vahl Davis and Jones [111].

The code was also evaluated through comparisons of the predicted values for u_{max} and v_{max} and their respective locations with the benchmark solution. As shown in Table 2.5, the performance of the code compared favourably with benchmark results reported by De Vahl Davis and Jones [111]: predicted maximum velocities were within 0.2% and their locations within 5%.

Table 2.5: Comparison of thermofluids code predictions with the benchmark solution. (Benchmark solution by De Vahl Davis and Jones [111].)

Ra		Present work	Benchmark [111]	% Difference
10^3	u_{max}	3.649	3.649	0.0
	$y\ (x=0)$	0.813	0.813	0.0
	v_{max}	3.694	3.697	0.08
	$x\ (y=0)$	0.172	0.178	3.4
10^4	u_{max}	16.175	16.178	0.02
	$y\ (x=0)$	0.828	0.823	0.6
	v_{max}	19.602	19.617	0.08
	$x\ (y=0)$	0.125	0.119	5.0
10^5	u_{max}	34.80	34.73	0.2
	$y\ (x=0)$	0.859	0.855	0.5
	v_{max}	68.57	68.59	0.03
	$x\ (y=0)$	0.063	0.066	4.5

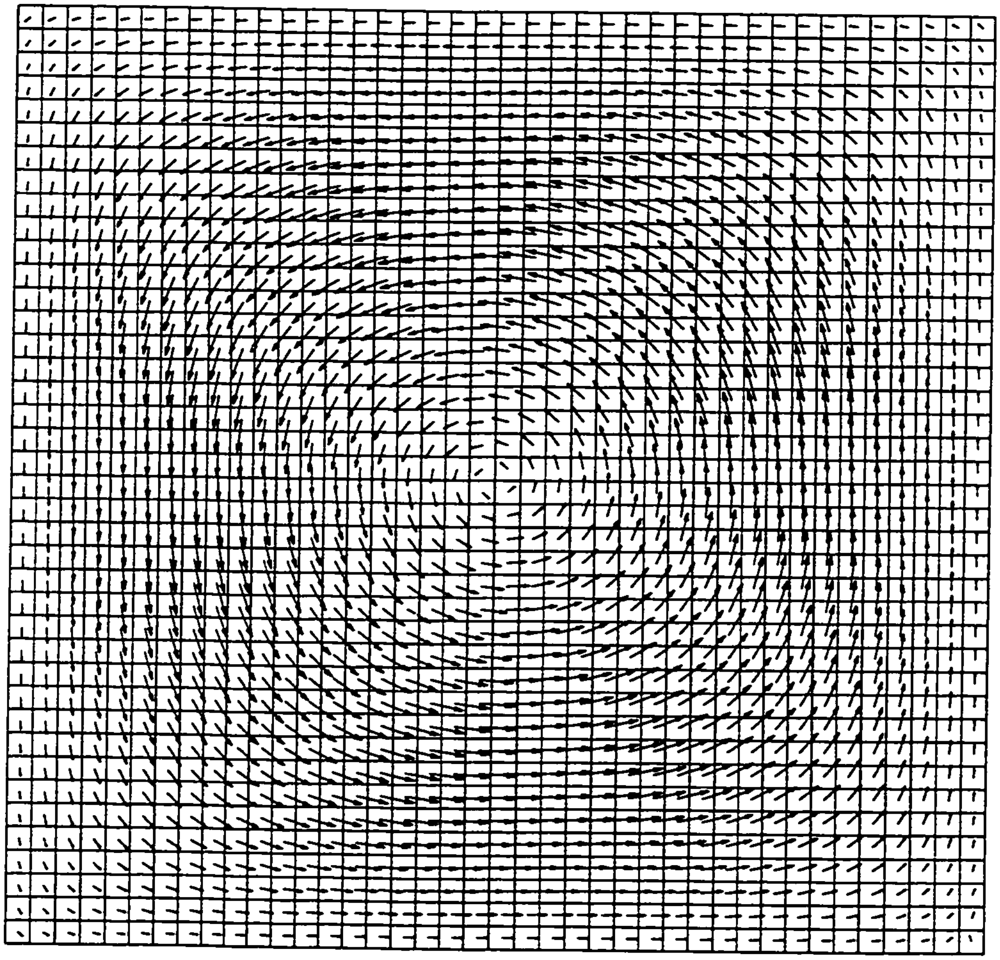

Figure 2.19: Flow pattern for buoyancy-driven flow with $Ra = 10^3$.

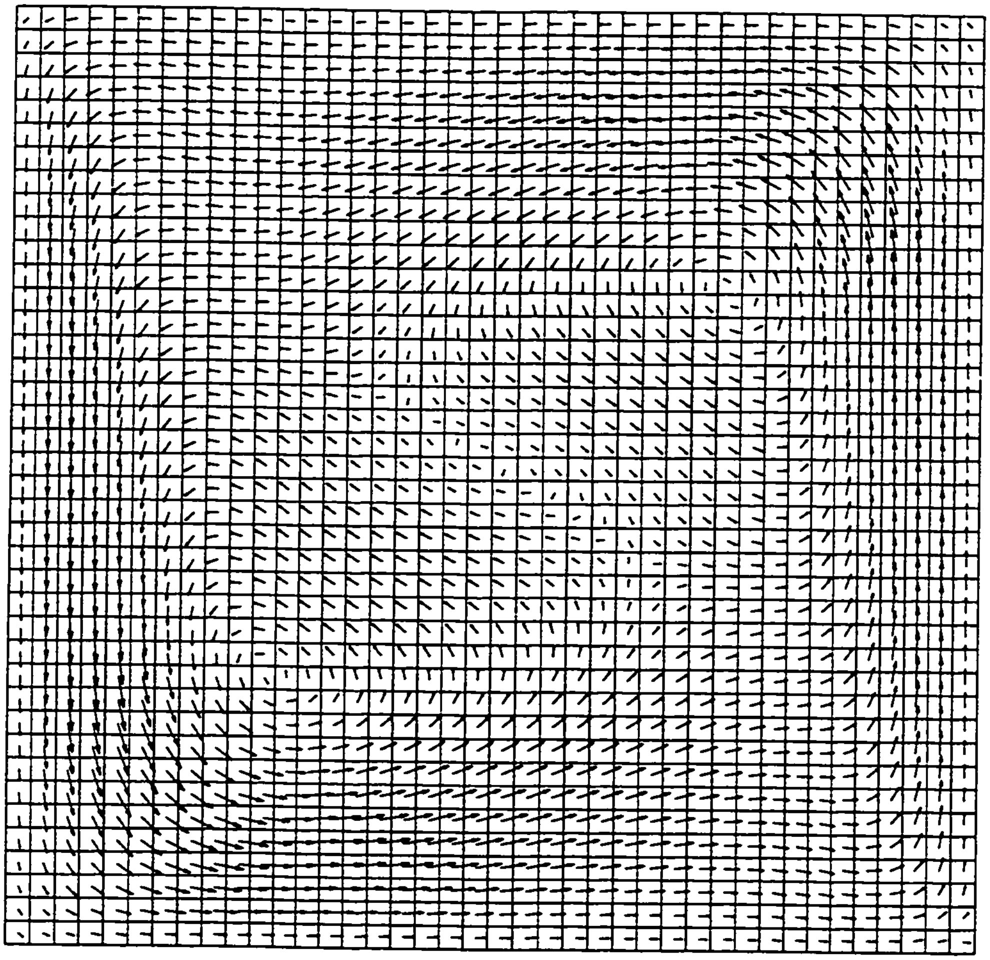

Figure 2.20: Flow pattern for buoyancy-driven flow with $Ra = 10^5$.

Marangoni Flow

The surface tension temperature gradient (Marangoni) test case is a two-dimensional problem which consists of a square cavity with differentially heated walls. Fluid flow is driven across the top by the surface tension gradient arising from the temperature difference between the two walls. The boundary conditions for this test case are shown in Figure 2.21: Dirichlet boundary conditions were imposed on each end, *i.e.*, $T = T_1$ and $T = T_2$, and a surface tension temperature gradient force on the top surface. Three mesh sizes were used: 10×10×1, 20×20×1, and 40×40×1.

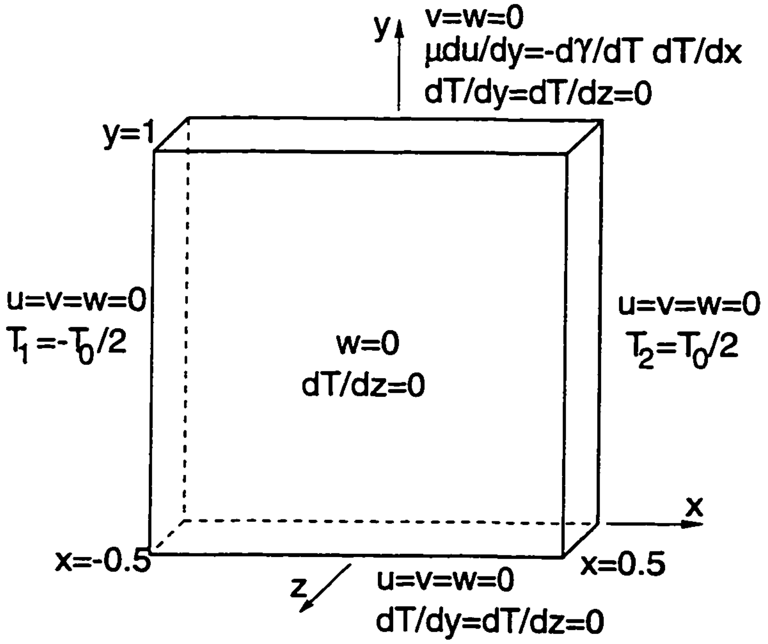

Figure 2.21: Marangoni flow problem configuration and boundary conditions.

Following Zebib *et al.* [112], the test case was performed for Marangoni numbers $Ma = 100$, 1000, and 10 000, where Ma is defined by

$$Ma = Re \times Pr = \frac{\partial \gamma}{\partial T}\left(\frac{\rho C_p L T_o}{\mu k}\right) \tag{2.53}$$

in which $T_o = (T_1 - T_2)/2$. An additional constraint is $Pr = 1$.

As an example, Figure 2.22 is the flow pattern for the $Ma = 1000$ case. The flow patterns for this test case at the three different Marangoni numbers show the circulation of a main eddy around a centre point of zero velocity.

Figures 2.23 through 2.28 show predicted non-dimensional temperature, T/T_o, at the top surface (*i.e.*, $y = 1$) versus x position with increasingly refined meshes, for Ma numbers of 100, 1000, and 10 000, respectively. The figures indicate that mesh independence is reached for the thermal field with relatively few elements and that these temperature fields are very strongly affected by the fluid flow for $Ma \geq 1000$.

Figures 2.28 through 2.30 show the non-dimensional top surface velocity, $u\gamma T_o/\mu$ versus x position with increasingly refined meshes, for Ma numbers of 100, 1000, and 10 000, respectively. The figures indicate that, in all cases, mesh independence with the 40×40×1 mesh is reached for the flow field only at the lowest Ma number; however at higher Ma numbers the 40×40×1 mesh is still not sufficiently refined. It is evident that the thermal field may be accurately predicted with fewer elements than the velocity field.

Values of temperature and velocity on the surface for the 40×40×1, compare well with published values by Zebib *et al.* [112], as shown in Tables 2.6 and 2.7.

Table 2.6: Comparison of predicted surface temperatures with Zebib *et al.* [112].

x	$Ma = 100$			$Ma = 1000$			$Ma = 10\ 000$		
	Present	[112]	%Diff	Present	[112]	%Diff	Present	[112]	%Diff
0.5	-0.500	-0.500	0.0	-0.500	-0.500	0.0	-0.500	-0.500	0.0
0.45	-0.399	-0.390	2.3	-0.095	-0.101	5.9	0.015	0.017	11.8
0.4	-0.302	-0.308	1.9	0.031	0.030	3.3	0.047	0.043	9.3
0.35	-0.215	-0.221	2.7	0.085	0.081	4.9	0.051	0.051	0.0
0.3	-0.140	-0.148	5.4	0.114	0.111	2.7	0.055	0.054	1.9
0.25	-0.075	-0.083	9.6	0.131	0.127	3.1	0.060	0.055	7.1
0.0	0.151	0.150	5.3	0.193	0.192	0.5	0.107	0.103	3.9
-0.25	0.324	0.329	1.5	0.305	0.299	2.0	0.212	0.205	3.4
-0.5	0.500	0.500	0.0	0.500	0.500	0.0	0.500	0.500	0.0

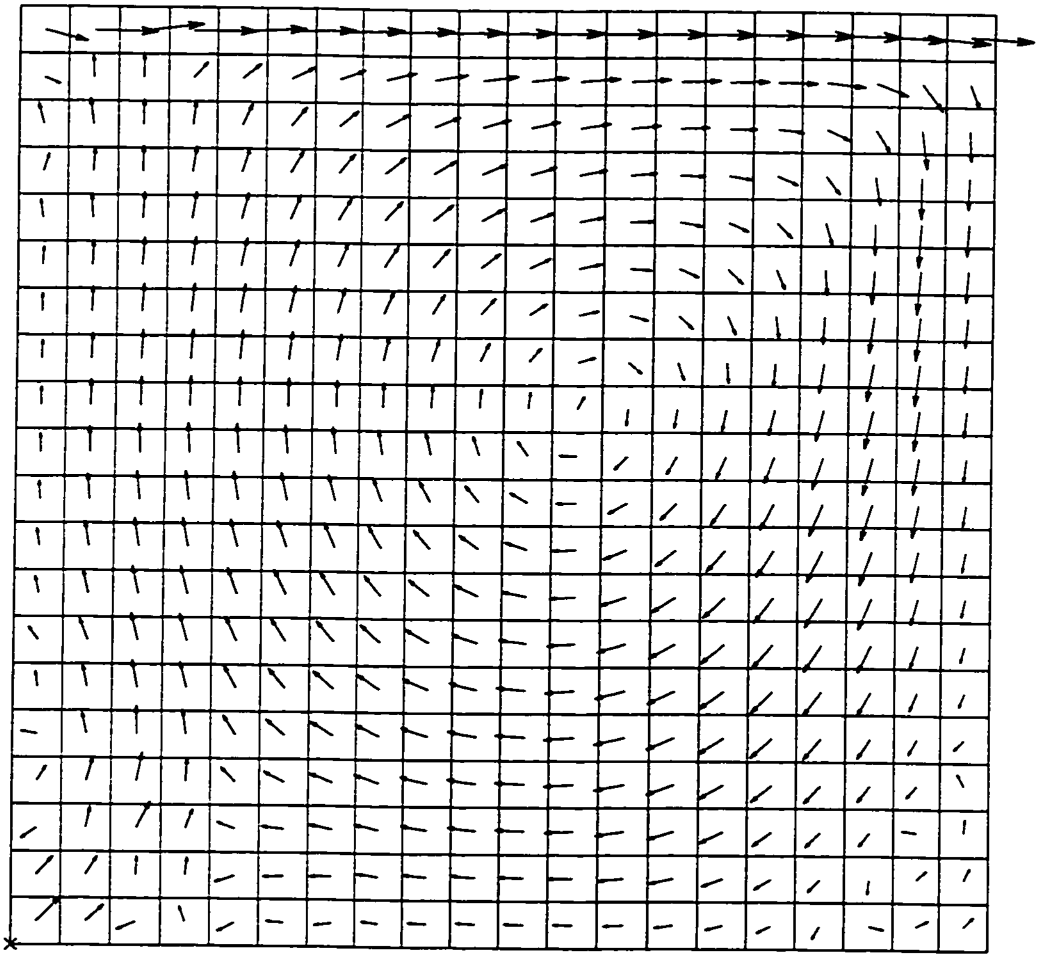

Figure 2.22: Flow pattern for square wall-driven cavity flow with $Ma = 1000$.

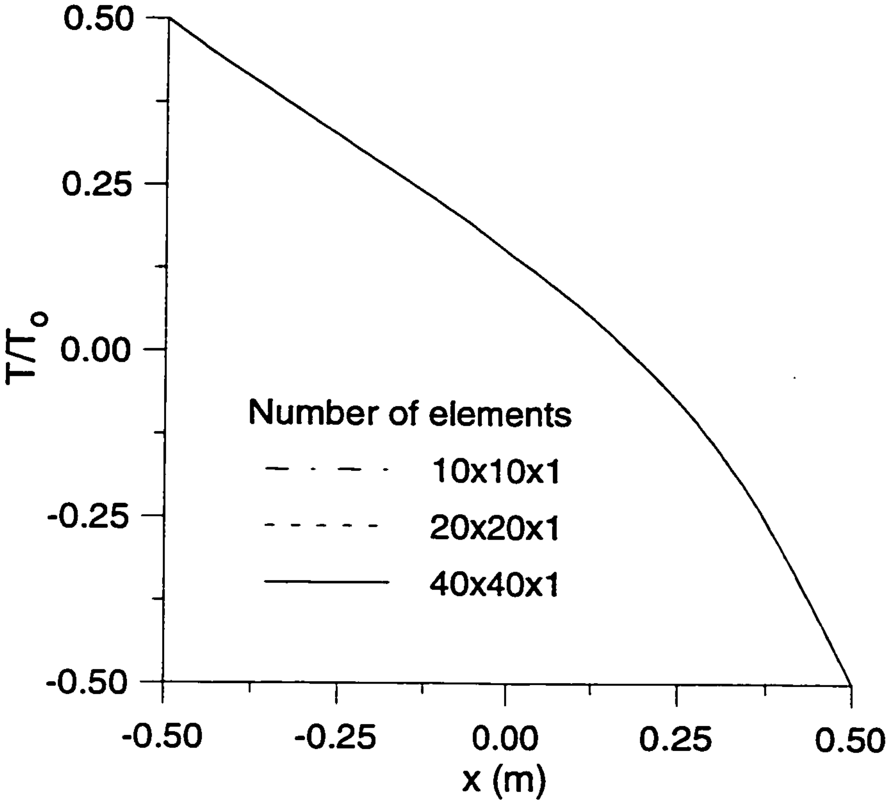

Figure 2.23: Non-dimensional surface temperature versus position for $Ma = 100$.

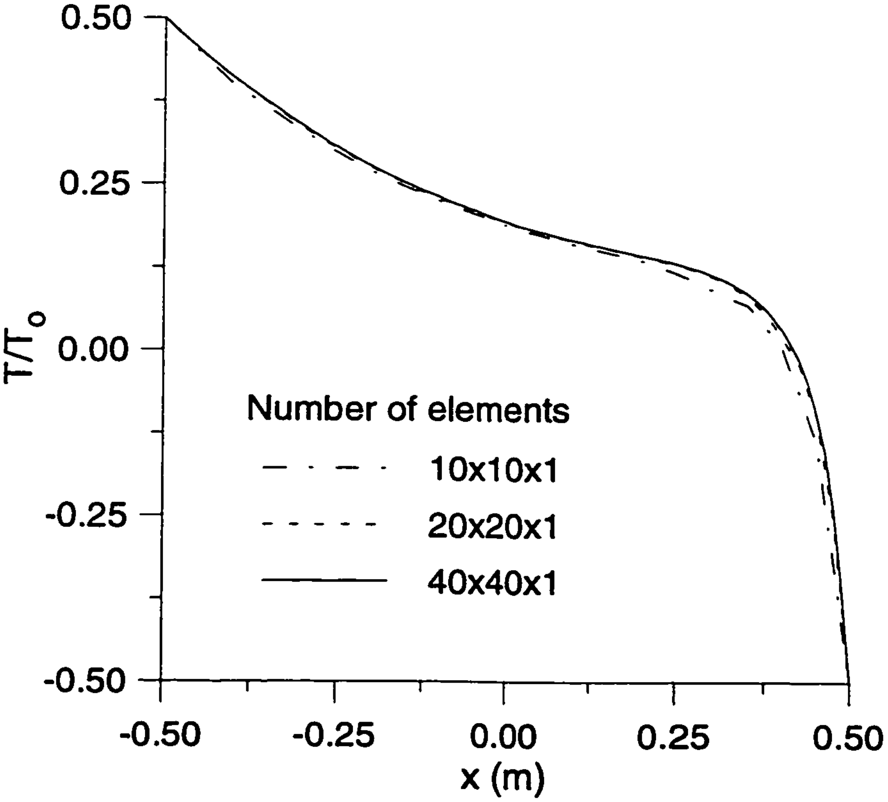

Figure 2.24: Non-dimensional surface temperature versus position for $Ma = 1000$.

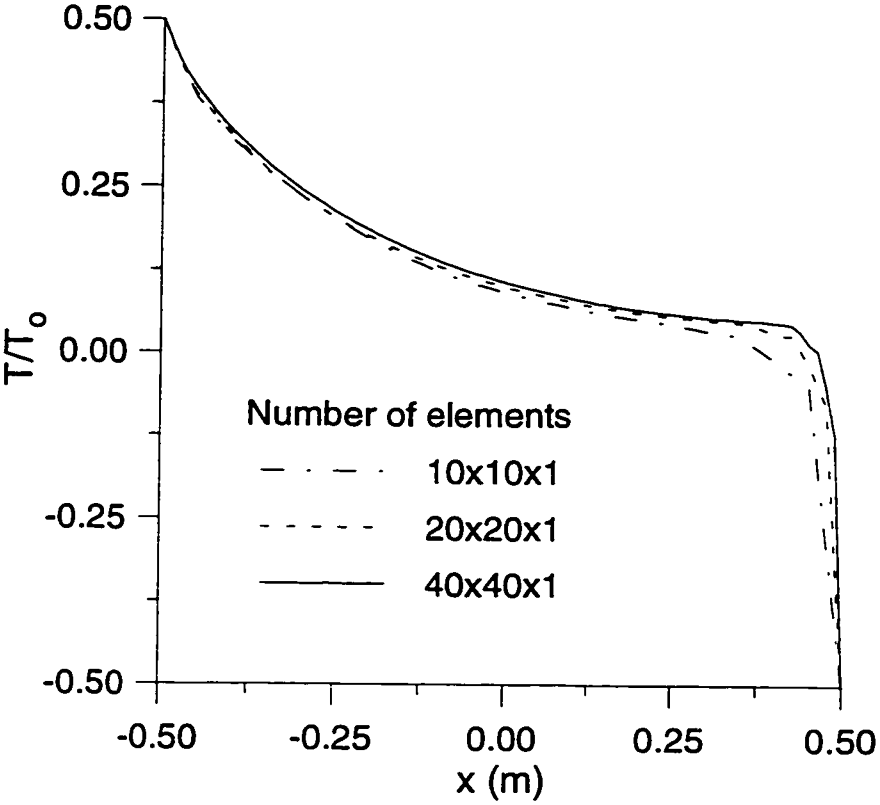

Figure 2.25: Non-dimensional surface temperature versus position for Ma = 10 000.

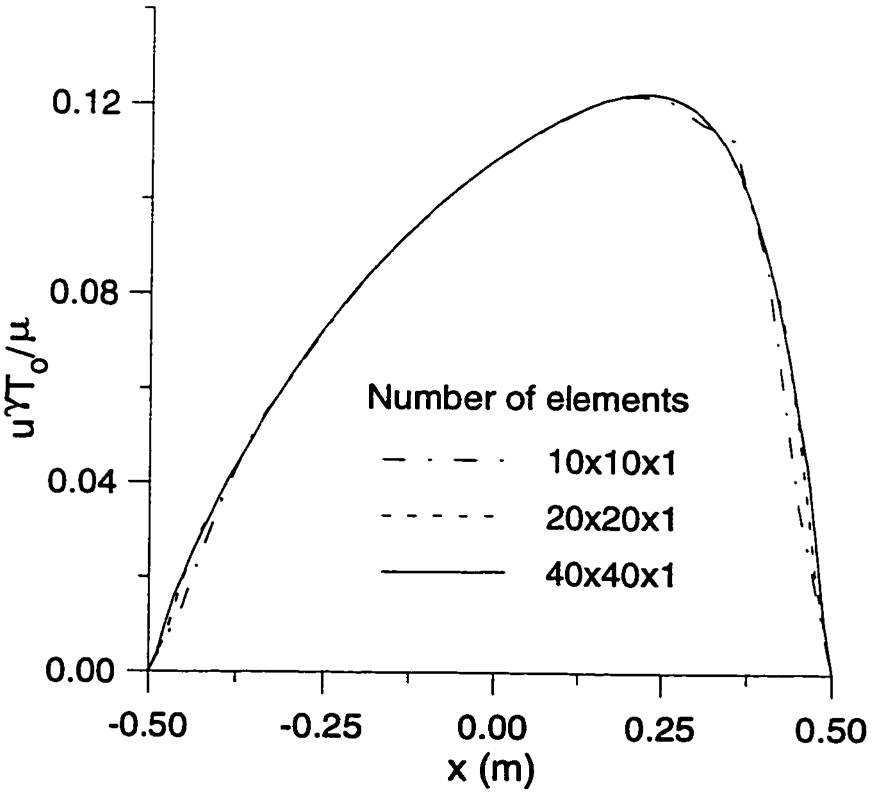

Figure 2.26: Non-dimensional surface velocity versus position for Ma = 100.

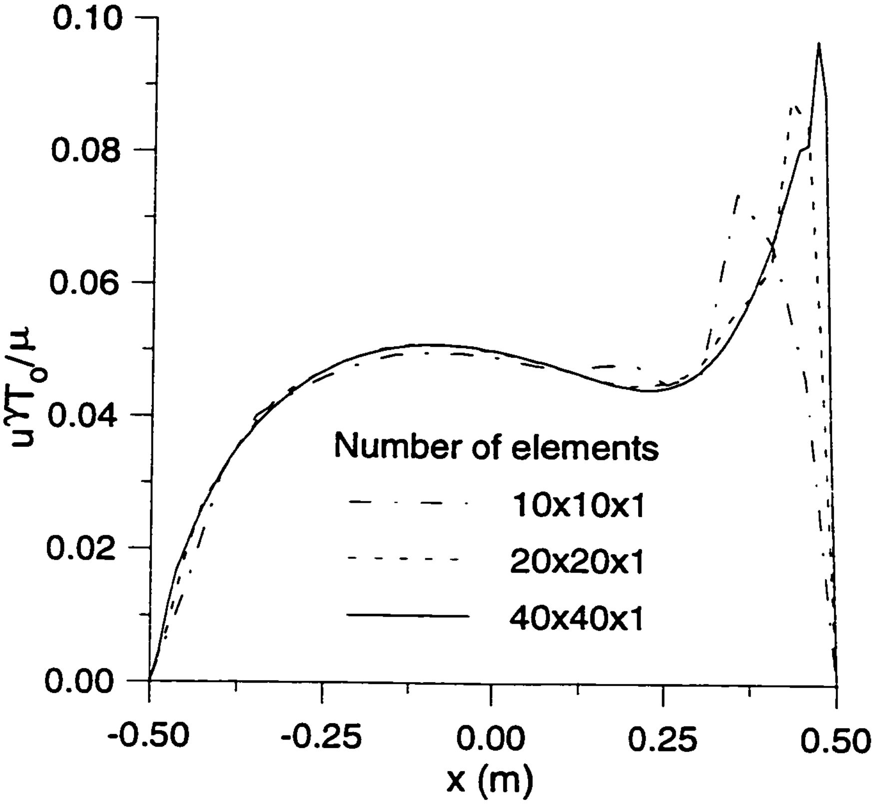

Figure 2.27: Non-dimensional surface velocity versus position for $Ma = 1000$.

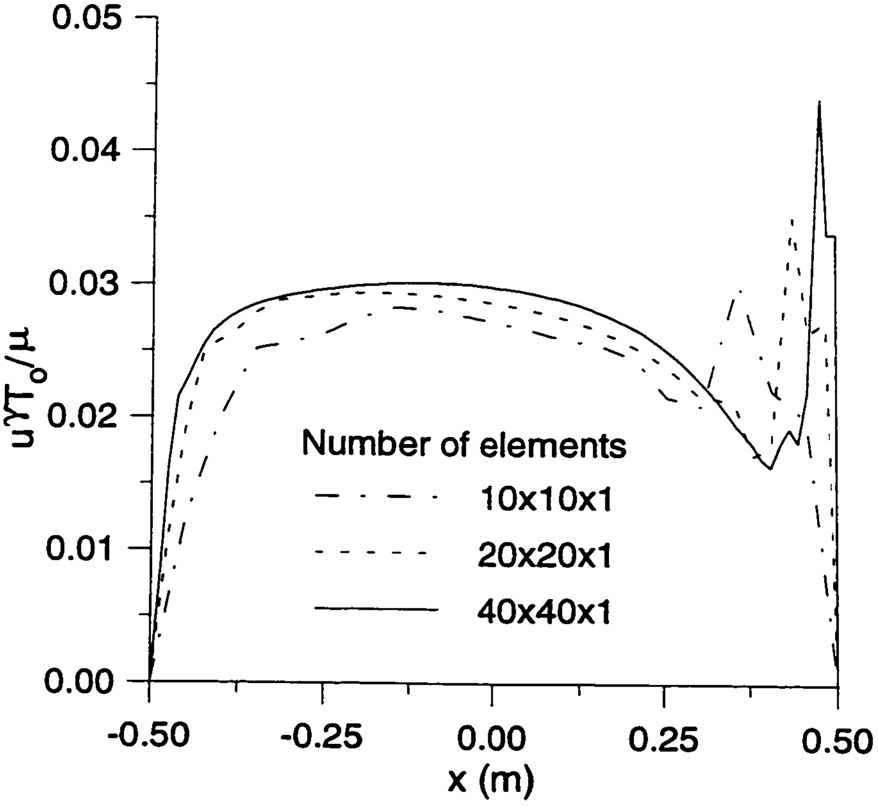

Figure 2.28: Non-dimensional surface velocity versus position for $Ma = 10\ 000$.

Table 2.7: Comparison of predicted surface velocities with Zebib *et al.* [112].

x	$Ma = 100$			$Ma = 1000$			$Ma = 10\ 000$		
	Present	[112]	%Diff	Present	[112]	%Diff	Present	[112]	%Diff
0.5	0.000	0.000	0.0	0.000	0.000	0.0	0.000	0.000	0.0
0.45	0.054	0.064	15.6	0.082	0.085	3.5	0.022	0.021	4.8
0.4	0.089	0.094	5.3	0.066	0.066	0.0	0.016	0.015	6.7
0.35	0.108	0.112	3.6	0.054	0.054	0.0	0.019	0.019	0.0
0.3	0.118	0.119	0.8	0.047	0.048	2.1	0.023	0.022	4.5
0.25	0.111	0.122	9.0	0.044	0.045	2.2	0.025	0.025	0.0
0.0	0.109	0.109	0.0	0.050	0.049	2.0	0.030	0.030	0.0
-0.25	0.073	0.074	1.4	0.047	0.047	0.0	0.030	0.031	3.3
-0.5	0.000	0.000	0.0	0.000	0.000	0.0	0.000	0.000	0.0

The results from the Marangoni flow test case suggest that in the present study, the thermal field may not be strongly influenced by the flow field, in particular for Al-4.5%Cu in which $Pr \approx 0.02$; therefore, the thermal behaviour of the pool may be modelled accurately using fewer elements than required for a mesh-independent fluid flow solution. Furthermore, the purpose of the present study is to accurately model the thermal behaviour of the weld pool, specifically the thermal gradient at the solid/liquid interface, G_L, and only model the fluid flow inasmuch as its influence on the thermal field is incorporated. Thus, in the present study, it may be possible to obtain accurate predictions of R and G_L without comprehensive and precise knowledge of the flow behaviour in the weld pool.

It is clear from the test case results that the thermofluids code functions well for isothermal and non-isothermal laminar flow scenarios. The test case results compared well with available published benchmark solutions.

Chapter 3

MATERIALS AND EXPERIMENTAL PROCEDURES

3.1 Materials

This study is concerned with elucidating the mechanisms involved in promoting a CET in a weld pool. As such, commercial alloys are much more difficult to work with since they contain alloying components and impurities which introduce many variables and added complexity into the system, particularly with respect to clear identification or control of the nucleation mechanisms. Pure binary aluminum-copper alloys were selected as a model solidification system for the experiments in this study since this alloy system is well characterized with respect to thermophysical properties. The alloys were fabricated by Alcan International Limited in Kingston, Ontario. Eight alloy samples were cast and then rolled into plates of approximately 2 mm thickness. Titanium diboride (TiB_2) was added in different amounts during casting to most of the alloys to act as a nucleating agent for equiaxed grains. The aluminum alloys contained nominal copper levels of 2 and 4%, and nominal titanium levels of < 0.001, 0.003, 0.015, and 0.03%. The measured levels of copper and titanium in these alloys are listed in Table 3.1

Table 3.1: Measured compositions of the Al-Cu experimental alloy system.

Sample	Al (wt%)	Cu (wt%)	Ti (wt%)
1	98.01 ± 1.22	1.97 ± 0.09	< 0.001
2	98.01 ± 1.22	1.98 ± 0.09	0.004 ± 0.001
3	98.01 ± 1.22	1.96 ± 0.09	0.013 ± 0.002
4	98.03 ± 1.22	1.93 ± 0.09	0.027 ± 0.004
5	96.15 ± 1.22	3.83 ± 0.15	< 0.001
6	96.13 ± 1.22	3.86 ± 0.15	0.003 ± 0.001
7	96.13 ± 1.22	3.85 ± 0.15	0.013 ± 0.002
8	96.12 ± 1.22	3.84 ± 0.15	0.026 ± 0.004

3.1.1 Specimen Preparation

Weld specimens measuring 76 mm × 200 mm were sheared from the rolled plates. The specimens were degreased in two stages: Varsol was used to clean roll lubricant and grease from the specimens, followed by n-Heptane to remove any Varsol residue. The top surface of the plates were then lightly abraded with a stainless steel wire brush to improve arc registration [113].

3.2 Welding Apparatus

The welding process chosen for the experiments was gas tungsten arc (GTA) welding. This process was selected as most suitable for the present study since the electrode is not consumed during welding and therefore will not alter the specimen composition and thereby introduce added complexity.

A photograph of the welding apparatus is shown in Figure 3.1 and a labelled schematic in Figure 3.2. The apparatus comprised the following items:

- *Welding torch*: A WELDCRAFT^{TM} model WP-27 GTA welding torch was mounted on a vertical rack-and-pinion-driven traversing mechanism which, in turn, was mounted on a stationary frame. The torch was water-cooled with a closed circuit pump operating with de-ionized water so as not to provide an alternative current path.

- *Specimen holder*: The welding specimens were clamped, as described later, in a specimen holder which was mounted on a horizontal moving carriage. Travel of the carriage was effected by a lead screw driven by a DC servo motor. Travel speed was feedback controlled by an ELECTRO-CRAFT^{TM} E-552-0 controller.

- *Welding power supply*: A THERMAL ARC^{TM} AC/DC inverter arc welder model 400 was employed to supply power to the torch. The supply was operated in alternating-current (AC) mode. This welding supply permitted control of welding current, duty cycle (*i.e.*, percentage of the AC pulse that is positive), AC frequency, and shielding gas pre- and postflow duration. The welder also featured a lift start option whereby the arc was initiated by touching the electrode to the workpiece and then lifting off.

- *Data acquisition system*: During welding, values of current, voltage, and travel speed were collected by a data acquisition system. This system will be described in detail in a later section.

Figure 3.1: Photograph of the welding apparatus

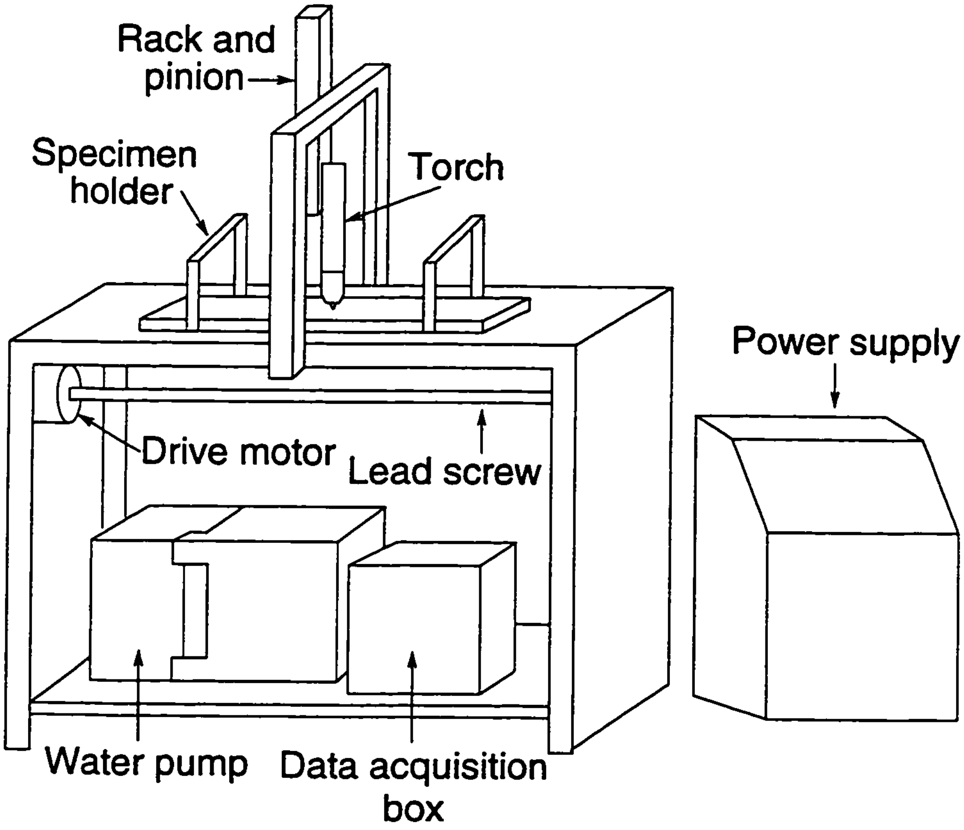

Figure 3.2: Schematic of the welding apparatus

3.2.1 Specimen Clamping

The high temperatures attained during GTA welding of thin aluminum plates cause considerable thermal distortion of the workpiece. Thus, clamping of the edges of the specimen was required on either side of the weld bead along the entire length of the plate. This prevented the plate from bowing upwards excessively, which would reduce the gap and may even allow the electrode to contaminate the weld pool. The clamping mechanism, however, could not be so close to the weld bead that it provided a direct current path to the arc or acted as a heat sink, thus modifying the weld pool dimensions.

A series of experiments was performed to determine the optimum clamp spacing (the total distance between the two clamps). Figure 3.3 is a plot of weld width *vs* clamp spacing. As indicated in the figure, a spacing of 45 mm was selected since beyond this distance the clamp spacing exhibited no influence on weld width and there was no possibility of the clamp providing a direct current path to the arc.

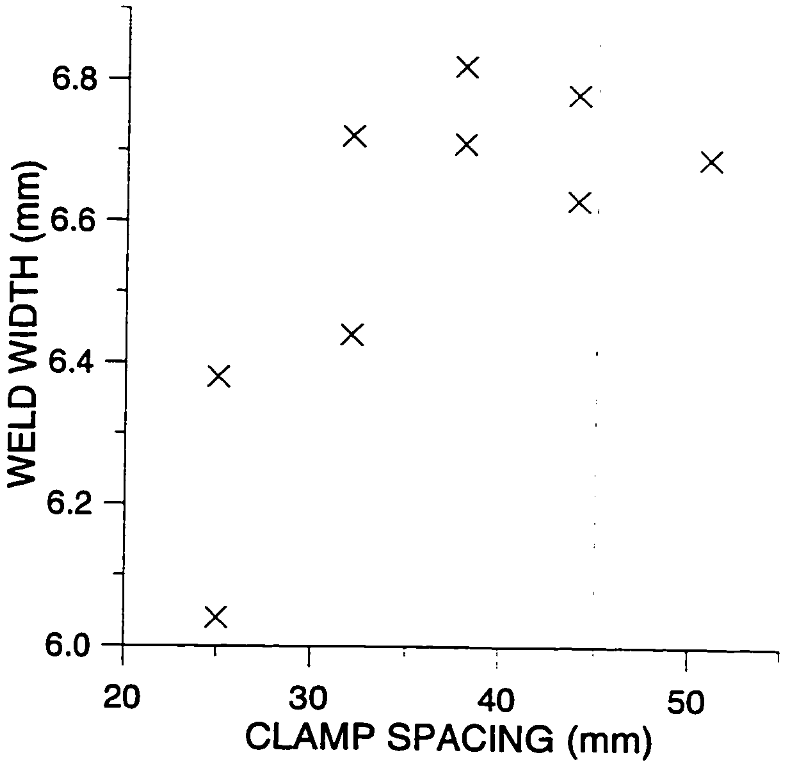

Figure 3.3: Weld width versus clamp spacing.

The clamps were fabricated from two AA6061 aluminum plates measuring 76 mm × 400 mm × 6.35 mm, each having a centreline slot measuring 200 mm × 45 mm. Weld specimens were sandwiched between the plates and clamped onto an aluminum specimen holder containing a centreline groove, as shown in Figures 3.4 and 3.5. The specimen holder was then mounted on the moving carriage and adjusted for level within ±0.25 mm end-to-end.

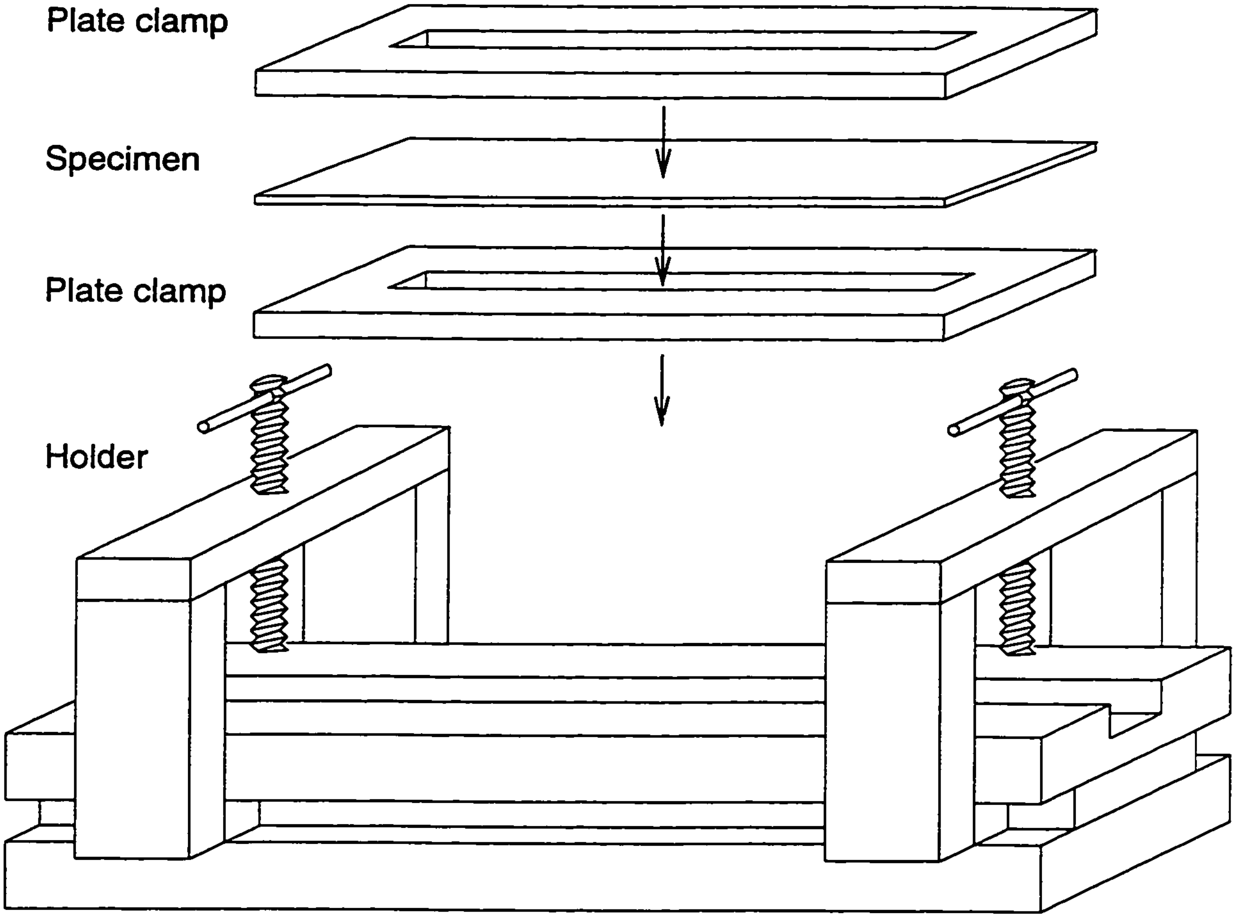

Figure 3.4: Schematic of specimen clamping mechanism.

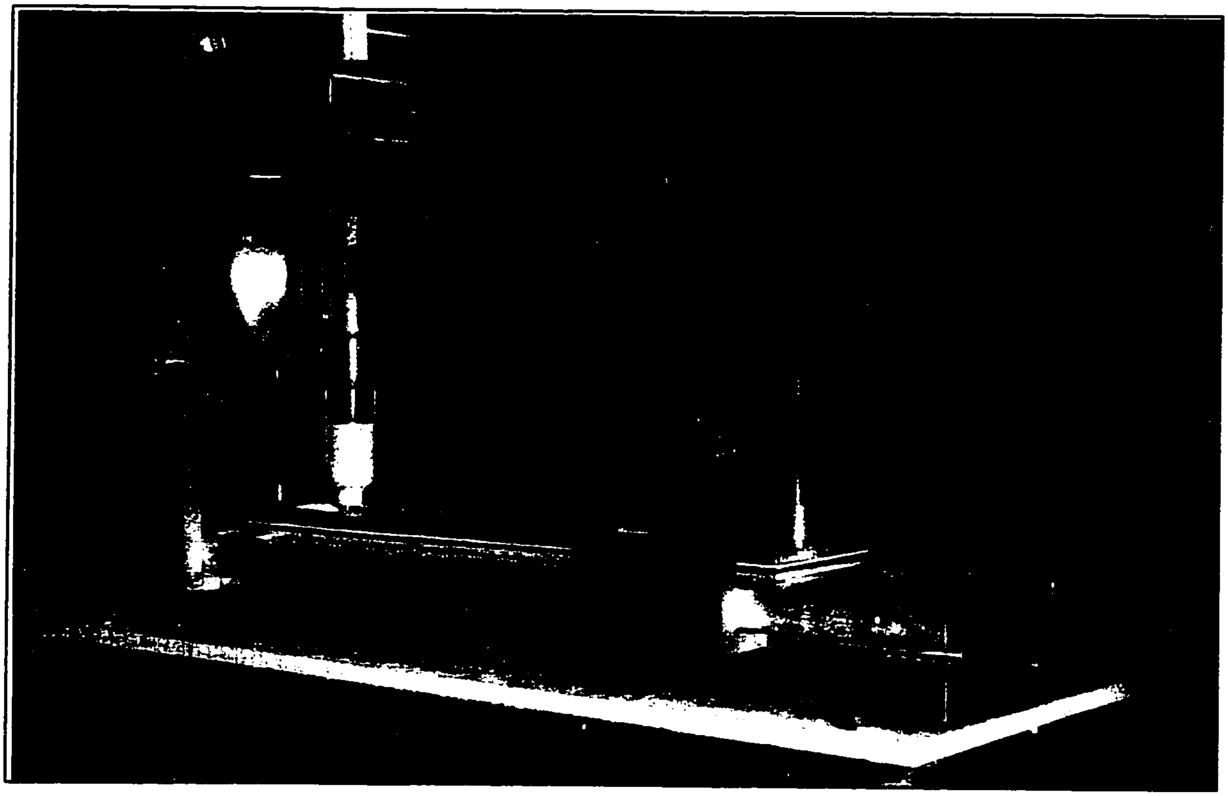

Figure 3.5: Photograph of the specimen holder.

3.3 Welding Process Conditions

Preliminary experiments were performed to establish the welding process conditions for successful bead-on-plate GTA welding of aluminum. Welding conditions were selected to give the best possible weld quality and are outlined below:

- *Duty cycle:* Of concern in GTA welding of aluminum is the tenacious surface oxide layer which must be removed in order for fusion of the metal to occur and the arc to be stable. In GTA welding, the arc is often operated in straight polarity (electrode negative) to optimize heat input to the workpiece, but for Al alloys this causes poor arc stability due to the oxide layer. The bombardment of ions on the surface oxide layer during welding with a reverse polarity arc is an effective means to remove the oxide [114]; however, a reverse polarity arc provides limited heat input to the workpiece and more heat input to the electrode. In GTA welding, this can cause melting of the tungsten electrode at relatively low currents. An alternating-current (AC) arc offers a good compromise between cleaning of the oxide and heating of the workpiece. An AC arc with a frequency of 60 Hz was used for this study. As depicted schematically in Figure 3.6, the pulse has a square waveform. The 'duty cycle' or 'cleaning' refers to the duration of pulse time spent in straight polarity compared to reverse polarity. In the present study, a duty cycle of 80% was used since this configuration optimized heating of the workpiece and cleaning of the oxide layer [113, 114]. As indicated in Figure 3.6, an 80% duty cycle implies that 80% of the wavelength is positive (straight polarity) and 20% negative (reverse polarity).

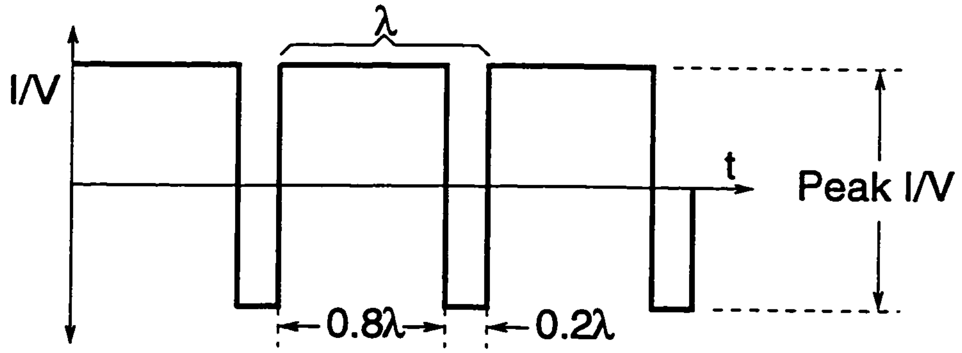

Figure 3.6: Schematic of AC signal.

- *Shielding gas:* Argon shielding gas was used since it provided good arc starting characteristics and arc stability, low arc voltage, and good cleaning compared to other shielding gasses [84, 115]. A flow rate of 0.85 m^3/h (30 CFH) was selected based on industrial practice [113]. A preflow duration of approximately 3 seconds was used to adequately flush the vicinity of the arc clear of air prior to welding. A postflow duration of 5 seconds was used to prevent oxidization of the electrode while it cooled [84]. A size 8 (12.7 mm inner diameter, shown in Figure 3.7) high impact ceramic nozzle was selected to provide sufficient shielding with the lowest possible flow rate [84, 116, 117]. A low flow rate is desirable since a turbulent stream of shielding gas may entrain atmospheric gasses which will cause porosity in the weld pool.

- *Electrodes:* Tungsten electrodes containing approximately 1% zirconium were employed since these support higher current levels, provide superior arc starting capability, and are less likely to contaminate the weld pool compared to pure tungsten electrodes [84, 115]. As well, zirconium additions prolong the electrode tip configuration when used with alternating current compared to thoriated electrodes which are generally used in direct current welding. An electrode size of 2.38 mm was selected based on its current-carrying capacity [84, 117]. As indicated in Figure 3.7, the distance that the electrode extended beyond the nozzle, or stickout, was one electrode diameter to ensure good shielding and prolonged nozzle life [84, 117]. The electrodes were ground to have an enclosed angle of approximately 75°.

- *Arc Length:* The arc length, or distance between the workpiece and the electrode, was set at 2 mm (shown in Figure 3.7). Preliminary experiments confirmed that this arc length was the best compromise between good arc stability and sufficient shielding.

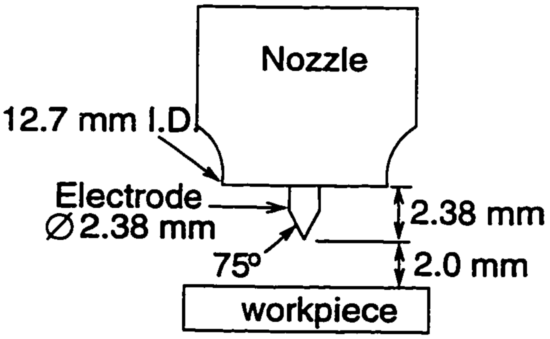

Figure 3.7: Schematic of nozzle.

3.3.1 Two-Dimensional Heat Flow

For clarity of interpretation of the weld microstructures for bead-on-plate welds on thin workpieces, it is desirable to have two-dimensional heat flow conditions [8], that is, parallel fusion boundaries and columnar grains which are parallel with the top surface of the plate. Figure 3.8 illustrates the potential difficulty in interpreting microstructures in welds having partial versus full penetration. As indicated in Figure 3.8(a), three-dimensional heat flow conditions, such as occur in partial-penetration welds, can produce a grain structure which appears to have a CET when viewed from the top surface, when, in fact, the central grains are merely the tips of columnar grains. Alternatively, as shown in Figure 3.8(b), two-dimensional heat flow conditions will produce columnar grains which are parallel with the top surface.

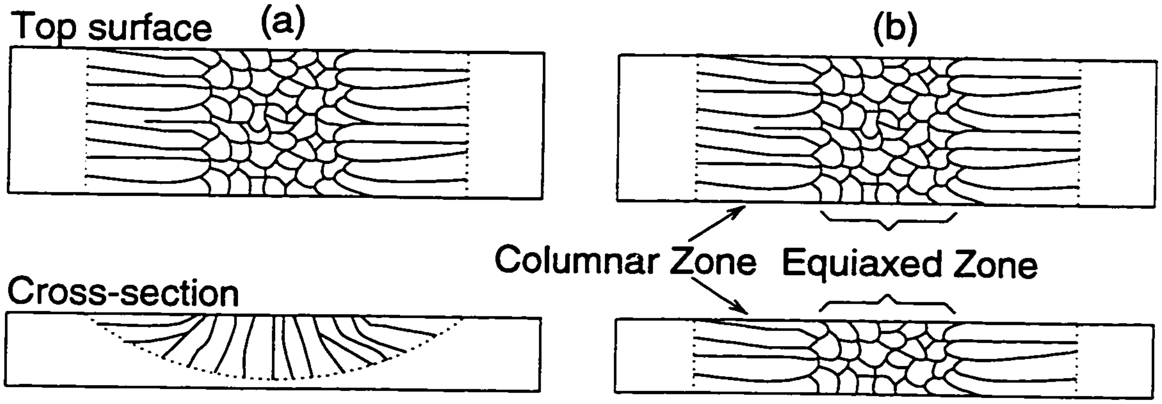

Figure 3.8: Schematic of weld sections exhibiting heat flow conditions of (a) three dimensions and (b) two dimensions.

Preliminary experiments were performed to ascertain, within the limitations of the experimental apparatus, feasible ranges of current and travel speed that give two-dimensional heat flow conditions, *i.e.*, full-penetration welds in the 2 mm thick plates. To ensure that the fusion boundaries were parallel, measurements of weld widths on the top and bottom surfaces were compared and cross-sections were observed for welds performed with four different currents at two travel speeds each. When the top and bottom weld widths were the same, then the fusion boundaries were parallel and heat flow was assumed to be fully two-dimensional. Feasible current and travel speed pairs are given in Table 3.2.

Table 3.2: Currents and travel speeds for full-penetration welds in 2 mm Al-Cu sheets.

Current (A)	Travel speed (mm/s)
100	3 & 4
120	4 & 5
140	6 & 7
160	8 & 9

3.4 Welding Procedure

The sequence of activities used in the present study for AC GTA welding is as follows:

1. A weld specimen was clamped onto the specimen holder.
2. The welding power supply was switched on and AC welding current, AC frequency, and shielding gas pre- and postflow durations were set. Travel speed was set.
3. The electrode-to-workpiece distance (*i.e.*, arc length) was set by adjusting the distance of the welding torch above the workpiece with the rack-and-pinion and inserting a spacer on the rack.
4. The data acquisition program on the computer was initiated.
   (The program waits for current to exceed 20 A then collects data.)
5. The cooling water pump was activated.
6. The power supply was activated for welding and the arc was then initiated by manually lowering the torch with the rack-and-pinion, touching the electrode to the workpiece, and then raising the torch to the preset electrode-to-workpiece distance, as set by the spacer.
7. The lead screw drive motor was activated.
8. Upon completion of the weld bead, the drive motor was switched off and the arc extinguished.

3.5 Data Acquisition

During welding, values of current, voltage, and travel speed were collected by a data acquisition system. Figures 3.9 and 3.10 are schematics of the circuits used for acquisition of welding current and welding voltage, respectively. AC welding current was obtained by means of a LEM^{TM} LT1000 SI Hall-effect current transducer which was factory calibrated to ±0.1 A. AC welding voltage was obtained by means of a LEM^{TM} LV100 voltage sensor with a precision of ±0.01 V. The AC voltage was measured across the terminals of the welding supply. The implications of measuring terminal voltage instead of directly measuring arc voltage will be discussed in the next section.

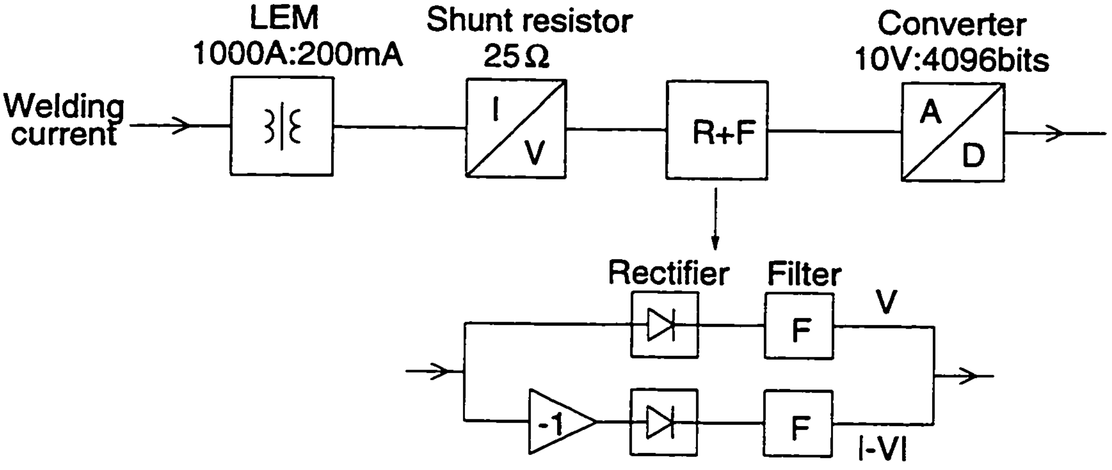

Figure 3.9: Schematic of circuit for acquisition of welding current.

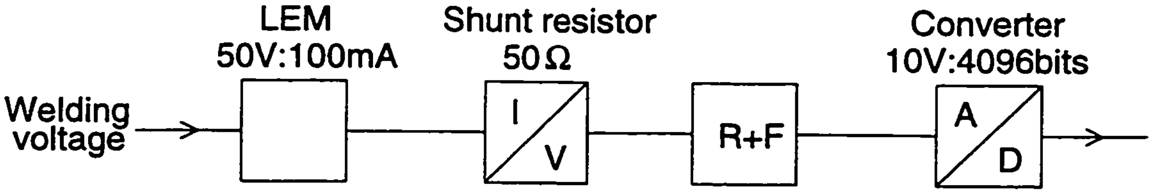

Figure 3.10: Schematic of circuit for acquisition of welding voltage.

As indicated in Figures 3.9 and 3.10, each LEM device produced a current signal which was proportional to the measured quantities. These current signals were subsequently converted to voltage signals by means of a shunt resistor. Although the LEM devices were fully capable of tracking the 60 Hz AC current and voltage signals, the IBM-386 computer used to acquire and store the signals was not. Thus, each AC voltage signal from the shunt resistor was rectified into its positive and negative components and these components were then filtered to give a constant voltage signal. Figure 3.11 is a schematic of the original AC signal, the rectified components, and the filtered output. Once rectified and filtered, the signals were converted to a digital format by an analog-to-digital converter and transferred to a data acquisition card in the IBM-386 computer. A custom data acquisition computer program sampled each of the signals eight values at a time. The sampling rate used in the present study was 1 Hz, but was adjustable. The program subsequently averaged the eight values and converted them using conversion factors associated with the each of the components in the data acquisition circuitry, as indicated in Figures 3.9 and 3.10, and wrote them to file.

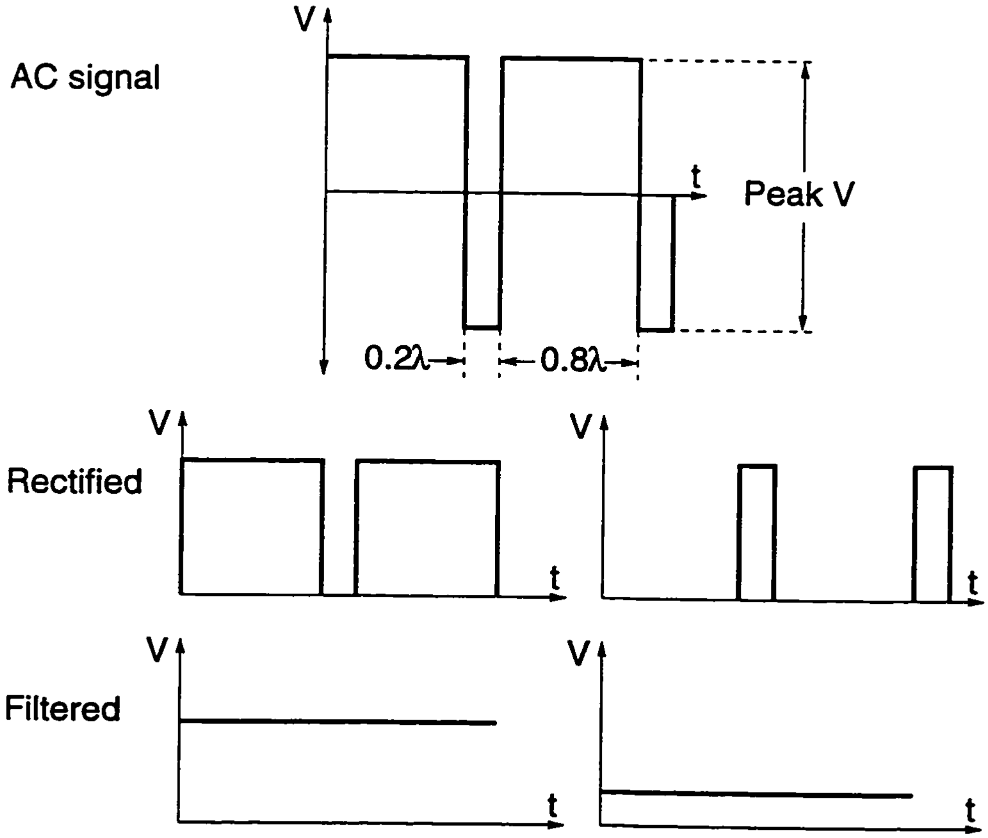

Figure 3.11: Schematic of AC signal, rectified components, and filtered output.

Thus, the recorded values, I_+, I_-, V_+, and V_-, for an 80% duty cycle are as follows:

$$I_+ = \frac{REC(1)}{8} \times \frac{1000\,A}{0.2\;A} \times \frac{1\;A}{25\,V} \times F_{I_+} \times \frac{10\;\;V}{4096\,bit} \tag{3.1}$$

$$I_- = \frac{REC(2)}{8} \times \frac{1000\,A}{0.2\;A} \times \frac{1\;A}{25\,V} \times F_{I_-} \times \frac{10\;\;V}{4096\,bit} \tag{3.2}$$

$$V_+ = \frac{REC(3)}{8} \times \frac{50\;V}{0.1\,A} \times \frac{1\;A}{50\,V} \times F_{V_+} \times \frac{10\;\;V}{4096\,bit} \tag{3.3}$$

$$V_- = \frac{REC(4)}{8} \times \frac{50\;V}{0.1\,A} \times \frac{1\;A}{50\,V} \times F_{V_-} \times \frac{10\;\;V}{4096\,bit} \tag{3.4}$$

Here, $REC(i)$ represents the eight summed signals and F_i are calibration factors, as discussed in the next section.

The recorded values, I_+, I_-, V_+, and V_-, in their final form, corresponded to the positive and negative components, respectively, of the steady-state welding current and voltage multiplied by their duty cycle. Values of peak current, I_{peak}, or voltage, V_{peak}, may be obtained from the recorded values, I_+, I_-, V_+, and V_-, for an 80% duty cycle as follows:

$$I_{peak} = \frac{I_+}{0.8} + \frac{I_-}{0.2} \tag{3.5}$$

$$V_{peak} = \frac{V_+}{0.8} + \frac{V_-}{0.2} \tag{3.6}$$

To illustrate more clearly, Table 3.3 shows an example of acquired and recorded data for an 80% duty cycle.

Values of travel speed were acquired with a precision of ±0.1 mm/s from the tachometer contained in the feedback controller for the drive motor. Values of travel speed were calculated as follows:

$$v_{ws} = \frac{REC(5)}{8} \times \frac{1\;\;mm/s}{82.7\,RPM} \times \frac{1000\,RPM}{3\quad V} \times \frac{10\;\;V}{4096\,bit} \tag{3.7}$$

Table 3.3: Example of acquired and recorded data for 80% duty cycle.

Nominal AC signal		Recorded value			
Current (A)	Voltage (V)	I_+ (A)	I_- (A)	V_+ (V)	V_- (V)
100	13	40	10	5.2	1.3
120	13	48	12	5.2	1.3
140	13	56	14	5.2	1.3
160	13	64	16	5.2	1.3

3.5.1 Verification and Calibration

Verification and calibration of the instrumentation and data acquisition system was performed to ensure the proper measurement of current, voltage, and travel speed signals.

To ensure that the acquired and recorded values of travel speed corresponded to the actual travel speed, values acquired by the computer were compared with readouts from a tachometer mounted on the lead screw. Comparisons between recorded values and those measured independently were made for the range of travel speeds used in the experiments and found to be consistently the same, thus no calibration factor was required for welding speed.

To evaluate whether the acquired and recorded values of current corresponded to the actual welding current, the welding supply was operated with a series of AC currents at the magnitudes, duty cycle, and frequency used in the experiments. The sequence was performed with (i) a calibrated resistance current shunt in the welding circuit in place of the torch and (ii) a live arc. The current shunt was used in addition to the live arc, since the live arc produced a very noisy signal. Comparisons were made between values of current from:

1. the welding supply, which provided a readout of peak current,
2. a NICOLET$^{\text{TM}}$ model 410 oscilloscope, which provided the entire AC current signal from the LEM transducer, and

3. the computer data acquisition program.

Peak values of current derived from the oscilloscope trace of the LEM signal were found to be consistently the same as those given by the welding supply readout. However, it was found that a discrepancy existed between the LEM signal and the negative current component recorded by the computer due to a small augmentation of the signal caused by inaccuracies in the electrical components of the rectifier+filter circuit. A calibration factor, $F_{I_-} = 0.91$ was therefore introduced in the data acquisition code to attenuate the signal back to the correct value. No discrepancy existed for the positive current component, thus $F_{I_+} = 1.00$.

Since the voltage measured across the current shunt was very small, voltage calibration was performed with a live arc only. Similar to the evaluation of the current, the recorded voltages were compared to the welding supply readout and the oscilloscope trace of the LEM signal. Discrepancies were found between the LEM signals and the recorded data for both positive and negative voltage components, again due to the rectifier+filter circuits. Thus calibration factors, $F_{V_+} = 0.85$ and $F_{V_-} = 0.88$, were introduced into the data acquisition code to accommodate the errors.

The AC voltage was measured across the terminals of the welding supply since it is experimentally very difficult to directly measure the arc voltage. Components of the welding apparatus, such as cabling, specimen, and specimen holder, may contribute resistive drops to the circuit and thus the measured terminal voltage would appear higher that the actual arc voltage. To ascertain whether large resistive drops existed across these components, a voltmeter was used to measure the voltage across each component during welding with a live arc using currents in the experimental range. The resistive drops were found to be negligibly small for all components. Thus, the terminal voltage could be expected to be a good indication of the actual arc voltage.

3.6 Metallographic Procedures

Values of weld bead width and % equiaxed in the weld bead were measured by mounting each of the specimens on an xy displacement table and observing them with an OLYMPUS^{TM} stereo microscope. A FUTABA PULSCALE^{TM} sensor with a precision of ±0.005 mm was used to measure the xy displacements. Some of the specimens were etched with Keller's reagent prior to measuring to improve clarity of interpretation. The preparation procedure for Keller's reagent is given in Table 3.4.

Higher magnification optical microscopy was used on some specimens to ensure parallel fusion boundaries, count grain size, and interpret microstructures. Sections were embedded in bakelite by means of a PRONTOPRESS-2^{TM} mounting press. The mounted specimens were polished using SiC metallurgical paper with subsequently finer grits: 320, 500, and 1200; using water as a lubricant. Final polishing was performed with STRUERS^{TM} 6 μm and 1 μm diamond abrasive on MICROCLOTH^{TM} polishing cloths using methanol as a lubricant. Specimens were given a final rinse with methanol and dried with a hot air gun. The specimens were etched using Keller's reagent and then observed under an OLYMPUS^{TM} optical microscope. Grain sizes were estimated using JAVA^{TM} image analysis program according to the procedure described in the ASTM standard E112-88 [119].

Table 3.4: Preparation of Keller's reagent [118].

Quantity (ml)	Chemical
10	HF
15	HCl
25	HNO_3
50	H_2O

Use as prepared for macroetch.

Dilute 9 to 1 with H_2O for microetch.

3.7 Thermocouple Procedures

A series of experiments were performed in which thermocouples were embedded in the specimens prior to welding. These experiments were used to provide comparisons of peak temperatures and temperature-time profiles between the experimental work and the thermofluids model. To locate the thermocouples, slots were milled on the bottom of a series of experimental specimens from the side edge to the centreline of the plate, as shown in Figure 3.12. The slots were concentrated towards the end of the plate that is exposed to the arc last. This was to ensure that steady-state conditions were achieved when the weld pool reached the thermocouples. The plates used for this work were slightly thicker than those used for the rest of the experiments (2.2 mm *vs.* 2.0 mm) to facilitate the installation of the thermocouples.

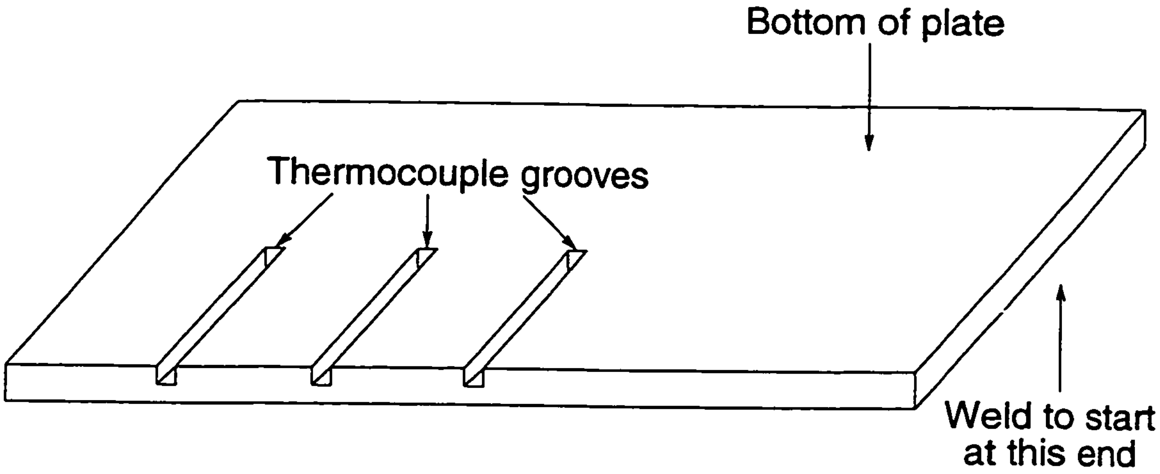

Figure 3.12: Schematic of thermocouple specimen.

K-type thermocouples were selected for the study. These were composed of a pair of 0.127 mm (0.005 in) diameter alumel and chromel wires enclosed in a 0.813 mm (0.032 in) diameter sheath of either 304 stainless steel or Inconel 600. This type of thermocouple gives a linear response in the temperature range 300 to 1480 K and has a time constant of less than 0.2 s.

Once the thermocouples were beaded, they were coated with a commercial die coat to protect them from dissolution in the molten aluminum. To install the coating, the thermocouples were heated to 600 K, dipped in STAHL BROWN^{TM} base coat, allowed to dry, and then dipped in DYCOTE 882^{TM} insulating coat. Comparisons were made between coated and uncoated thermocouples to ensure that response time was not impaired by the coating. Since the coating was very thin, response times were found to be comparable; however, the uncoated thermocouples rarely survived in the molten aluminum for the entire duration of the test. Once the thermocouples were fabricated and coated, they were peened into the prepared grooves. Figure 3.13 is a photograph of a prepared thermocouple specimen.

Thermocouple data was acquired using an ACRO 900^{TM} data acquisition and control with an ACRO 931^{TM} thermocouple module capable of cold-junction compensation. The acquired signals were transferred to an IBM-386 computer for storage and post-processing.

Figure 3.13: Photograph of prepared thermocouple specimen.

Chapter 4

RESULTS AND DISCUSSION

4.1 Mesh Independence Study

In order to ensure that the mesh (grid) used for the GTA welding thermofluids simulations was sufficiently fine, a mesh independence study was performed. For this study, as well as for the remainder of the GTA welding simulations, the problem and boundary conditions are those described in Section 2.1. The material simulated was Al-4.5%Cu, for which the properties are given in Tables 2.1 and 2.2. The vorticity-based turbulence model was invoked to model the effects of turbulence in the weld pool fluid flow.

It is traditionally accepted that a mesh independence study adhere to the following set of five rules [120]:

1. All material should be represented in all meshes.
2. The form of interpolation should not change from grid to grid.
3. Completeness of interpolation function should be maintained.
4. Geometric isotropy should be maintained.
5. Each grid should be contained in all subsequent finer grids.

An attempt was made during the mesh independence study to adhere to these rules, where possible; however, strict adherence to guideline 5 was not always possible given the unique and irregular geometry created by the dynamic grid remapping routine used in the present model of GTA welding. The mesh independence study was performed using four different mesh sizes: 352, 766, 3032, and 4752 elements. These meshes all had two elements in the z-direction. The welding process parameters used in the study are listed in Table 4.1.

Table 4.1: Welding process parameters used in the mesh independence study. (Values for σ_j and σ_h are based on reference [77].)

h (mm)	η	Peak I (A)	Peak V (V)	σ_j (mm)	σ_h (mm)	v_{ws} (mm/s)
2.0	0.50	100	13	1.40	1.60	4

In most mesh independence studies, a characteristic feature of the problem (*e.g.*, flow pattern, peak temperature or velocity) is used to evaluate and compare the performance of different sized meshes. The behaviour of the characteristic feature is tracked as the mesh is progressively refined. Once mesh independence is reached, the characteristic feature ceases to change regardless of how much more refined the mesh becomes. In the present study, there is no one characteristic feature of the problem; thus, mesh independence was evaluated by comparing several parameters, namely predicted weld pool key dimensions (as indicated in Figure 4.1), peak temperatures, thermal gradient at the weld pool tail, peak flow velocities, maximum turbulent Reynolds numbers, and average turbulent Reynolds numbers. The simulations were performed on a Digital Equipment AlphaServer 2100 5/250 which uses four CPUs.

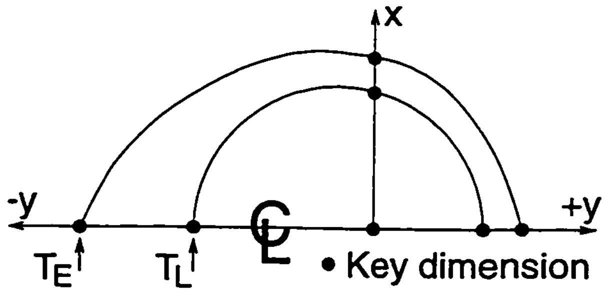

Figure 4.1: Schematic of weld pool indicating key dimensions.

The results of the mesh independence study are reported in Table 4.2. The table indicates that, based on key weld pool dimensions and peak temperatures and velocities, mesh independence is reached with the 766 element mesh. However, with 766 elements, mesh independence is still not reached with respect to maximum turbulent Reynolds number and thermal gradient, G_L, at the weld pool tail. A plot of G_L and CPU time versus number of elements is given in Figure 4.2. As seen in the figure, G_L is gradually approaching convergence at 3032 elements; however, the CPU time is getting quite large. Based on these observations and recognizing that G_L at the weld pool tail is a significant quantity in the present study, a mesh of 3032 elements was selected and used for all subsequent simulations in the numerical work. The final mesh obtained from this simulation of 3032 elements was shown in Figure 2.7 in Chapter 2. Other results, such as pool geometries, temperature isotherms, flow patterns, *etc.*, from this simulation and others will be presented and discussed in a later section.

Table 4.2: Results of the mesh independence study.

Number of elements	352	766	3032	4752
Number of nodes	2141	4506	17241	28674
T_L: x at $y = 0$ (mm)	3.70	3.74	3.73	3.76
$+y$ at $x = 0$ (mm)	2.89	2.93	2.91	2.94
$-y$ at $x = 0$ (mm)	-6.50	-6.63	-6.59	-6.70
T_E: x at $y = 0$ (mm)	4.64	4.69	4.68	4.72
$+y$ at $x = 0$ (mm)	3.53	3.56	3.56	3.59
$-y$ at $x = 0$ (mm)	-8.91	-9.02	-8.93	-9.05
Peak T (K)	835	837	836	837
G_L at pool tail (K/mm)	26.4	21.5	18.8	17.9
Peak $\vec{v}$ (mm/s)	34	35	35	36
Maximum Re_t	229	226	213	213
Average Re_t	109	111	111	111
CPU Time (min)	4	15	97	200

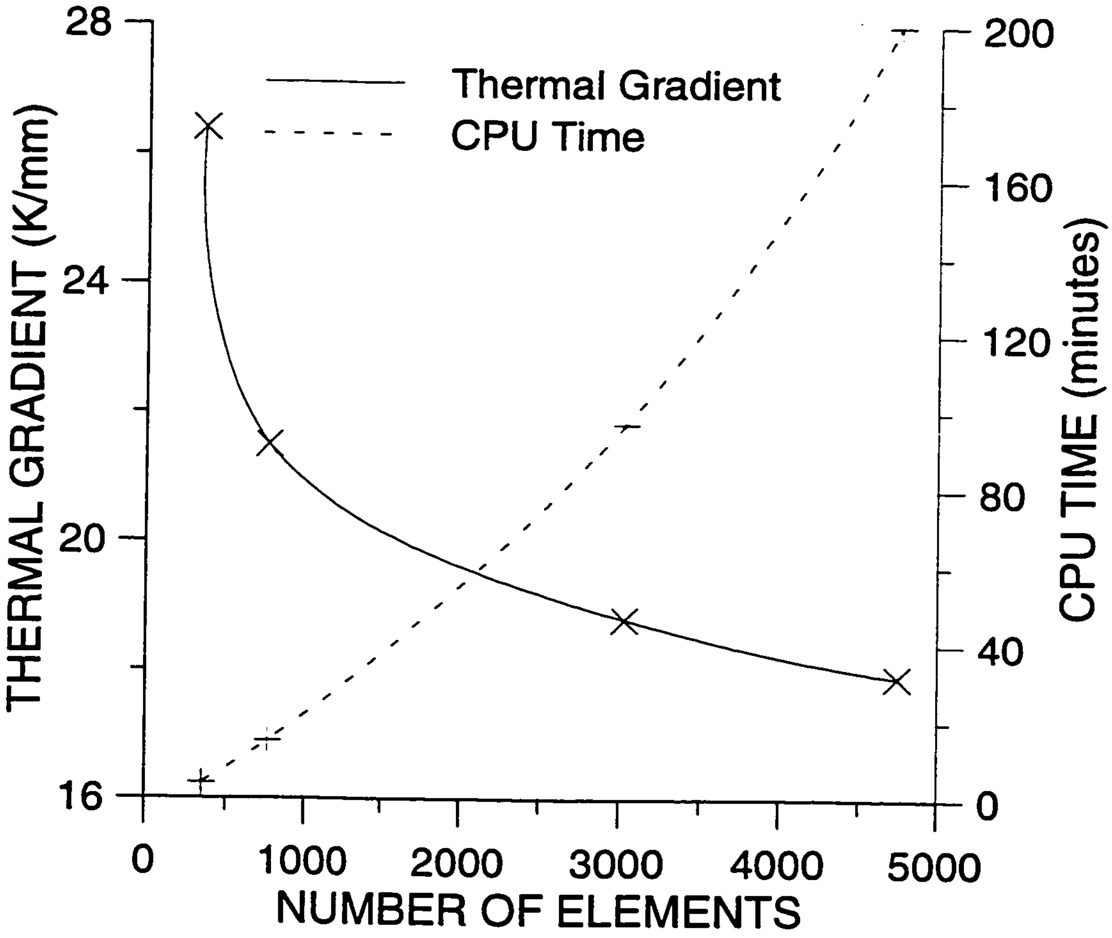

Figure 4.2: Plot of thermal gradient and CPU time versus number of elements.

4.2 Model Validation

To validate the thermofluids model and ascertain its applicability to actual welding results, the model was used to simulate a series of moving GTA welds in 2.2 mm thick plates of Al-5.5%Cu with the welding parameters listed in Table 4.3. These welding process parameters were selected to match a corresponding series of autogenous GTA welds performed on plates with thermocouples installed according to the procedure described in the preceding chapter. These plates were slightly thicker than those used in the CET experiments to facilitate the embedding of the thermocouples.

Table 4.3: Welding process parameters for the thermocouple investigation. (Values for σ_j and σ_h are based on reference [77].)

η	Peak I (A)	Peak V (V)	v_{ws} (mm/s)	σ_j (mm)	σ_h (mm)
0.50	100	13	2	1.40	1.60
0.46	120	13	3	1.57	1.78
0.45	140	13	4.5	1.72	1.94

Values of process efficiency, η, reported in Table 4.3 were adjusted to provide good comparison with experimental values of weld width and peak temperature, as tabulated later. These process efficiencies incorporate both (i) the arc efficiency which accounts for the heat lost to the environment during welding and (ii) the alternating-current duty cycle (80% in this study) which accounts for the fact that in AC welding more heat is input to the workpiece during the positive (straight polarity) component of the current cycle compared to the negative (reverse polarity) component. The arc efficiency is expected to decrease with increasing current since a hotter arc will lose more heat to the environment. These values of η compare well to those cited by Kou [14] for alternating-current GTA welding. Further, the constant C in the vorticity-based turbulence model was adjusted to improve the correlation between numerical predictions and experimental measurements of peak temperature. Good correlation was obtained with $C = 0.5$.

Two experiments were performed for each of the process conditions listed in Table 4.3. The recorded thermocouple data from these six experiments are very similar. An example of thermocouple data is shown in Figure 4.3 for an experiment with a current of 120 A and a welding speed of 3 mm/s. The recorded data from each of the three thermocouples are similar: they show a steep increase in temperature as the arc nears the thermocouple location, the achievement of a peak temperature (1115, 1129, and 1089 K, respectively) as the arc passes, and a gradual cooling as the arc continues and is finally extinguished. These thermocouple data are very similar in character to those recorded by Kou and Le [38] for GTA welds in thin plates of commercial 6061 aluminum. However, their plate thickness, welding conditions, and alloy content were different from the present study, and so no direct quantitative comparison was possible.

Figure 4.4 demonstrates good agreement between the experimental thermocouple data and the numerically predicted centreline temperature distribution for welding conditions 120 A at 3 mm/s. The predicted temperature distribution was obtained from a location 1.613 mm (0.040 in) from the bottom of the plate since this most closely corresponds to the thermocouple location. There is a discrepancy between the predicted and the measured heating-up rate. This is due to the Dirichlet (constant temperature) boundary condition imposed at the front of the plate (inlet) in order to make the problem tractable. This constant inlet temperature falsely forces the temperature down at the front of the plate and so forward diffusion of the heat is forced more sharply downwards than is evident in the experimental thermocouple trace. However, since this behaviour is limited to the solid at the front of the plate, it will have little effect on the thermal behaviour of the liquid weld pool which is of primary interest in the present study. Another small discrepancy exists at the tail of the weld pool near the equilibrium liquidus isotherm. This difference between the predicted and experimental temperature profile indicates that, although the weld pool width was predicted accurately (*cf.* Table 4.4), the predicted weld pool length is slightly greater than the actual weld pool length. It should be noted, however, that the predicted and experimental cooling rates are very similar.

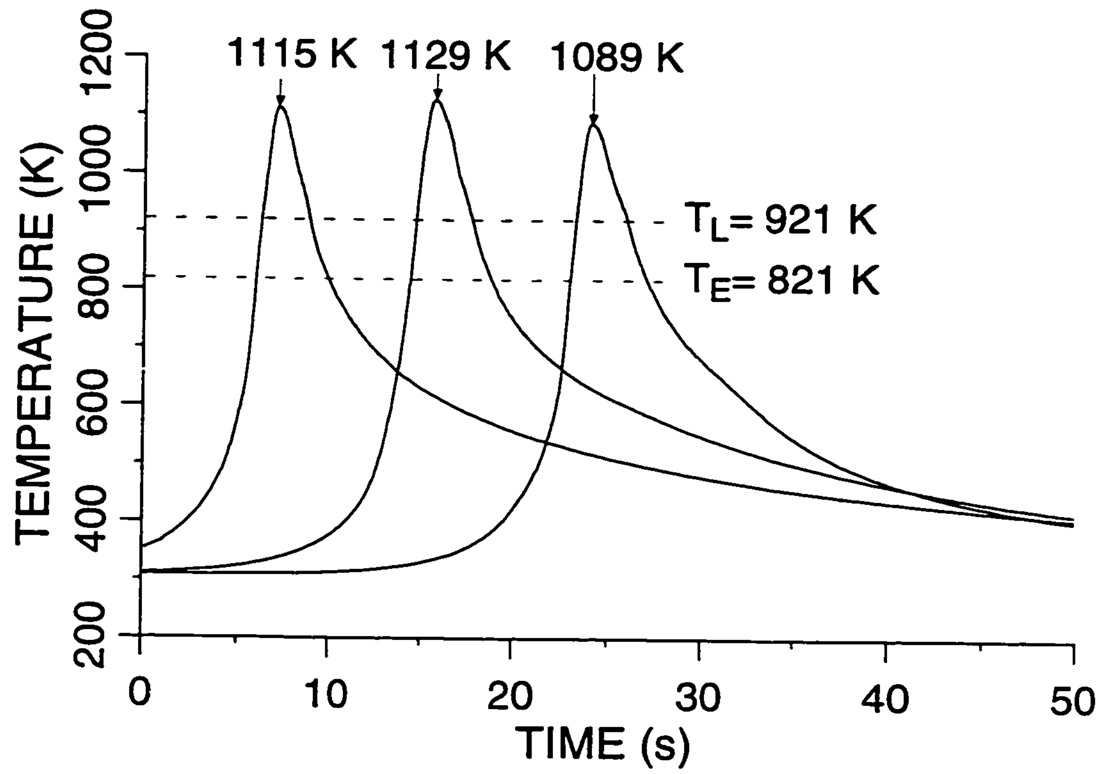

Figure 4.3: Acquired thermocouple data. Welding conditions: 140 A at 4.5 mm/s.

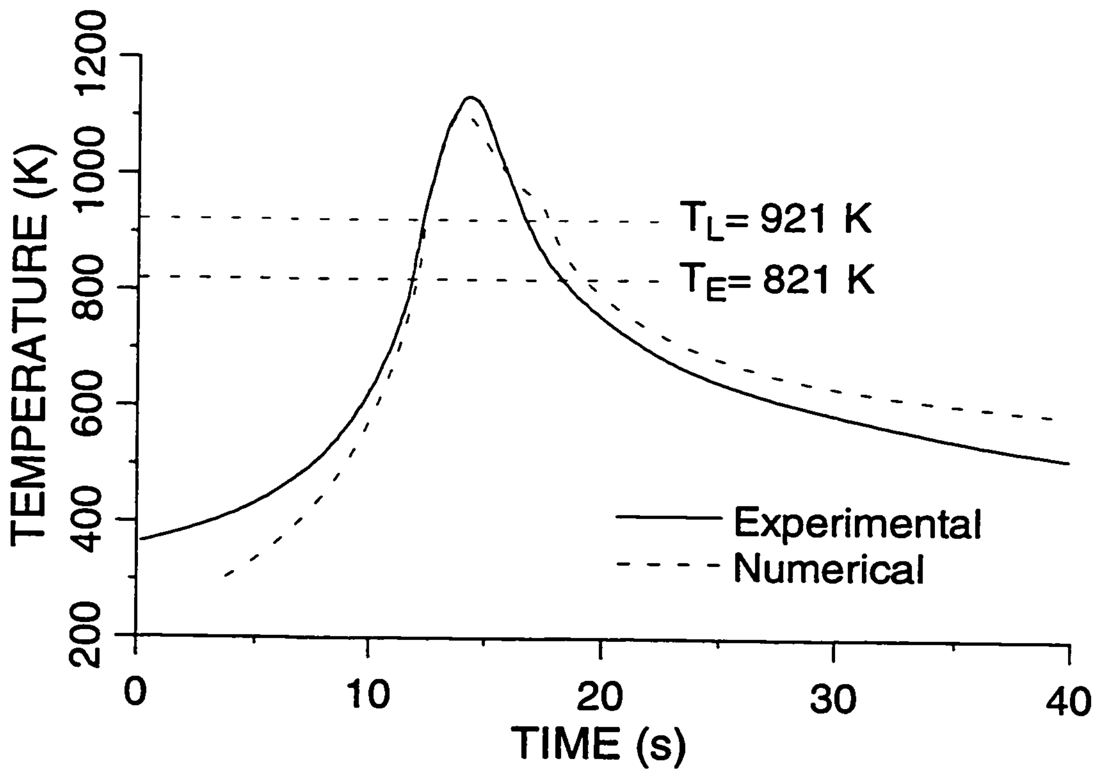

Figure 4.4: Experimentally acquired and numerically predicted centreline temperature distributions. Welding conditions: 120 A at 3 mm/s.

Experimentally measured and numerically predicted values of weld width and peak pool temperatures are compared in Tables 4.4 and 4.5, respectively. As seen in Table 4.4, the agreement between predicted and experimentally measured weld widths is very good with differences less than 10%. Table 4.5 again shows excellent agreement between predicted and experimental peak temperatures which are within approximately 6%.

Table 4.4: Experimental and predicted weld widths.
(2.2 mm thick Al-5.5%Cu plates.)

Welding Conditions		Weld Widths (mm)		
Peak I (A)	v_{ws} (mm/s)	Experimental	Predicted	% Difference
100	2	9.54	10.42	9.2
120	3	11.04	11.83	7.1
140	4.5	10.06	10.63	5.7

Table 4.5: Experimental and predicted peak temperatures.
(2.2 mm thick Al-5.5%Cu plates.)

Welding Conditions		Peak Temperature (K)		
Peak I (A)	v_{ws} (mm/s)	Experimental	Predicted	% Difference
100	2	1118	1084	-3.0
120	3	1162	1091	-6.1
140	4.5	1105	1073	-2.9

The ability of the thermofluids model to accurately predict both temperature distributions and weld widths for a range of welding conditions affirms that the model may be used with confidence to predict the thermal conditions in moving GTA weld pools.

4.3 Numerical Modelling Results

The finite element model was used to simulate a series of moving GTA welds in 2 mm thick plates of Al-4.5%Cu with the welding parameters listed in Table 4.6. This set of process parameters was selected to simulate and expand upon the welding process conditions used in the experimental investigation. The primary objectives of the numerical modelling work were (i) to observe the effect of welding process parameters on the macroscopic heat and fluid flow behaviour of the weld pool and (ii) to characterize the influence of welding process parameters on the solidification conditions in the weld pool which are pertinent to CET promotion, namely, thermal gradient in the liquid, G_L, and the growth rate of the solid/liquid interface, R.

Table 4.6: Welding process parameters used in the numerical modelling study.

η	Peak I (A)	Peak V (V)	v_{ws} (mm/s)	σ_j (mm)	σ_h (mm)
0.50	100	13	3 to 6	1.40	1.60
0.46	120	13	4 to 7	1.57	1.78
0.45	140	13	6 to 9	1.72	1.94
0.45	160	13	7 to 10	1.84	2.08

In the remainder of this section, the results of the numerical modelling effort will be presented and the predicted effects of process conditions on the weld pool geometry, temperature field, fluid flow field, and the solidification conditions pertinent to CET promotion, G_L and R, will be discussed.

4.3.1 Predicted Weld Pool Geometry

Predicted weld pool widths are given in Table 4.7 for all of the welding conditions simulated. These values were measured from the weld pool centreline to the equilibrium liquidus isotherm and then multiplied by two to give the predicted 'total' weld width. As expected, the table indicates that increasing welding speed for a given current or decreasing the current for a given welding speed (*i.e.*, decreasing heat input per unit distance), decreases the total weld width. Alternatively, to maintain a constant weld width (*e.g.*, welding conditions 100 A at 5 mm/s, 120 A at 6 mm/s, 140 A at 8 mm/s, and 160 A at 10 mm/s), the heat input per unit distance must be decreased with increasing current-welding speed combinations.

Table 4.7: Predicted total weld widths for 2 mm thick Al-Cu plate.

Welding Conditions I (A)	 v_{ws} (mm/s)	Heat Input/Unit Distance $\eta VI/v_{ws}$ (J/mm)	Weld Widths (mm)
100	3	216.7	10.81
	4	162.5	7.99
	5	130.0	6.75
	6	108.3	5.92
120	4	179.4	10.98
	5	143.5	8.14
	6	119.6	6.99
	7	102.5	6.20
140	6	136.5	9.09
	7	117.0	7.78
	8	102.4	6.90
	9	91.0	6.30
160	7	133.7	10.01
	8	117.0	8.54
	9	104.0	7.70
	10	93.6	6.95

Figure 4.5 shows predicted liquidus isotherm profiles for four simulations (welding conditions 100 A at 5 mm/s, 120 A at 6 mm/s, 140 A at 8 mm/s, and 160 A at 10 mm/s). These four simulations were selected for comparison since the welding conditions produce approximately the same weld pool width (Table 4.7). Although the weld pool widths are

similar, the figure indicates that the different welding conditions have a significant impact on the actual configuration of the pool: higher current-welding speed pairs produce pools that are increasingly elongated, approaching a teardrop shape at the highest values of welding speed. The elongation of the pool at high welding speeds to approach a teardrop shape is a well-known phenomenon [14]. The implications of pool geometry on CET promotion will be discussed in a subsequent section.

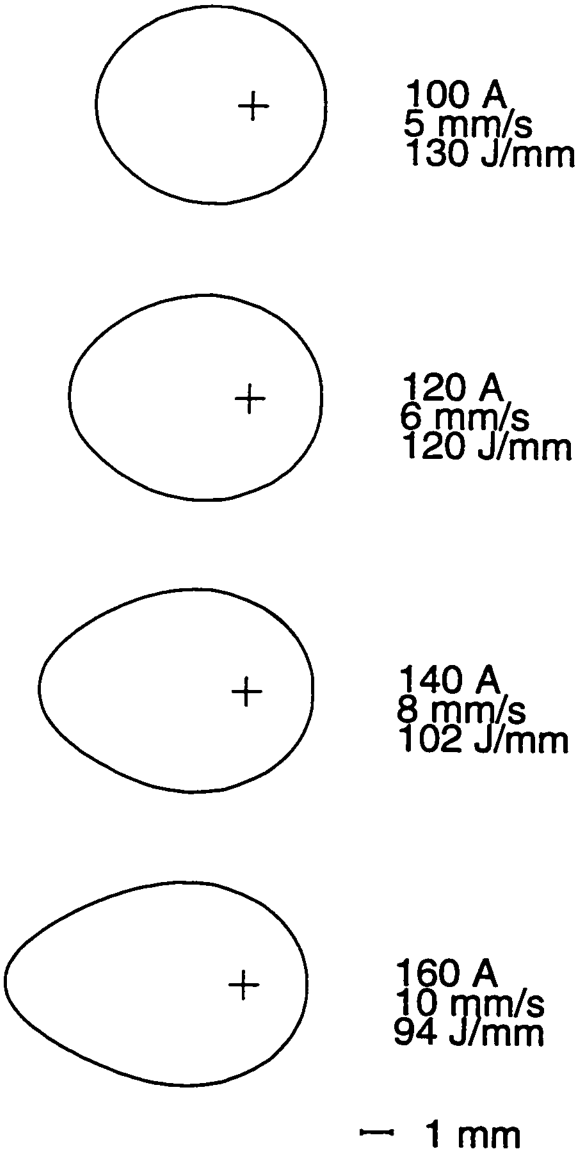

Figure 4.5: Predicted weld pool profiles.

4.3.2 Predicted Temperature Fields

Figure 4.6 is a contour plot of a predicted temperature field in the welded plate. These results are for welding conditions 100 A at 4 mm/s, but are generally typical of temperature contours for all the simulations. A peak temperature of 1109 K was predicted for this simulation. Since the heat flow conditions were two-dimensional, a similar thermal field exists through the thickness of the plate, except directly under the arc where, because of direct contact with the arc plasma, the temperature was about 96 K higher on the top surface than the bottom surface. The peak temperature does not occur directly under the centreline of the arc, but rather at a short distance behind the arc origin due to the combined effects of the fluid flow in the weld pool (convection) and the forward motion of the plate (advection). Also, the isotherms are compressed at the front of the plate, particularly in the vicinity of the hot weld pool, and elongated at the rear sides and end of the plate.

Figure 4.7 is a more detailed plot for the same simulation showing the temperature contours in the vicinity of the weld pool and mushy zone only. For comparison, a detailed temperature contour plot for the simulation with welding conditions 160 A at 9 mm/s is given in Figure 4.8. This simulation was selected for comparison since it predicted a similar weld width to the 100 A at 4 mm/s simulation, but had much higher welding current and welding speed. As expected, not only are the temperature contours much more elongated in the tail of the weld pool for the 160 A simulation, but the isotherms are also more compressed at the front of the pool due to the higher welding speed. These thermal fields are similar in character to those predicted by Kou and Wang [58] for 6061 aluminum; however, their plate thickness and welding conditions were different from the present study, and so no direct quantitative comparison was possible.

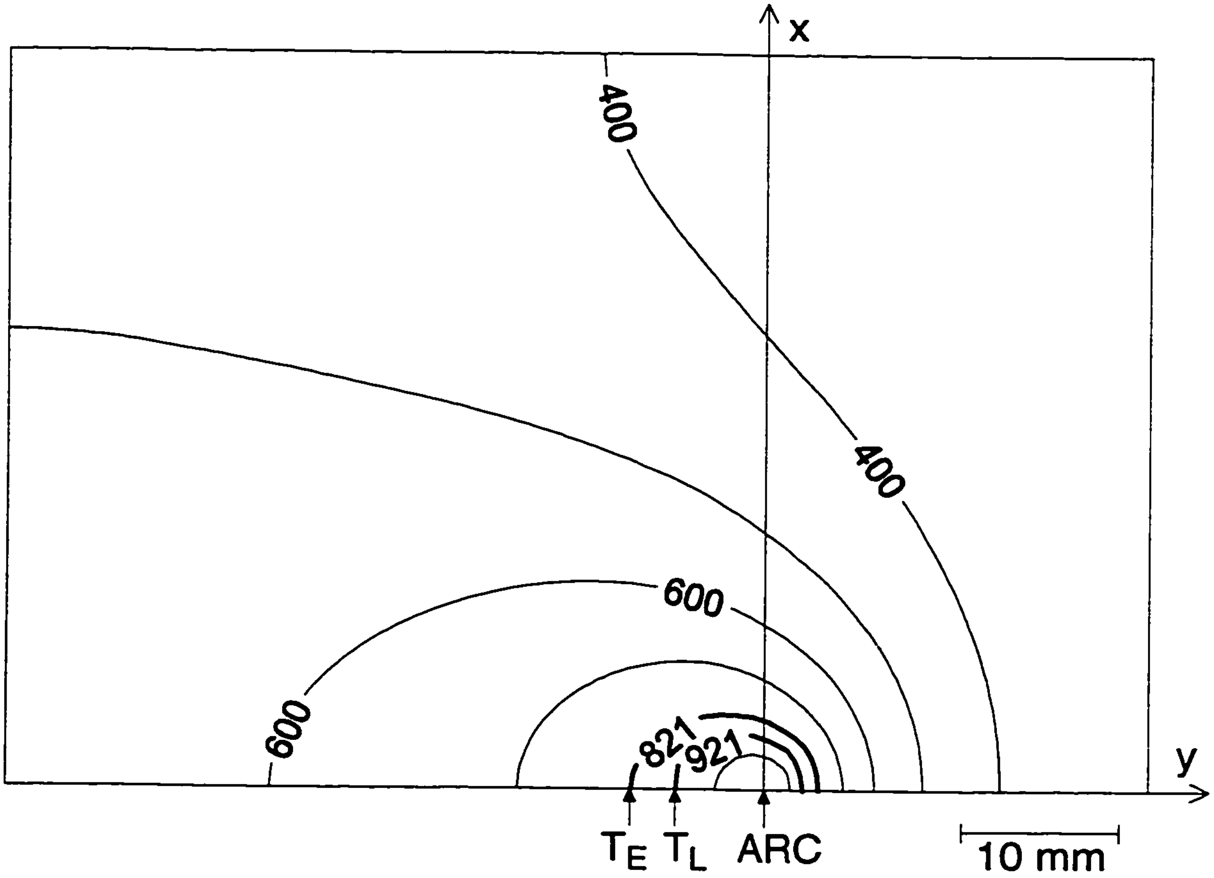

Figure 4.6: Predicted top surface temperature field. Welding conditions: 100 A at 4 mm/s; temperatures in K; peak T = 1109 K.

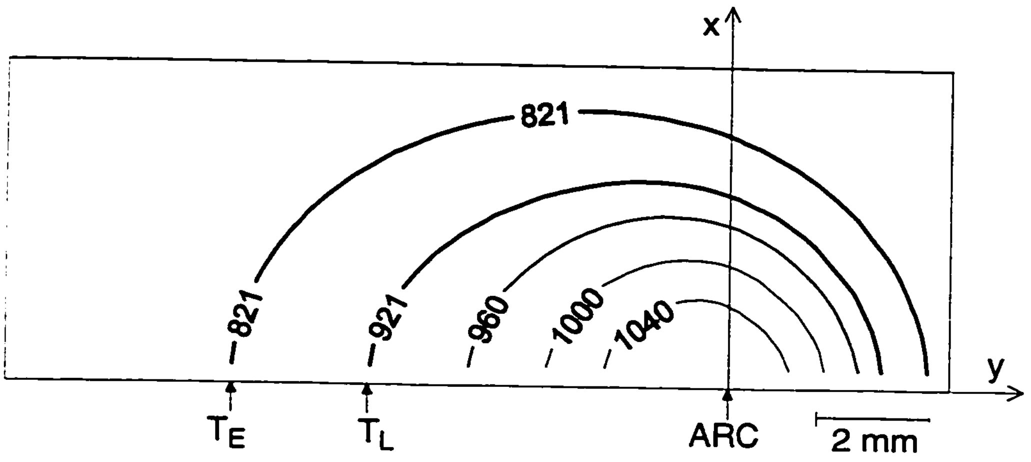

Figure 4.7: Predicted top surface temperature field in the weld pool and mushy zone. Welding conditions: 100 A at 4 mm/s; temperatures in K; peak $T = 1109$ K.

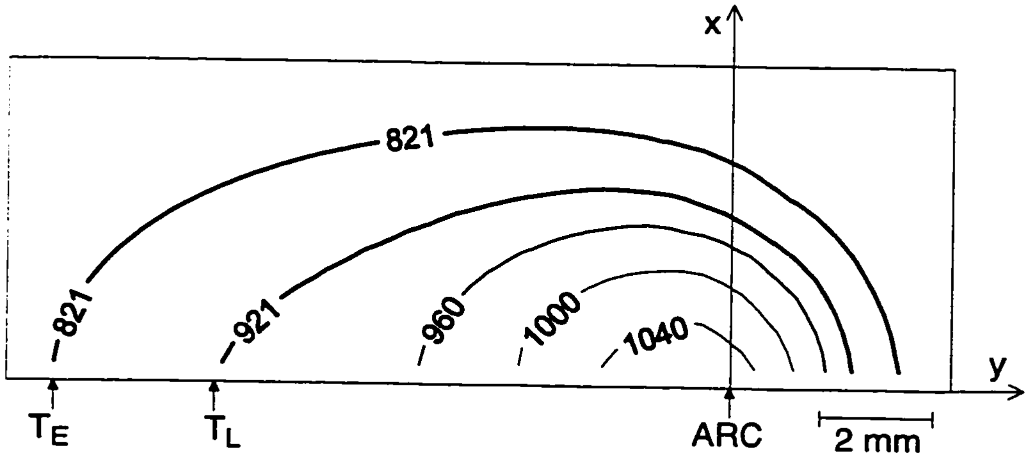

Figure 4.8: Predicted top surface temperature field in the weld pool and mushy zone. Welding conditions: 160 A at 9 mm/s; temperatures in K; peak $T = 1068$ K.

4.3.3 Predicted Weld Pool Flow Fields

Figure 4.9 shows typical predicted flow fields on the top surface, plane of symmetry, and bottom surface of the weld pool. These results are for welding conditions 100 A at 4 mm/s and are typical of the flow patterns for all simulations. To obtain more detail, the simulation was performed with a substructured weld pool mesh containing 3840 elements with 8 z-direction elements. On the top and bottom surfaces of the weld pool, there was a strong Marangoni-driven flow towards the outer edges of the pool. This was because Al-Cu alloys have a negative surface tension temperature gradient: $\partial\gamma/\partial T$ = -0.00035 N/m·K. The source point for the Marangoni flow on the top and bottom surfaces was not centred directly under the arc, but was displaced slightly behind the arc to a location corresponding to the peak temperature in the weld pool. In the vicinity of the arc, there was strong, downwards Lorentz-driven flow. A buoyancy force was also active in driving fluid flow; however, it was weak relative to the Marangoni and Lorentz forces. These combined fluid flow driving forces produced a complicated recirculation pattern, as seen in the plane of symmetry. At the front of the weld pool, the downward Lorentz-driven flow and the outwards Marangoni-driven flows on both the top and bottom surfaces combined to produce a flow pattern containing two small recirculation loops and resembling a backwards 'S'. In the rear of the pool, the top and bottom surface Marangoni flows combined to produce two recirculation loops in the upper and lower regions of the pool with flow towards the tail of the weld on the surfaces and flow back towards the centre of the weld midway through the plate thickness. Closer to the arc where the Lorentz forces had more influence, there is a third recirculation eddy having a centrepoint midway through the plate thickness, slightly behind the arc. The peak velocity for this simulation was 21 mm/s and occurred near the bottom surface ahead of the arc due to the combined effects of Marangoni and Lorentz driven flow in this region. Kou and Wang [58] and Zacharia *et al.* [71, 121] have noted similar fluid flow patterns in their numerical simulations of moving GTA welds in aluminum alloys and concur that Marangoni flow is dominant; however, their studies were for partial-penetration welds in commercial alloys, and so no direct quantitative comparison is possible.

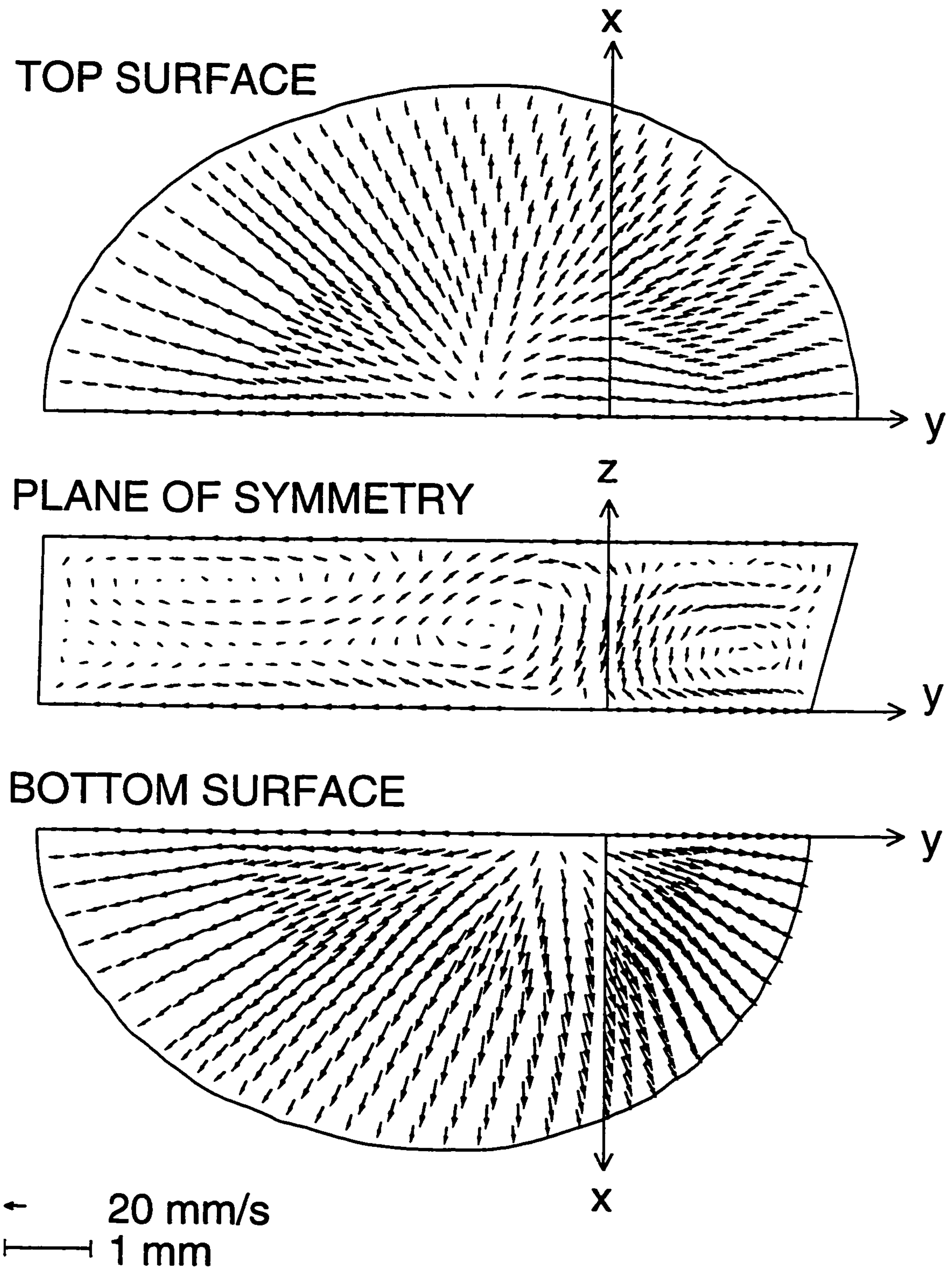

Figure 4.9: Predicted flow fields on top surface, plane of symmetry, and bottom surface of the weld pool. Welding conditions: 100 A at 4 mm/s; peak $\vec{v} = 21$ mm/s.

One method to estimate the level of turbulence in fluid flow is to examine the values of dimensionless viscosity, μ_t/μ, also known as the turbulent Reynolds number, Re_t. Figure 4.10 is an isopleth plot of turbulent Reynolds numbers for the simulation with welding conditions 100 A at 4 mm/s. This plot is typical of all the simulation results. Figure 4.10 indicates that there are high levels of turbulence (*i.e.*, $Re_t > 100$) throughout the weld pool and particularly at the front of the pool where the velocities are large.

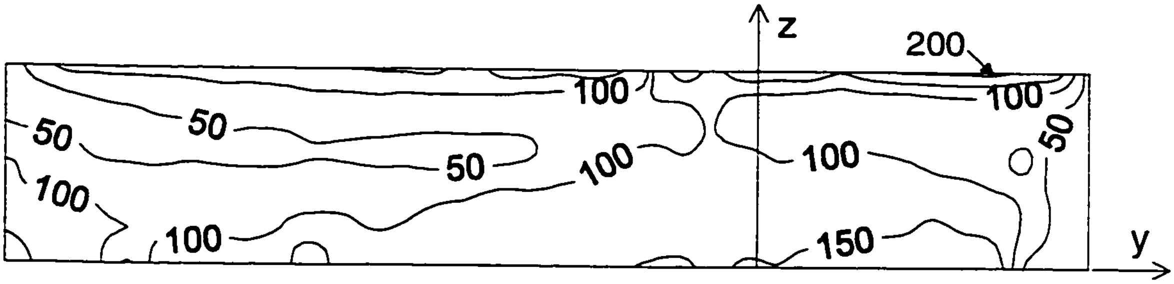

Figure 4.10: Predicted isopleth plot of dimensionless viscosity on the plane of symmetry. Welding conditions 100 A at 4 mm/s; maximum $Re_t = 213$; average $Re_t = 111$.

Maximum and average values of Re_t were determined for all the simulations and are reported in Table 4.8. From Table 4.8, it is seen that the average values of Re_t are generally around 100 and maximum values around 200. It is traditionally accepted that fully turbulent flow exists when Re_t exceeds 100, which suggests that the predicted flow fields for all the welding conditions simulated were fully turbulent. One effect of fully developed turbulence is enhancement of the rate of thermal energy diffusion throughout the liquid, thus lowering the peak and overall temperatures in the liquid weld pool.

Choo and Szekely [85] and Hong *et al.* [86, 87] have found that incorporating turbulence in their model led to better comparison between predicted weld dimensions and experimental results. In particular, Hong *et al.* [86] predicted that fluid flow in high-conductivity (lower Prandtl number) metals, such as aluminum alloys, is very turbulent compared to lower-conductivity metals, such as stainless steel. However, the turbulence was predicted to have less of an influence on weld pool dimensions and temperatures in the high-conductivity/low-Prandtl-number material since energy transport within the weld pool of such a material is conduction-dominated and not strongly influenced by mass convection/fluid flow.

Table 4.8: Predicted turbulent Reynolds numbers.

Welding Conditions		Turbulent Reynolds Number	
I (A)	v_{ws} (mm/s)	Maximum	Average
100	3	249	122
	4	213	111
	5	195	103
	6	174	94
120	4	257	120
	5	210	113
	6	187	106
	7	176	98
140	6	225	116
	7	212	111
	8	216	106
	9	230	100
160	7	252	120
	8	242	117
	9	251	112
	10	258	108

To isolate and examine the effects of weld pool fluid flow on predicted thermal behaviour, a simulation (again with welding conditions 100 A at 4 mm/s) was performed in which the driving forces for the fluid flow, namely buoyancy, Marangoni, and Lorentz forces, were turned off. Figure 4.11 is a plot of the centreline temperature distribution along the top surface of the weld pool for the simulations with and without fluid flow. The figure illustrates how much the fluid flow lowers the peak temperatures of the weld pool (1521 K for the conduction only predictions versus 1109 K for the thermofluids prediction). In addition, the fluid flow lowers the local thermal gradient at the solid/liquid interface at the tail of the pool. Clearly, the agreement between the predicted and experimental peak temperatures presented in Table 4.5 and temperature profiles in Figure 4.4 would not have been possible without the incorporation of turbulent fluid flow in the model.

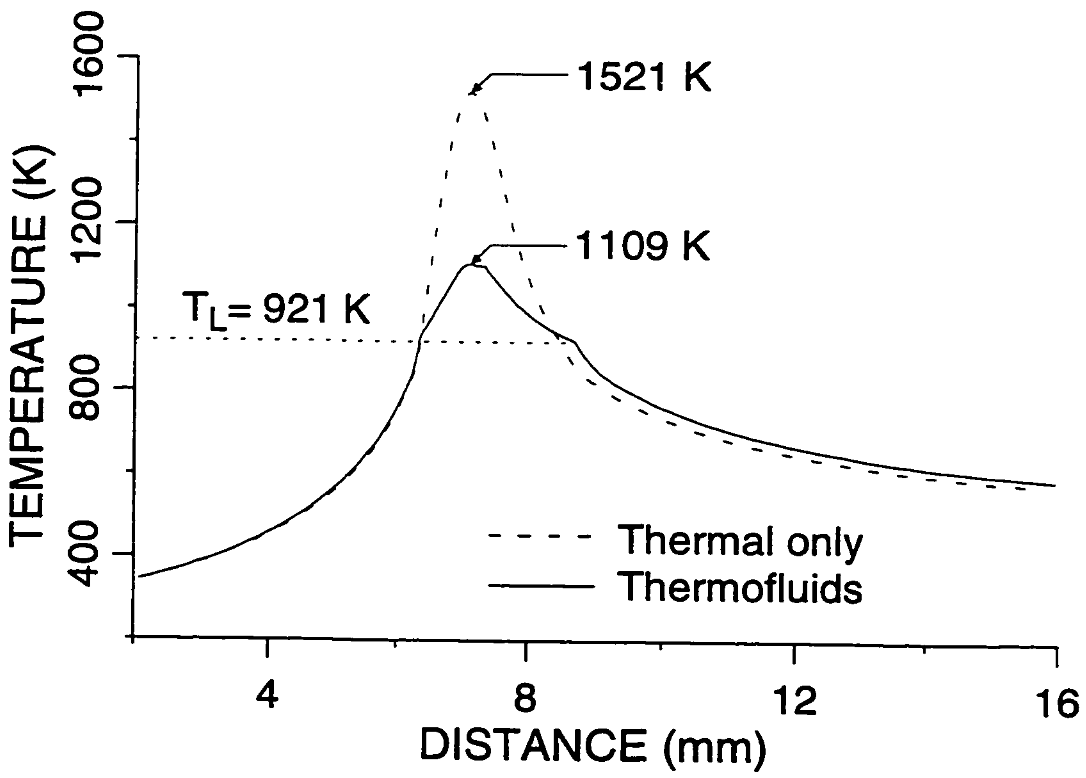

Figure 4.11: Predicted centreline surface temperatures for simulations with and without fluid flow. Welding conditions: 100 A at 4 mm/s.

4.3.4 Predicted Thermal Gradients and Growth Rates

Values of thermal gradient, G_L, and solid/liquid interface growth rate, R, were extracted from the simulations. Using the predicted thermal field, values of G_L were determined in the local growth direction (assumed to be perpendicular to the solid/liquid interface) along the liquidus isotherm from the weld pool tail to the fusion boundary. Values of R were determined along the liquidus isotherm from the weld pool tail to the fusion boundary using Equation 1.1. An example of G_L and R versus percentage of weld pool half-width is shown in Figure 4.12 for welding conditions 100 A at 4 mm/s. The growth rates and thermal gradients show similar behaviour in all the simulations. As seen in the figure, G_L is at its lowest value of approximately 19 K/mm at the tail of the weld pool (since this location is the furthest from the heat source) and increases to a maximum value of approximately 40 K/mm at the fusion boundary. Conversely, R is at its highest value of 4 mm/s at the tail of the weld pool since $R = v_{ws}$ here; values of R then decrease to reach approximately 0 at the fusion boundary. The thermal conditions are predicted to be most favourable to CET promotion (*i.e.*, lowest G_L and largest R) at the tail of the weld pool along the centreline. This predicted behaviour is consistent with previously reported experimental observations of equiaxed grains at the centreline of welds [8, 37, 38] and earlier semi-quantitative analyses [39].

Predicted centreline values of G_L at the tail of the pool for all the simulations are reported in Table 4.9 and plotted against welding speed in Figure 4.13. For comparison, the results are plotted with an estimate of centreline thermal gradient for thin plates based upon a two-dimensional analytical solution for heat conduction in welding by Rosenthal [41]:

$$G_L = 2\pi k \rho C_p \left(\frac{h}{\eta VI}\right)^2 v_{ws}(T_L - T_o)^3 \tag{4.1}$$

As discussed in Chapter 2, this expression has been frequently employed by previous researchers to estimate G_L. Both the numerical and analytical predictions show that, for a given current, G_L increases with increasing v_{ws}. Alternatively, at a given welding speed, decreasing the current increases G_L. For current-welding speed combinations

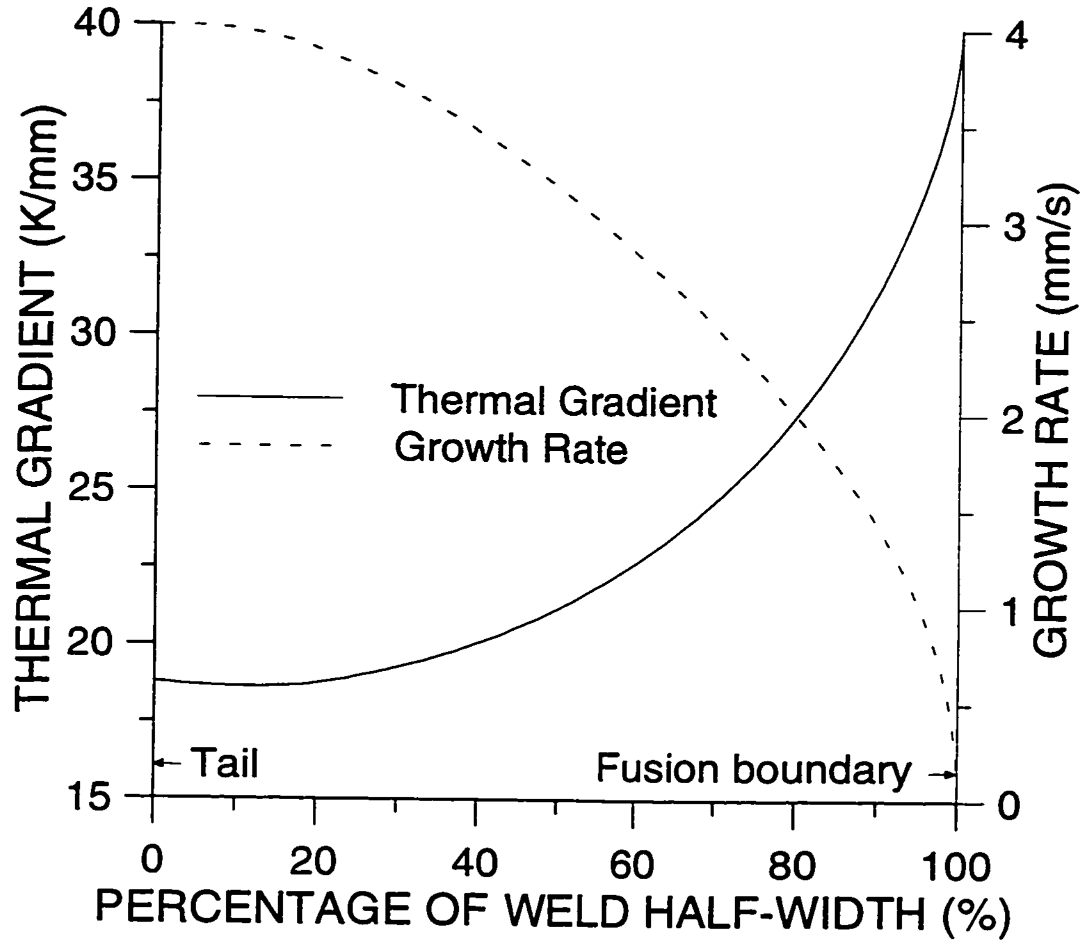

Figure 4.12: Predicted G_L and R versus percentage of weld half-width. Welding conditions: 100 A and 4 mm/s.

giving approximately constant weld widths (*e.g.*, welding conditions 100 A at 5 mm/s, 120 A at 6 mm/s, 140 A at 8 mm/s, and 160 A at 10 mm/s from Table 4.7, indicated with '*' in Table 4.9), the higher current-welding speed combinations are also predicted to result in lower G_L values.

This dependence of G_L on welding conditions is consistent with expectations of the behaviour of G_L based on the weld pool geometry. Recalling from Subsection 4.3.1, the weld pool is much more elongated for higher current-welding combinations. Since a more extended weld pool tail is further from the heat source, G_L would be expected to be lower at high current-welding speed combinations. Furthermore, at high welding speeds,

R is, of course, larger than at lower welding speeds. Thus, we would expect the CET to be most favoured at high current-welding speed combinations. Indeed, this was found to be the case in many previous experimental studies [34]-[39].

Table 4.9: Predicted thermal gradients at the weld pool tail. (% difference estimated with respect to numerical prediction.)

	Welding Conditions		Thermal Gradient (K/mm)		
	I (A)	v_{ws} (mm/s)	Analytical	Numerical	% Difference
	100	3	26.68	18.84	41.6
	100	4	35.57	18.77	89.5
*	100	5	44.47	23.39	90.1
	100	6	53.36	25.85	106.4
	120	4	24.70	13.71	80.2
	120	5	30.88	14.71	109.9
*	120	6	37.06	18.35	102.0
	120	7	43.23	22.33	93.6
	140	6	27.23	8.74	211.6
	140	7	31.76	10.15	212.9
*	140	8	36.30	12.14	199.0
	140	9	40.84	24.49	66.8
	160	7	24.32	4.26	470.9
	160	8	27.79	5.14	440.7
	160	9	31.27	6.73	364.6
*	160	10	34.74	10.15	242.3

* Designates welding conditions producing similar weld widths.

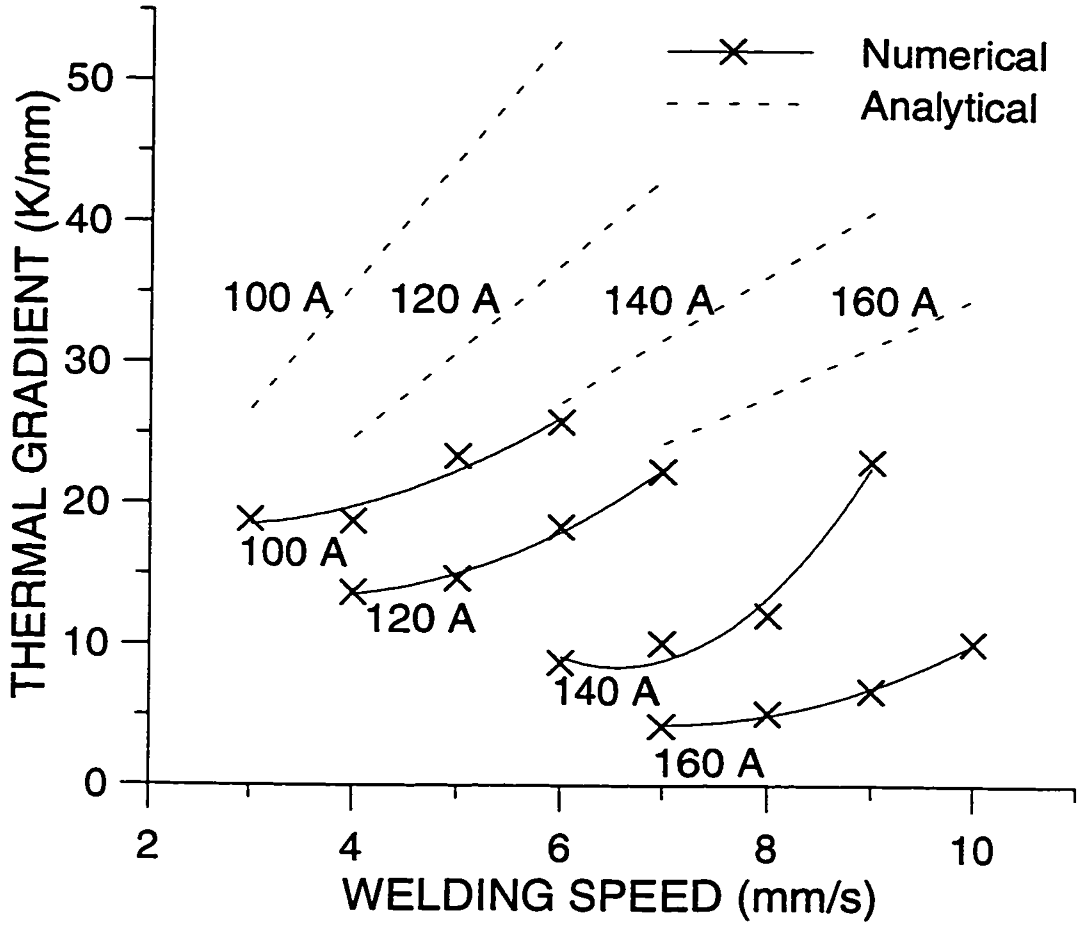

Figure 4.13: Predicted centreline thermal gradient at the weld pool tail versus welding speed for different welding currents.

A discrepancy exists between the analytical and numerically predicted values of G_L, particularly at high current and welding speed pairs: the analytical predictions are 42 to 471% higher than the numerical predictions. The lower G_L values predicted by the numerical model can be attributed to the incorporation of fluid flow, latent heat of fusion, temperature dependence of material properties, and distributed arc heat source effects and are consistent with the results shown in Figure 4.11. These dependencies of G_L at the centreline (*i.e.*, G_L increasing with increasing v_{ws} for a given current, G_L decreasing with increasing current for a given v_{ws}, and lower G_L at high current-welding speed combinations), have been observed by other researchers numerically [39] as well as experimentally [38].

4.4 Microstructure Modelling Results

An analytical model for the CET, incorporating Hunt's model [1], was used to predict the CET based on the thermal conditions in the weld pool as predicted by the numerical thermofluids model. Prior to the implementation of this CET model, however, it is constructive to examine some details of, and assumptions concerning, the microscopic growth at the solid/liquid interface and their influence on the modelling of the CET. The microscopic growth considerations, the implementation of the CET model, and the CET predictions will be presented and discussed in the present section.

4.4.1 Microscopic Growth Considerations

Once the numerical thermofluids model was employed to predict the weld pool thermal conditions, it was possible to examine in more detail the growth conditions at the solid/liquid interface and their implications with respect to CET modelling. The material properties relevant to the present discussion are given in Table 4.10.

Table 4.10: Properties for Al-4.5%Cu alloy.

(Taken from references [2, 94, 122].)

m_L (K/wt%)	C_o (wt%)	k_o	Γ (K·m)	ΔT_o (K)	D_o (m^2/s)	Q (J/mol)
-2.6	4.5	0.14	1.1×10^{-7}	77	1.1×10^{-7}	23 800

Planar and Dendritic Growth

It was necessary to determine the morphology of the advancing solid/liquid interface of the molten weld pool. At the initial stage of the solidification there is, of course, a transition from planar to cellular to dendritic depending on the extent of constitutional undercooling present at the solid/liquid interface. Recall from Chapter 1 that a planar interface will exist if $G_L/R > \Delta T_o/D$. Using the values in Table 4.10 gives $G_L/R >$ 15 714 K·s/mm^2. For example, from the simulation with welding conditions 100 A at 4 mm/s, $G_L \approx 40$ K/mm at the fusion boundary (worst case scenario). Thus, R would have to be less than approximately 0.0026 mm/s in order for a planar interface to exist. As discussed in Chapter 1, R varies around the perimeter of the weld pool as $R = v_{ws} \cos\theta$. At the fusion boundary, θ is theoretically equal to 0 and thus $R = 0$ mm/s; however, if θ changes by only a tenth of a degree (which corresponds to a distance of < 9 μm), $R = 0.007$ mm/s and the interface breaks down. Thus, in the present study, typical values of the G_L/R ratio were such that the interface morphology would make the transition into fully developed dendrites very rapidly.

Distribution Coefficient

The equilibrium distribution coefficient, k_o, which appears in Table 4.10 and is a relevant parameter with respect to microscopic growth, is implicitly assumed to be independent of growth rate. To check whether the use of a velocity-independent distribution coefficient was valid in the present work, the value of k_o was compared to the value of the non-equilibrium velocity-dependent distribution coefficient, k_v. The coefficient k_v is related to k_o through [13]

$$k_v = \frac{k_o + P_i}{1 + P_i} \tag{4.2}$$

The interface Peclet number is $P_i = a_o R / D_i$ where a_o is the interface diffusion length and D_i is the diffusion coefficient of solute in the liquid at the interface. For the Al-4.5%Cu alloy used in this study $P_i < 0.0026$ and so $k_v \approx k_o$. Thus, the use of the equilibrium partition coefficient was appropriate.

Dendrite Growth Models

As discussed above, the solid/liquid interface of the GTA weld pool had a dendritic morphology for all the welding conditions in the study. Thus, it was necessary to employ a growth model applicable for fully developed dendrites. As described in Chapter 1, the growth undercooling is comprised primarily of solutal and dendrite tip curvature undercooling [9]. The kinetics of transfer of atoms from the liquid to the crystal were neglected. This is reasonable for the non-faceted growth morphology of metals in which the transfer of atoms from liquid to solid is very rapid [9].

Hunt's model [1] employed an empirical relation for the growth undercooling of the columnar grain front, ΔT_C (Equation 1.17 from Chapter 1). Since this empirical relation was correlated to casting experiments in Al-3%Cu in which the interface growth rates were much smaller than those experienced in welding (0.3 mm/s compared to 11 mm/s in the present study), this relation cannot be expected to apply in a welding scenario.

An analytical model for ΔT_C developed by Burden and Hunt [11] was also presented in Chapter 1 (Equation 1.6). This model was compared to experimental casting data for Al-2%Cu for a range of growth rates from 0 to 0.3 mm/s. Again, since these growth rates are very small compared to those obtained in welding, this expression would not be appropriate in the present study.

Instead, in the present study, an analytical 'marginal stability' expression for ΔT_C, developed by Kurz *et al.* [2, 3], was employed, which is restated here:

$$\Delta T_C = m_L C_o \left(1 - \frac{1}{1 - (1 - k_o)\pi \sqrt{\dfrac{R\Gamma}{D \Delta T_o k_o}}} \right) \tag{1.7}$$

in which the diffusion coefficient, D, is calculated using

$$D = D_o \exp\left(\frac{-Q}{R_g T}\right) \tag{4.3}$$

Equation 1.7 is applicable for interface growth rates in which

$$R > \frac{G_L D}{\Delta T_o k_o} \tag{4.4}$$

To assess the applicability of the marginal stability expression in the present study, the most extreme case was considered. The lowest thermal gradient predicted in the simulations was approximately 4 K/mm (at the weld pool tail for welding conditions 160 A at 7 mm/s). This implies that in order for the marginal stability expression to be valid $R > 0.0018$ mm/s. At the fusion boundary, $R = 0$ mm/s; however, (similar to the discussion above) if θ changes by only a tenth of a degree, $R = 0.012$ mm/s and the marginal stability expression becomes valid. Furthermore, this analytical dendrite growth model agreed very well with experimental data for growth rates up to 100 mm/s [2, 3].

Implementation of Hunt's model

In the present study, an analytical model developed by Hunt [1] was employed as the basis for predicting the CET in moving GTA welds. Hunt's model was derived in detail in Chapter 1 and is restated here for convenience. A fully equiaxed grain structure is predicted to occur when

$$G_L < 0.617 N_o^{\frac{1}{3}} \left[1 - \frac{(\Delta T_N)^3}{(\Delta T_C)^3} \right] \Delta T_C \tag{1.16}$$

Hence, by determining G_L from the numerical thermofluids simulations, invoking the marginal stability dendrite growth model to evaluate ΔT_C, and employing appropriate estimates for the population density of heterogeneous nucleants, N_o, and their nucleation undercooling, ΔT_N, it should be possible to examine and predict the CET using this analytical expression.

Nucleation Parameters

Values for N_o were determined metallographically for the series of weld specimens used in the experimental study, as described in a later section. For the purpose of the numerical study, however, a wide range of values for N_o encompassing and expanding upon the experimentally determined values was assumed in order to examine the effect of changing N_o on the CET in welds. The latent heat of fusion evolved during the solidification of equiaxed grains was assumed to have a negligible effect on the local thermal gradient since high diffusivity metals like aluminum alloys are able to quickly conduct away the evolved heat into the liquid [123].

There is much controversy in the literature concerning values of nucleation undercooling, ΔT_N [124]. Thus in the numerical study, a range of values for ΔT_N was employed to examine the implications of changing ΔT_N on the CET. For the experimental work, ΔT_N was assumed to be a constant 0.75 K, following Hunt [1].

4.4.2 Predicting the CET

Predicted values of thermal gradient, G_L, and solid/liquid interface growth rate, R, were obtained from the numerical thermofluids model along the liquidus isotherm from the weld pool tail to the fusion boundary. Examples of these predicted thermal conditions for four simulations (welding conditions 100 A at 5 mm/s, 120 A at 6 mm/s, 140 A at 8 mm/s, and 160 A at 10 mm/s) are plotted in Figure 4.14. These four simulations were selected for comparison since they produce similar weld widths (Table 4.7) and will thus permit an evaluation of the effects of process parameters on the CET while holding the weld size constant. Estimates of the conditions necessary for a CET were obtained from the analytical CET model for alloys containing both 2% and 4% Cu, and are also presented in the figures. These CET predictions were made assuming N_o = 50 000 nucleants/mm^3 and $\Delta T_N = 0.75$ K.

Critical values of thermal gradient, G_L, and solid/liquid interface growth rate, R, required to produce a CET were determined from Figure 4.14 by ascertaining the points of intersection between the predicted R versus G_L results with the CET model. For alloys containing 2% Cu, this intersection occurs at $R \approx 3.1$ mm/s and $G_L \approx 28$ K/mm for all four simulation results presented. For alloys containing 4% Cu, this intersection occurs at $R \approx 1.3 - 1.4$ mm/s and $G_L \approx 32 - 35$ K/mm. As indicated in the figure and as described in Chapter 2, these values of R and G_L were calculated along the liquidus isotherm from the weld pool tail to the fusion boundary. The predicted % equiaxed in the weld bead was assumed to be equal to the % weld pool half-width at which the critical thermal conditions occur. For example, the predicted values of R and G_L are plotted versus % weld pool half-width in Figure 4.15 for welding conditions 140 A at 8 mm/s. As indicated in the plot, the critical values of R and G_L for the alloy containing 2% Cu occur at 85% of the weld pool half-width, thus the predicted % equiaxed is 85%. Values of % equiaxed were similarly determined for all other welding conditions and copper contents for N_o = 50 000 nucleants/mm^3 and $\Delta T_N = 0.75$ K and are presented in Table 4.11. It is evident from Figure 4.15 and Table 4.11 that increasing the copper content or welding at a higher current and welding speed combination are predicted to favour the CET.

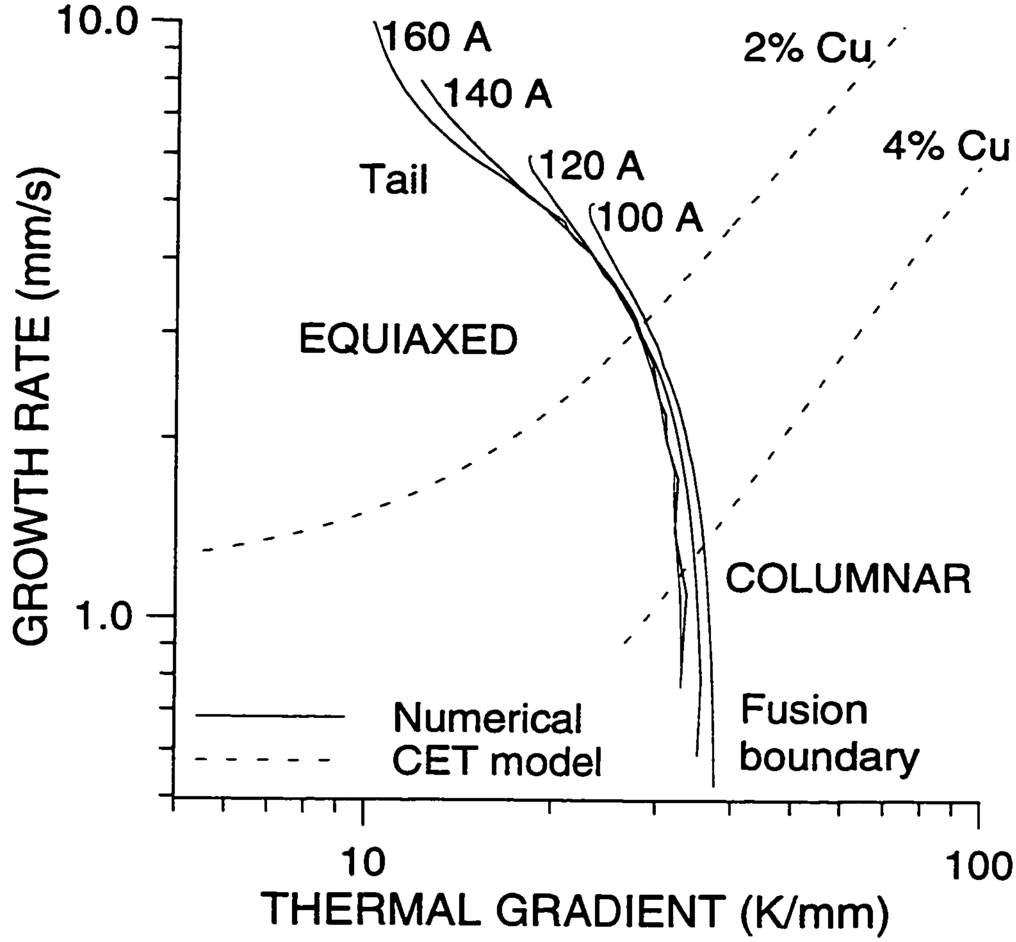

Figure 4.14: Predicted R versus G_L compared with the CET model. $\Delta T_N = 0.75$ K; $N_o = 50\ 000$ nucleants/mm^3.

Table 4.11: Predicted % equiaxed.

($\Delta T_N = 0.75$ K and $N_o = 50\ 000$ nucleants/mm^3.)

Cu	Equiaxed % of Weld Width			
(%)	100 A, 5 mm/s	120 A, 6 mm/s	140 A, 8 mm/s	160 A, 10 mm/s
2	68	77	85	90
4	94	96	98	98

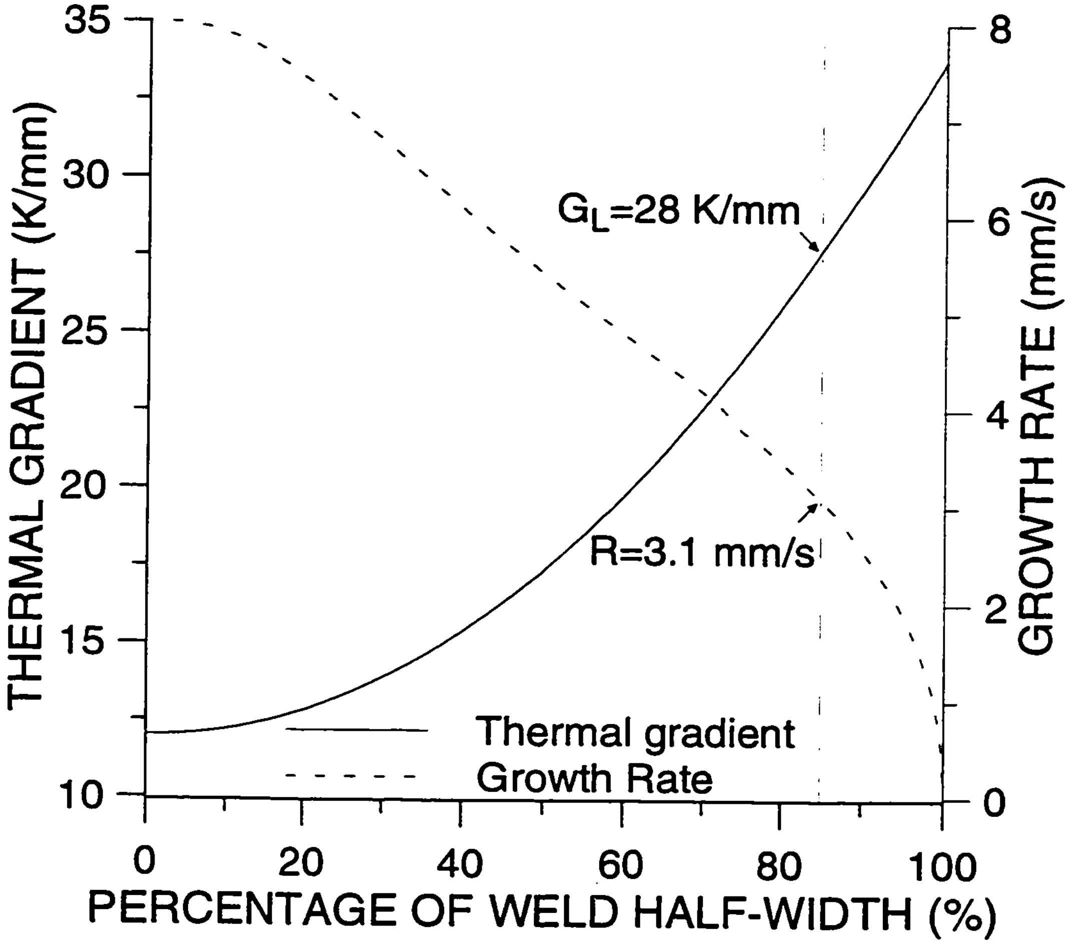

Figure 4.15: Predicted R and G_L versus % of weld pool half-width. Welding conditions: 140 A at 8 mm/s.

4.4.3 Predicted Effects of Nucleant Population Density

Figures 4.16 and 4.17 show the effect of changing N_o on the predicted % equiaxed, assuming $\Delta T_N = 0.75$ K. The welding conditions for the results shown are 100 A at 5 mm/s, 120 A at 6 mm/s, 140 A at 8 mm/s, and 160 A at 10 mm/s, since they produce similar weld widths (Table 4.7). The corresponding % equiaxed values as a fraction of weld width are reported in Tables 4.12 and 4.13. As seen in the figures and the tables, increasing N_o by progressive orders of magnitude increases the % equiaxed from 0 to approximately 100%. Further, it is seen that for a given welding condition, the % equiaxed is higher for the 4% copper compared to the 2% copper.

Table 4.12: Predicted % equiaxed for different N_o.
(2% Cu; $\Delta T_N = 0.75$ K.)

N_o	Equiaxed % of Weld Width			
(nucleants/mm^3)	100 A, 5 mm/s	120 A, 6 mm/s	140 A, 8 mm/s	160 A, 10 mm/s
50	0	0	0	0
500	0	0	18	35
5000	0	42	61	66
50 000	68	77	85	90
500 000	89	93	96	96

Although a large heterogeneous nucleant population density will promote a CET for any of the welding conditions, particularly at the higher copper content, when N_o is small, the welding conditions play an important role in CET promotion. More specifically, when nucleants are few, a CET is most favoured when a high current-welding speed combination is used.

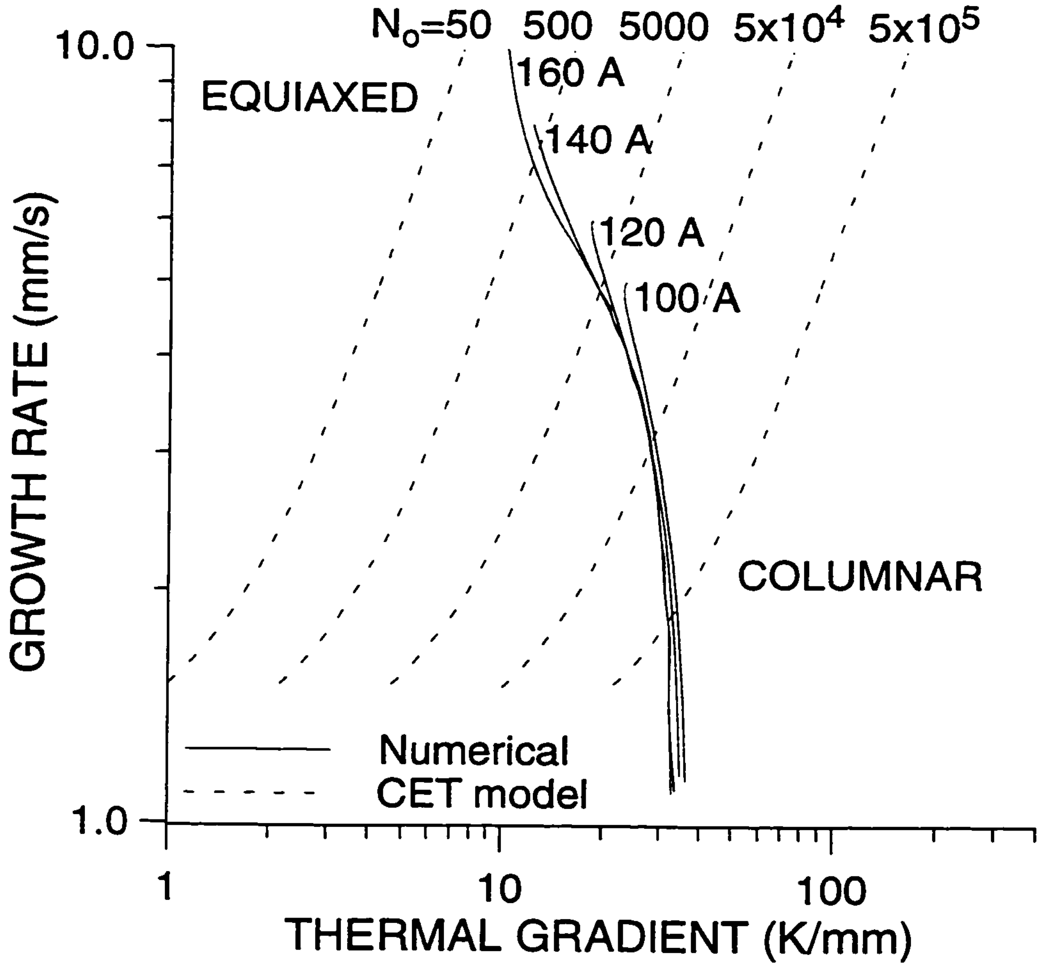

Figure 4.16: Predicted R versus G_L compared with the CET model for different N_o. Welding conditions: 100 A at 5 mm/s, 120 A at 6 mm/s, 140 A at 8 mm/s, and 160 A at 10 mm/s; 2% Cu; $\Delta T_N = 0.75$ K; N_o in nucleants/mm^3.

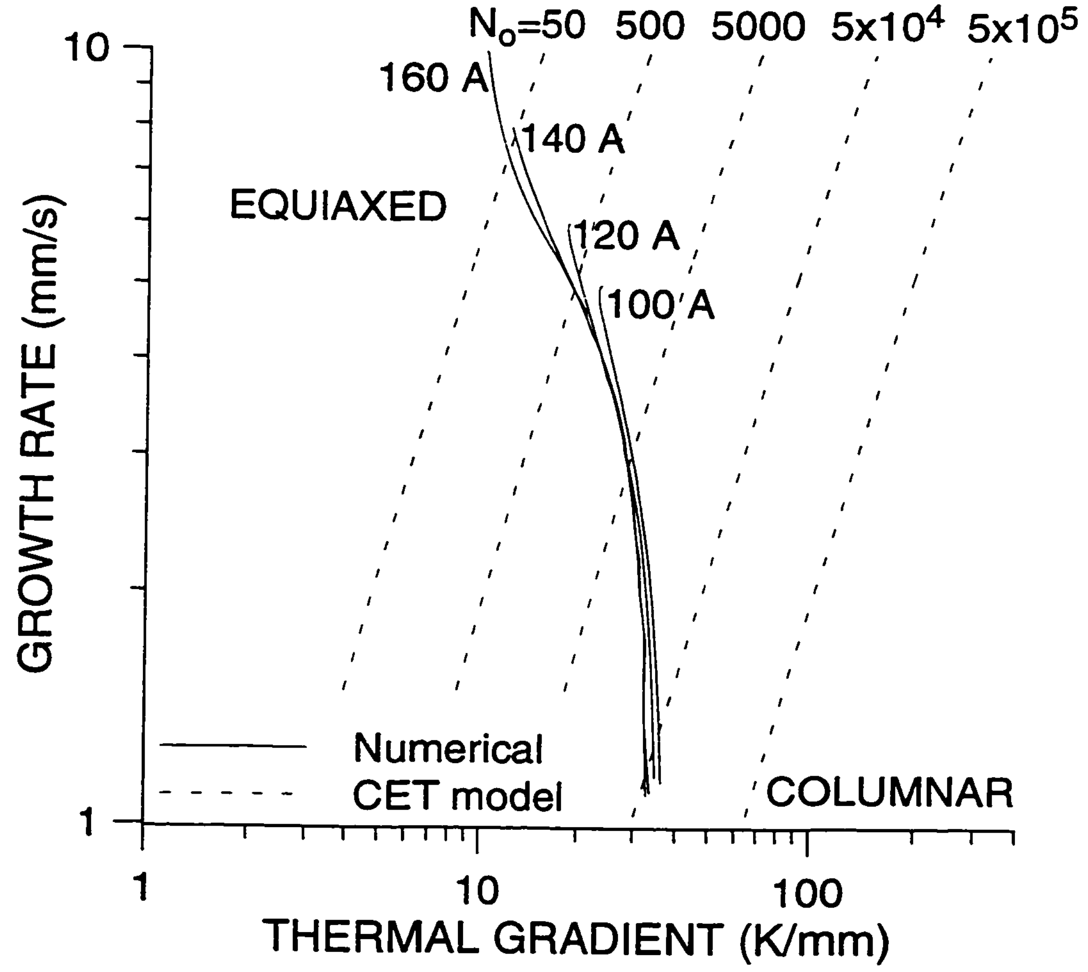

Figure 4.17: Predicted R versus G_L compared with the CET model for different N_o. Welding conditions: 100 A at 5 mm/s, 120 A at 6 mm/s, 140 A at 8 mm/s, and 160 A at 10 mm/s; 4% Cu; $\Delta T_N = 0.75$ K; N_o in nucleants/mm^3.

Table 4.13: Predicted % equiaxed for different N_o.

(4% Cu; $\Delta T_N = 0.75$ K.)

N_o	Equiaxed % of Weld Width			
(nucleants/mm^3)	100 A, 5 mm/s	120 A, 6 mm/s	140 A, 8 mm/s	160 A, 10 mm/s
50	0	0	4	31
500	0	37	57	66
5000	71	79	87	92
50 000	94	96	98	98
500 000	100	100	100	100

4.4.4 Predicted Effects of Nucleation Undercooling

There is much controversy in the literature concerning values of ΔT_N [124]. Due to this uncertainty, it is useful in the present work to consider the effect of ΔT_N on the prediction of a CET. Figures 4.18 and 4.19 show predictions of G_L and R from the four simulations, compared with the CET model for different values of ΔT_N, assuming N_o = 50 000 nucleants/mm^3. The corresponding % equiaxed values as a fraction of weld width are reported in Tables 4.14 and 4.15. As seen in the figures and the tables, increasing the efficiency of the nucleants (*i.e.*, decreasing ΔT_N) increases the % equiaxed in the weld bead. The higher copper content also favours larger equiaxed zones. It is apparent that the efficacy of the heterogeneous nucleants is an important factor for CET promotion; however, the welding conditions are also important, particularly when the nucleants are inefficient.

Table 4.14: Predicted % equiaxed for different ΔT_N.

(2% Cu; N_o = 50 000 nucleants/mm^3.)

ΔT_N	Equiaxed % of Weld Width			
(K)	100 A, 5 mm/s	120 A, 6 mm/s	140 A, 8 mm/s	160 A, 10 mm/s
3	0	0	0	13
1.5	0	51	64	71
0.75	68	77	85	90
0	76	82	90	92

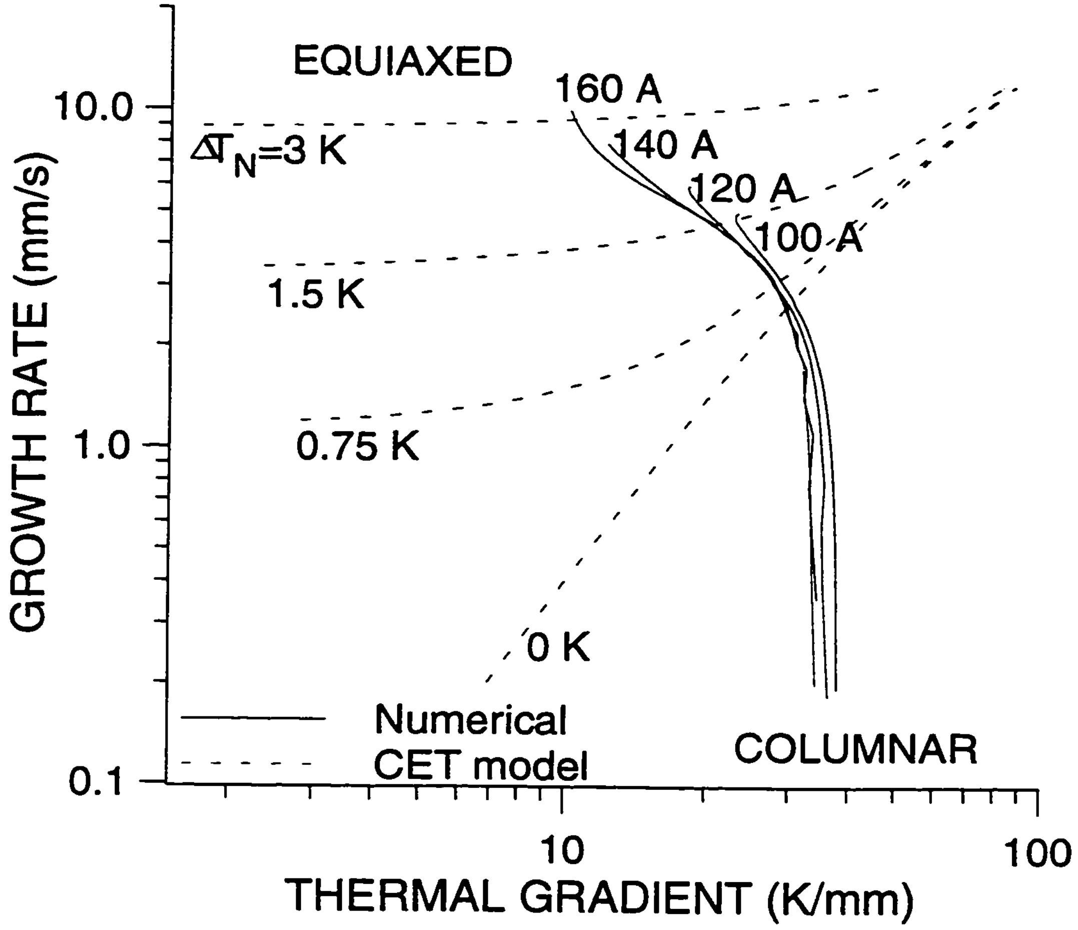

Figure 4.18: Predicted R versus G_L compared with the CET model for different ΔT_N. Welding conditions: 100 A at 5 mm/s, 120 A at 6 mm/s, 140 A at 8 mm/s, and 160 A at 10 mm/s; 2% Cu; N_o = 50 000 nucleants/mm^3.

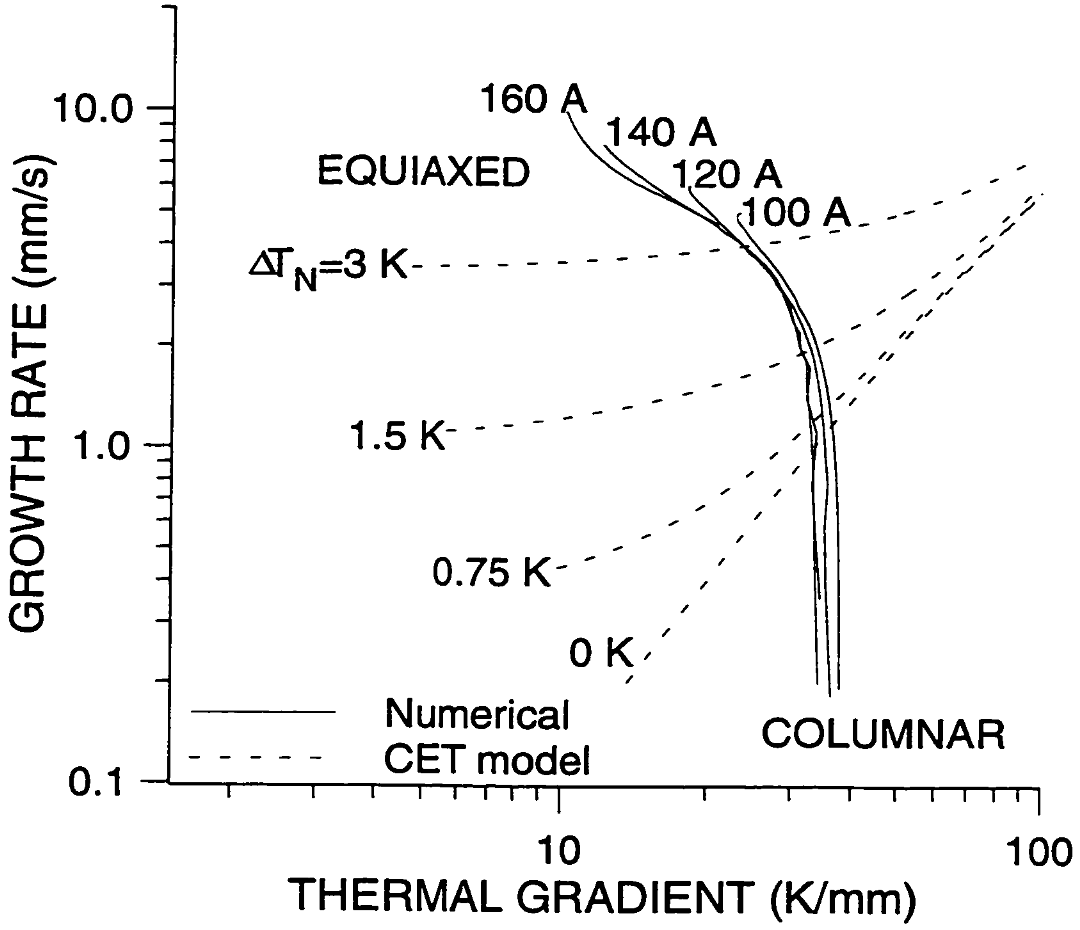

Figure 4.19: Predicted R versus G_L compared with the CET model for different ΔT_N. Welding conditions: 100 A at 5 mm/s, 120 A at 6 mm/s, 140 A at 8 mm/s, and 160 A at 10 mm/s; 4% Cu; $N_o = 50\ 000$ nucleants/mm^3.

Table 4.15: Predicted % equiaxed for different ΔT_N.
(4% Cu; N_o = 50 000 nucleants/mm^3.)

ΔT_N	Equiaxed % of Weld Width			
(K)	100 A, 5 mm/s	120 A, 6 mm/s	140 A, 8 mm/s	160 A, 10 mm/s
3	47	59	73	80
1.5	87	90	94	96
0.75	94	96	98	98
0	95	97	99	99

4.5 Experimental Results

A series of autogenous bead-on-plate moving GTA welds was performed on 2 mm thick plates of Al-Cu alloys with the welding process parameters listed in Table 4.16. Two welds were performed for each set of process conditions. The aluminum alloys contained nominal copper levels of 2 and 4 wt%, and nominal titanium levels of < 0.001 (trace), 0.003 (low), 0.015 (intermediate), and 0.03 wt% (high), introduced as TiB_2 during the casting of the alloys.

Table 4.16: Experimental welding process parameters.

Peak I (A)	Peak V (V)	v_{ws} (mm/s)
100	13	3 & 4
120	13	4 & 5
140	13	6 & 7
160	13	8 & 9

4.5.1 Verification of Two-Dimensional Heat Flow Conditions

As described in an earlier section, it was desirable to have two-dimensional heat flow conditions for clarity of microstructural interpretation. Two-dimensional heat flow conditions will produce parallel fusion boundaries and columnar grains which are parallel with the top surface of the plate. For example, Figure 4.20 shows a transverse section of an experimental specimen containing 2% Cu and exhibiting a CET. This specimen was welded with a current of 160 A at a welding speed of 8 mm/s. As seen in the figure, the fusion boundary is perpendicular to the top surface of the base plate. In addition, the columnar grains which extend from the fusion boundary are parallel to the top and bottom surfaces of the base plate.

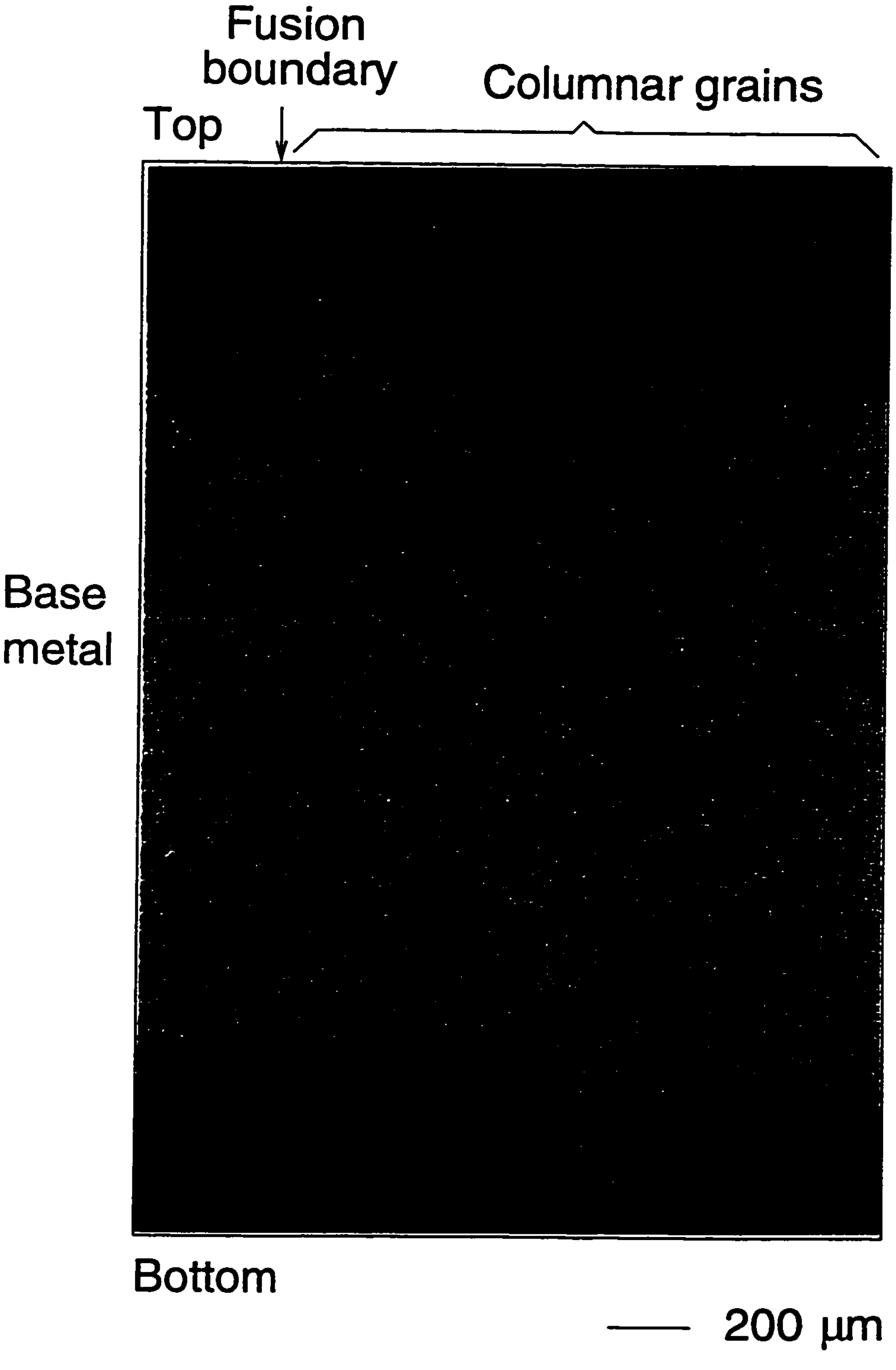

Figure 4.20: GTA welded specimen of Al-2%Cu exhibiting evidence of two-dimensional heat flow conditions. Welding conditions: 160 A at 8 mm/s.

4.5.2 Predicted and Experimental Weld Widths

Tables 4.17 and 4.18 show a comparison between experimentally measured and numerically predicted weld widths for the series of CET experiments and matching numerical thermofluids simulations, described previously. The experimental values reported in the table represent the average weld widths at the listed welding process conditions for all three TiB_2 contents, since TiB_2 did not have an appreciable effect on the weld width. Values of weld width for the 2 and 4% Cu alloys containing only a trace amount of TiB_2 are not included in these averages since these specimens often exhibited a centreline crack and underwent considerable thermal distortion which rendered accurate measurement of the weld width difficult. Tables 4.17 and 4.18 indicate good agreement between the predicted and experimentally measured values of weld width which further corroborates the accuracy of the numerical thermofluids model.

Table 4.17: Experimental and predicted weld widths for Al-2%Cu. (% difference with respect to experimental value.)

Welding Conditions		Weld Widths (mm)		
Peak I (A)	v_{ws} (mm/s)	Experimental	Predicted	% Difference
100	3	8.94 ± 0.64	10.68	19.5
	4	6.94 ± 0.47	7.99	15.1
120	4	9.96 ± 0.61	10.98	10.2
	5	7.65 ± 0.39	8.14	6.4
140	6	8.68 ± 0.51	9.09	4.7
	7	7.66 ± 0.36	7.78	1.6
160	8	8.53 ± 0.43	8.54	0.1
	9	7.31 ± 0.29	7.70	5.3

Table 4.18: Experimental and predicted weld widths for Al-4%Cu. (% difference with respect to experimental value.)

Welding Conditions		Weld Widths (mm)		
Peak I (A)	v_{ws} (mm/s)	Experimental	Predicted	% Difference
100	2	10.14 ± 0.67	10.68	5.3
	3	7.84 ± 0.38	7.99	1.9
120	4	10.73 ± 0.67	10.98	2.3
	5	8.85 ± 0.41	8.14	-8.0
140	6	9.84 ± 0.36	9.09	-7.6
	7	8.53 ± 0.36	7.78	-8.8
160	8	9.17 ± 0.35	8.54	-6.9
	9	8.33 ± 0.34	7.70	-7.6

4.5.3 Grain Structure and % Equiaxed

The grain structures and values of % equiaxed grains in the weld bead were determined from the experimental specimens and are reported in Tables 4.19 and 4.20. The reported % equiaxed values represent averages of measurements from the two specimens welded at each set of process conditions.

The results are first summarized with respect to general trends, then examined in more detail. As indicated in Tables 4.19 and 4.20, specimens containing trace amounts of TiB_2 solidified with a fully columnar structure, some even exhibiting a centreline solidification crack, for both Cu contents. Low and intermediate levels of TiB_2 in specimens of either Cu content produced feathery crystals at low current-welding speed pairs and a CET at higher current-welding speed pairs. A fully equiaxed structure was observed for all welding conditions and both Cu contents with the high level of TiB_2. In aluminum alloys, many other researchers [34, 35, 37, 38, 44, 46, 49, 50] have also found that elevated levels of heterogeneous nucleants, such as TiB_2, favour the CET in welds. In addition, this trend is consistent with CET predictions using Hunt's model [1] (Equation 1.16).

Table 4.19: Experimentally measured % equiaxed for 2% Cu.

Ti (wt%)	Peak I (A)	v_{ws} (mm/s)	% Equiaxed	Observations
trace	140	7	0	columnar structure with centreline crack
	160	9	0	columnar structure with centreline crack
0.004	100	3	0	feathery crystals
		4	0	feathery crystals
	120	4	0	feathery crystals
		5	0	feathery crystals
	140	6	28.6	CET
		7	22.9	CET
	160	8	36.7	CET
		9	25.6	CET
0.013	100	3	0	feathery crystals
		4	0	feathery crystals
	120	4	48.8	CET
		5	34.7	CET
	140	6	55.8	CET
		7	39.0	CET
	160	8	56.4	CET
		9	47.0	CET
0.027	100	3	100	very fine equiaxed
		4	100	very fine equiaxed
	120	4	100	very fine equiaxed
		5	100	very fine equiaxed
	140	6	100	very fine equiaxed
		7	100	very fine equiaxed
	160	8	100	very fine equiaxed
		9	100	very fine equiaxed

Table 4.20: Experimentally measured % equiaxed for 4% Cu.

Ti (wt%)	I (A)	v_{ws} (mm/s)	% Equiaxed	Observations
trace	100	3	0	fully columnar structure
		4	0	fully columnar structure
	120	5	0	fully columnar structure
	140	6	0	fully columnar structure
		7	0	fully columnar structure
	160	8	0	columnar structure with centreline crack
		9	0	columnar structure with centreline crack
0.003	100	3	0	feathery crystals
		4	0	feathery crystals
	120	4	49.3	CET
		5	40.7	CET
	140	6	50.6	CET
		7	42.5	CET
	160	8	45.7	CET
		9	48.8	CET
0.013	100	3	75.3	CET
		4	0	very fine feathery crystals
	120	4	80.2	CET
		5	77.4	CET
	140	6	79.7	CET
		7	68.0	CET
	160	8	76.3	CET
		9	70.1	CET

Table 4.20: Experimentally measured % equiaxed for 4% Cu (continued).

Ti (wt%)	I (A)	v_{ws} (mm/s)	% Equiaxed	Observations
0.026	100	3	100	very fine equiaxed
		4	100	very fine equiaxed
	120	4	100	very fine equiaxed
		5	100	very fine equiaxed
	140	6	100	very fine equiaxed
		7	100	very fine equiaxed
	160	8	100	very fine equiaxed
		9	100	very fine equiaxed

When a CET occurred, the % equiaxed was generally larger at the lowest welding speed for a given current, and at higher current-welding speed combinations. Other researchers, for example Kou and Le [38] and Ganaha *et al.* [37], have also noted the transition from fully columnar structures at low currents and welding speeds and for low levels of grain refiner additions, to a CET at higher currents and welding speeds when a larger number of inoculants are present. For the same welding conditions, a higher % equiaxed was consistently produced in specimens containing 4% copper compared to 2% copper. Previous research with aluminum alloys by Matsuda *et al.* [34, 35] also showed that increasing the alloy composition favours the CET. This trend is also consistent with Hunt's model [1].

An example of a fully columnar grain structure is shown in Figure 4.21 for a specimen of Al-2%Cu containing a trace amount of TiB_2. This specimen was welded with 120 A at 5 mm/s. As seen in the figure, the columnar grains extend from the fusion boundary. Along the centreline there is an axial structure composed of continuous grains which grew in the welding direction. This centreline structure renders the weld susceptible to brittle fracture and solidification cracking. Indeed, such a crack is seen in Figure 4.21. Figure 4.22 is a photomicrograph of an Al-2%Cu specimen welded with 140 A at 6 mm/s, which shows columnar grains extending from the fusion boundary and exhibits solidification cracking along several grain boundaries. Columnar structures such as these have also been observed in GTA welds in aluminum alloys by other researchers, for example Ganaha *et al.* [37].

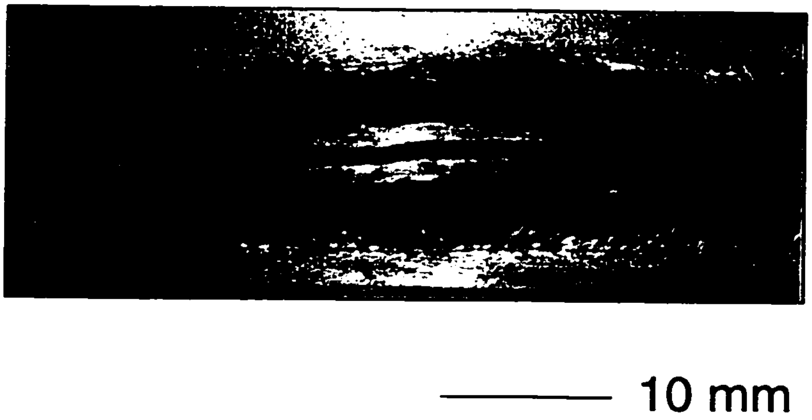

Figure 4.21: GTA welded specimen of Al-2%Cu exhibiting a fully columnar grain structure with a centreline solidification crack. Welding conditions: 120 A at 5 mm/s.

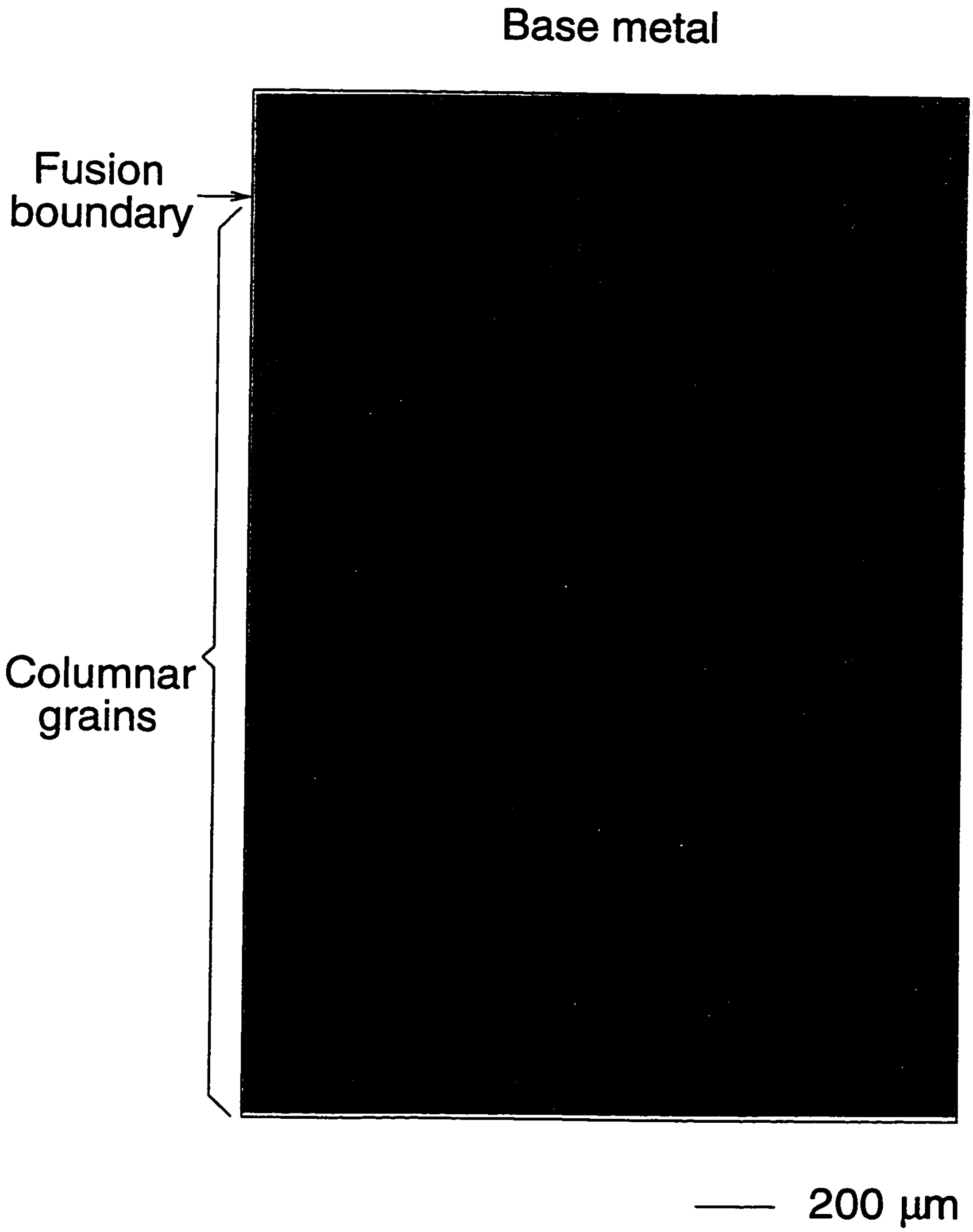

Figure 4.22: GTA welded specimen of Al-2%Cu exhibiting a columnar grain structure with solidification cracking. Welding conditions: 140 A at 6 mm/s.

As indicated in Tables 4.19 and 4.20, welding with a low current and low welding speed on alloys containing low and intermediate levels of TiB_2 produced structures with feathery crystals. An example of this structure is shown in Figure 4.23 for an Al-4%Cu specimen inoculated with 0.003 wt% Ti and welded with 100 A at 3 mm/s. The feathery grains are seen to extend outwards from the centreline of the weld to meet the columnar grains. This feathery crystal structure is more clearly seen in Figures 4.24 and 4.25 which are photomicrographs of top view and transverse section of the specimen, respectively. On the top surface, the feathery crystals are seen blocking the advancing columnar grains. The long straight lines are twin boundaries. In the transverse section, the twin structure of the feather crystal is seen to extend into the depth of the weld. Feathery crystals and their characteristic twin structure have also been observed in some castings of aluminum alloys [125, 126] and in GTA welds in some aluminum alloys [37]. These grains, although not truly equiaxed, are nucleated in the bulk of the weld pool in the manner of equiaxed grains, and do not originate epitaxially from the fusion boundary as do columnar grains [127]. Thus, feathery crystals represent an intermediate structure between a fully columnar structure and a CET in these alloys [37, 127].

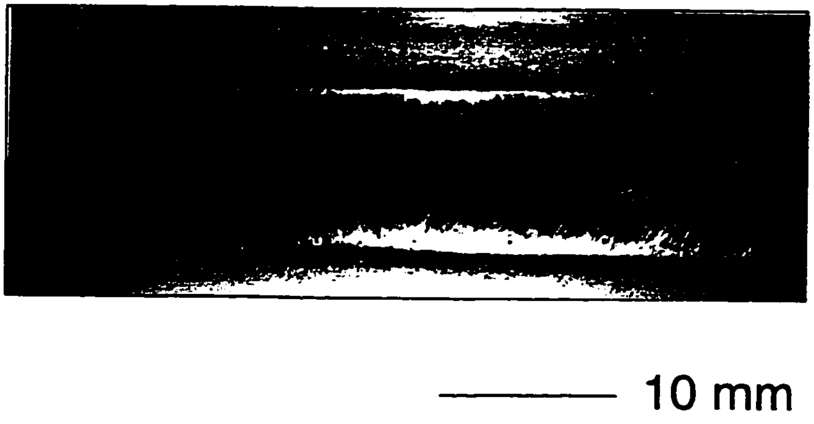

Figure 4.23: GTA welded specimen of Al-4%Cu inoculated with 0.003 wt% Ti exhibiting a feathery crystal structure. Welding conditions: 100 A at 3 mm/s.

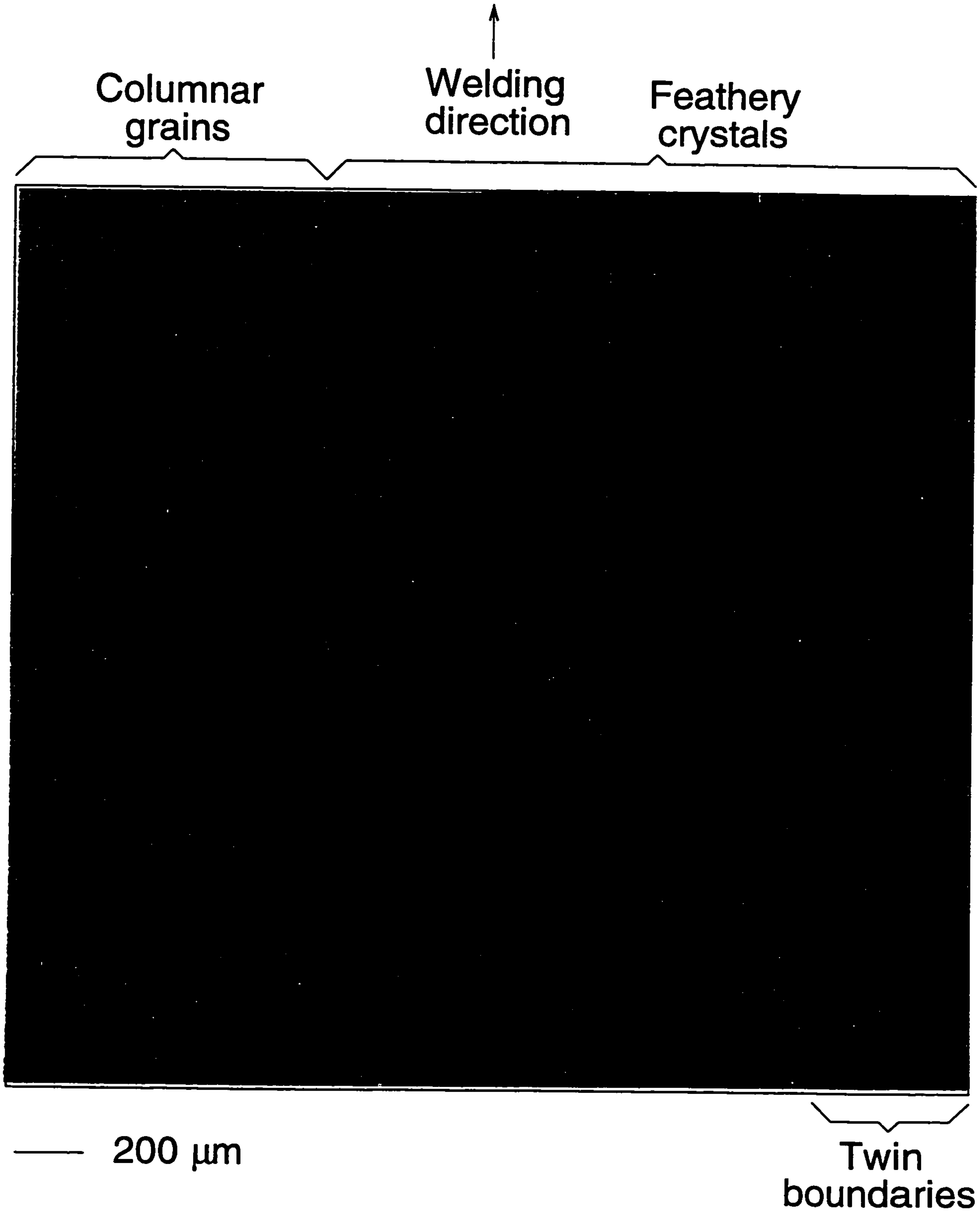

Figure 4.24: Top view of a GTA welded specimen of Al-4%Cu inoculated with 0.003 wt% Ti exhibiting a feathery crystal structure. Welding conditions: 100 A at 3 mm/s.

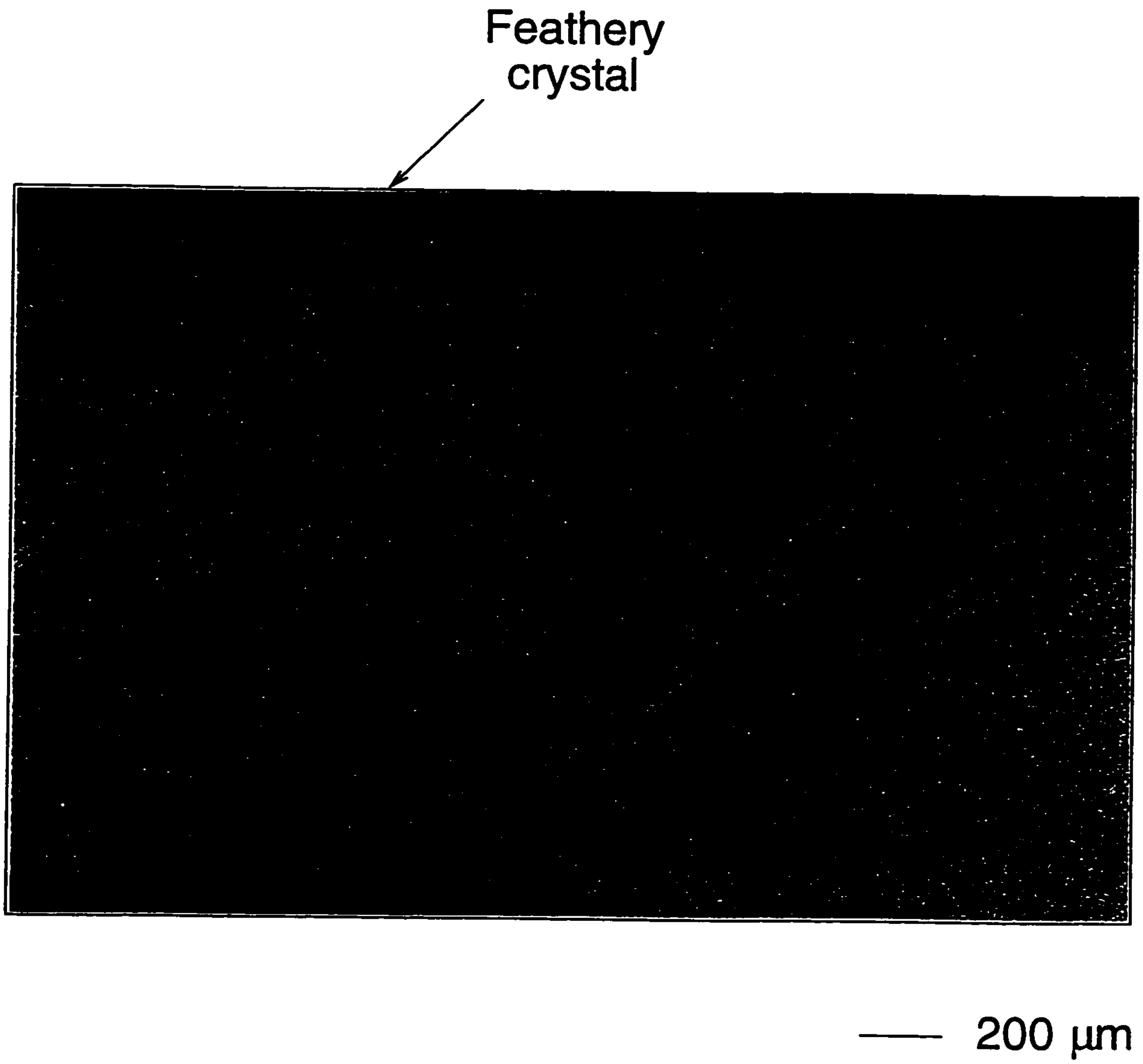

Figure 4.25: Transverse section of a GTA welded specimen of Al-4%Cu inoculated with 0.003 wt% Ti exhibiting a feathery crystal structure. Welding conditions: 100 A at 3 mm/s.

Higher current-welding speed combinations on alloys containing low and intermediate TiB_2 contents produced a CET with distinct columnar and equiaxed zones, as shown in Figure 4.26 for an Al-2%Cu specimen inoculated with 0.013 wt% Ti and welded with 120 A at 5 mm/s. The specimen has approximately 50% equiaxed grains. Figure 4.27 is a photomicrograph of a CET for an Al-2%Cu specimen inoculated with 0.004 wt% Ti and welded with 160 A at 8 mm/s. As seen in both figures, the columnar grains extend from the fusion boundary, but do not meet at the centreline since their progress was successfully blocked by the equiaxed grains which nucleated in the undercooled zone ahead of the advancing columnar interface.

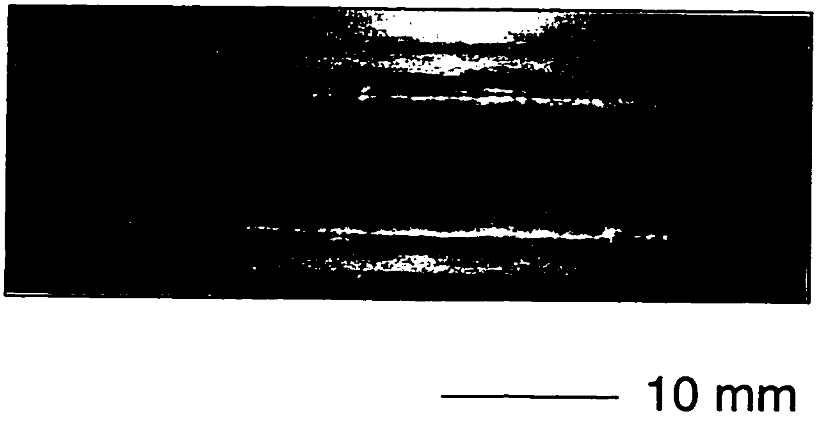

Figure 4.26: GTA welded specimen of Al-2%Cu inoculated with 0.013 wt% Ti and exhibiting a CET. Welding conditions: 120 A at 5 mm/s.

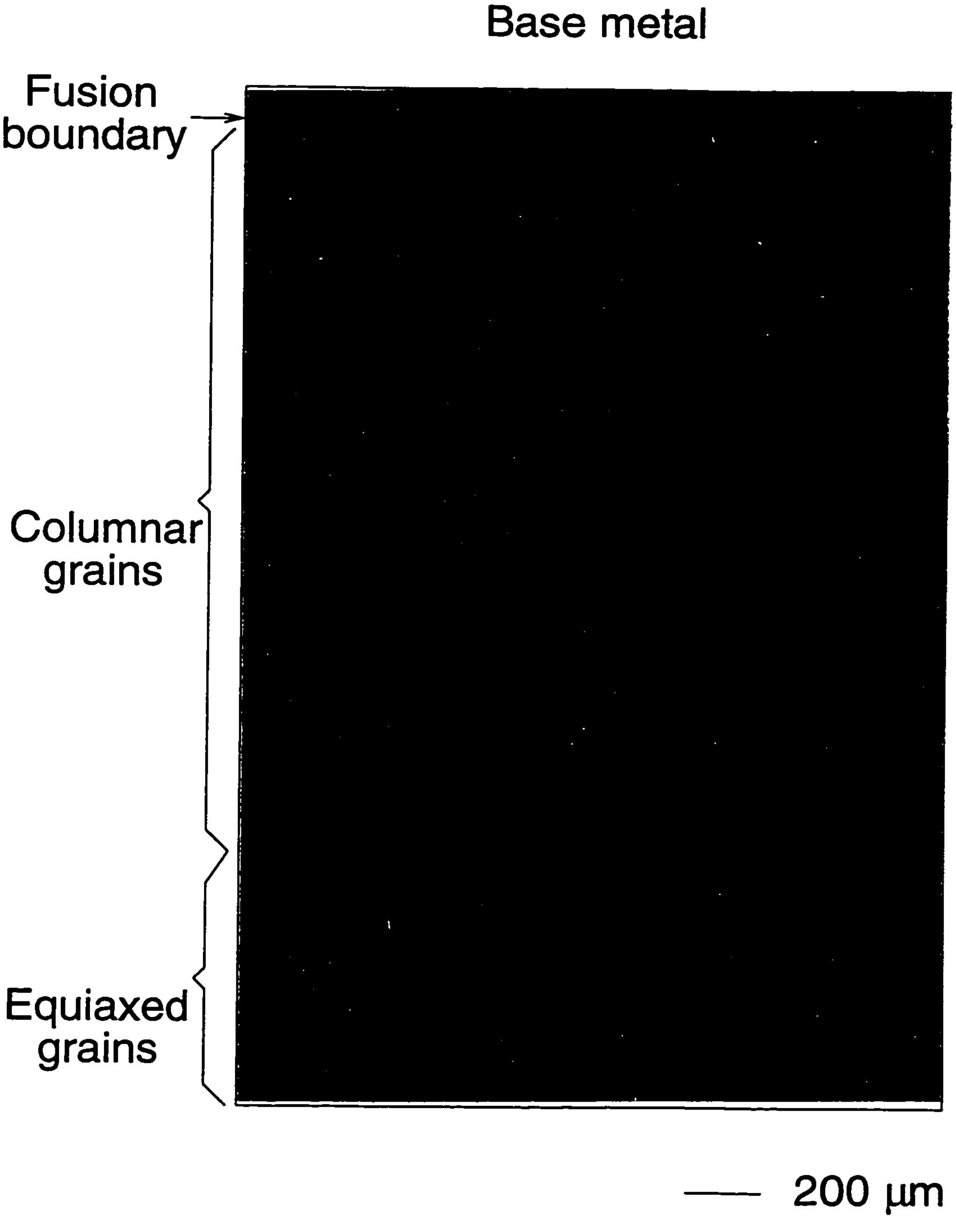

Figure 4.27: GTA welded specimen of Al-2%Cu inoculated with 0.004 wt% Ti and exhibiting a CET. Welding conditions: 160 A at 8 mm/s.

Welds performed on specimens containing a high level of TiB_2 for both copper contents produced a fully equiaxed structure regardless of the welding conditions. An example of a fully equiaxed structure is given in Figure 4.28 for a specimen of Al-4%Cu containing 0.026 wt% Ti and welded with 100 A at 4 mm/s. As seen in the figure, the entire weld bead is composed of equiaxed grains and no columnar zone is evident. Figure 4.29 is a photomicrograph of the top surface of an Al-4%Cu specimen containing 0.026 wt% Ti and welded with 160 A and 8 mm/s. As seen in the figure, the weld bead is composed of very fine equiaxed grains which extend right up to the fusion boundary.

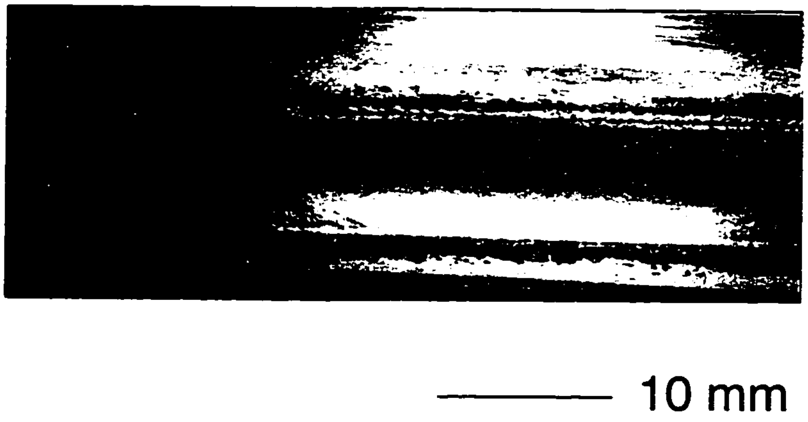

Figure 4.28: GTA welded specimen of Al-4%Cu inoculated with 0.026% Ti and exhibiting a fully equiaxed structure. Welding conditions: 100 A at 4 mm/s.

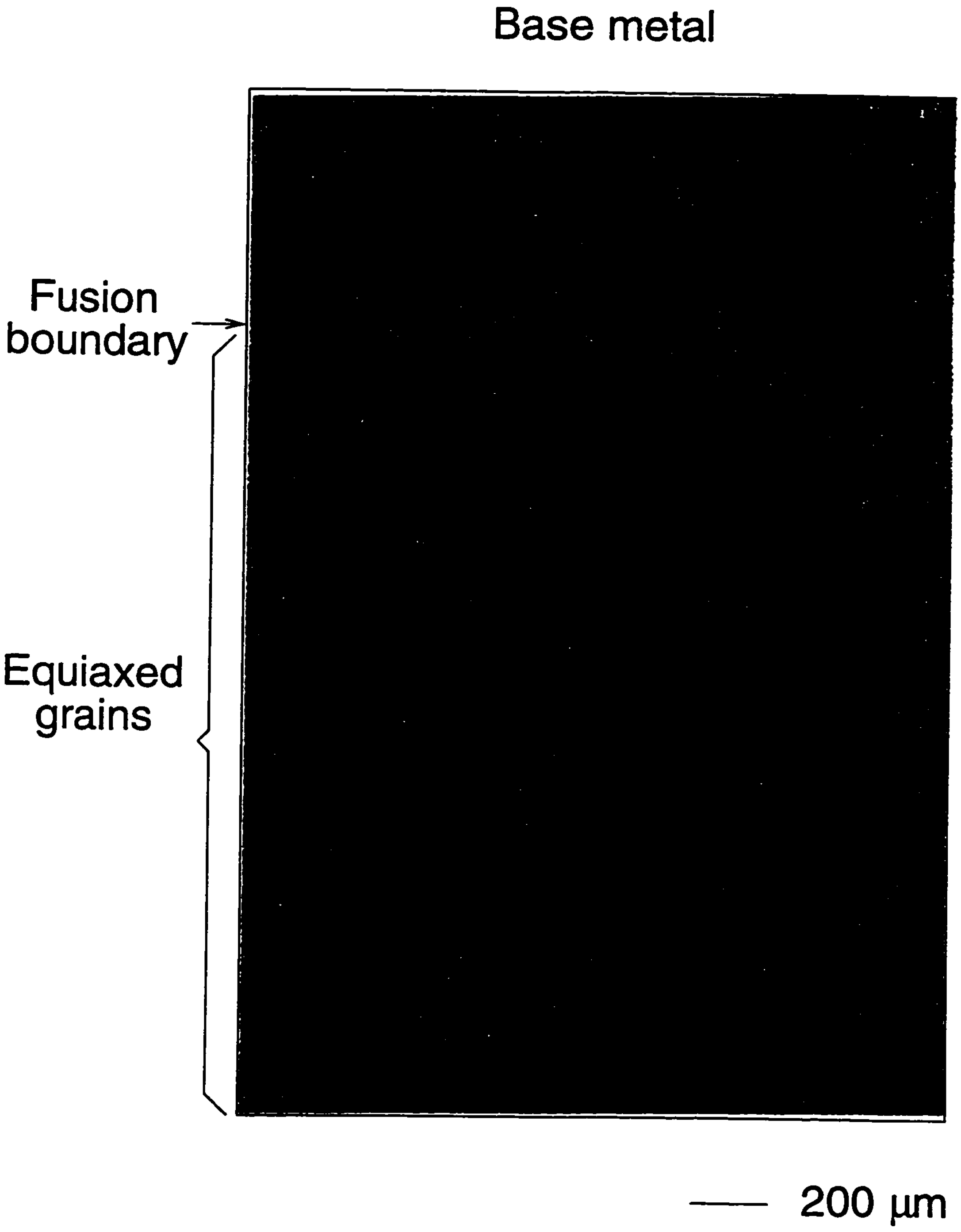

Figure 4.29: GTA welded specimen of Al-4%Cu inoculated with 0.026% Ti and exhibiting a fully equiaxed structure. Welding conditions: 160 A at 8 mm/s.

The experimental results indicated that a CET is strongly promoted by the following conditions:

- increasing the population density of heterogeneous nucleants, N_o; *i.e.*, increasing the wt% Ti,
- increasing the copper content, C_o ,
- welding with a high current-welding speed combination, and
- for a given current, welding at a lower speed.

4.5.4 Heterogeneous Nucleant Population Density

Since there is no known relationship between the wt% of an inoculant and the resultant population density of heterogeneous nucleants, values of N_o were determined metallographically from the experimental specimens. Standard metallographic techniques, as described previously, were used to determine the average equiaxed grain size for a given specimen from which the average grain volume was determined. It was assumed that each equiaxed grain developed by heterogeneous nucleation on a single TiB_2 particle, thus the nucleant population density was obtained by simply inverting the average grain volume. These values of N_o are reported in Table 4.21. The three conditions marked with '*' are specimens which exhibited either feathery crystals having very elongated structure or a CET with many stray equiaxed grains extending into the columnar zone, and were not included in the calculation of N_o since their structures rendered estimation of grain volume difficult.

Table 4.21: Heterogeneous nucleant population density.

Nominal Alloy Constituents		N_o (nucleants/mm^3)		
Cu (wt%)	Ti (wt%)	120 A, 4 mm/s	140 A, 6 mm/s	160 A, 8 mm/s
2	trace	0	0	0
2	0.003	*	*	819
2	0.015	9099	7164	8344
2	0.03	17 313	15 756	12 340
4	trace	0	0	0
4	0.003	*	1958	3325
4	0.013	11 004	6686	7194
4	0.026	19 007	13 071	14 188

* Denotes conditions for which equiaxed grain size could not be determined.

Figure 4.30 is a plot of the measured values of N_o versus wt% Ti reported in Table 4.21. As seen in the figure, the values of N_o have an approximately linear relationship with respect to wt% Ti. In addition, the values of N_o appear, in general, to be independent of welding conditions and Cu content. Thus, for the purpose of comparing the experimental results with the modelling predictions, average values of N_o according to nominal titanium content were used, as indicated in Figure 4.30 and listed in Table 4.22.

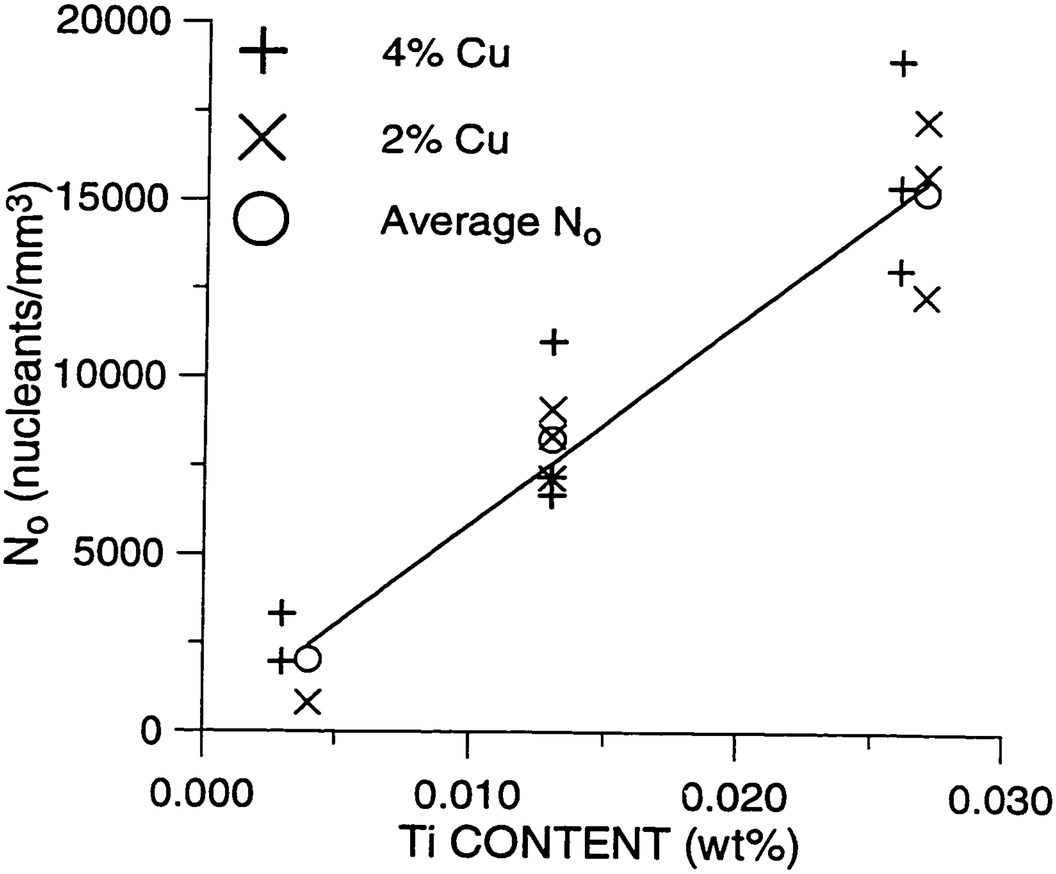

Figure 4.30: Measured values of N_o versus wt% Ti.

Table 4.22: Average heterogeneous nucleant population density.

Nominal Ti (wt%)	N_o (nucleants/mm^3)
Trace	0
0.003	2034
0.015	8249
0.03	15 279

4.6 Comparison of Experimental Measurements with Modelling Predictions

For comparison with the modelling results, the numerical predictions of G_L and R for each set of welding process conditions are plotted versus the CET model in Figures 4.31 through 4.34. The CET model curves were calculated using the average values of N_o determined from the experimental specimens (Table 4.22) and assuming $\Delta T_N = 0.75$ K. As described in a previous section, the expected % equiaxed were determined from the intersections of the predicted G_L and R curve with the CET model. These predicted % equiaxed values are reported in Table 4.23 and compared to the experimentally measured values. Experimental specimens which are listed in Table 4.23 as having 0% equiaxed produced a feathery crystal structure, similar to those shown previously in Figures 4.23 through 4.25. It should also be noted that no attempt was made to predict a CET for the alloys containing only a trace amount of TiB_2 since $N_o = 0$ which would give $G_L < 0$ in the CET model (Equation 1.16).

The results presented in Table 4.23 indicate that the CET model was able to correctly predict the general trends, as follows:

- The model was usually able to predict whether or not a CET would occur.
- No CET is produced at low current-welding speed combinations when TiB_2 levels are low.
- The % equiaxed grains in the weld bead increases with increasing TiB_2 content.
- The % equiaxed in the weld bead is greater for the alloy containing 4% Cu compared to that containing 2% Cu; *i.e.*, the % equiaxed increases with increasing Cu content.
- The % equiaxed is greater for welds performed with higher current-welding speed combinations.
- For a given current, the % equiaxed is greater with lower welding speed.

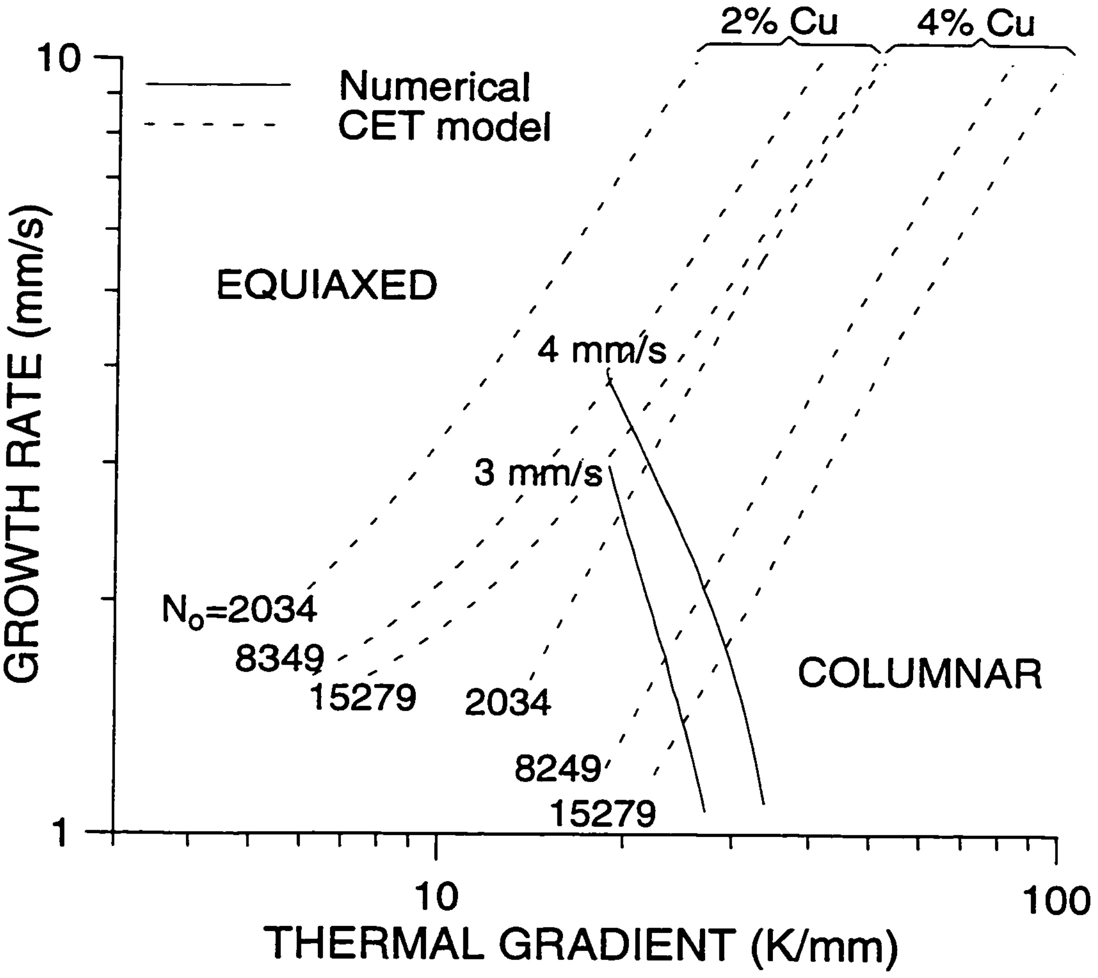

Figure 4.31: Predicted R versus G_L compared with the CET model. Welding current: 100 A; $\Delta T_N = 0.75$ K; N_o in nucleants/mm^3.

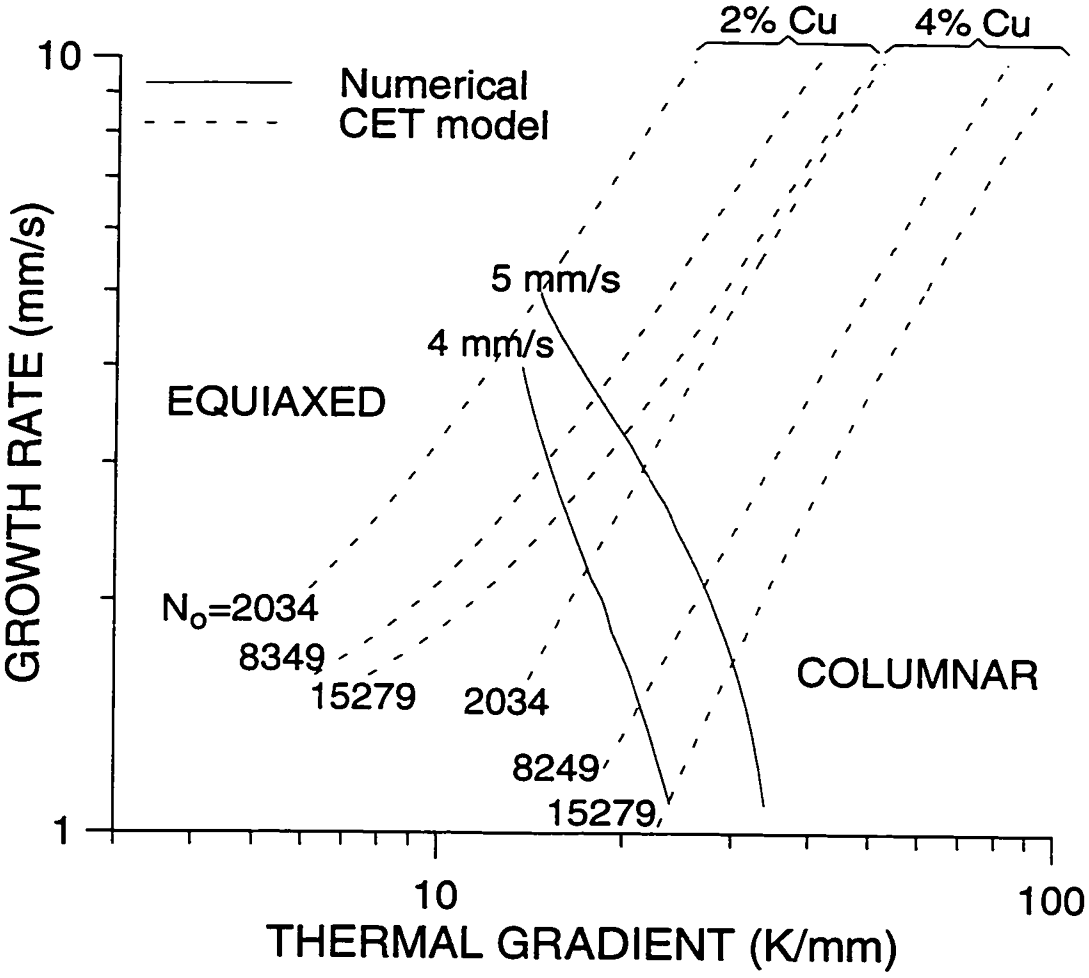

Figure 4.32: Predicted R versus G_L compared with the CET model. Welding current: 120 A; $\Delta T_N = 0.75$ K; N_o in nucleants/mm^3.

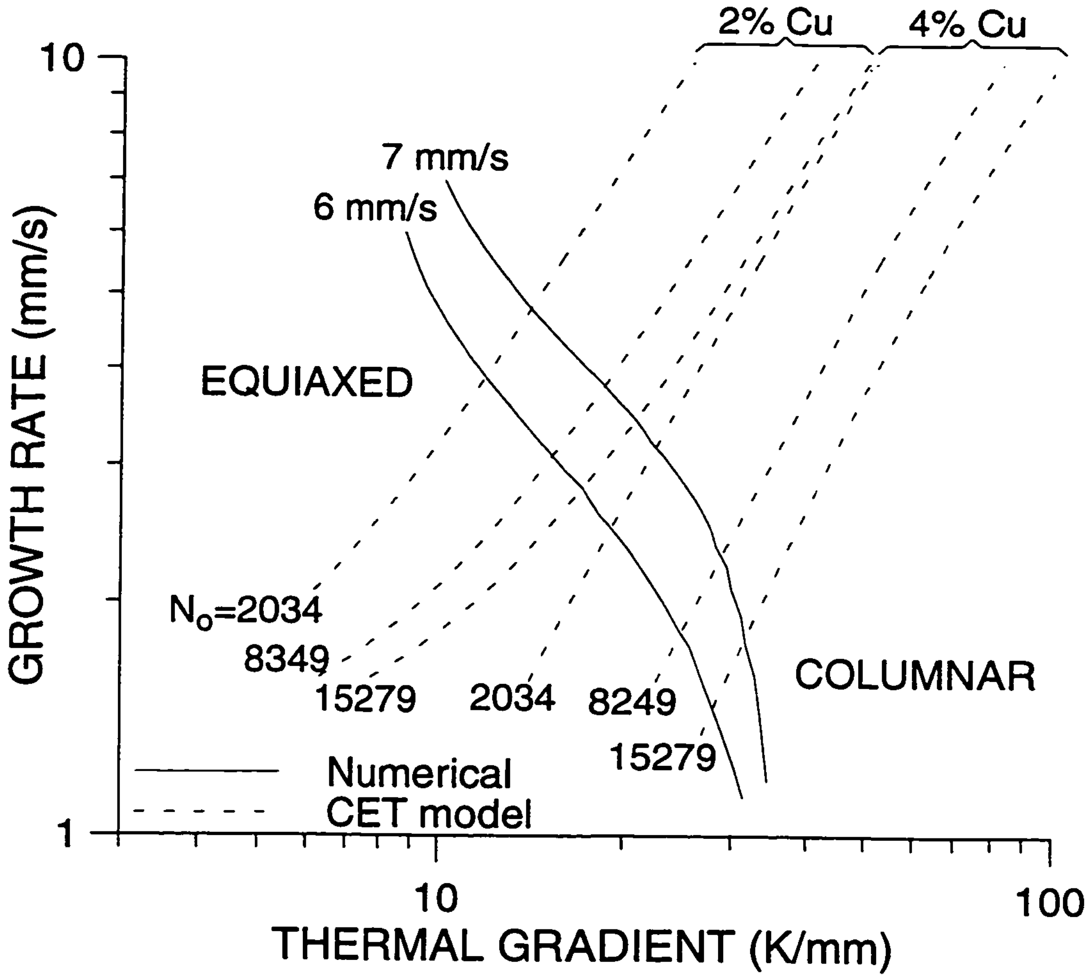

Figure 4.33: Predicted R versus G_L compared with the CET model. Welding current: 140 A; $\Delta T_N = 0.75$ K; N_o in nucleants/mm^3.

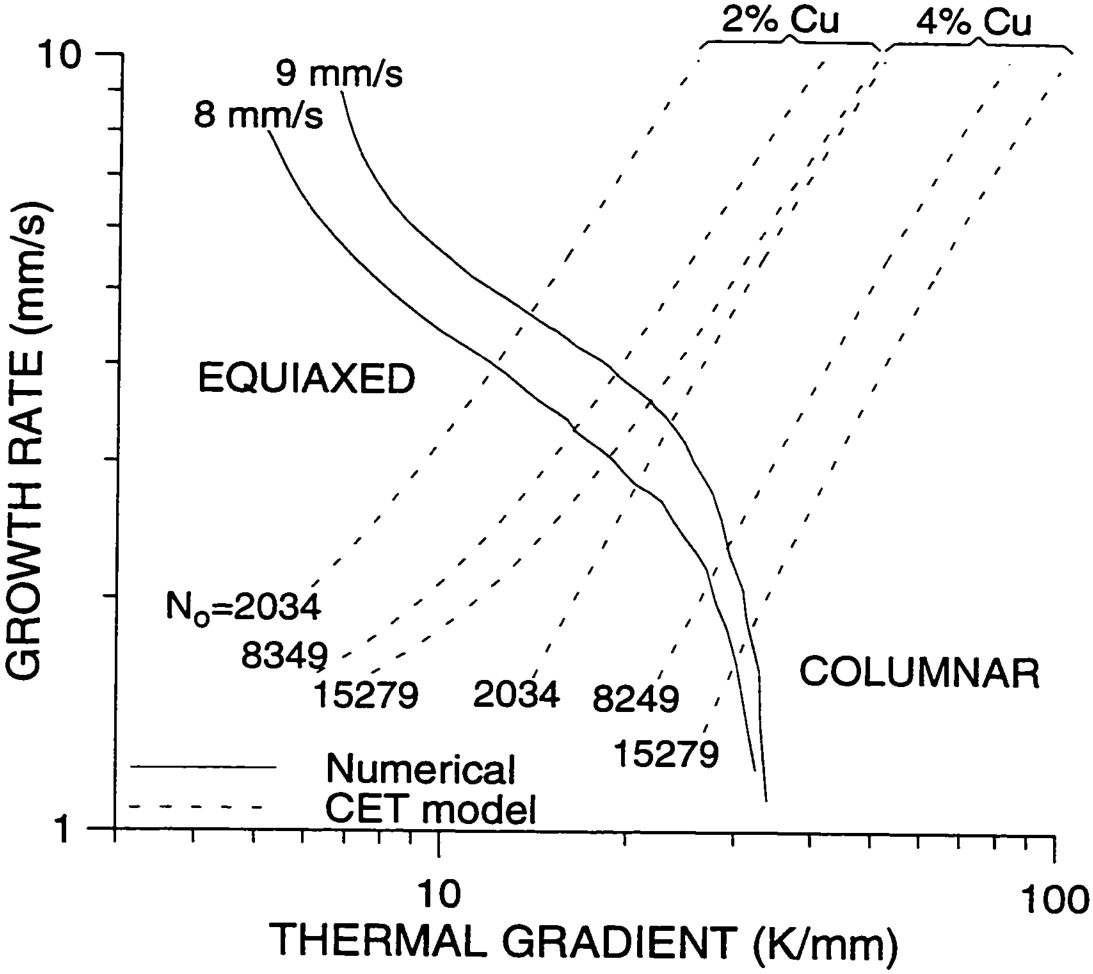

Figure 4.34: Predicted R versus G_L compared with the CET model. Welding current: 160 A; $\Delta T_N = 0.75$ K; N_o in nucleants/mm^3.

Table 4.23: Experimental and predicted % equiaxed.
(% difference with respect to experimental value.)

Ti	Welding Conditions		% Equiaxed for 2% Cu			% Equiaxed for 4% Cu		
(wt%)	I (A)	v_{ws} (mm/s)	Exp	Num	% Diff	Exp	Num	% Diff
0.003-4	100	3	0	0	0	0	44	100
		4	0	0	0	0	54	100
	120	4	0	0	0	49	69	41
		5	0	0	0	41	66	61
	140	6	29	46	59	51	76	49
		7	23	45	96	43	75	74
	160	8	37	59	59	46	80	74
		9	26	56	115	49	78	59
0.013	100	3	0	0	0	75	72	-4
		4	0	0	0	0	80	100
	120	4	49	48	-2	80	97	21
		5	35	48	37	77	83	8
	140	6	56	65	16	80	88	10
		7	39	62	59	68	88	29
	160	8	56	74	32	76	92	21
		9	47	70	49	70	92	31
0.026-7	100	3	100	0	-100	100	90	-10
		4	100	42	-58	100	98	- 2
	120	4	100	64	-36	100	100	0
		5	100	63	-37	100	99	-1
	140	6	100	72	-28	100	99	-1
		7	100	72	-28	100	99	-1
	160	8	100	76	-24	100	98	-2
		9	100	72	-28	100	96	-4

When a CET did occur, the model was able to predict the % equiaxed within approximately 50% and frequently within 30%. The agreement is somewhat better for the 4% copper compared to the 2% copper, which might be expected since the numerical thermofluids model incorporated the material properties for Al-4.5%Cu. The agreement between the predicted and measured % equiaxed is excellent (within 10% difference) for the specimens containing 4% copper and the high level of TiB_2.

The CET model was able to correctly predict general trends with respect to the effect of welding conditions, copper content, and wt% inoculants on the CET; however, the numerical agreement between predicted and experimental % equiaxed values was sometimes only moderate. In general, the model overestimated the % equiaxed at the low TiB_2 level, somewhat overestimated the % equiaxed at the intermediate TiB_2 level, and underestimated the % equiaxed at the highest TiB_2 level for the 2% copper content.

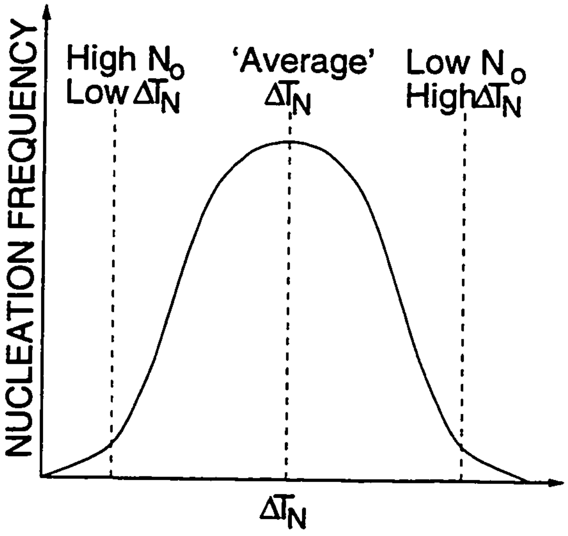

Figure 4.35: Schematic of nucleation frequency versus nucleation undercooling.

There are probably several factors contributing to these discrepancies between the predicted and measured values. Let us address first the issue of the model overpredicting at lower TiB_2 levels and underpredicting at high levels. This is possibly due to a saturation of the heterogeneous nucleants at the high TiB_2 level: at low and intermediate levels, all or almost all the potential nucleants are used in nucleating equiaxed grains; however, at high levels, a number of the nucleants are redundant and do not participate in the nucleation event [124]. Furthermore, in the present study, the nucleation undercooling was assumed to be a constant 0.75 K; however, ΔT_N may be distributed [29], as shown schematically in Figure 4.35. This would imply that, statistically, some nucleants will nucleate at a very low ΔT_N and some at a higher ΔT_N, so that a constant assumed value actually represents an 'average' nucleation undercooling. If such is the case, then when N_o is low, all the inoculant particles may be required to participate in the nucleation event to produce a CET and the 'effective' nucleation undercooling will actually appear to be greater than the assumed constant value of 0.75 K. Alternatively, in a saturated situation in which N_o is high, only the most efficient nucleants, *i.e.*, the ones with the lowest ΔT_N's, will actually nucleate sufficient equiaxed grains to produce a CET and the more inefficient nucleants will be redundant. The result will be that at levels of TiB_2 in which saturation occurs, the 'effective' nucleation undercooling will appear less than the assumed constant value of 0.75 K. In the context of the CET model employed in the present work to predict the % equiaxed, a lower effective ΔT_N value would increase the predicted % equiaxed at the high TiB_2 level and thus improve the model's predictions (*cf.* Figures 4.18 and 4.19). Alternatively, increasingly higher effective values of ΔT_N would decrease the predicted % equiaxed and improve the predictions for the intermediate and low levels of TiB_2, respectively (once again, *cf.* Figures 4.18 and 4.19). Furthermore, there is much controversy in the literature surrounding values of ΔT_N and, indeed, the exact mechanism of heterogeneous nucleation on TiB_2 particles is still not fully understood [124]. Thus, the selection of $\Delta T_N = 0.75$ K may have introduced error into the predictions, particularly since ΔT_N is cubed in the CET model (*cf.* Equation 1.16). In addition, the fact that copper may in some way operate in the nucleation event cannot be discounted and may also explain the difference in error for the 2% Cu alloys versus the 4%.

The assumption of constant ΔT_N only explains a limited portion of the discrepancy between the predicted and experimental values: a lower 'effective' ΔT_N would certainly improve the predictions for the high TiB_2 levels. However, unrealistically large values of ΔT_N would be needed to entirely eliminate the discrepancy between the predicted and experimental values at the intermediate and low levels of TiB_2. For example, for the alloy containing 4 wt% Cu and 0.013 wt% Ti, welded with 160 A at 9 mm/s, a nucleation undercooling of ≈ 2.8 K would be required in the CET model to obtain correlation between the predicted and experimental % equiaxed, compared to $\Delta T_N = 0.75$ K used in the present study (selected based on Hunt's work [1]). Thus, other factors must have been operational in introducing error. It is helpful, therefore, to examine the validity of another assumption made in developing the CET model: that the latent heat of fusion evolved during the solidification of equiaxed grains was assumed to have a negligible effect on the local thermal gradient. This assumption is not unreasonable since high diffusivity metals like aluminum alloys should be able to quickly conduct away the evolved heat into the liquid. Indeed, other researchers [15, 16, 17, 123] have made this same assumption in their CET models. However, since the number of nucleants was relatively large, it was possible that the latent heat of fusion from all of the equiaxed grains together would actually make a significant contribution and have increased the thermal gradient in the liquid ahead of the solid/liquid interface.

Let us now examine the potential effect of increasing G_L on the CET predictions. As shown in Figure 4.36, increasing the predicted values of G_L will result in a shift of the predicted $\log(R)$-$\log(G_L)$ curve from its original position such that less of the predicted $\log(R)$-$\log(G_L)$ curve will reside in the equiaxed zone. This effect will lower the predicted % equiaxed value for a given solidification condition. Such a result would potentially improve the agreement between the predicted and experimentally measured values of % equiaxed grains, particularly at the low and intermediate TiB_2 levels.

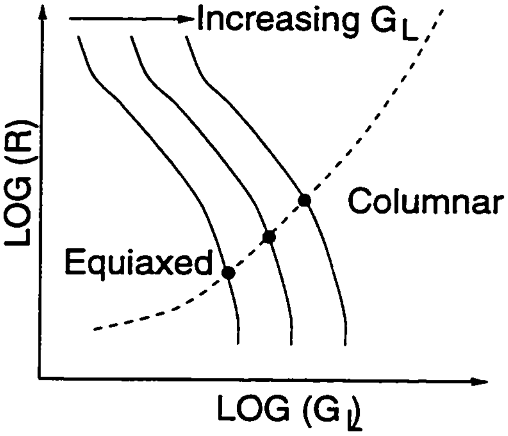

Figure 4.36: Schematic of the effect of increasing G_L on the CET.

To examine whether the equiaxed grains evolve a significant amount of latent heat of fusion and thereby influence G_L, the numerical thermofluids model was employed to perform a simple one-dimensional advection-diffusion simulation. This simulation was designed to represent a volume of liquid between the solid/liquid interface and the nucleation interface, as indicated in Figure 4.37, at the tail of the weld pool for welding conditions 160 A at 9 mm/s. The solution domain and boundary conditions for this simple study are also represented schematically in Figure 4.37. To simulate the solid, a constant temperature equaling the equilibrium liquidus temperature less the growth

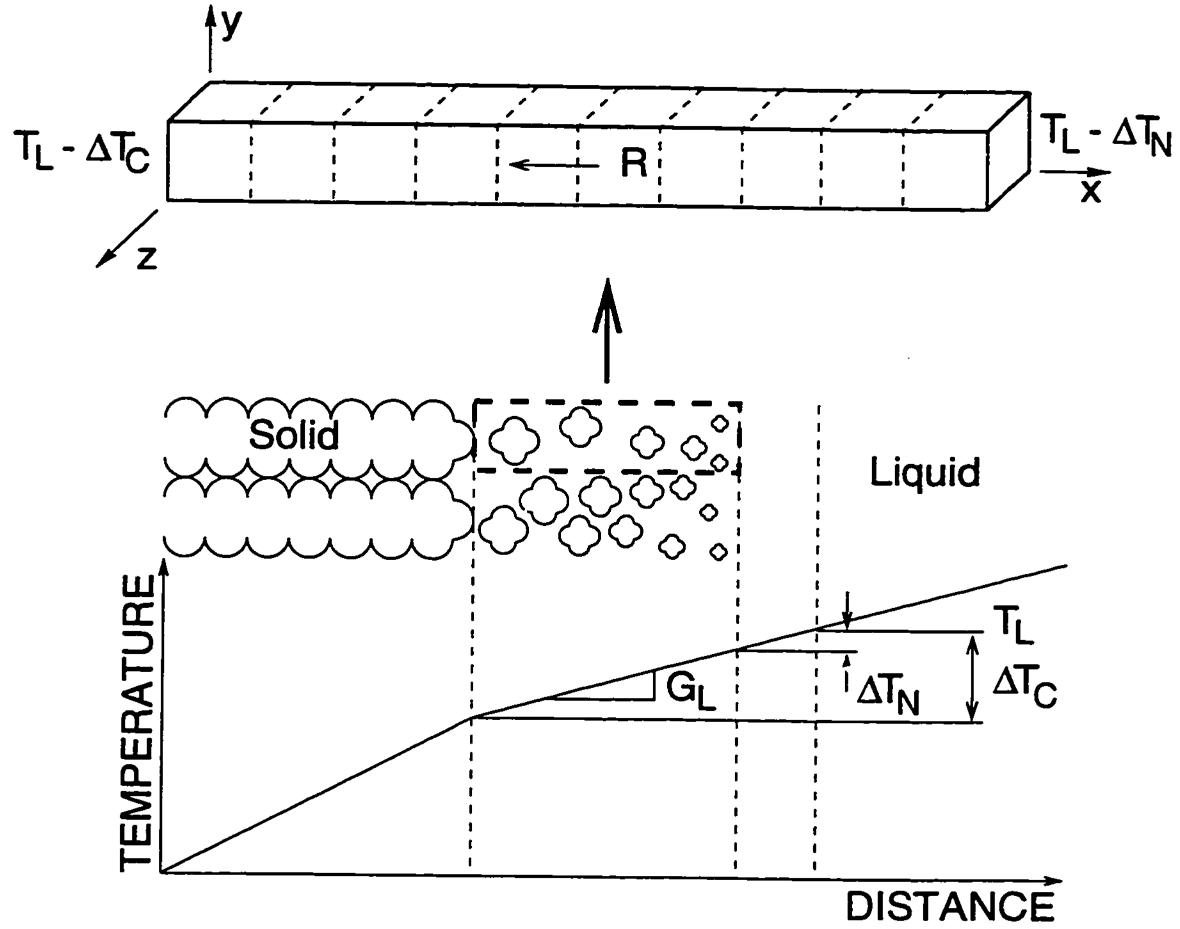

Figure 4.37: Schematic of solution domain and boundary conditions for heat conduction simulation of the undercooled zone.

undercooling, $T_L - \Delta T_C = 914.9$ K, was imposed on the solid/liquid interface boundary. The value for ΔT_C was obtained from the post-processed results for the thermofluids simulation with welding conditions 160 A at 9 mm/s. A constant temperature equaling the equilibrium liquidus temperature less the nucleation undercooling, $T_L - \Delta T_N =$ 920.25 K, was imposed on the boundary corresponding to the nucleation interface (*i.e.*, ΔT_N isotherm). While it was recognized that the length of the solution domain would be affected by the evolution of latent heat, for the purpose of this simplified analysis, the length of the solution domain was fixed and selected to give an initial thermal gradient ahead of the solid/liquid interface the same as that at the tail of the weld pool for the thermofluids simulation with welding conditions 160 A at 9 mm/s. Adiabatic conditions were imposed on all other boundaries. The material properties were assumed to vary with temperature as in all the thermofluids simulations. Fluid flow was assumed to be negligible, which is reasonable since the undercooled zone is in the mushy zone where the fluid flow is limited. The latent heat of fusion, ΔH_f, evolved by the growing equiaxed grains was modelled as a volumetric heat source through modification of the specific heat in the same manner as described in Section 2.2 for the treatment of latent heat of fusion in the mushy zone using the Scheil equation [103].

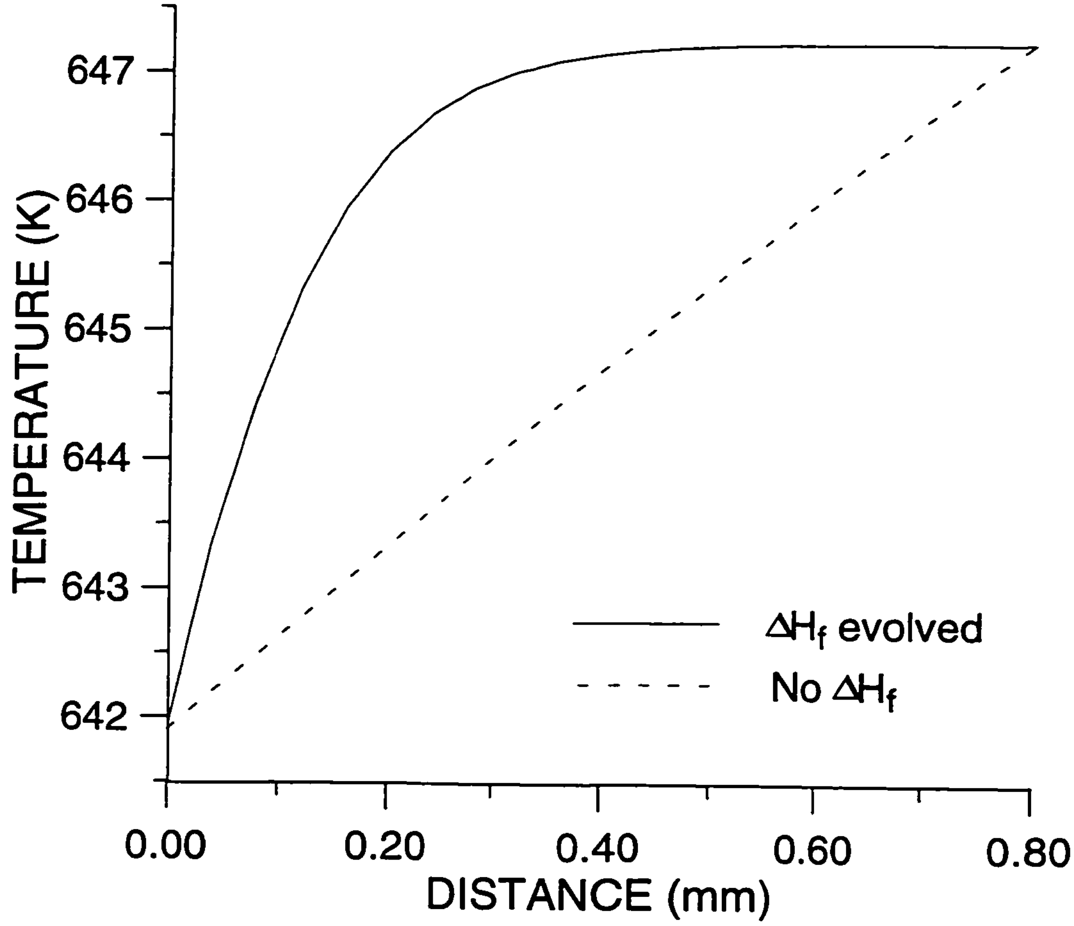

Figure 4.38: Temperature versus distance for simulations with and without latent heat of fusion evolution by equiaxed grains. Welding conditions: 160 A at 9 mm/s.

Figure 4.38 is a plot of temperature versus distance for simulations with and without the incorporation of latent heat of fusion evolution by equiaxed grains. As seen in the figure, the latent heat of fusion evolved by the equiaxed grains contributes a significant amount of heat to the system. The heat contribution from the equiaxed grains was sufficient to increase the thermal gradient local to the solid/liquid interface at the tail of the weld pool from 6.7 K/mm to 32.0 K/mm. Since this one-dimensional advection-diffusion problem was simplified in order to be tractable (*e.g.*, the length of the domain was fixed), accurate quantitative estimates cannot be expected; however, the analysis confirms the hypothesis that the latent heat evolved by equiaxed grains is not negligible. It should be noted, however, that this heat of fusion effect will only be operative when there are, indeed, conditions which produce a CET. Of course, if no equiaxed grains are solidifying, then no heat of fusion is evolved. This effect explains why the model is adept at predicting whether or not a CET is produced and may partially account for the quantitative error between predicted and experimental values of % equiaxed.

A second ramification of the latent heat evolved by the equiaxed grains is that this heat increases the local temperature which, in turn, reduces the undercooling of the equiaxed grains. With less undercooling, the equiaxed grains will grow more slowly and will not reach as large a size, and consequently will not produce as large a % equiaxed as predicted by the CET model. The magnitude of this effect can be estimated by comparing the predicted final radius of equiaxed grains growing with the original undercooling (*i.e.*, that corresponding to the 'No ΔH_f' curve in Figure 4.38) and those growing with the new undercooling (*i.e.*, that corresponding to the 'ΔH_f evolved' curve in Figure 4.38). Following Hunt's [1] arguments, after a time t, a spherical equiaxed grain growing in the undercooled zone will reach a radius

$$r = \int_0^t R_e dt \tag{4.5}$$

Where R_e is the growth rate of the equiaxed grain. For simplicity, and since we are limited to a qualitative assessment only, Hunt's [1] growth model was used; *i.e.*

$$R_e = \frac{A(\Delta T_C)^2}{C_o} \tag{4.6}$$

where $A = 300\ \mu\mathrm{ms}^{-1}\mathrm{wt}\%^{-1}\mathrm{K}^2$. Substituting Equation 4.6 for R_e in Equation 4.5 and changing the limits of integration gives

$$r = \int_0^{x_{uc}} \frac{A(\Delta T)^2}{v_{ws} C_o} dx \tag{4.7}$$

where $x_{uc} = 0.8$ mm is the length of the undercooled zone and $v_{ws} = 9$ mm/s. The radius of the equiaxed grain can now be estimated through numerical integration of Equation 4.7 and assuming the predicted values of undercooling given in Figure 4.38. For the case in which the latent heat of fusion evolved by the equiaxed grains was ignored $r = 54$ μm. Incorporating the latent heat of fusion gives $r = 13$ μm. Thus, when the effect of latent heat of fusion is included, the equiaxed grains will not reach as large a size, and consequently as large a % equiaxed, as predicted by the CET model. This effect may also have contributed to the quantitative error between predicted and experimental values of % equiaxed.

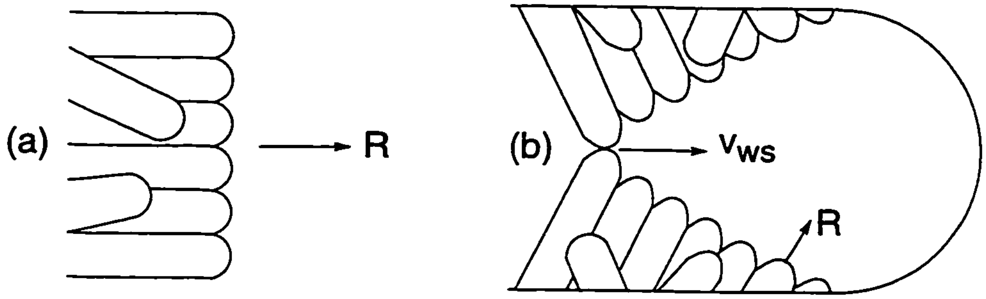

Figure 4.39: Schematic of the solidification of a casting compared to that of a weld.

It is worthwhile, at this point, to also examine whether the geometry of the weld pool has any influence on the CET predictions. Hunt's model [1] was developed for directional solidification of a casting, in which the growth of the solid/liquid interface proceeds unidirectionally, as indicated in Figure 4.39(a). The GTA weld pool, however, has a curved geometry, as indicated in Figure 4.39(b). At the tail of the weld pool, the solidification proceeds forward at a growth rate, $R = v_{ws}$; however, along the perimeter, the growth rate (as discussed earlier) varies as $R = v_{ws} \cos\theta$. In addition, in the CET model, the equiaxed grains are assumed to follow the same growth rate dependence on undercooling as the columnar grains. As indicated in Figure 4.40(a), as the weld pool proceeds forward, the equiaxed grains that are at the tail of the pool grow while the solid/liquid interface approaches them at a rate $R = v_{ws}$, similar to a casting. As we proceed around the perimeter of the weld pool, the growth rate of the equiaxed and

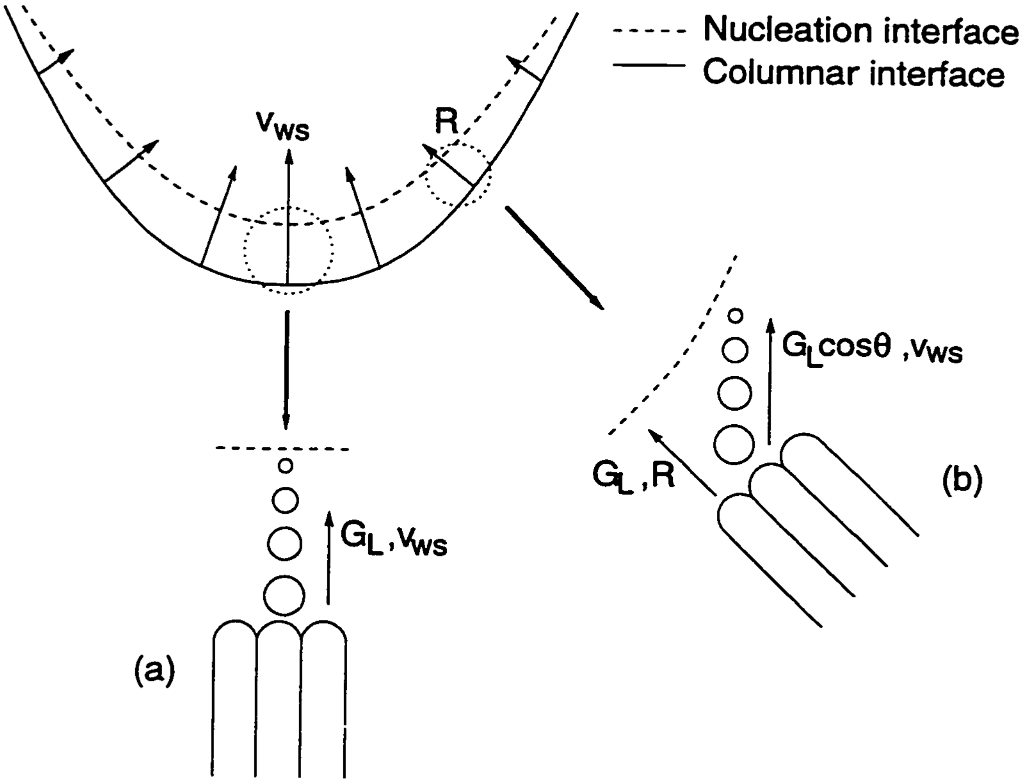

Figure 4.40: Schematic of the thermal gradient and rate of approach of the solid/liquid interface towards an equiaxed grain at (a) the tail of the weld pool, and (b) a distance around the perimeter.

columnar grains is $R = v_{ws} \cos\theta$. However, since the weld pool is travelling forward at a velocity, v_{ws}, the solid/liquid interface actually approaches the equiaxed grains at v_{ws} which is faster than R, as indicated in Figure 3.40(b). This implies that the equiaxed grains have less time to grow than is accounted for in the CET model. However, the thermal gradient which determines the time available for growth of these equiaxed grains, (parallel to the welding direction) is not the same as G_L influencing the columnar front (which is perpendicular to the solid/liquid interface). Instead, the thermal gradient influencing the time for equiaxed growth is equivalent to $G_L \cos\theta$, and extends over a longer distance (as indicated in Figure 4.40(b)). Thus, the equiaxed grains will have a larger distance within which to grow. We can evaluate the relative influence of these two geometry effects by incorporating these values in the CET model. Recall that in Hunt's derivation [1], the radius of the equiaxed grains is

$$r = \int_{\Delta T_N}^{\Delta T_C} \frac{A(\Delta T)^2}{R G_L C_o} d(\Delta T) \tag{4.8}$$

However, for the equiaxed grains in the weld pool, the G_L term becomes $G_L \cos\theta$ and R becomes v_{ws} which is actually equivalent to $R/\cos\theta$; thus,

$$r = \int_{\Delta T_N}^{\Delta T_C} \frac{A(\Delta T)^2}{\frac{R}{\cos\theta} G_L \cos\theta C_o} d(\Delta T) \tag{4.9}$$

Since both '$\cos\theta$' terms cancel, we have an equivalent situation to the original casting model. Thus, although the geometry of the weld pool does introduce two effects on the equiaxed grain growth, these effects cancel out each other.

To summarize, then, the CET model was able to correctly predict whether or not a CET would occur. When a CET was predicted, the model was able to correctly predict general trends with respect to the effect of welding process conditions, alloy content, and wt% inoculants. However, there was only moderate quantitative agreement between the predicted values of % equiaxed in the weld bead and the experimental measurements. The discrepancies between the observed and predicted % equiaxed were possibly due to two factors: (i) the assumption of a constant value for ΔT_N, (ii) the assumption that the latent heat of fusion evolved by the growing equiaxed grains was conducted away and did not influence the thermal conditions in the weld pool. A more judicious selection of ΔT_N, or the incorporation of a distributed ΔT_N which could account for the kinetics of heterogeneous nucleation and the saturation of nucleants at high wt% inoculants, would have lessened both the underprediction of % equiaxed at the high TiB_2 level and the overprediction of % equiaxed at the low and intermediate TiB_2 levels. In addition, as seen in the simple one-dimensional heat conduction study, the latent heat evolved by the growing equiaxed grains may increase the thermal gradient seen by the advancing columnar front and also reduce the growth undercooling of the equiaxed grains. These effects would both decrease the % equiaxed predicted by the CET model and improve the accord with the experimental results.

Chapter 5

CLOSURE

A columnar-to-equiaxed grain transition (CET) in gas tungsten arc (GTA) welds may reduce susceptibility to solidification cracking and brittle fracture and improve weld properties, such as toughness, ductility, and strength. A CET may be promoted in the weld pool by providing both (i) a supply of embryos from which equiaxed grains may develop and (ii) thermal conditions which favour the nucleation and growth of these embryos into equiaxed grains. However, the relationship between solidification and thermal conditions in the weld pool and process parameters which are controllable during welding is not well understood.

The objective of the present work was to examine the relationships between controllable welding process parameters and weld pool thermal conditions, in order to better understand and predict the CET in full-penetration moving GTA welds. To this end, the research comprised three major components:

- modelling the macroscopic thermofluids behaviour in the bulk weld pool,
- modelling the main aspects of growth at the weld pool solid-liquid interface, and
- comparing the predictions of the macroscopic and microscopic models with experimental observations.

Since it is experimentally difficult to control and characterize the thermal conditions in a moving weld pool, numerical simulations of the macroscopic heat and fluid flow behaviour in the full-penetration GTA weld pool were made using a detailed thermofluids model. This finite element model was formulated for three-dimensional, steady-state, moving GTA welds. The model incorporated temperature-dependent material properties, latent heat of fusion, Gaussian-distributed arc heat and current inputs, plus heat losses due to convection and radiation. Turbulent fluid flow driven by buoyancy, electromagnetic forces, and surface tension temperature gradient forces was also modelled. The model was then used to simulate moving, full-penetration GTA welds on thin sheets of binary aluminum-copper alloys using an experimentally realistic range of welding currents and steady-state welding speeds. Results from the numerical thermofluids simulations were post-processed to obtain estimates of weld pool thermal and solidification parameters, such as thermal gradient in the liquid and local solid/liquid interface growth rate, and thus predict the influence of welding process parameters on weld pool thermal conditions in Al-Cu alloys. An analytical model was then invoked to predict the CET based on the thermal conditions in the weld pool as predicted by the numerical thermofluids model. The analytical CET model was based on Hunt's expression for the CET [1], but was modified to accommodate the higher solidification rates encountered in welding by incorporating the marginal stability dendrite growth model developed by Kurz *et al.* [2, 3] to predict the growth undercooling of the columnar grain front.

A complementary experimental program was performed for validation of the model's predictions. Experiments were executed using autogenous, alternating-current GTA welding for a range of welding currents and steady-state welding speeds. Full-penetration welds were produced on thin plates to ensure two-dimensional heat flow and thus facilitate microstructural interpretation. Binary aluminum-copper alloys were selected as a model solidification system since this alloy system is well-characterized with respect to material properties and is also particularly susceptible to solidification cracking. The experimental alloys nominally contained 2 and 4% copper and were inoculated with varying amounts of TiB_2 particles to act as heterogeneous nucleating agents for equiaxed grains. Measurements were made of % equiaxed grains in the weld bead and compared to the CET predictions made using the coupled thermofluids and analytical CET models.

5.1 Innovations of the Thesis

The major innovation of the present work was twofold: (i) the development of a thermofluids model for GTA welding and (ii) the coupling of this numerical thermofluids model with an analytical model for the CET.

The specific innovations of this study are as follows:

- A finite element thermofluids model for moving GTA welds was developed in this study. Using this model, various physical phenomena in the weld pool were studied, including thermal and turbulent fluid flow behaviour.
- A unique dynamic mesh remapping algorithm was incorporated in the numerical model. This technique not only facilitated the treatment of latent heat of fusion evolution in the mushy zone, but also enabled accurate geometric representation of the weld pool which, in turn, provided accurate estimates of the thermal gradients in the weld pool at the solid/liquid interface which are so important for CET promotion. In addition, by employing this dynamic mesh remapping routine, the flow fluid equations were required to be solved only in the liquid weld pool, and thus the simulations are far less computationally intensive.
- An algebraic vorticity-based turbulence model was employed to predict turbulent fluid flow in the weld pool. This model offers the advantage of low computational complexity compared to the $K-\epsilon$ turbulence model, particularly in this three-dimensional formulation.
- The model is capable of predicting the effects of changing welding process parameters on the thermal conditions in the weld pool from which weld pool thermal and solidification parameters, such as thermal gradient, interface growth rate, and growth undercooling, can be estimated. Thus, the influence of welding process parameters on weld pool thermal conditions in Al-Cu alloys can be ascertained.
- An analytical model for the CET was developed. This model was based on a CET model derived by Hunt [1] for casting, but was modified to render it more applicable

to welding. In particular, the CET model (i) incorporated the variation of growth rate around the perimeter of the weld pool, and (ii) employed a marginal stability expression developed by Kurz *et al.* [2, 3] to predict the growth undercooling of the columnar front, which is more applicable to the higher growth rates found in welding compared to casting. The analytical model was employed to predict the CET based on the thermal conditions as predicted by the numerical model. Although the technique of coupling macroscopic models with microstructure models is not new, until now this technique had never been employed specifically to study the CET in moving GTA welds.

5.2 Summary of Findings

The findings from this study are summarized as follows:

- The numerical thermofluids model for GTA welding successfully predicted weld widths in aluminum-copper alloys for a range of realistic welding conditions.
- The numerical thermofluids model demonstrated excellent agreement with experiments in comparisons of predicted values with thermocouple measurements of peak temperatures and centreline temperature profiles.
- The numerical thermofluids model predicted that in aluminum-copper alloys, the average turbulent Reynolds numbers in the weld pool were approximately 100 and maximum turbulent Reynolds numbers exceeded 200. This suggests that the weld pool fluid flow is fully turbulent for GTA welds in aluminum-copper alloys.
- The numerical thermofluids model predicted that thermal conditions which favour the CET, namely low thermal gradients in the liquid and high solid/liquid interface growth rates, occur first at the tail of the weld pool.
- Further, the thermofluids model predicted that the welding conditions which produce low thermal gradients and high interface growth rates, and thus favour a CET, are (i) for a given current, decreasing welding speed, or (ii) a high current and welding speed combination.
- Application of the analytical CET model to the weld pool thermal conditions as predicted by the numerical thermofluids model permitted the prediction of % equiaxed grains in the weld bead. The CET model predicted that a large population density of heterogeneous nucleants having low nucleation undercooling will promote a CET for any of the welding conditions simulated in the study.
- Further, the CET model predicted that when the nucleants are inefficient or their numbers are low, the welding conditions become increasingly important for CET promotion.

- The experimental results indicated that a CET is favoured in GTA welds in Al-Cu alloys by (i) for a given current, decreasing welding speed, (ii) a high current and welding speed combination, (iii) increasing copper content, and (iv) increasing the wt% of the nucleating agent for equiaxed grains.
- In comparison with experiment, the CET model was able to correctly predict whether or not a CET would occur as a function of weld process parameters, alloy composition, and heterogeneous nucleant population density.
- When a CET was predicted to occur, the CET model was able to correctly predict the general trends, as follows:
  - The % equiaxed grains in the weld bead increases with increasing TiB_2 content.
  - The % equiaxed in the weld bead is greater for the alloy containing 4% Cu compared to that containing 2% Cu; *i.e.*, the % equiaxed increases with increasing Cu content.
  - The % equiaxed is greater for welds performed with higher current-welding speed combinations.
  - For a given current, the % equiaxed is greater with lower welding speed.
  - A fully columnar grain structure is produced at low current-welding speed combinations when TiB_2 levels are low.
- When a CET did occur, the CET model was able to predict the % equiaxed within approximately 50% and frequently within 30%. The agreement was somewhat better for the 4% copper compared to the 2% copper, possibly since the numerical thermofluids model incorporated the material properties for Al-4.5%Cu. The agreement between the predicted and measured % equiaxed was excellent (within 10% difference) for the specimens containing 4% copper and the high level of TiB_2.
- The numerical comparison of the predicted values of % equiaxed with the experimental measurements accorded moderately. The discrepancies between the observed and predicted % equiaxed were suggested to be due to two factors: (i) the

assumption of a constant value for ΔT_N and (ii) the assumption that the latent heat of fusion evolved by the growing equiaxed grains was conducted away and did not influence the thermal conditions in the weld pool. A more judicious selection of ΔT_N, or the incorporation of a distributed ΔT_N which could account for saturation of nucleants at high wt%, would have lessened both the underprediction of % equiaxed at the high TiB_2 level and the overprediction of % equiaxed at the low and intermediate TiB_2 levels. In addition, the results of a simple one-dimensional heat conduction study suggested that the latent heat evolved by the growing equiaxed grains may increase the thermal gradient at the solid/liquid interface and also reduce the growth undercooling of the equiaxed grains. These effects would decrease the % equiaxed predicted by the CET model and improve the accord with the experimental results.

5.3 Conclusions

Based on the findings in the present work, the following conclusion are proposed:

- The study revealed that the technique of coupling the predictions of a macroscopic thermofluids model with a microstructural model for the CET is an effective technique for the predictions of qualitative trends with respect to the CET as a function of GTA weld process parameters, alloy composition, and heterogeneous nucleant population density.
- Good correlation between experimental measurements of weld widths, peak temperatures, and temperature profiles and the numerical predictions was only possible when the effects of turbulent fluid flow were incorporated in the numerical model.
- The study demonstrated that a CET is favoured in GTA welds in Al-Cu alloys by (i) for a given current, decreasing welding speed, (ii) a high current and welding speed combination, (iii) increasing copper content, and (iv) increasing the wt% of the nucleating agent for equiaxed grains. Although a CET will be produced at all welding conditions in the presence of a large population density of heterogeneous nucleants, when the nucleants are inefficient or their numbers are low the welding conditions become increasingly important for CET promotion.
- Better agreement between the measured and predicted % equiaxed values would require (i) a more sophisticated CET model which is capable of accounting for a distributed nucleation undercooling, ΔT_N, and (ii) an iterative coupling between the macroscopic thermofluids model and the CET model to account for the synergistic relationship between the latent heat of fusion released by the equiaxed grains ahead of the columnar grain interface and the growth of these equiaxed grains as well as the thermal gradients in the weld pool.

5.4 Future Work

Areas of research which would constitute a natural extension to this study are

- An experimental GTA welding program incorporating extensive thermocouple measurements would be worthwhile for two reasons: (i) to ascertain the effect of latent heat of fusion evolution of inoculants on the thermal gradients at the solid/liquid interface and (ii) to evaluate predictions of growth undercooling of the columnar front. The former could be accomplished by performing careful thermocouple measurements on plates inoculated with varying amounts of TiB_2 and welded with the same process conditions. The latter could be accomplished by observing thermocouple traces: if the thermocouple data are acquired rapidly enough then a small point of inflection should reflect the location of the non-equilibrium solid/liquid interface. Comparisons between this temperature and the equilibrium liquidus temperature for the alloy would provide an estimate of the growth undercooling. These experiments would require extremely accurate and rapid thermocouple measurements and data acquisition.

- The study revealed that the technique of coupling of macroscopic thermofluids predictions with microstructure models is an effective technique for predicting the qualitative trends with respect to the occurrence of a CET; however, it does not accurately predict the % equiaxed once a CET has occurred. This may be because, in such a coupling, some aspects of the synergistic relationship between the solidification process and the thermofluids behaviour in the weld pool are not accounted for. In the present study for example, it was suggested that the latent heat of fusion evolved by the equiaxed grains may have influenced the thermal gradients at the weld pool interface; however, this latent heat contribution was not accounted for in the numerical model. It would be worthwhile in future work to combine the macro/micro models in an iterative scheme in which the effects of the solidification phenomena, such as equiaxed grain growth, could be incorporated in the numerical thermofluids model. Such a synergistic coupling may improve the quantitative agreement between predicted and measured % equiaxed in the present study and also offer the advantage of permitting the incorporation and examination of other solidification phenomena. For example, the dynamic mesh remapping routine could be invoked to map to the non-equilibrium solid/liquid interface.

- The numerical thermofluids model incorporated the thermophysical properties for Al-4.5%Cu, which is a high-conductivity material. A worthwhile endeavour would be to incorporate the material properties for other materials, in particular a lower-conductivity metal such as stainless steel. A comparative study of weld pool thermofluids behaviour, and its implications with respect to the CET, in high- versus low-conductivity metals would be of interest.
- The welding power supply used in the present study was operated in alternating-current mode with an AC frequency of 60 Hz and a duty cycle of 80%. Although the effects of changing welding current and welding speed on the CET were evaluated in the present study, it would also be of value to assess the effects, if any, of changing AC frequency and duty cycle on the CET. These quantities are known to have an effect on the distribution of the arc, and therefore may also influence the thermal gradients in the weld pool and affect CET promotion.

BIBLIOGRAPHY

[1] J.D. Hunt, "Steady State Columnar and Equiaxed Growth of Dendrites and Eutectic", *Materials Science and Engineering*, Vol. 65, 1984, 75-83.

[2] W. Kurz and D.J. Fisher, "Dendrite Growth at the Limit of Stability: Tip Radius and Spacing", *Acta Metallurgica*, Vol. 29, 1981, 11-20.

[3] W. Kurz, B. Giovanola, and R. Trivedi, "Theory of Microstructural Development During Rapid Solidification", *Acta Metallurgica*, Vol. 34, No. 5, 1986, 823-830.

[4] G.E. Linnert, *Welding Metallurgy*, American Welding Society, New York, 1965.

[5] K. Easterling, *Introduction to the Physical Metallurgy of Welding*, Second Edition, Butterworth-Heinemann, Oxford, 1992.

[6] G.J. Davies and J.G Garland, "Solidification Structures and Properties of Fusion Welds", *International Metallurgical Reviews*, Vol. 20, 1975, 83-106.

[7] S.A. David and J.M. Vitek, "Correlation Between Solidification Parameters and Weld Microstructures", *International Materials Reviews*, Vol. 34, No. 5, 1989, 213-245.

[8] H.W. Kerr, "Solidification and Grain Structures in Welds", *Trends in Welding Research*, S.A. David and J.M Vitek, Editors, ASM International, Metals Park, OH, 1992, 157-166.

[9] W. Kurz and D.J. Fisher, *Fundamentals of Solidification*, Third Edition, Trans Tech Publications, Switzerland, 1989.

[10] J.D. Hunt and S.-Z. Lu, "Numerical Modeling of Cellular/Dendritic Array Growth: Spacing and Structure Predictions", *Metallurgical and Materials Transactions A*, Vol. 27A, 1996, 611-623.

[11] M.H. Burden and J.D. Hunt, "Columnar and Dendritic Growth II", *Journal of Crystal Growth*, Vol. 22, 1974, 109-116.

[12] M.H. Burden and J.D. Hunt, "Columnar and Dendritic Growth I", *Journal of Crystal Growth*, Vol. 22, 1974, 99-108.

[13] R. Trivedi and W. Kurz, "Dendritic Growth", *International Materials Reviews*, 1994, Vol. 39, No. 2, 49-74.

[14] S. Kou, *Welding Metallurgy*, John Wiley & Sons, New York, NY, 1987.

[15] S.C. Flood and J.D. Hunt, "A Numerical Study of the Columnar-Equiaxed Transition", *Modeling of Casting and Welding Processes II* J.A. Dantzig and J.T. Berry, Editors, The Metallurgical Society of AIME, 1984, 207-218.

[16] S.C. Flood and J.D. Hunt, "Columnar and Equiaxed Growth; I. A Model of a Columnar Front with a Temperature Dependent Velocity", *Journal of Crystal Growth*, Vol. 82, 1987, 543-551.

[17] S.C. Flood and J.D. Hunt, "Columnar and Equiaxed Growth; II. Equiaxed Growth Ahead of a Columnar Front", *Journal of Crystal Growth*, Vol. 82, 1987, 552-560.

[18] S.G.R. Brown and J.A. Spittle, "A 2D Implicit Finite Difference Model to Simulate the Columnar to Equiaxed Zone Transition", *Modeling of Casting, Welding and Advanced Solidification Processes V* M. Rappaz, M.R. Osgu, and K.W. Mahin, Editors, The Minerals, Metals & Materials Society, 1991, 395-402.

[19] J.A. Spittle and M.R. Tadayon, "Observations on the Numerical Prediction of the Columnar to Equiaxed Grain Transition in Castings", *Cast Metals* Vol. 7, No. 2, 1994, 123-126.

[20] J.A. Spittle and S.G.R. Brown, "A Computer Simulation of the Influence of Processing Conditions on As-Cast Grain Structures", *Journal of Materials Science*, Vol. 23, 1989, 1777-1781.

[21] J.A. Spittle and S.G.R. Brown, "Computer Simulation of the Effects of Alloy Variables on the Grains Structures of Castings", *Acta Metallurgica*, Vol. 37, No. 7, 1989, 1803-1810.

[22] S.G.R. Brown and J.A. Spittle, "Computer Simulation of Grain Growth and Macrostructure Development During Solidification", *Materials Science and Technology*, Vol 5, 1989, 362-368.

[23] Ch.-A. Gandin, and M. Rappaz, "Probablilistic Modelling of Microstructure Formation in Solidification Processes", *Acta Metallurgica et Materialia*, Vol. 41, No. 2, 1993, 345-360.

[24] Ch.-A. Gandin, M. Rappaz, and R. Tintillier, "Three-Dimensional Probabilistic Simulation of Solidification Grain Structures: Application to Superalloy Precision Castings", *Metallurgical and Materials Transactions A*, Vol. 24A, 1993, 467-479.

[25] Ch.-A. Gandin, M. Rappaz, and R. Tintillier, "3-Dimensional Simulation of the Grain Formation in Investment Castings", *Metallurgical and Materials Transactions A*, Vol. 25A, 1994, 629-635.

[26] C. Beckermann and C.Y. Wang, "Incorporating Interfacial Phenomena in Solidification Models", *Journal of Materials*, Vol. 46, No.1, 1994, 42-47.

[27] B.Q. Li and P.N. Anyalebechi, "A Micro/Macro Model for Fluid Flow Evolution and Microstructure Formation in Solidification Processes", *International Journal of Heat and Mass Transfer*, Vol. 38, No. 13, 1995, 2367-2381.

[28] Ch.-A. Gandin and M. Rappaz, "A Coupled Finite Element-Cellular Automaton Model for the Prediction of Dendritic Grain Structures in Solidification Processes", *Acta Metallurgica et Materialia*, Vol. 42, No. 7, 1994, 2233-2246.

[29] M. Rappaz, Ch.-A. Gandin, J.-L. Desboilles, and P. Thévoz, "Prediction of Grain Structures in Various Solidification Processes", *Metallurgical and Materials Transactions A*, Vol. 27A, 1996, 695-705.

[30] Z. Yang and T. DebRoy, "Weld Metal Microstructure Prediction from Fundamentals of Transport Phenomena and Phase Transformation Theory", *Science and Technology of Welding and Joining*, Vol. 2, No. 2, 1997, 53-58.

[31] K. Mundra, T. DebRoy, S.S. Babu, and S.A. David, "Weld Metal Microstructure Calculations from Fundamentals of Transport Phenomena in the Arc Welding of Low-Alloy Steels", *Welding Journal*, Vol. 76, No. 4, 1997, 163s-171s.

Spot Welds 28-39.

[32] Y. Sharir, J.Pelleg, and A. Grill, "Effect of Arc Vibration and Current Pulses on Microstructure and Mechanical Properties of TIG Tantalum Welds", *Metals Technology*, Vol. 5, 1978, 190-196.

[33] E.V. Bardokin, V.I. Livenets, V.A. Okishor, V.N. Dubrov, I.G. Tyumentsev, "Structure and Properties of Weld Metal in Welding in an Alternating Longitudinal Electromagnetic Field of Low Frequency", *Svar. Proiz.*, No. 11, 1975, 12-14.

[34] M. Kato, F. Matsuda, and T. Senda, "Solidification Mode in Aluminum Weld Metal", *Transactions of the Japan Welding Society*, Vol. 3, No. 1, 1972, 69-76.

[35] Y. Arata, F. Matsuda, and A. Matsui, "Effect of Welding Condition on Solidification Structure in Weld Metal of Aluminum Alloy Sheets", *Transactions of the Japan Welding Research Institute*, Vol. 3, No. 1, 1974, 89-97.

[36] T. Ganaha and H.W. Kerr, "TIG Weld Solidification Structures in Carbon Sheet Steels", *Metals Technology*, Vol. 5, 1978, 62-69 .

[37] T. Ganaha, B.P. Pearce, and H.W. Kerr, "Grain Structures in Aluminum Alloy GTA Welds", *Metallurgical Transactions A*, Vol. 11A, No. 8, 1980, 1351-1359.

[38] S. Kou and Y. Le, "Welding Parameters and the Grain Structure of Weld Metal - A Thermodynamic Consideration", *Metallurgical Transactions A*, Vol. 19A, 1988, 1075-1082.

[39] J.C. Villefuerte, E. Pardo and H.W. Kerr, "The Effect of Alloy Composition and Welding Conditions on Columnar-Equiaxed Transitions in Ferritic Stainless Steel Gas-Tungsten Arc Welds", *Metallurgical Transactions A*, Vol. 21A, No. 7, 1990, 2009-2019.

[40] D. Rosenthal, "Mathematical Theory of Heat Distribution During Welding and Cutting", *Welding Journal*, Vol. 20, No. 5, 1941, 220s-234s.

[41] D. Rosenthal, "The Theory of Moving Sources of Heat and Its Application to Metal Treatments", *Transactions of the ASME*, November, 1946, 849-866.

[42] J.G. Garland, "Weld Pool Solidification Control", *Metal Construction*, Vol. 6, No. 4, 1974, 121-127.

[43] J.C. Villefuerte and H.W. Kerr, "The Effect of Abrasive Cleaning on Columnar-to-Equiaxed Transitions in Ferritic Stainless Steel GTA Welds", *Trends in Welding Research*, S.A. David and J.M Vitek, Editors, ASM International, Metals Park, OH, 1992, 187-191.

[44] B.P. Pearce and H.W. Kerr, "Grain Refinement in Magnetically Stirred GTA Welds of Aluminum Alloys", *Metallurgical Transactions B*, Vol. 12A, 1981, 479-486.

[45] D.L. Hallum and W.A. Baeslack III, "Nature of Grain Refinement in Titanium Alloy Welds By Microcooler Inoculation", *Welding Journal*, Vol. 69, No. 9, 1990, 326s-336s.

[46] F. Matsuda, H. Nakagawa, K. Nakata, and R. Ayani, "Effect of Electromagnetic Stirring on Weld solidification Structure of Aluminum Alloys", *Transactions of the Japan Welding Research Institute*, Vol. 7, No. 1, 1978, 111-127.

[47] J.C. Villefuerte and H.W. Kerr, "Electromagnetic Stirring and Grain Refinement in Stainless Steel GTA Welds", *Welding Journal*, Vol. 69, No. 1, 1990, 1s-13s.

[48] J.C. Villefuerte, H.W. Kerr, and S.A. David, "Mechanisms of Equiaxed Grain Formation in Ferritic Stainless Steel Gas Tungsten Arc Welds", *Materials Science and Engineering*, Vol. A194, 1995, 187-191.

[49] Y. Le and S. Kou, "Formation of Three Types of New Grains in the Weld Metal", *Advances in Welding Science and Technology*, S.A. David, Editor, ASM International., Metals Park, OH, 1986, 139-144.

[50] S. Kou and Y. Le, "Nucleation Mechanisms and Grain Refining of Weld Metal", *Welding Journal*, Vol. 65, No. 12, 1986, 305s-313s.

[51] J.C. Villefuerte and H.W. Kerr, "Grain Structures in Gas Tungsten Arc Welds of Austenitic Stainless Steels with Ferrite Primary Phase", *Metallurgical Transactions A*, Vol. 21A, No. 4, 1990, 979-985.

[52] G.N. Heintze and R. McPherson, "Solidification Control of Submerged Arc Welds in Steels By Inoculation with Ti", *Welding Journal*, Vol. 65, No. 3, 1986, 71s-82s.

[53] W.A. Petersen, "Fine Grained Weld Structures", *Welding Journal*, Vol. 52, No. 2, 1973 74s-79s.

[54] E. Pardo and D.C. Weckman, "A Numerical Model of the Gas Metal Arc Welding Process", *Modeling of Casting and Welding Processes IV*, A.F. Giamei and G.J. Abbaschian, Editors, The Minerals, Metals & Materials Society, 1988, 187-195.

[55] E. Pardo and D.C. Weckman, "Prediction of Weld Pool and Reinforcement Dimensions of GMA Welds Using a Finite-Element Model", *Metallurgical Transactions B*, Vol. 20B, 1989, 937-947.

[56] S. Kou and D.K. Sun, "Fluid Flow and Weld Penetration in Stationary Arc Welds", *Metallurgical Transactions A*, Vol. 16A, 1985, 203-213.

[57] S. Kou and Y.H. Wang, "Weld Pool Convection and Its Effect", *Welding Journal*, Vol. 65, No. 3, 1986, 63s-70s.

[58] S. Kou and Y.H. Wang, "Computer Simulation of Convection in Moving Arc Weld Pools", *Metallurgical Transactions A*, Vol. 17A, 1986, 2271-2277.

[59] T. Zacharia, S.A. David, J.M. Vitek and T. DebRoy, "Weld Pool Development during GTA and Laser Beam Welding of Type 304 Stainless Steel, Part I- Theoretical Analysis", *Welding Journal*, Vol. 68, No. 12, 1989, 499s-509s.

[60] T. Zacharia, S.A. David, J.M. Vitek and T. DebRoy, "Weld Pool Development during GTA and Laser Beam Welding of Type 304 Stainless Steel, Part II- Experimental Correlation", *Welding Journal*, Vol. 68, No. 12, 1989, 510s-519s.

[61] C.S. Wu and K.C. Tsao, "Modelling the Three-Dimensional Fluid Flow and Heat Transfer in a Moving Weld Pool", *Engineering Computing*, Vol. 7, 1990, 241-248.

[62] S-D. Kim and S-J. Na, "Effect of Weld Pool Deformation on Weld Penetration in Stationary Gas Tungsten Arc Welding", *Welding Journal*, Vol. 71, No. 5, 1992, 179s-193s.

[63] R.T.C. Choo and J. Szekely, "The Effect of Gas Shear Stress on Marangoni Flows in Arc Welding", *Welding Journal*, Vol. 70, No. 9, 1991, 223s-233s.

[64] A. Matsunawa and S. Yokoya, "Fluid Flow and its Effect on Penetration Shape in Stationary Arc Welds", *Trends in Welding Research*, S.A. David and J.M Vitek, Editors, ASM International, Metals Park, OH, 1989, 31-35.

[65] A. Matsunawa, "Modeling of Heat and Fluid Flow in Arc Welding", *Trends in Welding Research*, S.A. David and J.M Vitek, Editors, ASM International, Metals Park, OH, 1992, 3-16.

[66] T. Zacharia, S.A. David and J.M. Vitek, "Effect of Evaporation and Temperature-Dependent Material Properties on Weld Pool Development", *Metallurgical Transactions B*, Vol. 22B, 1991, 233-241.

[67] M.C. Tsai and S. Kou, "Weld Pool Convection and Expansion due to Density Variations", *Numerical Heat Transfer, Part A*, Vol. 17, 1990, 73-89.

[68] M.C. Tsai and S. Kou, "Electromagnetic-Force-Induced Convection in Weld Pools with a Free Surface", *Welding Journal*, Vol. 69, No. 6, 1990, 241s-246s.

[69] M.C. Tsai and S. Kou, "Marangoni Convection in Weld Pools with a Free Surface", *International Journal for Numerical Methods in Fluids*, Vol. 9, 1989, 1503-1516.

[70] T. Zacharia, A.H. Eraslan, and D.K. Aidun, "Modeling of Autogenous Welding", *Welding Journal*, Vol. 67, No. 3, 1988, 53s-62s.

[71] T. Zacharia, A.H. Eraslan, and D.K. Aidun, and S.A. David, "Three-Dimensional Transient Model for Arc Welding Process", *Metallurgical Transactions B*, Vol. 20B, 1989, 645-659.

[72] T. Zacharia, S.A. David, J.M. Vitek and H.G. Kraus, "Computational Modeling of Stationary Gas-Tungsten-Arc Weld Pools and Comparison to Stainless Steel 304 Experimental Results", *Metallurgical Transactions B*, Vol. 22B, 1991, 243-257.

[73] C.S. Wu and L. Dorn, "Computer Simulation of the Fluid Dynamics and Heat Transfer in Full- Penetrated TIG Weld Pools with Surface Depression", *Computational Materials Science*, Vol. 2, 1994, 341-349.

[74] K. Hong, "A Comprehensive Thermo-Fluids Model of Arc Welding Processes", Ph.D. Thesis, University of Waterloo, 1995.

[75] G.M. Oreper and J. Szekely, "Heat- and Fluid-flow Phenomena in Weld Pools", *Journal of Fluid Mechanics*, Vol. 147, 1984, 53-79.

[76] M. Lu and S. Kou, "Power and Current Distributions in Gas Tungsten Arcs", *Welding Journal*, Vol. 67, No. 2, 1988, 29s-34s.

[77] N.S. Tsai and T.W. Eagar, "Distribution of the Heat and Current Fluxes in Gas Tungsten Arcs", *Metallurgical Transactions B*, Vol. 16B, 1985, 841-846.

[78] R.T.C. Choo, J. Szekely, and R.C. Westhoff, "Modeling of High-Current Arcs with Emphasis on Free Surface Phenomena in the Weld Pool", *Welding Journal*, Vol. 69, No. 9, 1990, 346s-361s.

[79] H.B. Smartt, J.A. Stewart, and C.J. Einerson, "Heat Transfer in Gas Tungsten Arc Welding", in Proceedings of the Conference *'85 ASM International Welding Congress*, Toronto, Ontario, 14-17 October 1985.

[80] M.C. Tsai and S. Kou, "Heat Transfer and Fluid Flow in Welding Arcs Produced by Sharpened and Flat Electrodes", *International Journal of Heat and Mass Transfer*, Vol. 33, No. 10, 1990, 2089-2097.

[81] S-Y. Lee and S-J. Na, "A Numerical Analysis of a Stationary Gas Tungsten Welding Arc Considering Various Electrode Angles", *Welding Journal*, Vol. 75, No. 9, 1996, 269s-279s.

[82] P. Dutta, Y. Joshi, and R Janaswamy, "Thermal Modeling of Gas Tungsten Arc Welding with Nonaxisymmetric Boundary Conditions", *Numerical Heat Transfer, Part A*, Vol. 27, 1995, 499-518.

[83] W.-H. Kim, H.G. Fan, and S.-J. Na, "A Mathematical Model of Gas Tungsten Arc Welding Considering the Cathode and the Free Surface of the Weld Pool", *Metallurgical and Materials Transactions B*, Vol. 28A, 1997, 679-686.

[84] ASM Committee on GTAW, "Gas Tungsten Arc Welding", *Metals Handbook, Volume 6: Welding, Brazing, and Soldering*, Ninth Edition, 1983, 182-213.

[85] R.T.C. Choo and J. Szekely, "The Possible Role of Turbulence in GTA Weld Pool Behaviour", *Welding Journal*, Vol. 73, No. 2, 1994, 25s-31s.

[86] K. Hong, D.C. Weckman and A.B. Strong, "The Influence of Thermo-fluids Phenomena in Gas Tungsten Arc Welds in High and Low Thermal Conductivity Metals", submitted to *Canadian Metallurgical Quarterly*, 1996.

[87] K. Hong, D.C. Weckman, and A.B. Strong, "The Predicted Influence of turbulence in Stationary Gas Tungsten Arc Welds", *Trends in Welding Research*, S.A. David and J.M Vitek, Editors, ASM International, Metals Park, OH, 1995, 399-404.

and 35th

[88] M. Kanouff and R. Greif, "The Unsteady Development of a GTA Weld Pool", *International Journal of Heat and Mass Transfer*, Vol. 35, No. 4, 1992, 967-979.

[89] S.-D. Kim and S.-J. Na, "A Study on Heat and Mass Flow Stationary Gas Tungsten Arc Welding Using the Numerical Mapping Method", *Proceedings of the Institution of Mechanical Engineers, Part B: Journal of Engineering Manufacture*, Vol. 203, 1989, 233-242.

[90] F.M. White, *Fluid Mechanics*, Second Edition, McGraw-Hill, New York, 1986.

[91] B.E. Launder and D.B. Spalding, *Lectures in Mathematical Models of Turbulence*, Academic Press, London and New York, 1972.

[92] J. Szekely, *Fluid Flow Phenomena in Metals Processing*, Academic Press, New York, 1979.

[93] J.R. Welty, C.E. Wicks, and E. Wilson, *Fundamentals of Momentum, Heat and Mass Transfer*, Third Edition, John Wiley & Sons, New York, 1984.

[94] *Metals Handbook - Vol. 8 Metallography, Structures and Phase Diagrams*, Eighth Edition, T. Lyman, Editor, ASM International, Materials Park, OH, 1973, 259.

[95] R.D. Pehlke, A. Jeyarajan and H. Wada, *Summary of Thermal Properties for Casting Alloys and Mold Materials*, NTIS Report No. NSF/MEA-82028, University of Michigan, Ann Arbor, MI, 1982.

[96] T. Iida and R.I.L. Gutherie, *The Physical Properties of Liquid Metals*, Oxford University Press, New York, NY, 1988.

[97] J.P. Holman, *Heat Transfer*, Seventh Edition, McGraw-Hill Publishing Company, New York, NY, 1990.

[98] C.Y. Ho, M.W. Ackerman, K.Y. Wu, S.G. Oh and T.N. Havill, "Thermal Conductivity of Ten Selected Binary Alloy Systems", *Journal of Physical and Chemical Reference Data*, Vol. 7, No. 3, 1978, 959-1177.

[99] S. Ganesan and D.R. Poirier, "Densities of Aluminum-Rich Aluminum-Copper Alloys during Solidification", *Metallurgical Transactions A*, Vol. 18A, 1987, 721-723.

[100] A.B. Strong, Professor of Engineering, University of Waterloo, *private communication.*

[101] X. Huang and B.G. Thomas, "Modeling of Steel Grade Transition in the Continuous Slab Casting Process", *Metallurgical Transactions B*, Vol. 24B, 1993, 379-393.

[102] K.H. Huebner and E.A. Thornton, *The Finite Element Method for Engineers*, Second Edition, John Wiley & Sons, New York, 1982.

[103] I. Jin and J.G. Sutherland, "Thermal Analysis of Solidification of Aluminum Alloys during Continuous casting", *Solidification and Casting of Metals*, A. Nicholson, Editor, Sheffield Metallurgical and Engineering Association and University of Sheffield, Sheffield, 1977, 256-259.

[104] A.N. Brooks and J.T.R. Hughes, "Streamline Upwind/Petrov-Galerkin Formulations for Convection Dominated Flows with Particular Emphasis on The Incompressible Navier-Stokes Equations", *Computer Methods in Applied Mechanics and Engineering*, Vol. 32, 1982, 199-259.

[105] D.W. Kelly, S. Nakazawa, O.C. Zienkiewicz and J.C. Heinrich, "A Note on Upwinding and Anisotropic Balancing Dissipation in Finite Element Approximation to Convective-Diffusion Problems", *International Journal of Numerical Methods in Engineering*, Vol. 15, 1980, 1705-1711.

[106] J.E. VanderKwaak, P.A. Forsyth, K.T.B. MacQuarrie and E.A. Sudicky, *WATSOLV Ver. 2.06, Iterative Sparse Matrix Solver Package*, Waterloo Centre for Groundwater Research, University of Waterloo, 1995.

[107] F.M. White, *Viscous Fluid Flow*, Second Edition, McGraw-Hill, New York, 1991.

[108] F. Thomasset, *Implementation of Finite Element Methods for Navier-Stokes Equations*, Springer-Verlag, New York, 1981.

[109] M. Bercovier and M. Engelman, "A Finite Element for the Numerical Solution of Viscous Incompressible Flows", *Journal of Computational Physics*, Vo. 30, 1979, 181-201.

[110] M. Fortin and F. Thomasset, "Mixed Finite-Element Methods for Incompressible Flow Problems", *Journal of Computational Physics*, Vol. 31, 1979, 113-145.

[111] G. De Vahl Davis, and I.P. Jones, "Natural Convection in a Square Cavity: A Comparison Exercise", *International Journal for Numerical Methods in Fluids*, Vol. 3, 1983, 227-248.

[112] A. Zebib, G.M. Homsy, and E. Meiburg, "High Marangoni number convection in a square cavity", *Physics of Fluids*, Vol. 28, No. 12, 1985, 3467-3476.

[113] Christy, Bill, Welding Technologist, Alcan International Limited, *private communication.*

[114] Lancaster, J.F., Editor, *The Physics of Welding*, Second Edition, Pergamon Press, Oxford, 1986.

[115] Aluminum Association Technical Committee on Welding and Joining, "Arc Welding of Aluminum Alloys", *Metals Handbook, Volume 6: Welding, Brazing, and Soldering*, Ninth Edition, 1983, 373-399.

[116] The Aluminum Association, *Welding Aluminum*, The American Welding Society.

[117] *Instructions for HW-27 TIG Welding Torch*, Form 11-332-B, Union Carbide Welding Products, 1971.

[118] Roy L. Anderson, "Revealing Microstructures in Metals", *Scientific Paper 425-C000-P2*, Westinghouse Research Laboratories, Pittsburgh, Pennsylvania, December 22, 1961.

[119] "ASTM Standard E112-88, Standard Test Methods for Determining Average Grain Size", *Annual Book of ASTM Standards*, Vol. 03.01, Philadelphia, PA, 1994, p. 227-252.

[120] Ottosen, N. and H. Petersson, *Introduction to the Finite Element Method*, Prentice Hall, New York, 1992.

[121] T. Zacharia, A.H. Eraslan and D.K. Aidun, "Modeling of Autogenous Welding", *Welding Journal*, Vol. 67, No. 3, 1988, 53s-62s.

[122] T. Ejima, T. Yamamura, N. Uchida, Y. Matsuaki, and M. Nikaido, *Journal of the Japan Institute for Metals*, Vol. 44, 1980, 316-323.

[123] M. Gaumann, R. Trivedi, and W. Kurz, "Nucleation ahead of the Advancing Interface in Directional Solidification", in Proceedings of the Conference *Rapidly Quenched Alloys*, Hungary, 1996.

[124] D.G. McCartney, "Grain Refining of Aluminium and its Alloys Using Inoculants", *International Materials Reviews*, Vol. 34, No. 5, 1989, 247-260.

[125] L.R. Morris, J.R. Carruthers, A. Plumtree, and W.C. Winegard, "Growth Twinning in Aluminum Alloys", *Transactions of the Metallurgical Society of AIME*, **236**, September 1966, 1286-1291.

[126] S. Henry, P. Jarry, and M. Rappaz, "EBSD Investigation of the Texture of Feathery Crystals in Aluminum Alloys", in Proceedings of the Conference *Solidification Processing*, J. Beech and H. Jones, Editors, University of Sheffield, UK, 7-10 July, 1997, 660-664.

[127] M. Katoh, Professor of Engineering, Kyushu Institute of Technology, Japan, *private communication.*

IMAGE EVALUATION
TEST TARGET (QA-3)

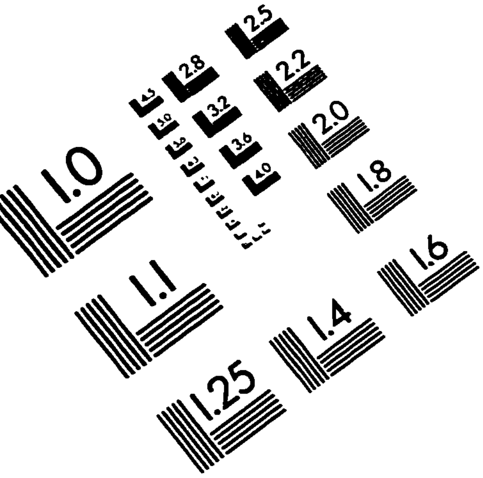

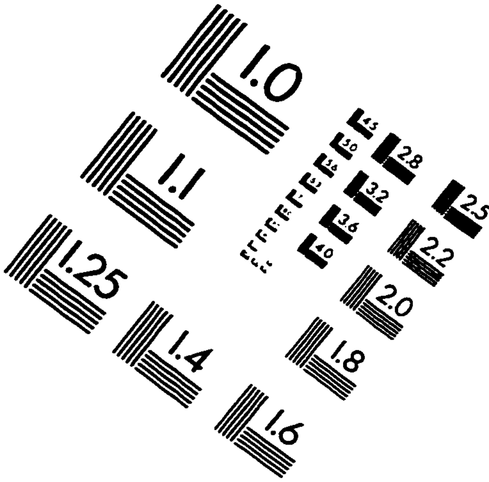

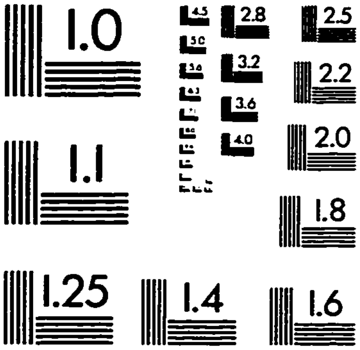

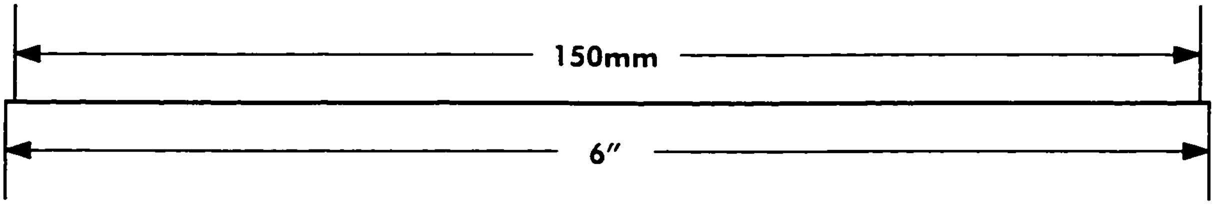

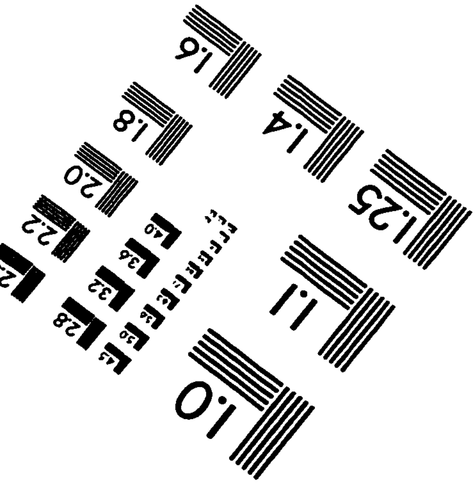

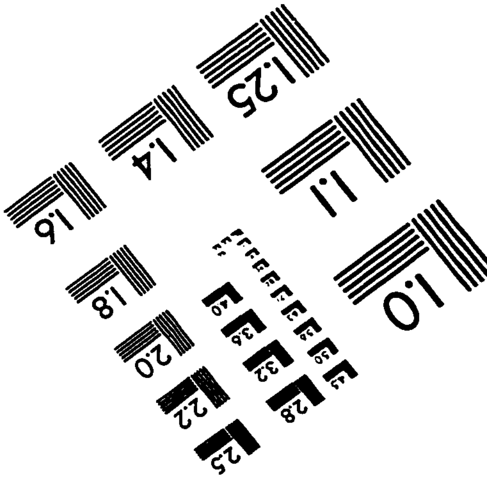

APPLIED IMAGE, Inc
1653 East Main Street
Rochester, NY 14609 USA
Phone: 716/482-0300
Fax: 716/288-5989